Hydrodésoxygénation de composés phénoliques modèles. Évaluation de phases actives : sulfures, oxyde, métallique et phosphure

Vinicius Ottonio Oliveira Gonçalves

THÈSE

Pour l'obtention du Grade de

DOCTEUR DE L'UNIVERSITE DE POITIERS

(Faculté des Sciences Fondamentales et Appliquées)
(Diplôme National - Arrêté du 25 mai 2016)

Ecole Doctorale : Sciences pour l'environnement GAY LUSSAC N°523

Secteur de Recherche : Chimie organique, minérale, industrielle

Présentée par :

Vinicius Ottonio OLIVEIRA GONÇALVES

Ingénieur Chimiste

****

HYDRODÉSOXYGÉNATION DE COMPOSÉS PHÉNOLIQUES MODÈLES. ÉVALUATION DE PHASES ACTIVES : SULFURES, OXYDE, MÉTALLIQUE ET PHOSPHURE

****

Directeur de Thèse : Frédéric Richard, Maître de Conférences – HDR, Université de Poitiers

Soutenue le 24 mai 2017 devant la Commission d'Examen

****

JURY

Rapporteurs :
Françoise MAUGE, Directeur de Recherche CNRS, LCS Caen
Sébastien ROYER, Professeur, Université Lille 1

Examinateurs :
Michael BADAWI, Maître de Conférences, Université de Lorraine
Fabio BELLOT NORONHA, Professeur, National Institute of Technology, Brésil
Jean-Marc CLACENS, Directeur de Recherche CNRS, IC2MP
Frédéric RICHARD, Maître de Conférences - HDR, Université de Poitiers

Remerciements

Ces travaux de thèse ont été réalisés au sein de l'équipe Catalyse et Milieux non-Conventionnels (E4) de l'Institut de Chimie des Milieux et Matériaux de Poitiers (IC2MP).

Je tiens à remercier mon directeur de thèse Monsieur Frédéric Richard. Pour avoir dirigé mes travaux, pour toutes les discussions scientifiques très enrichissantes et surtout pour m'avoir laissé la liberté de proposer des sujets et des protocoles de travail tout au long de ces trois années de travail. Ses conseils et son orientation m'ont permis de dépasser les difficultés souvent rencontrées dans un travail de recherche en général et bien évidement au cours d'une thèse.

Je tiens à remercier le Conselho Nacional de Desenvolvimento Científico e Tecnológico (CNPq) pour avoir financé ma bourse de thèse dans le cadre du programme « Sciences sans Frontière ».

Les caractérisations et les mesures expérimentales, nécessaires à cette étude, n'auraient pu être réalisées sans la plateforme et l'aide des techniciens de l'IC2MP que je tiens à remercier.

Je veux exprimer ma reconnaissance aux rapporteurs, à Madame Françoise. MAUGE (Directrice de recherche CNRS au LCS de Caen) et à Monsieur Sébastien Royer (Professeur à l'Université de Lille). Je suis également honoré de la présence dans mon jury de thèse de Monsieur Fabio Bellot Noronha (Professeur au NIT, Brésil), de Monsieur Jean-Marc Clacens (Directeur de recherche à l'IC2MP) et de Monsieur Michael Badawi (Université de Lorraine).

A tous mes amis du « Hall Réacteurs sous pression », du bâtiment B27 et de l'ENSIP. Je vous remercie pour l'amitié quotidienne, l'aide avec les expériences et discussions très enrichissantes.

Pour conclure, je dédie mon manuscrit à ma famille et la remercie infiniment pour son soutien durant ces années d'étude.

L'ordre de mes remerciements n'a pas d'importance. Tous ceux que j'ai nommés m'ont apporté à un moment ou à un autre, un soutien décisif.

A tous ceux que j'aime

Sommaire

Sommaire

Sommaire

Sommaire

Introduction générale

Introduction générale

En raison de l'augmentation continue de la demande énergétique mondiale, de la diminution graduelle des ressources d'origine fossile et de la modification de l'équilibre biologique due aux émissions des gaz à effet de serre, l'utilisation de nouvelles sources pour la production durable de carburants et de produits chimiques est aujourd'hui devenue primordiale.

Dans ce contexte, la valorisation de la biomasse lignocellulosique en produits à haute valeur ajoutée et en biocarburants, est d'un intérêt crucial, notamment car ce type de biomasse n'entre pas en compétition avec l'alimentation humaine. La transformation de cette biomasse pourra être réalisée dans une bioraffinerie dont le concept rappelle celui développé dans le raffinage des produits pétroliers. En effet, il s'agit d'un ensemble industriel, mettant en œuvre de nombreux procédés technologiques (thermiques, chimiques et biochimiques), afin de permettre la transformation de nombreuses sources de biomasse, qui peuvent être d'origine agricole, forestière ou algale, en produits biosourcés (biocarburants, biomolécules, agromatériaux,…).

Ces travaux de thèse s'intéressent particulièrement à la valorisation de composés obtenus soit directement après pyrolyse de la biomasse lignocellulosique, soit plus spécifiquement après dépolymérisation de la lignine. Par exemple, les biohuiles obtenues ne peuvent pas être utilisées directement comme carburants en raison notamment de leur faible pouvoir calorifique et de leur mauvaise stabilité au cours du temps. Pour les valoriser comme carburants, il est donc nécessaire de leur faire subir des traitements permettant de les désoxygéner. De plus, comme ces huiles contiennent des motifs aromatiques oxygénés (composés phénoliques), elles peuvent également être valorisées pour la production de molécules aromatiques simples (Benzène, Toluène, Xylènes). La désoxygénation de ces molécules phénoliques peut être obtenue par la mise en œuvre d'un procédé catalytique d'hydrodésoxygénation (HDO), analogue au procédé d'hydrodésulfurisation (HDS) au cours duquel le soufre est éliminé sous forme d'H_2S, et au procédé d'hydrodésazotation (HDN) au cours duquel l'azote est éliminé sous forme de NH_3, ces deux procédés étant largement utilisés dans le traitement des charges pétrolières.

L'objectif de ce travail de thèse est de modéliser la désoxygénation de ces fractions phénoliques en mettant en évidence la nature des sites actifs des différentes phases catalytiques

étudiés, ainsi que les mécanismes réactionnels impliqués. Pour cela, les isomères du crésol (o-, m- et p-crésol) ont été utilisés comme molécules oxygénées modèles. Leur transformation a été examinée dans des conditions expérimentales relativement sévères (2 - 4 MPa et 250 – 340 °C). Plusieurs phases catalytiques ont été évaluées : des solides à base de molybdène (phases sulfures et oxyde) et à base de nickel (phases métallique et phosphure). L'influence du support catalytique a également été examinée, que ce soit sur les oxydes de molybdène (SiO_2, SBA-15, Al_2O_3) ou sur les phases à base de nickel (SiO_2 et ZrO_2).

Ce mémoire de thèse est divisé en six chapitres. Le premier chapitre est une étude bibliographique axée notamment sur la présentation des différents types de biocarburants, du concept de bioraffinerie et des procédés technologiques mis en œuvre, des catégories de matières premières susceptibles d'être transformées ainsi que des produits qui peuvent être obtenus. Ce chapitre s'intéresse également aux réactions d'hydrodésoxygénation de composés phénoliques effectuées en présence des phases catalytiques les plus utilisées.

Ensuite, le deuxième chapitre est dédié à la présentation des modes de préparation des différents solides, des techniques de caractérisations employées ainsi qu'à la description des dispositifs expérimentaux utilisés pour mesurer les propriétés catalytiques des différents solides préparés.

Le troisième chapitre porte sur l'étude de deux catalyseurs sulfures à base de molybdène (Mo/Al_2O_3 et $CoMo/Al_2O_3$) en transformation des trois isomères du crésol. L'influence de la position du groupement méthyle sur l'activité et la sélectivité des deux catalyseurs est discutée. La nature de la phase sulfure (MoS_2 vs CoMoS) sur ses propriétés désoxygénantes est également montrée.

Le quatrième chapitre est consacré à l'influence du support de l'oxyde de molybdène en HDO du m-crésol. Cette étude a été réalisée dans le cadre d'une collaboration avec l'UCCS (Unité de Catalyse et Chimie du Solide, Lille). Dans ce cas, une silice mésoporeuse non ordonné (SiO_2), une silice mésoporeuse de haute surface spécifique (SBA-15) et une alumine (Al_2O_3) ont été choisies comme supports catalytiques. Les propriétés catalytiques en HDO du m-crésol ont pu notamment être reliées aux différentes caractéristiques des matériaux mesurées à l'aides

de différentes techniques (chimisorption d'oxygène, microscopie électronique, thermodésorption d'ammoniac, réduction en température programmée).

Le cinquième chapitre est dédié à l'étude cinétique de la transformation des isomères de crésol sur une phase phosphure de nickel (Ni_2P) supportée sur SiO_2. Cette étude a notamment permis d'aider à la description de la nature des sites actifs de cette phase catalytique. Cette étude a été réalisée dans le cadre d'une collaboration avec le NIT (National Institute of Technology, Rio de Janeiro, Brésil). Plusieurs paramètres ont également été étudiés : l'influence (i) de la position du groupement méthyle, (ii) de la pression et (iii) de la température.

Le dernier chapitre porte sur la comparaison de catalyseurs à base de nickel soit sous forme métallique (Ni/SiO_2 et Ni/ZrO_2), soit sous forme phosphure (Ni_2P/SiO_2 et Ni_2P/ZrO_2), la réaction modèle utilisée étant l'HDO du m-crésol. Cette étude a été également réalisée en partenariat avec le NIT (National Institute of Technology, Rio de Janeiro, Brésil). Les différents solides ont été préparés et caractérisés par plusieurs techniques afin de mieux comprendre l'impact de l'ajout du phosphore sur un catalyseur à base de nickel, mais également d'examiner le rôle du support (SiO_2 vs ZrO_2) pour ces deux phases (Ni et Ni_2P).

Chapitre 1 : Partie bibliographique

Chapitre 1 : Partie bibliographique

Ce chapitre présente les biocarburants dits de première génération, le concept de bioraffinerie et son importance, ainsi que les méthodes de transformation de la biomasse en produits chimiques et biocombustibles. Les propriétés catalytiques de différentes phases (sulfures, métalliques et phosphures) en HDO de composés phénoliques seront également présentées et discutées.

Les ressources énergétiques de la société actuelle dépendent principalement de sources non renouvelables telles que le pétrole, le charbon, et le gaz naturel. Actuellement, plus de 80% de l'énergie et 90% des produits organiques sont issus des matières pétrolières (Figure 1-1) [1,2].

L'augmentation de la demande énergétique et la diminution graduelle des sources fossiles montrent qu'il est nécessaire de développer des sources renouvelables pour avoir une production durable d'électricité, de chaleur, de carburants, de combustibles, de produits organiques et de polymères [3].

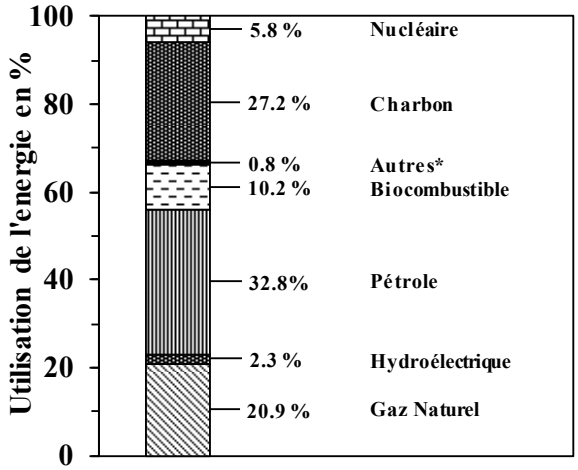

Figure 1-1 : Origine actuelle de l'énergie. *Autres : énergies géothermique, solaire, éolienne, etc [2].

Parmi les sources renouvelables, la biomasse est souvent considérée comme la source la plus importante permettant d'obtenir des composés chimiques et ainsi de diminuer la

dépendance actuelle vis-à-vis des matières fossiles. Sa transformation en produits à haute valeur ajoutée, comme les composés organiques pour l'industrie pharmaceutique ou les biocombustibles, est donc en très grand essor.

Les carburants issus de la biomasse sont dits soit de première, soit de seconde génération [2]. Par exemple, les biocarburants de première génération sont des molécules produites à partir de matières premières comestibles, ils rentrent donc en compétition avec la production alimentaire pour l'homme et les animaux. Ainsi, le développement de la production de ces biocarburants dans une large échelle conduit à des préoccupations éthiques, politiques et environnementales. En revanche, les biocarburants dits de deuxième génération sont produits à base de déchets, de résidus ou de matières non-alimentaires. Leur valorisation n'entraine donc pas ces problèmes. C'est pour cette raison, que le développement de cette famille de biocarburants est d'un intérêt crucial pour de nombreux pays et fait donc appel à de nombreux travaux de recherche et développement.

1. Biocarburants de première génération

Les biocarburants de première génération sont produits à partir des sucres, des amidons, des huiles végétales en utilisant des technologies classiques. La fraction utilisée de ces végétaux se limite généralement aux grains et graines (par exemple, le colza, le soja ou le tournesol) et ne représente qu'une seule partie de la biomasse disponible. Ces matières premières sont souvent des graines de blé, de maïs et de colza. Par exemple, la plantation de 3,4 t/ha de colza peut fournir 40% d'huile, soit 1,4 t/ha [4]. Les biocarburants les plus importants sont le bioéthanol, le biodiesel et le biogaz. Comme le montre la Figure 1-2, la production mondiale de bioéthanol et de biodiesel est en constante augmentation depuis les années 2000 [5].

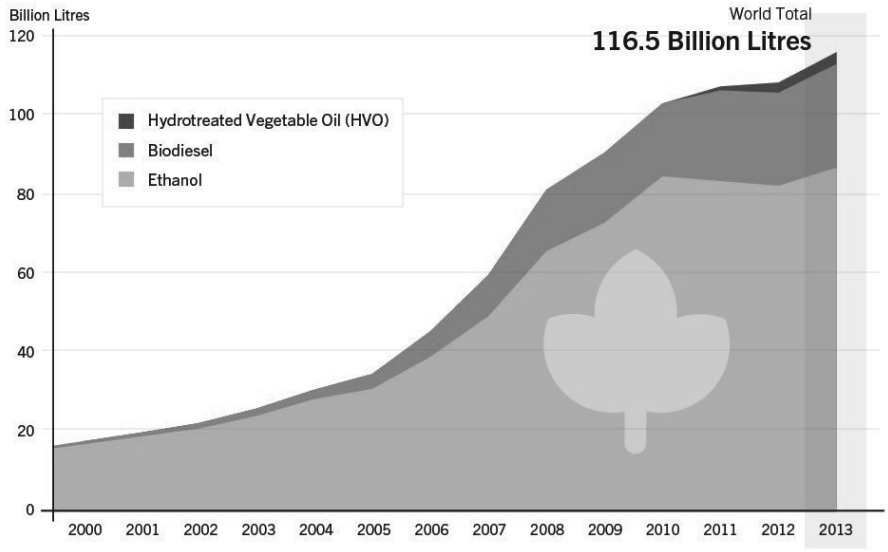

Figure 1-2 : Production mondiale de bioéthanol entre 2000 et 2013 [5].

Le bioéthanol est le biocarburant le plus utilisé au monde [2]. Il peut être obtenu à partir de canne à sucre, de betterave à sucre ou des cultures d'amidon (maïs et blé). La production mondiale totale a atteint 83 milliards de litres en 2013. Plus de 70% de la production provient de deux pays. Les États-Unis sont actuellement les plus grands producteurs de bioéthanol, avec une production de 31 milliards de litres par an, le maïs étant la principale matière première. Le Brésil, le deuxième plus grand producteur et premier exportateur mondial, utilise la canne à sucre comme matière première. La production est d'environ 27 milliards de litres par an. L'Union Européenne et la Chine sont encore très minoritaires sur le marché [5–7].

En 2013, la production mondiale de biodiesel a dépassé 23 milliards de litres (Figure 1-2) dont 10 milliards provenant de l'Union Européenne, notamment d'Allemagne, ce dernier étant le plus gros producteur. Les Etats-Unis ont une production de plus de 4 milliards de litres [7]. Le biodiesel est produit à partir de cultures comme le colza, le tournesol, le soja, mais aussi de l'huile de palme et des huiles utilisées dans l'industrie agroalimentaire.

Le biogaz est aussi une importante source d'énergie renouvelable. Il est obtenu après digestion anaérobique de mélange d'amidon, de fumier, de déchets organiques et de certaines

graisses. Par exemple, il peut être utilisé à la fois pour la production de chaleur, d'électricité ou comme carburant [8]. Toutefois, lorsque le biogaz provient principalement des déchets et des résidus, il peut être classé comme biocarburant de 2ème génération car la matière première n'est pas en concurrence avec l'industrie alimentaire. La production de biogaz est très courante dans la plupart des pays du monde. Ces dernières années, elle a été mise en place par plusieurs pays européens ce qui est économiquement avantageux pour la production d'électricité.

Les principaux avantages de ces matières premières par rapport à celles utilisées pour produire les biocarburants dits de deuxième génération sont liés à leur teneur élevée en sucre ou en huile et à leur conversion facile en biocarburants. Cependant, comme cela a déjà été indiqué, l'inconvénient le plus important est leur concurrence avec les industries alimentaires. Par conséquent, cette utilisation massive entraine une augmentation du prix des céréales et des produits de consommation alimentaire, mais peut également conduire à une diminution de la fertilité des sols [9].

2. Le concept de bioraffinerie

Le concept de bioraffinerie peut englober un grand nombre de technologies visant la conversion de diverses sources de biomasse (bois, herbes, maïs ...) en monomères constitutifs. Il englobe aussi les procédés de transformation de ces monomères en produits à haute valeur ajoutée, mais également en carburants. La bioraffinerie est une installation complexe qui est susceptible d'intégrer des procédés de séparation et de transformation de la matière première pour produire des biocarburants, de l'énergie et des produits chimiques. Ce concept est donc très similaire à celui développé dans les années 50 correspondant au raffinage de pétrole, dans lequel il existe de multiples étapes de séparation, de transformation et de purification [10].

Les principaux piliers d'une bioraffinerie sont basés sur l'idée de diminuer la dépendance actuelle vis-à-vis du pétrole dans un équilibre biologique durable. La représentation de cet équilibre « durable » est illustrée dans la Figure 1-3 [11]. En effet, le carbone produit sous forme de dioxyde de carbone par l'industrie et les moyens de transports est consommé par les plantes. Le CO_2 est ensuite utilisé pour produire des composés constituants de la plante.

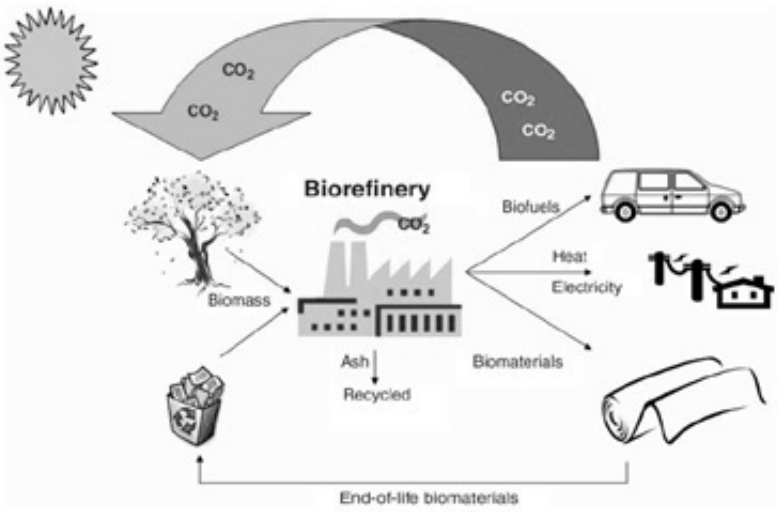

Figure 1-3 : Technologie durable de la bioraffinerie [11]

A l'heure actuelle, les principales matières premières pour la synthèse de biocombustibles et de produits chimiques sont l'amidon, les huiles et la cellulose. Il existe déjà sur le marché plusieurs produits biosourcés qui sont compétitifs avec ceux produits par des voies conventionnelles. Ces produits sont des produits d'entretien, des adhésifs, des colorants, des encres, des lubrifiants, des emballages, du papier, des plastiques et des polymères [10]. Cependant, la tendance dans les prochaines années sera plutôt d'utiliser des sources lignocellulosiques pour la production de ces produits [2,12–14].

Il est possible d'obtenir plusieurs types de molécules habituellement issues du pétrole, celles-ci pouvant être produites dans des complexes de type bioraffinerie. Cependant, il y a encore des avancées à faire aux niveaux scientifiques et technologiques avant que la société puisse bénéficier des molécules issues des résidus lignocellulosiques provenant des plantations et des déchets, et qui sont disponibles en grandes quantités. Les sources de matières premières peuvent donc être à la fois déjà existantes (surtout les déchets) ou provenant de cultures non alimentaires. Par exemple, la Figure 1-4 montre le schéma de principe d'une bioraffinerie uniquement basée sur le bois. La première étape consiste à fractionner cette matière première en lignine d'une part et en cellulose et hemicellulose d'autre part. Ces deux types de polymères

pourraient ensuite être transformés en glucose qui après fermentation conduirait à l'éthanol dit de seconde génération. La lignine pourrait, quant à elle, subir différents traitements : craquage, pyrolyse ou gazéification.

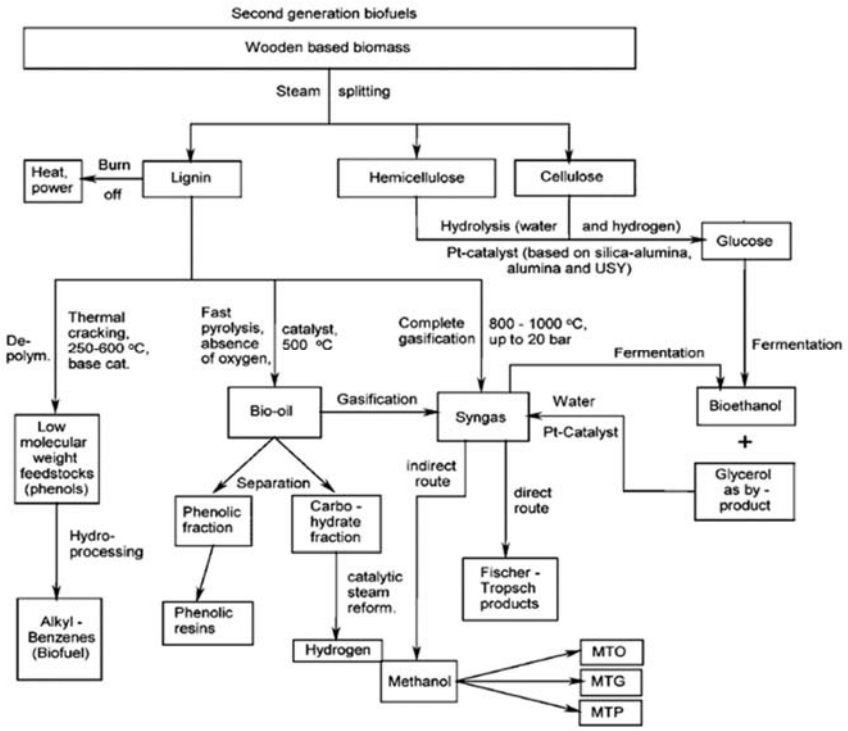

Figure 1-4 : bioraffinerie basée sur la valorisation du bois [2].

La Figure 1-5 présente un schéma plus complet d'une bioraffinerie dans laquelle différents types de matières premières pourront être transformés : des triglycérides, des polysaccharides (amidon par exemple) et des matières lignocellulosiques. Ces matières premières pourraient subir différents traitements (hydrolyse, pyrolyse, hydrotraitement, gazéification,…) pour conduire aux produits de base utilisés dans le pool pétrochimique (éthylène, promènes, butènes, benzène, toluène et xylènes) ainsi qu'aux différents carburants (essence, kérosène et gazole) [1,15,16]

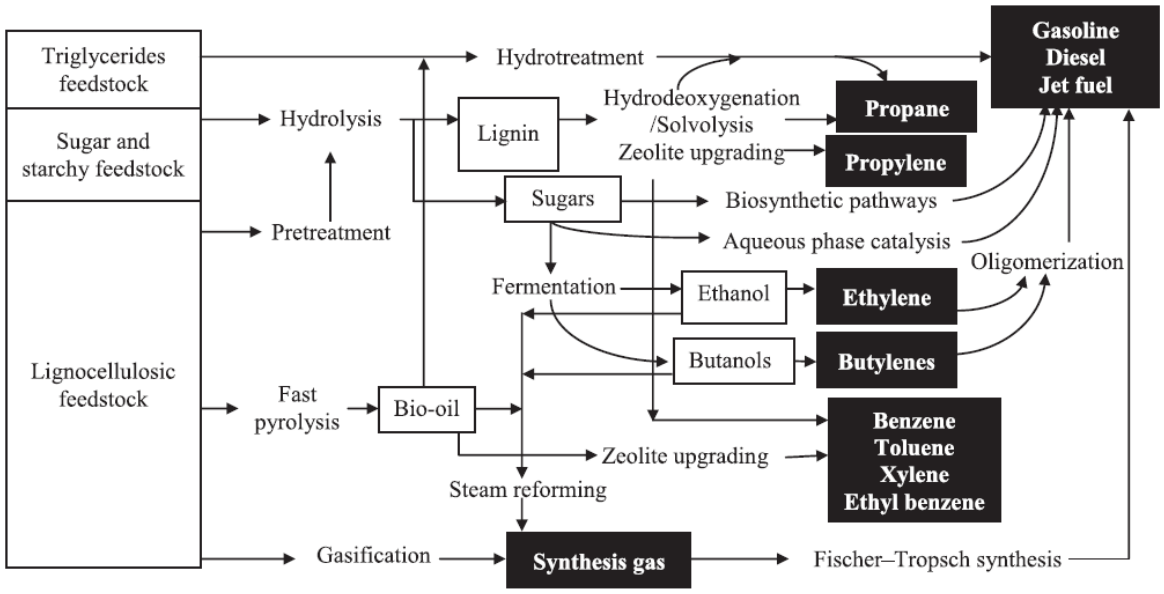

Figure 1-5 : Production d'hydrocarbures à partir des différentes matières premières présentes issus de la biomasse [2].

Plusieurs facteurs sont importants pour le succès des unités de bioraffinage. Par exemple, l'utilisation des ressources énergétiques non renouvelables (pétrole, charbon) dans le traitement de la biomasse dans la bioraffinerie doit évidemment être minimisée. De plus, il est nécessaire :

- d'analyser les trois cycles importants de l'agriculture et de la foresterie, à savoir le cycle du carbone (respiration, photosynthèse et décomposition de la matière organique), de l'eau (précipitation, évaporation, infiltration et ruissellement) et de l'azote (fixation de N, minéralisation, dénitrification) et leurs interdépendances [17] ;
- d'évaluer la performance des traitements de transformation de la biomasse [10] ;
- de vérifier et d'estimer les impacts environnementaux [18] ;

Contrairement au raffinage du pétrole qui implique souvent de très grands centres industriels, les bioraffineries peuvent présenter différentes tailles. Ainsi, l'installation d'une bioraffinerie peut conduire au développement de complexes industriels dans des zones rurales

et ainsi aider à leur revitalisation puisque ces zones sont de plus en plus désertées. Il peut être aussi admis que plusieurs types d'industries peuvent se combiner afin d'avoir différentes étapes de transformation de la biomasse. Par exemple, la lignine, qui est un résidu de l'usine de production d'éthanol, peut être transformée par une autre usine spécialisée, ce qui implique des systèmes intégrés. Ce type de configuration est observé dans l'usine de Domsjö Fabriker située à Örnsköldsvik en Suède qui produit du bioéthanol, de la pâte dissoute, de la lignine, de l'acide carbonique et du biogaz à partir de bois [14]. Au Canada, l'usine de Tembec à Témiscaming produits des résines phénoliques, des lignosulfonates et de l'éthanol [14].

Le modèle de bioraffinerie intégrée est un modèle qui peut être effectivement rentable à condition qu'il soit développé d'une manière durable. En termes d'efficacité et performance, surtout concernant l'environnement, l'avenir de l'utilisation de la matière de deuxième génération est donc beaucoup plus prometteuse par rapport aux matières de première génération [2,12,13].

3. Les matières premières susceptibles d'être transformées dans une bioraffinerie

La biomasse est produite naturellement par les plantes par photosynthèse convertissant le dioxyde de carbone atmosphérique et l'eau en sucres (Figure 1-6) [11]. Les plantes utilisent le sucre pour synthétiser les matériaux complexes qui sont classiquement appelés biomasse.

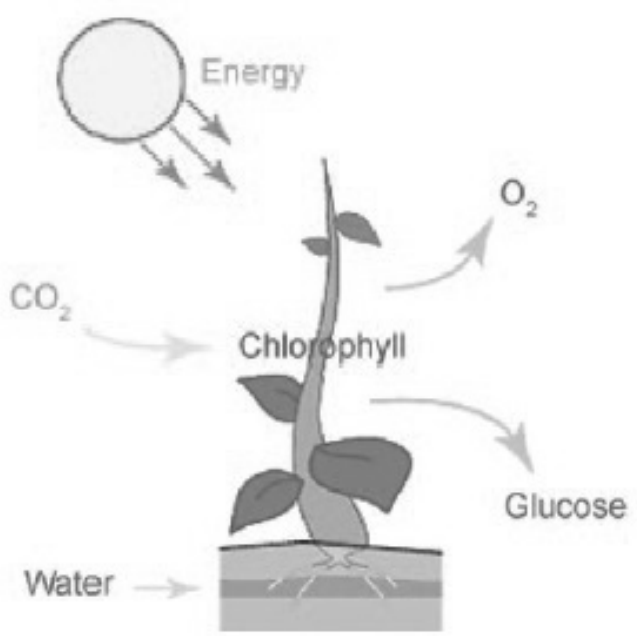

Figure 1-6 : Principe de la photosynthèse [11].

L'une des étapes importantes pour le succès de la bioraffinerie est évidement l'approvisionnement régulier en matières premières, qui doit être planifié pour être continu pendant toute l'année en tenant compte les périodes de développement des plantes[19]. Des prétraitements sur les sites de production, notamment pour les liquéfier, pourraient être nécessaires afin notamment de réduire les coûts de transport et de stockage.

Les prix de vente des produits obtenus à partir de la biomasse peuvent varier énormément selon leur spécificité, le procédé utilisé et leur volume de production. Sur la Figure 1-7 [20], la cellulose produite est de l'ordre de 10^{11} kg et son prix de marché est d'environ 1000 $/t. Par contre, après certains procédés et des étapes de traitement, ce produit affiné peut être vendu à des industries cosmétiques ou agroalimentaires à un prix de l'ordre de 3000 $/t.

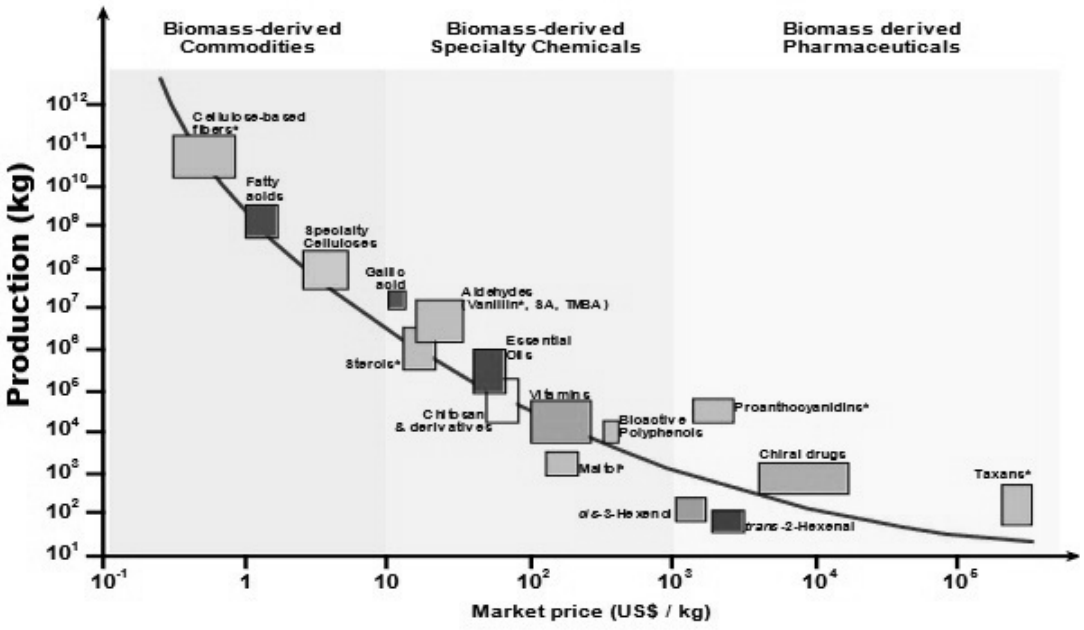

Figure 1-7 : Relation entre la taille du marché et le prix [20].

Différents types de matières premières (cultures dédiées ou des résidus) peuvent être utilisés dans une bioraffinerie, ils proviennent de quatre secteurs différents :

- Agriculture (cultures dédiés et déchets) ;
- Foresterie ;
- Déchets industriels ;
- Déchets municipaux.

Les produits obtenus après la transformation de la biomasse fournie par des cultures dédiées ou par des déchets sont illustrés dans la Figure 1-8. En effet, les principaux types de matières premières peuvent être classés dans quatre grandes catégories : les résidus organiques, les triglycérides, les glucides et la lignocellulose.

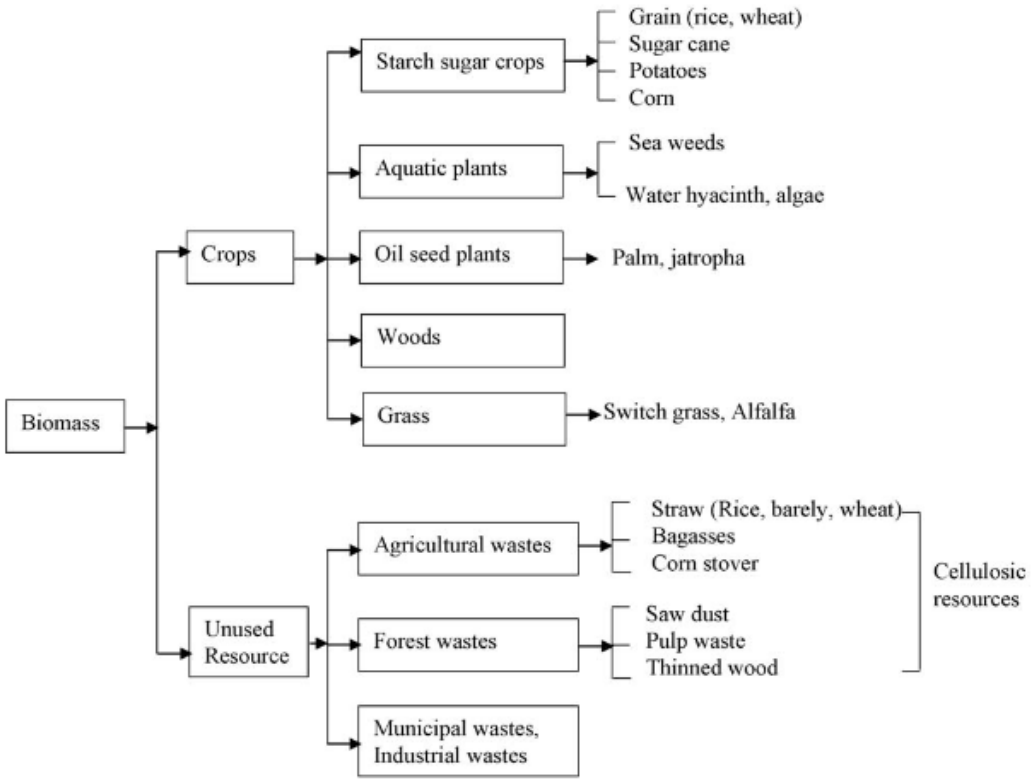

Figure 1-8 : Schéma général de l'utilisation de la biomasse dans la bioraffinerie [21].

3.1. Les résidus/déchets organiques

L'augmentation de l'urbanisation dans le monde a entraîné une croissance des déchets comme montré dans la Figure 1-9 [22]. En effet, les déchets municipaux, le fumier, et les résidus de l'industrie alimentaire peuvent être utilisés pour la production de carburants et de produits chimiques [23]. Cependant, les caractéristiques physiques et chimiques de ces matières premières sont très variées et, contrairement aux autres matières premières, leur valorisation nécessite des prétraitements supplémentaires. Par exemple, des déchets municipaux organiques peuvent être contaminés par des métaux lourds ou d'autres éléments [24].

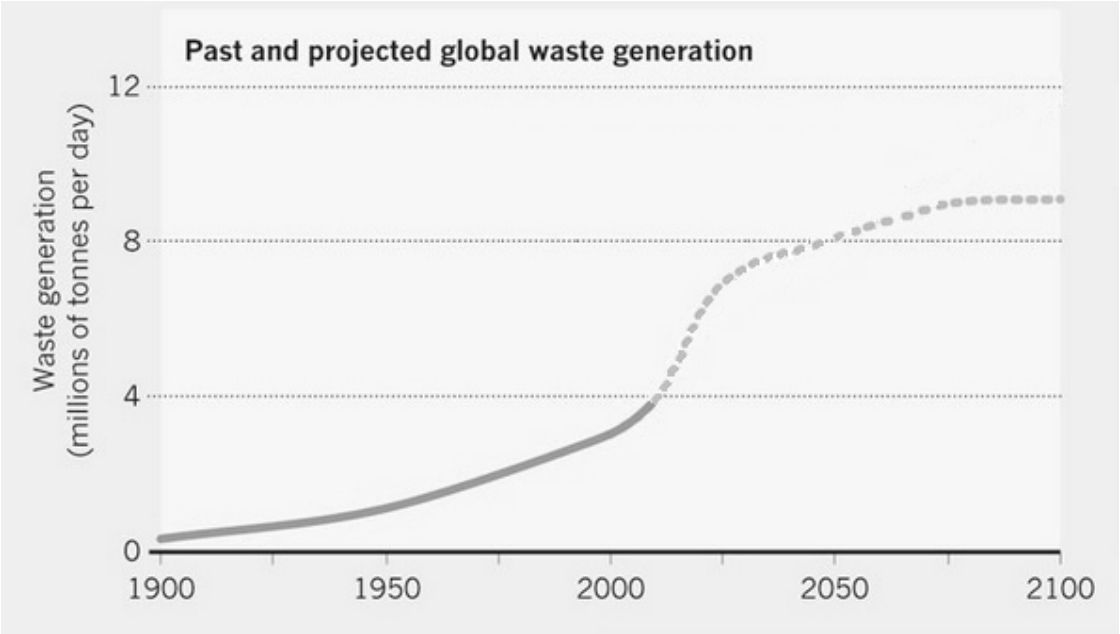

Figure 1-9 : Génération de déchets depuis 1900 et les prédictions jusqu'à 2100.

(--) Projections.

Ainsi, les déchets constituent une énorme ressource peu couteuse parce qu'il y a des centaines de mégatonnes produites à travers le monde (Figure 1-9). Il est possible d'envisager un large éventail d'opportunités et donc plusieurs technologies sont à l'étude pour traiter ces matières, notamment pour la production de biohydrogène et de bioéthane [25]. Le plus intéressant pour ce type de matière première serait d'avoir des technologies capables de transformer d'énormes quantités de matières afin de produire des lubrifiants, des tensioactifs, des monomères pour matières plastiques, des fibres et des solvants industriels. De plus, en exploitant les déchets dans les prochaines années, il sera possible de diminuer les émissions de gaz à effet de serre.

Dans cette perspective environnementale, la transformation des déchets dans des produits chimiques très spécifiques à hautes valeurs ajoutées aurait un impact négligeable, car la demande pour de tels produits chimiques est encore faible. Par contre, il subsiste ici un intérêt économique.

3.2. Les triglycérides

Les huiles obtenues à partir des végétaux, des graisses animales et plus récemment des algues sont des triglycérides. Un triglycéride (Figure 1-10) est une molécule de glycérol liée à trois acides gras qui peuvent être saturés ou insaturés (leur longueur de chaîne varie entre C8 et C20). Ces huiles végétales peuvent provenir de cultures céréalières (soja, colza, tournesol…) mais également de cultures dédiées (jatropha, mahua, karanjaetc…). Les huiles de soja, de palme, de colza et de tournesol sont les plus importantes en termes de production mondiale [26]. Comme les cultures de sucre et d'amidon, les cultures oléagineuses se caractérisent par un faible rendement et une forte utilisation des intrants.

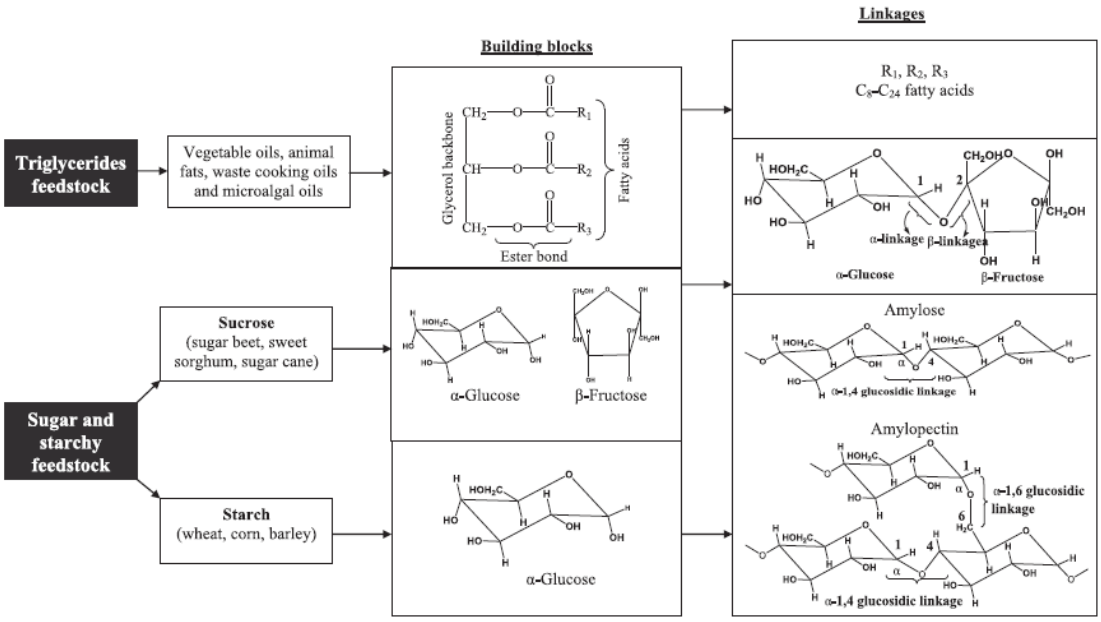

Figure 1-10 : Sources et compositions de triglycérides et des glucides/carbohydrates [2].

Les huiles végétales sont aujourd'hui utilisées pour la production de biodiesel, via une réaction de transestérification en présence d'un alcool (méthanol ou éthanol). Cependant, elles peuvent également être utilisées directement comme substrats pour différentes réactions chimiques [27].

Dans l'avenir, les cultures de matières premières non comestibles (Jatropha curcas par exemple) peuvent devenir les matières premières les plus répandues pour l'approvisionnement des bioraffineries, en particulier dans les régions arides et semi-arides [28]. D'autres sources d'huiles végétales peuvent être trouvées dans les déchets industriels, notamment dans les usines agroalimentaires [29].

Les triglycérides peuvent être également obtenus par les algues, généralement appelés biocarburants de troisième génération. Cette source est très prometteuse grâce à la haute efficacité photosynthétique des algues ce qui confère une productivité facile comparée aux cultures conventionnelles, surtout pour la production de biodiesel [30].

3.3. Les glucides

Les glucides sont des composés chimiques avec un groupe carbonyle (aldéhyde ou cétone) et au moins deux groupes hydroxyles (-OH) comme représenté dans la Figure 1-10. Les glucides sont habituellement répartis entre oses (monosaccharides tels le glucose, le galactose ou le fructose) et osides, qui sont des polymères d'oses (oligosaccharides et polysaccharides). Ces polymères doivent d'abord subir une étape de dépolymérisation avant d'être transformés dans une bioraffinerie. Une fois que les polysaccharides ont été dépolymérisés (pour les cultures d'amidon) ou extraits (pour les cultures sucrières), ils peuvent par exemple être facilement fermentés en éthanol [31].

3.4. La biomasse lignocellulosique

La biomasse lignocellulosique est composée de cellulose (40-50 %), d'hémicellulose (25-35 %) et de lignine (10-20 %) [32,33]. En général, la composition de ces trois constituants dépend du type de culture (Tableau 1-1) ainsi que la position géographique de la plantation [34].

Tableau 1-1 : Fraction massique de la composition de la biomasse lignocellulosique [34].

Matière première	Cellulose	Hémicellulose	Lignine
Maïs	37,5%	22,4%	17,6%
Blé	38,2%	21,2%	23,4%
Bois	49,9%	17,4%	18,1%

La Figure 1-11 schématise les composants de la matière lignocellulosique présents dans les parois cellulaires d'une plante. Cette matière peut aussi contenir des cendres et des extractifs (des sucres, des composés azotés et de la chlorophylle) en faibles quantités.

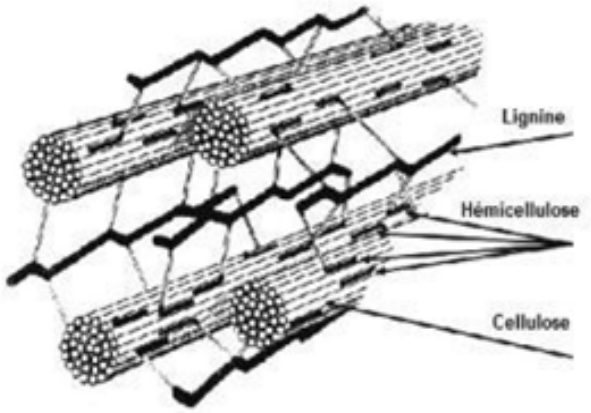

Figure 1-11 : Constituants de la matière lignocellulosiques [35].

La cellulose $(C_6H_{10}O_6)_n$ (Figure 1-12), principal constituant de ce type de biomasse, a une structure moléculaire formée par des longues chaînes de molécules de glucose (5000 à 10000 unités) et a un poids moléculaire supérieur à 10^6 kg kmol^{-1}. La cellulose est très cristalline avec une partie amorphe. Sa structure fait qu'elle est complètement insoluble dans l'eau et difficile à hydrolyser. La production mondiale actuelle de cellulose est de l'ordre de 1,5 trillion de tonnes par an [36].

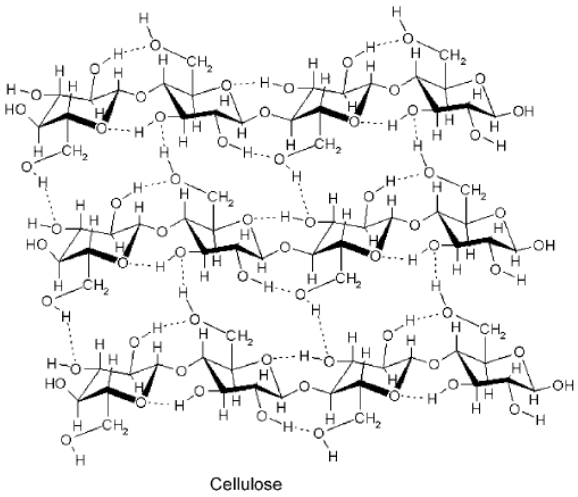

Figure 1-12 : Représentation de la cellulose [11].

L'hémicellulose $(C_5H_8O_5)_n$ (Figure 1-13) est un polymère relativement amorphe constitué d'un mélange de sucres en C6 (galactose, glucose et mannose) et en C5 (xylose et arabinose) [11]. L'hémicellulose assure la liaison entre la cellulose et la lignine (Figure 1-11) garantissant la rigidité de cette biomasse solide. Contrairement à la cellulose, l'hémicellulose est composée d'homopolymères et d'hétéropolymères de monosaccharides. Le nombre de monosaccarides répétés est seulement de l'ordre de 150. L'autre différence par rapport à la cellulose est que l'hémicellulose est très soluble dans l'eau, son hydrolyse conduisant aux différents monomères est donc relativement facile [33].

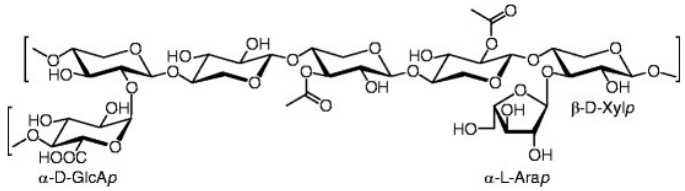

Figure 1-13 : Représentation de l'hémicellulose [37]

La lignine $(C_9H_{10}O_2(OCH_3)_n)$ est un macropolymère lourd (6.10^5 – 15.10^6 kg kmol-^{1}) constitué par des unités phénoliques (Figure 1-14) [11], sa structure est très variée et ce matériau fourni la rigidité à la structure des plantes et des arbres. La lignine est un polymère amorphe et tridimensionnel composé de trois unités différentes de phénylpropane méthoxylées (l'alcool

coniférylique, l'alcool sinapylique et l'alcool cumérique) qui sont liées entre eux par différents types de liaisons (Figure 1-15) [2]. La distribution de ces phénylpropane méthoxylées dépend du type de biomasse [38]. Elle est la source renouvelable de composés aromatiques la plus importante.

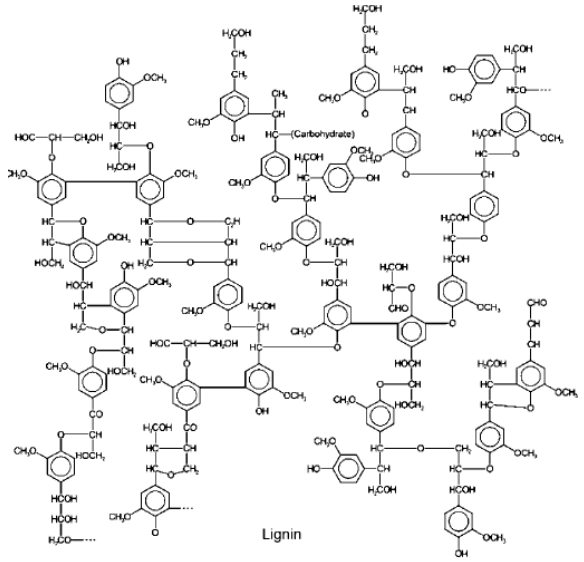

Figure 1-14 : Représentation de la lignine [11].

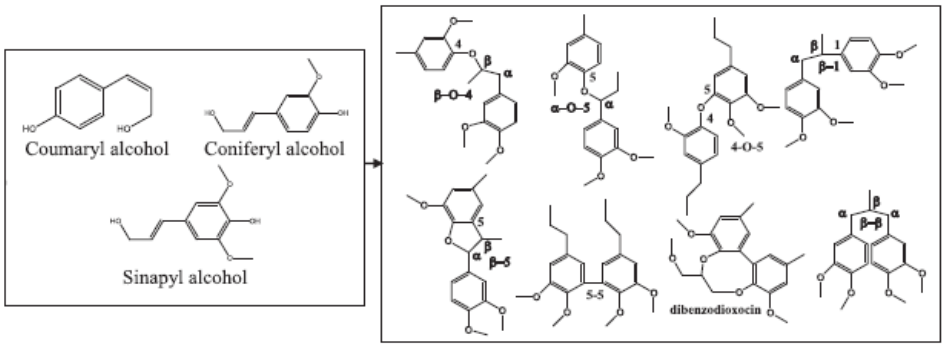

Figure 1-15 : Les trois unités différentes de phénylpropane méthoxylées et les liaisons entre elles présentes dans la lignine [2].

Alors que la cellulose et l'hémicellulose (composés par des polysaccharides) peuvent être hydrolysés en sucres et puis fermentés en éthanol par exemple, la lignine ne peut pas être

utilisée en fermentation. La valorisation de ce dernier type de matière première est cependant d'un intérêt crucial car elle est actuellement produite en grandes quantités, notamment par l'industrie du papier et pour la production d'éthanol [38]. Il est envisageable que la lignine soit utilisée dans l'avenir pour la fabrication des matériaux contenant des noyaux aromatiques comme des bio résines, des biopolymères et des bio dispersants [39].

Il est clair que la biomasse lignocellulosique (cellulose, hémicellulose et lignine) a beaucoup de potentiel comme source des produits chimiques et biocombustibles, surtout parce que cette matière première est très facilement accessible, soit à partir de cultures dédiées (comme Jatropha curcas), soit à partir des résidus (bagasse de canne à sucre, par exemple) [40].

4. Procédés technologiques susceptibles d'être mis en œuvre dans les bioraffineries

De nombreux procédés et les technologies pouvant être mise en œuvre dans une bioraffinerie sont encore à l'étude, mais il est estimé que de tels procédés pourront fonctionner dans la prochaine décennie [10]. Les facteurs les plus importants pour envisager de développer ces technologies se basent sur le fait que les matières premières ne sont pas chères, disponibles et renouvelables. De plus, leur valorisation pourrait permettre de remplacer en totalité ou partiellement le pétrole pour assurer la production de carburants, des composés chimiques à haute valeur ajoutée ainsi que l'électricité et la chaleur [41].

Les principaux objectifs d'une bioraffinerie sont de permettre une dépolymérisation et une désoxygénation des composants de la biomasse. Cela nécessite la mise en œuvre de différents procédés technologiques. Ces procédés peuvent être divisés en trois grandes catégories : les procédés thermochimiques, biochimiques et chimiques.

4.1. Procédés thermochimiques

Les procédés thermochimiques reposent sur la dégradation de la biomasse suite à des réactions chimiques intervenant à des températures élevées. Il y a deux principaux procédés thermochimiques pour convertir la biomasse en biocombustibles et en produits chimiques : la pyrolyse et la gazéification [42].

La principale voie thermochimique pour la conversion de la biomasse est la pyrolyse effectuée en absence d'oxygène et à des températures comprises entre 300-600 ºC. La Figure 1-16 illustre un type de réacteur qui peut être utilisé. Ce procédé convertit la biomasse en huile pyrolytique (ou bio-huile), en charbon et en gaz légers (semblables au gaz de synthèse) [43,44]. Leurs rendements peuvent varier en fonction des conditions opératoires utilisées. La bio-huile pyrolytique est un mélange complexe contenant plusieurs composés oxygénés. Généralement, les bio-huiles de pyrolyse contiennent principalement de l'eau (20-30 %pds), de la lignine (5-10 %pds), des aldéhydes (10-20 %pds), des acides carboxyliques (10-15 %pds), des glucides (5-10 %pds), des phénols (2-5 %pds), des furfural (1-4 %pds), des alcools (2-5 %pds) et des cétones (1-5 %pds) [45]. Les teneurs élevées en eau et en oxygène ainsi que la présence d'un grand nombre de composés chimiques limitent toutefois les applications directes de la bio-huile pyrolytique comme combustible à cause de problèmes comme son instabilité chimique, sa corrosivité, son faible pouvoir calorifique, sa viscosité élevée et sa faible miscibilité avec le pétrole [1]. La mise en place de procédés spécifiques pour la valoriser, comme indiqué dans le schéma de bioraffinerie montré dans la Figure 1-5 est alors nécessaire.

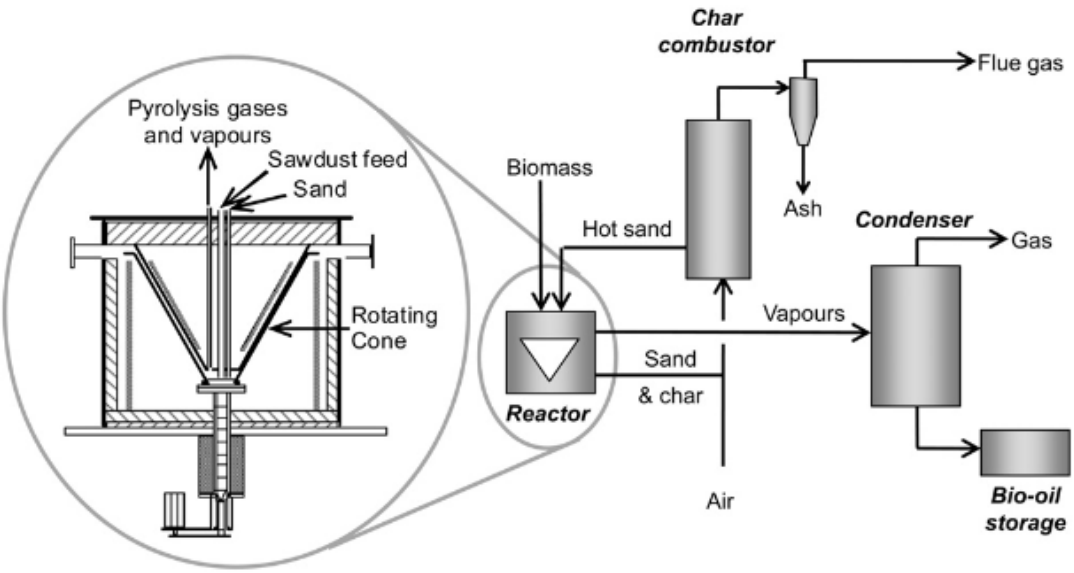

Figure 1-16 : Réacteur de pyrolyse de biomasse

La deuxième voie thermique est la gazéification de la biomasse qui peut être définie comme la combinaison d'une pyrolyse suivie d'une oxydation partielle en présence d'oxygène. Dans ce cas, il est nécessaire de maintenir la biomasse à haute température (au-dessus de 700 °C) avec des teneur en oxygène très faibles pour produire du gaz de synthèse (CO, H_2) [46]. Le produit de la gazéification contient du monoxyde de carbone (CO), du dioxyde de carbone (CO_2) et de l'hydrogène (H_2). Ce produit peut être utilisé directement comme biocombustible ou comme intermédiaire chimique pour la production d'autres combustibles (éthanol, éther diméthylique, isobutène, hydrocarbures plus lourds via la synthèse de Fischer-Tropsch) et des produits chimiques (organiques, ammoniac, alcools, acides, méthanol).

La combustion directe de la biomasse est également un procédé thermochimique. Il s'agit de la forme la plus ancienne de conversion de la biomasse qui permet principalement la production de chaleur, celle-ci étant cependant peu rentable [47].

4.2. Procédés biochimiques

Contrairement aux procédés thermochimiques, les procédés biochimiques se font à des températures plus basses mais avec des vitesses de réaction plus faibles. La fermentation et la digestion anaérobie sont les procédés biochimiques les plus connus. La fermentation utilise des microorganismes et/ou des enzymes. L'éthanol est actuellement le produit de fermentation le plus important, la Figure 1-17 montre un exemple de la production du bioéthanol à partir de l'hémicellulose provenant de la biomasse lignocellulosique [6]. De plus, la production d'hydrogène et de méthanol fait l'objet de travaux de recherche récents [48].

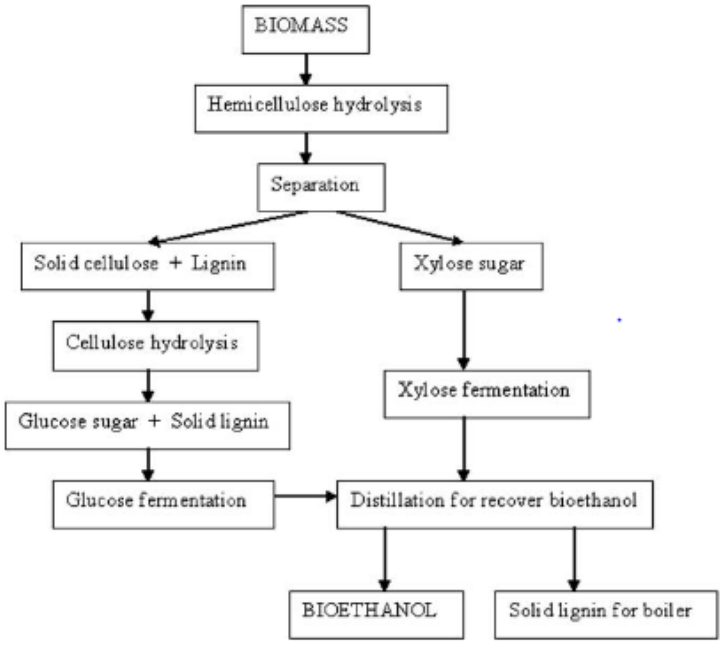

Figure 1-17 : Production de bioéthanol à partir de l'hémicellulose [6].

La digestion anaérobie est un autre procédé biochimique très important qui implique la décomposition bactérienne de matières organiques en absence de l'oxygène à des températures d'environ 30 à 60 °C. Le produit principal de ce procédé est le biogaz [49].

4.3. Procédés chimiques

Les procédés chimiques sont des procédés qui entraînent une modification de la structure chimique de la molécule par réaction avec d'autres substances. Les procédés chimiques les plus courants impliqués dans la conversion de la biomasse dans la bioraffinerie sont l'hydrolyse, l'hydrotraitement (hydrodésoxygénation), le reformage à la vapeur et la synthèse Fisher-Tropsh, comme indiqué dans la Figure 1-5.

L'hydrolyse des polysaccharides permet de les dépolymériser en sucres constitutifs (par exemple, le glucose, la dextrine et l'isomaltose) [50]. Cette étape, nécessaire pour la production de bioéthanol, est usuellement catalysée par des enzymes telles quel la pullulanase et la glucoamylase.

Il est envisagé que la lignine puisse devenir une source importante de composés aromatiques. Pour cela, il est tout d'abord nécessaire de dépolymériser ce bio polymère afin d'obtenir des composés phénoliques. Différentes techniques se développent actuellement comme l'oxydation catalytique [51,52] et l'hydroconversion [53,54].

Les bio-huiles obtenues par pyrolyse ainsi que les produits issus de la dépolymérisation de la lignine peuvent également être valorisés par le procédé d'hydrodésoxygénation (HDO). En effet, en présence d'hydrogène (0,1 à 30 MPa) et à des températures comprises entre 250-450 ºC, la bio-huile peut être transformée en hydrocarbures totalement ou partiellement désoxygénés en présence de catalyseurs spécifiques [55]. L'étude du procédé d'HDO fait l'objet de cette thèse et sera discuté en détail dans les prochains chapitres.

5. Produits formés dans une bioraffinerie

Les produits issus d'une bioraffinerie sont soit à visée énergétique ou/et non énergétique. Les produits énergétiques, sont généralement le bioéthanol, le biodiesel et le biométhane [56]. Les produits comme les composés phénoliques, l'acide levulinique, le butanol entre autres sont considérés de produits non énergétique et ils sont dédiées à la synthèse de

produits à haute valeur ajoutée comme les résides, les produits pharmaceutique et les polymères [23,56]. Contrairement aux raffineries classiques, les bioraffineries sont spécifiques, les procédés dépendant des matières premières à transformer.

A titre d'exemple, la Figure 1-18 montre les différents produits susceptibles d'être obtenus à partir d'une charge composée de triglycérides (biodiesel, glycérol, gaz de synthèse…) ainsi que les procédés à mettre en œuvre (transestérification, hydrolyse, hydrodésoxygénation…) [2]. Mise à part les procédés de transestérification et d'hydrolyse, les autres procédés sont similaires à ceux utilisés dans les raffineries classiques visant à transformer les ressources pétrolières en carburants.

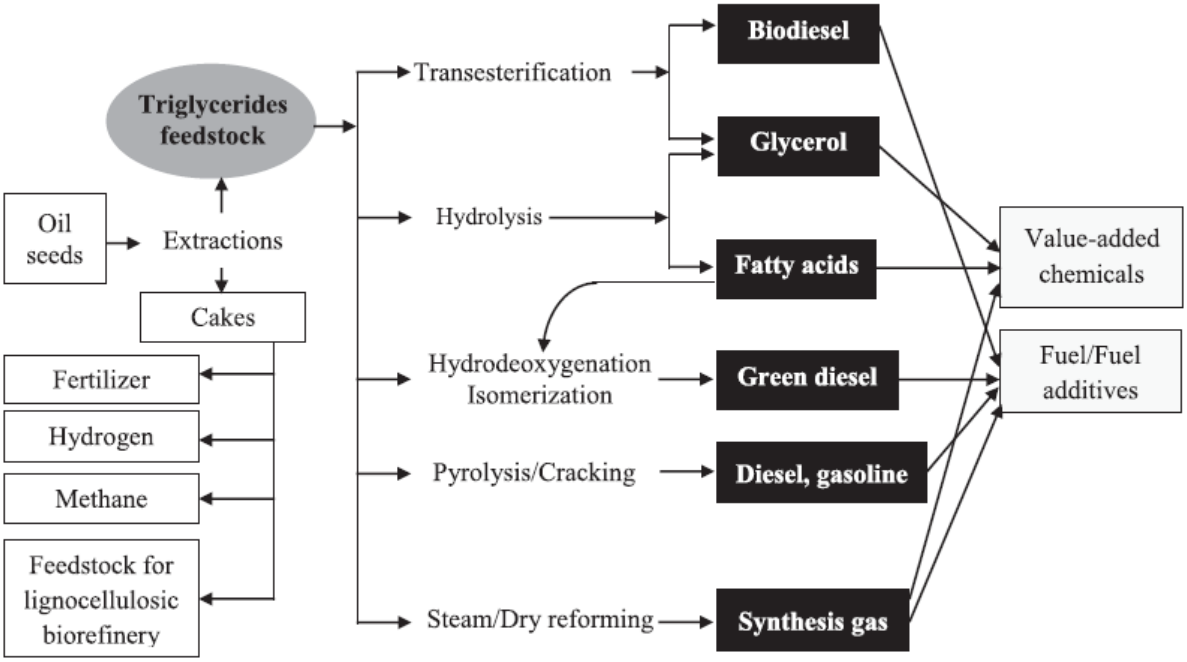

Figure 1-18 : Valorisation d'huiles dans une bioraffinerie [2].

Un deuxième exemple présenté dans la Figure 1-19 montre les principaux produits attendus à partir de matières premières riches en polysaccharides [2]. La valorisation de ce type de matière première sera plus axée vers la synthèse de produits oxygénés spécifiques, comme par exemple l'acide lévulinique (utilisé dans la production des polymères), et l'éthanol. Ce

dernier est dit de seconde génération, car il ne provient pas directement des graines des plantes sucrières et n'entre donc pas directement en compétition avec l'alimentation humaine.

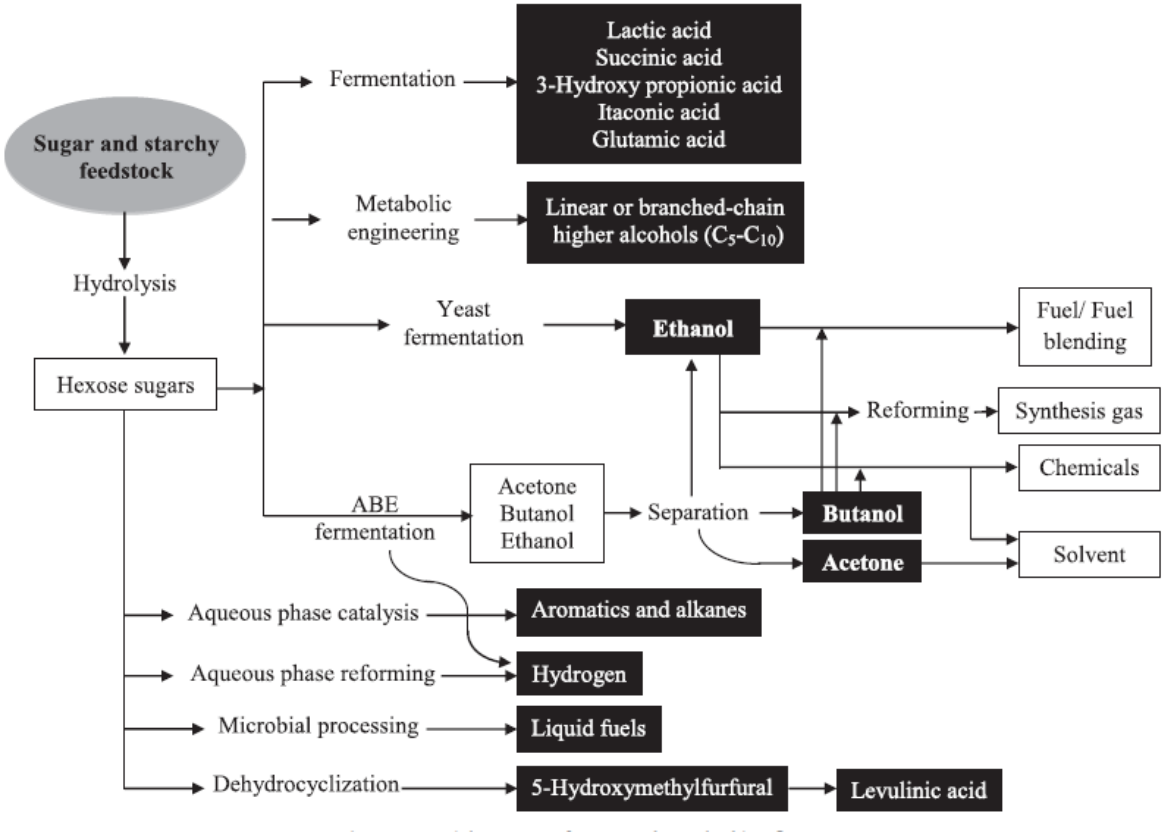

Figure 1-19 : Valorisation de matières premières à base de polysaccharides dans une bioraffinerie [2].

Un troisième exemple présenté dans la Figure 1-20 montre les principaux produits attendus à partir de matières premières lignocellulosiques. De nouveau, un panel important de produits est possible, qu'ils soient oxygénés (acide lévulinique, methanol, ethanol, buthanol…) ou totalement désoxygénés (aromatiques, alcanes…).

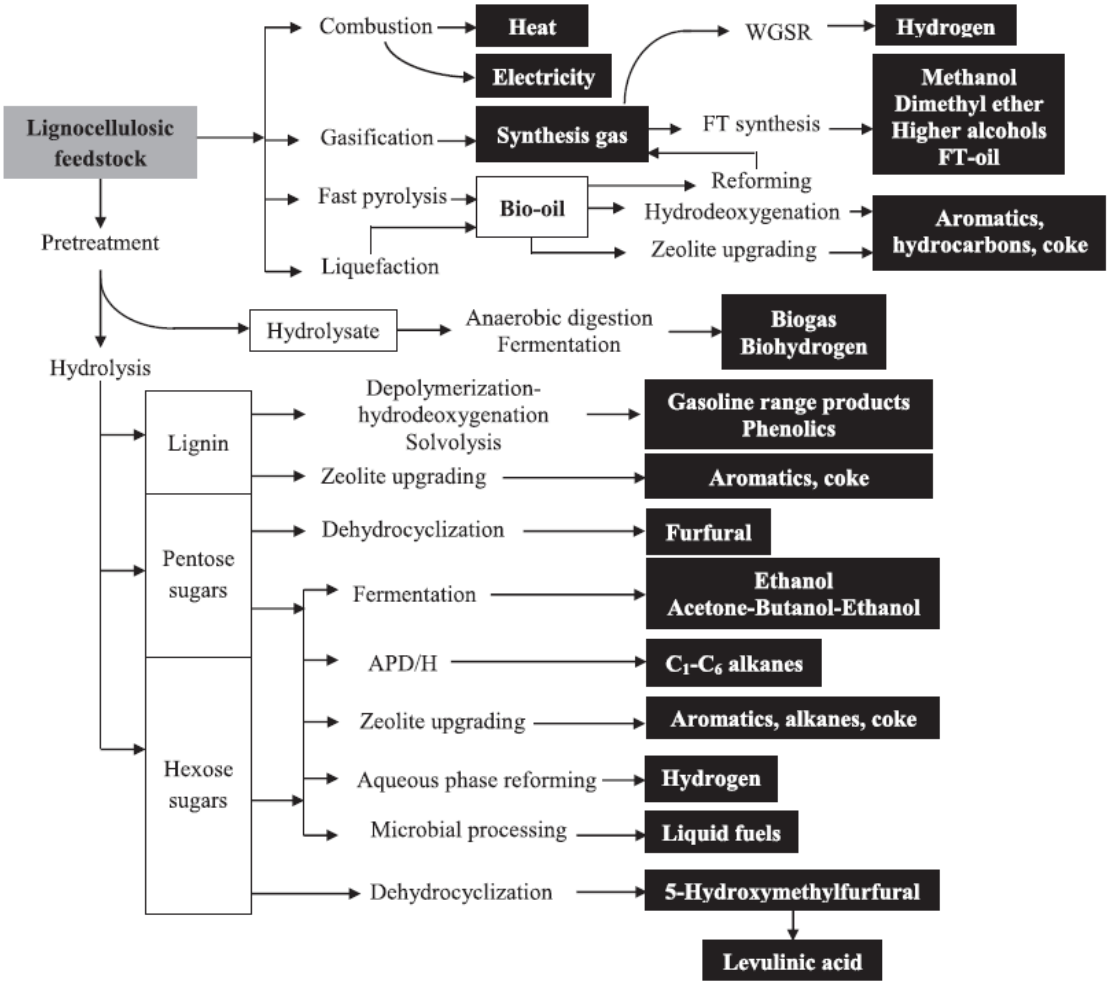

Figure 1-20 : Plateforme des produits chimiques à partir de matières premières riches en amidon et en sucres [2]

Il est intéressant de souligner que ces différentes matières premières, et plus spécifiquement la lignine, peuvent être transformées en synthons aromatiques (benzène, toluène, xylènes), qui sont des intermédiaires clés dans la synthèse de nombreux produits, notamment en chimie des polymères (Figure 1-21). Ces intermédiaires aromatiques simples peuvent par exemple être obtenus par catalyse alcaline suivie par un procédé d'hydrodésoxygénation.

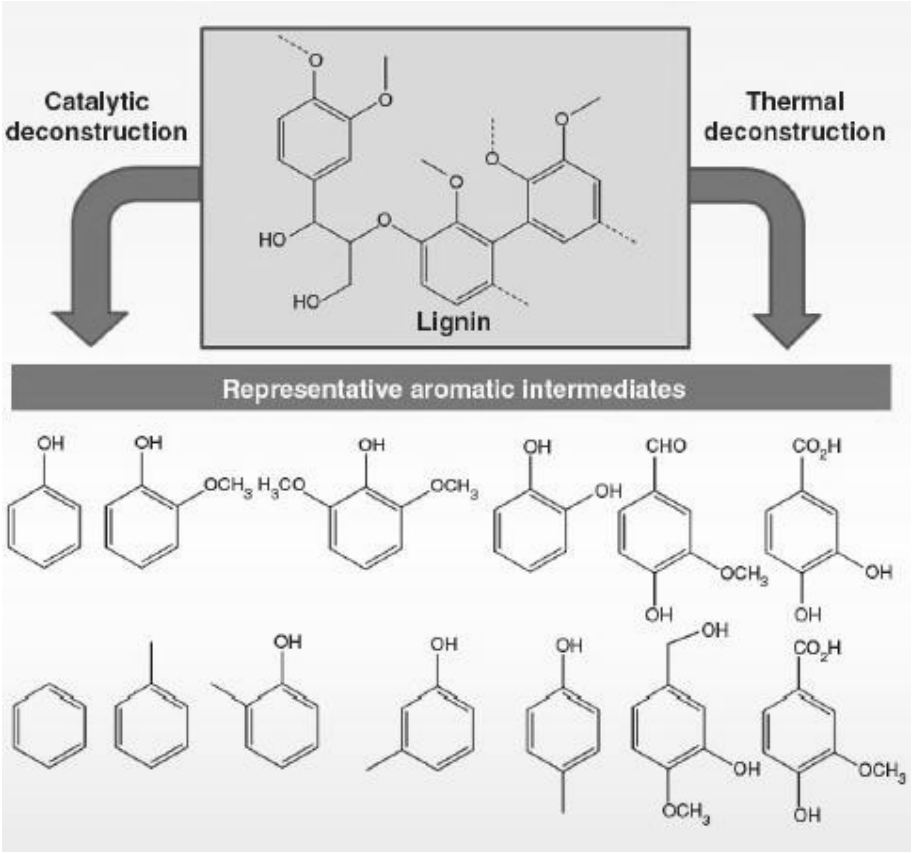

Figure 1-21 : Déconstruction catalytique et thermique de la lignine en produits aromatiques simples [57].

Dans la suite de ce chapitre, la réactivité de composés phénoliques modèles sera étudiée plus spécifiquement car ils peuvent être obtenus à partir de la dépolymérisation de la lignine et ils sont également présents dans les bio-huiles issues des procédés de pyrolyse.

6. Procédé d'hydrodésoxygénation : vers la valorisation des bio-huiles et des produits de dépolymérisation de la lignine.

Ces travaux de thèse s'intéressent plus spécifiquement au procédé d'hydrodésoxygénation (HDO) qui est le procédé envisagé pour valoriser les bio huiles et les produits issues de la dépolymérisation de la lignine [58]. Pour cela, il est nécessaire de faire réagir les molécules oxygénées en présence d'un catalyseur solide sous atmosphère d'hydrogène à des températures élevées. En utilisant le solide adéquat, il est possible d'éliminer l'oxygène de ces molécules sous forme d'eau, voire d'oxydes de carbone (CO et CO_2), suivant les fonctions oxygénées présentes, afin d'obtenir des hydrocarbures.

La réaction d'hydrodésoxygénation impliquant l'élimination de l'oxygène sous forme d'H_2O est analogue aux réactions d'hydrodésulfurisation (soufre éliminé sous forme d'H_2S) et aux réactions d'hydrodésazotation (N éliminé sous forme de NH_3), ces procédés étant utilisés dans le traitement des charges pétrolières [59,60]. En général, pour des composés similaires la difficulté d'élimination des hétéroatomes (O-, N- et S-) suit l'ordre suivant : HDS > HDO > HDN [58].

La température de traitement dépend de la charge à traiter. Généralement, celle-ci est comprise entre 300 °C et 450 °C. Par exemple, Grange et al. [61] ont rapporté les températures de travail utilisées en HDO de différentes molécules oxygénées afin d'obtenir des conversions identiques sur $CoMoS/Al_2O_3$, les énergies d'activation associées sont également indiquées (Tableau 1-2). Dans ces conditions, les éthers et les alcools sont plus réactifs que les cétones, alors que les composés phénoliques apparaissent comme les plus réfractaires. C'est la raison pour laquelle les travaux de cette thèse se sont focalisés sur l'étude de l'hydrodésoxygénation de composés phénoliques, notamment les crésols (methylphénols).

Tableau 1-2 : Énergies d'activation et températures pour avoir iso conversion pour différentes molécules/groupe fonctionnelles sur un catalyseur $CoMoS/Al_2O_3$ [61].

Molécules/groupe	Énergie d'activation (kJ mol^{-1})	Température à iso-conversion (ºC)
Cétone	50	203
Acide carboxylique	110	282
Guaiacol	113	301
4-methylphénol	140	340
2-éthylphenol	150	367

Les propriétés catalytiques des principales phases actives utilisées en HDO de molécules phénoliques modèles sont présentées ci-après. Les introductions des différents chapitres de ce manuscrit reprennent des études bibliographiques assez complètes sur différentes phases catalytiques utilisées en HDO. Ainsi, afin d'éviter des redondances trop importantes, nous nous limiterons dans la partie à suivre à la présentation de quelques résultats marquants obtenus en HDO de composés phénoliques sur des catalyseurs à base soit de phases sulfures (MoS_2, CoMoS et NiMoS), soit de métaux nobles (Pt, Pd et Ru), ou non précieux (Ni, Co et Fe), et sur des phases phosphures (Ni_2P, MoP et CoP).

6.1. Catalyseurs sulfures

Les catalyseurs présentant des phases sulfures non promues à base de molybdène (Mo/Al_2O_3) et promues par du cobalt ($CoMo/Al_2O_3$) ou du nickel ($NiMo/Al_2O_3$) ont été les premiers solides utilisés en HDO à cause de leur succès dans les procédés d'HDS, les réactions impliquées étant relativement proches (O éliminé sous forme H_2O et S sous forme H_2S). Dans le cadre d'un co-traitement HDO de charges ex-biomasse et HDS de charges pétrolières classiques, l'utilisation de ce type de catalyseur est tout à fait raisonnable.

Les phases sulfures sont créées par la procédure de sulfuration de l'oxyde de molybdène en utilisant le sulfure d'hydrogène en présence d'H_2 (Équation 1-1).

$$MoO_3 + 2H_2S + H_2 \longrightarrow MoS_2 + 3H_2O \qquad \text{Équation 1-1}$$

La phase active des catalyseurs non promus est composée de sulfure de molybdène (ou de tungstène) de type MoS_2 (ou WS_2). Cette phase se présente sous forme de feuillets hexagonaux disposant de deux types de bords : les bords métalliques ($10\bar{1}0$) et les bords soufres ($\bar{1}010$). La Figure 1-22 illustre une représentation de cette phase, ainsi que des deux types de bords observés.

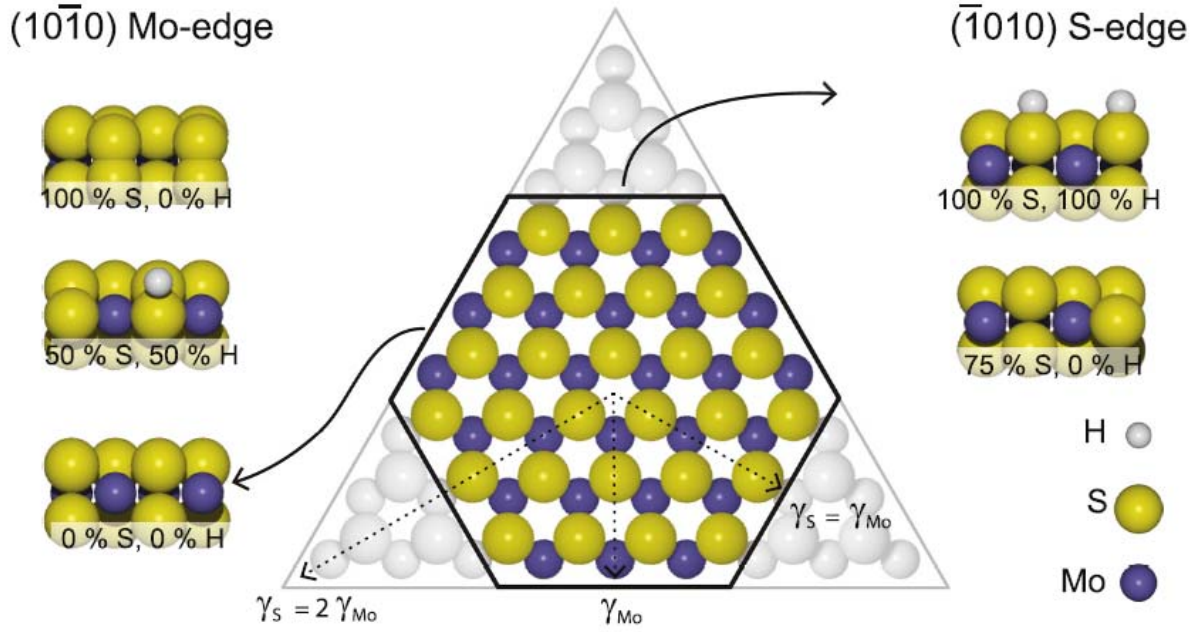

Figure 1-22 : Représentation à l'aide d'un modèle de balles d'un feuillet MoS_2 exposant deux types de bords [62].

Concernant ces phases actives, il est généralement admis que les lacunes en soufre (lacunes anioniques) situées aux bords des nanoclusters des feuillets hexagonaux de MoS_2 (ou

WS_2) sont les sites actifs de ce type de catalyseur [62–64]. Par conséquent, les lacunes anioniques jouent un rôle important dans la rupture de la liaison carbone-hétéroatome [65]. Il est possible d'ajouter du cobalt ou du nickel sur la phase MoS_2 pour former des phases mixtes CoMoS et NiMoS, respectivement. En effet, il est connu que le cobalt ou le nickel dans la phase mixte donne des électrons au molybdène, ce qui conduit à un affaiblissement de la liaison métal-soufre [66]. Ainsi, cet affaiblissement favorise l'élimination des atomes de soufre et augmente le nombre de sites actifs en comparaison à la phase MoS_2.

Les composés phénoliques utilisés comme molécules modèles représentatives des composés oxygénés présents dans les bio-huiles et/ou provenant de la dépolymérisation de la lignine, peuvent être divisés en deux catégories : les phénols substitués avec un groupement alkyle, tel que le crésol, et les composés phénoliques méthoxylés tel que le guaiacol. Plusieurs voies de transformations de ces molécules sont possibles. Par exemple, la désoxygénation de l'un des composés les plus étudié en HDO, le guaiacol, implique quatre voies de transformation (Figure 1-23) [67,68]:

1) la déméthylation pour produire le catéchol, qui est ensuite désoxygéné en phénol ;

2) la déméthoxylation pour produire directement le phénol ;

3) la rupture de la liaison C-O entre le groupe hydroxyle et le noyau aromatique pour produire le méthoxybenzène ;

4) l'hydrogénation du cycle aromatique suivie de la rupture du groupe méthyle ou du groupe hydroxyle.

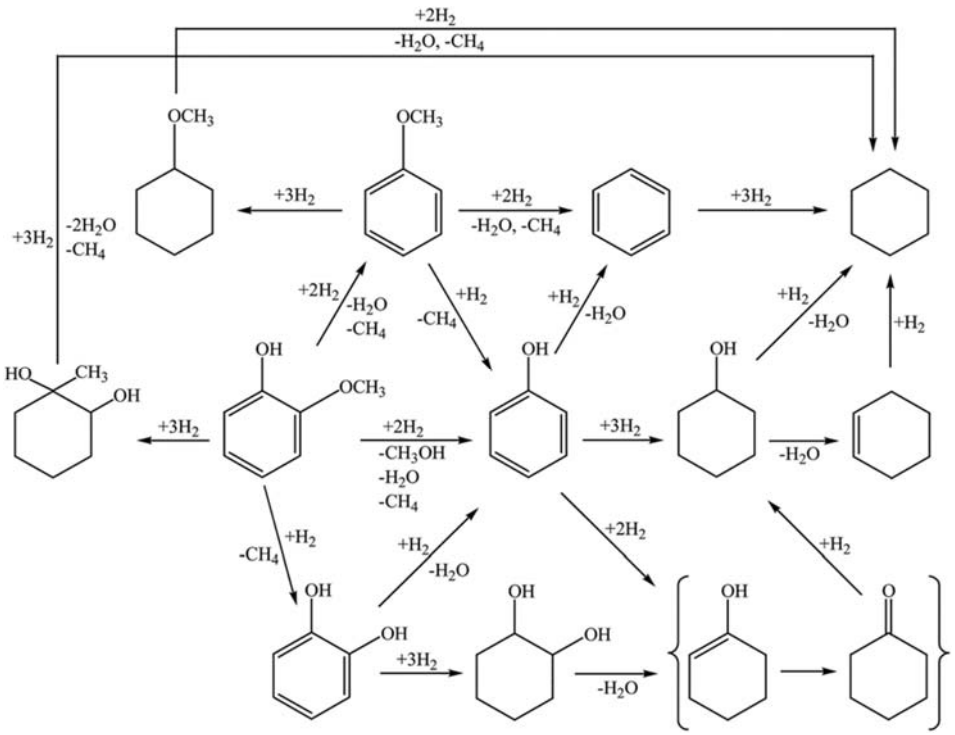

Figure 1-23 : Voies de transformation du guaiacol [67].

Comme observé sur la Figure 1-23, le phénol est un intermédiaire de la transformation du guaiacol. Il est connu que les composés phénoliques se transforment selon deux voies de transformation. L'une est couramment appelée voie de désoxygénation directe (voie DDO) qui consiste en la rupture directe de la liaison C-O et produisant un composé aromatique. La deuxième voie de transformation implique l'hydrogénation du noyau aromatique phénolique (voie HYD) [58]. A titre d'exemple, la transformation du phénol sur $CoMoS/Al_2O_3$, illustré dans la Figure 1-24, conduit soit à la formation du benzène par rupture directe de la liaison C-O, soit à des produits hydrogénés par hydrogénation du noyau aromatique [69].

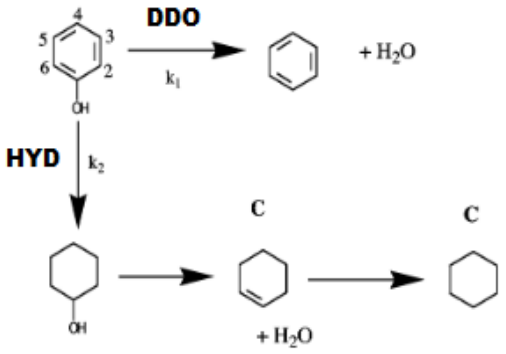

Figure 1-24 : Transformation du phénol en benzène par la voie DDO et en cyclohexane par la voie HYD sur $CoMoS/Al_2O_3$ [69].

Romero et al. [70] ont proposé un mécanisme de transformation du 2-éthylphénol sur un catalyseur MoS_2/Al_2O_3. Dans le mécanisme de désoxygénation directe (voie DDO, Figure 1-25), l'hydrogène est activé par dissociation hétérolytique pour former un groupement S-H et un groupement Mo-H. Ainsi, l'oxygène présent dans l'éthylphénol peut s'adsorber sur une lacune anionique. Le carbocation est alors formé par déprotonation du groupe S-H, impliquant la rupture de la liaison C-O et formation de l'éthylbenzene. Le site activé est ensuite régénéré par désorption d'eau.

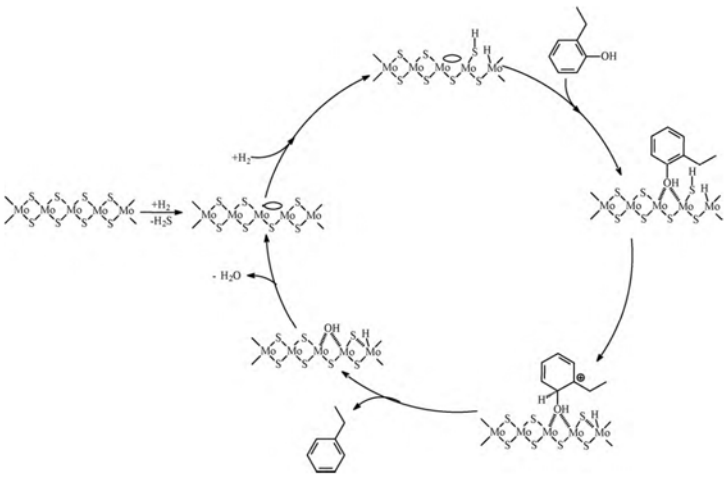

Figure 1-25 : Mécanisme de la voie DDO pour la transformation de l'éthylphénol sur MoS_2/Al_2O_3 [70].

Il est également proposé que le 2-éthylphénol puisse réagir par la voie HYD lorsque le noyau aromatique est adsorbé sur les lacunes anioniques (Figure 1-26). Dans ce cas, il est proposé l'existence de lacunes multiples comme site actif. Après son adsorption à plat, le cycle aromatique du composés phénolique est totalement hydrogéné et conduit à la formation du 2-éthylcyclohexanol. Cet alcool est ensuite déshydraté sur un support acide (Al_2O_3 dans ce cas) produisant des alcènes ensuite hydrogénés en éthylcyclohexane.

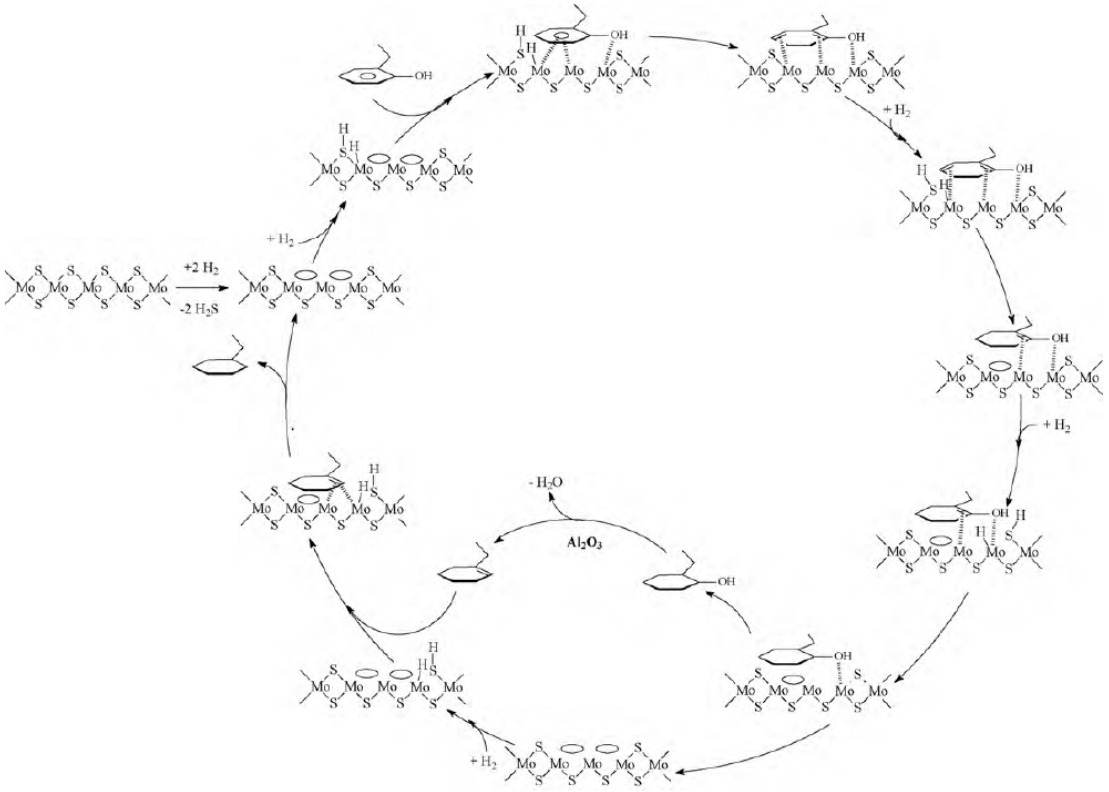

Figure 1-26 : Mécanisme de la voie HYD pour la transformation de l'éthylphénol sur MoS_2/Al_2O_3 [70].

Le Tableau 1-3 résume les principaux catalyseurs sulfures utilisant différents supports dans des études d'HDO de charges modèles. Pour les composés phénoliques, la contribution de chaque voie (DDO vs. HYD) dans la distribution des produits est fortement dépendante de la nature de la phase active [69–78]. Par exemple, Odebumni et al. [78] et Wandas et al. [74] ont

montré que la formation des composés aromatiques est favorisée sur la phase CoMoS (voie DDO), alors que les produits formés par la voie HYD (cycloalcènes et cycloalcanes) sont prédominants sur des phases MoS_2 et NiMoS (sous 4-7 MPa, 250-340 °C) [75,79,80].

Tableau 1-3 : Catalyseurs sous forme sulfure utilisé en HDO.

Charge	Catalyseur	Température (ºC)	Pression (MPa)	Reference
Phénol	$NiMo/Al_2O_3$	350	7,5	Şenol et al. [81]
Phénol	NiW/C	250-300	1,5	Echeandia et al. [76]
Phénol	$CoMo/Al_2O_3$	340	7	Badawi et al. [77]
Méthylphénols	$CoMo/Al_2O_3$	360	7	Wandas et al. [74]
Méthylphénols	$CoMo/Al_2O_3$	375-400	2,85	Massoth et al. [69]
Méthylphénols	$CoMo/Al_2O_3$	225-400	6,8	Odebunmi et al. [78]
Éthylphénol	$CoMo/Al_2O_3$, $NiMo/Al_2O_3$	340	7	Romero et al. [70]

Malgré leur activité désoxygénante relativement élevée, l'inconvénient de l'utilisation de ces catalyseurs sulfures en HDO est lié au fait qu'il est nécessaire d'ajouter une certaine quantité de soufre dans la charge pour assurer leur stabilité, notamment afin d'éviter la réoxydation des phases sulfures à cause de l'eau produite. Cet ajout peut éventuellement conduire à la formation de composés soufrés [82,83].

6.2. Catalyseurs à base de métaux nobles

Dans la mesure où ce type de procédé sera mis en place afin d'assurer la désoxygénation de charges ex-biomasse, il serait plutôt intéressant de travailler avec des catalyseurs qui n'ont pas besoin de soufre pour fonctionner. Ainsi, des catalyseurs comportant des phases métalliques, notamment nobles (Pd et Pt) ont été utilisées en HDO de molécules phénoliques [84]. En effet, ces solides sont connus pour leur fort pouvoir hydrogénant, et ainsi favorisent la désoxygénation de composés oxygénés [71].

Lors de l'HDO des composés phénoliques sur des catalyseurs supportés à base de métaux nobles, il est généralement accepté que l'H_2 est adsorbé et activé sur le métal, tandis que les composés oxygénés sont adsorbés soit sur les sites actifs du métal, soit sur le support. Les atomes d'hydrogène adsorbés sur le métal peuvent ainsi réagir avec les intermédiaires oxygénés adsorbés conduisant à la rupture de la liaison C-O, à la formation des composés désoxygénés et à la libération d'eau [85,86]. Un exemple d'adsorption du phénol sur l'Al_2O_3 et l'activation de l'hydrogène est montré dans la Figure 1-27.

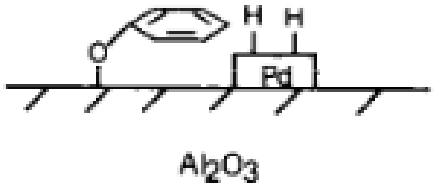

Figure 1-27 : Adsorption du composé phénolique et activation de l'H_2 sur Palladium [86].

De Souza et al. [87,88] ont étudié la performance de catalyseurs à base de palladium supporté sur SiO_2, Al_2O_3 et ZrO_2 en HDO du phénol à 300 ° C sous pression atmosphérique. Lorsque le Pd est supporté sur SiO_2 et Al_2O_3, la cyclohexanone apparait comme le produit majoritaire. Cependant, lors de l'utilisation d'un support « oxophilique », tel que ZrO_2, la sélectivité en benzène est favorisée, les produits oxygénés (cyclohexanone et cyclohexanol) étant formés en plus faibles quantités.

Mortensen et al. [84] ont étudié l'HDO du phénol en phase liquide à 275 ºC et sous 10 MPa en utilisant les métaux nobles Pt, Pd et Ru supportés sur carbone. Les auteurs ont rapporté l'ordre d'activité en désoxygénation suivant : Ru > Pd > Pt.

Malgré leur pouvoir désoxygénant élevé, la disponibilité de ces catalyseurs nobles ainsi que leur coût sont des désavantages qui devraient limiter leur utilisation dans les procédés d'hydrodésoxygénation à mettre en place dans les bioraffineries [71].

6.3. Catalyseurs à base de métaux non nobles

Il a également été montré que les catalyseurs à base de métaux non nobles réduits tels que le Fe, le Ni et le Co, sont des catalyseurs particulièrement actifs en HDO. Par exemple, l'étude de l'HDO du guaiacol sous des pressions comprises entre 1 et 5 MPa à des températures élevées (300-350 ºC) a été réalisé par Mochizuki et al. [89] sur différents catalyseurs (Ni/SiO_2, Co/SiO_2, Pt/SiO_2, Pd/SiO_2 et $CoMoS/Al_2O_3$). Les résultats montrent que Co/SiO_2 et Pd/SiO_2 sont les catalyseurs qui permettent d'obtenir les taux de désoxygénation les plus élevés parmi les solides testés, ce qui montre que les métaux non nobles sont également intéressant en HDO. De plus, il est à noter que ces catalyseurs présentent des sélectivités différentes, le catalyseur Pd/SiO_2 conduit plutôt à des composés hydrogénés, tandis que Co/SiO_2 conduit à la production d'aromatiques.

Olcese et al. [90] ont également étudié l'HDO du guaiacol sur Fe/SiO_2 à pression atmosphérique entre 350 et 450 ºC dans un réacteur fermé. Comme montré sur la Figure 1-28, le taux de désoxygénation est encore relativement faible sur ce type de catalyseur, puisque que la teneur en benzène est très inférieure à la teneur en phénol.

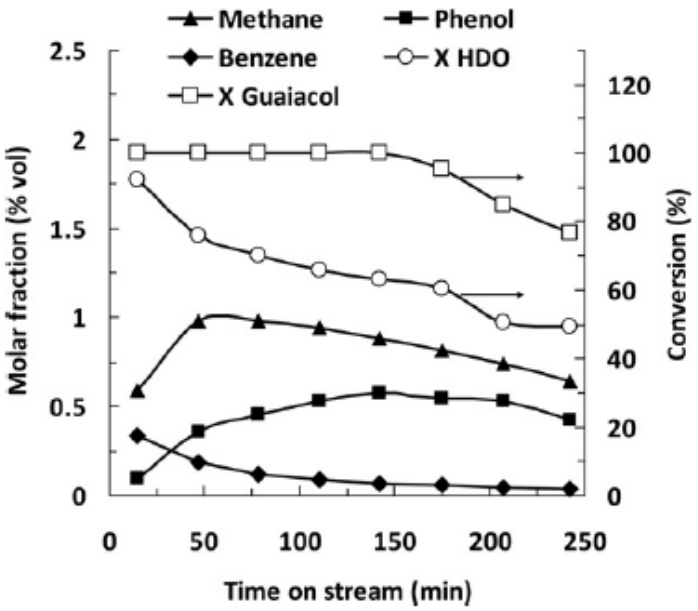

Figure 1-28 : HDO du guaiacol sur Fe/SiO_2 (T = 350 ºC, P = 1 atm, $m_{cat}/\dot{m}_{GUA}$ = 1.50 g_{cat} h g_{GUA}^{-1}) [90].

Il est connu que les groupements OH du support, qui présente un caractère plutôt acide, peuvent interagir avec les atomes des composés oxygénés. Il est souvent proposé que l'oxygène d'un composé phénolique (par exemple, le guaiacol) interagisse avec le support de la phase métallique (SiO_2) comme montré dans la Figure 1-29. Comme pour les métaux nobles, il est proposé que l'hydrogène soit activé sur le site métallique, l'hydrure formé provoque ensuite la rupture de la liaison C-O [91].

Le rôle des supports « oxophiliques » est également important pour les phases métalliques non nobles. Dans le cas de ce type de support (par exemple ZrO_2 ou TiO_2), l'interaction des composés oxygénés a plutôt lieu avec les cations du support (Zr^{+4} ou Ti^{+4}), ce qui pourrait favoriser leur désoxygénation [92]. Par exemple, l'amélioration de l'activité en HDO des catalyseurs à base de nickel a été observée grâce l'utilisation de la zircone comme support [84,87]. En HDO du phénol à 300 ºC sous pression atmosphérique, il a été montré que le catalyseur Ni/ZrO_2 est plus sélectif en produit désoxygéné que Ni/SiO_2 [87]. Mortensen et al. [22] ont également rapporté que Ni/ZrO_2 est le catalyseur qui présente les meilleures

performances en désoxygénation du phénol (275 °C, 10 MPa) parmi une série de solides à base de nickel (Ni/Al_2O_3, Ni/SiO_2, $Ni/MgAl_2O_4$, Ni/CeO_2-ZrO_2, Ni/CeO_2, Ni/C).

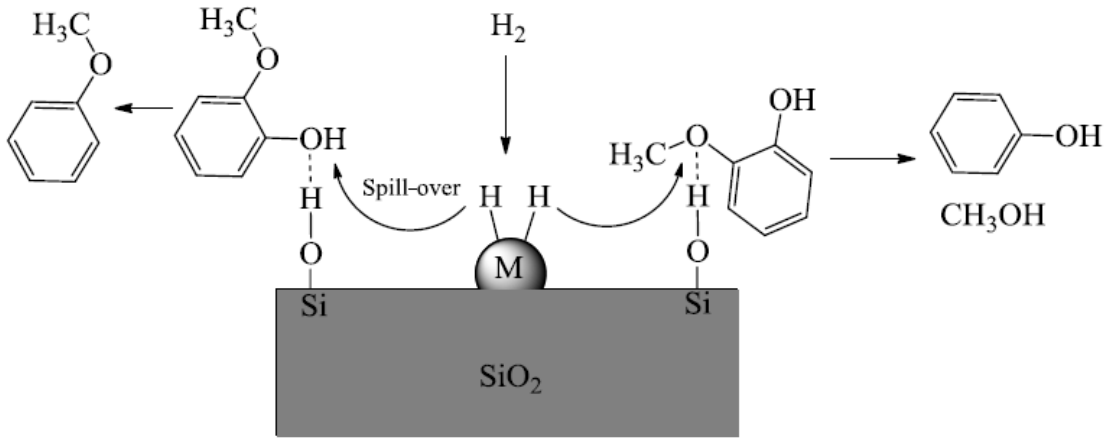

Figure 1-29 : Mécanisme proposé pour l'HDO du guaiacol sur des catalyseurs non nobles [90].

6.4. Catalyseurs phosphures

Les phases phosphures sont apparues à partir de la modification dans la préparation des catalyseurs métalliques classiques en introduisant du phosphore dans la synthèse, ce qui a conduit à des phases très prometteuses en hydrodésulfuration (HDS) et en hydronitrogenation (HDN) [93,94]. Les structures cristallines de différentes phases phosphures sont montrées sur la Figure 1-30.

Il est proposé que les sites actifs dans ce type de catalyseur M_xP_y sont les métaux $M^{\delta+}$ (M représente un métal comme Ni ou Co qui porte de faibles charges positives) [95]. Des sites acides de Brønsted et de Lewis sont aussi présents [94]. Ces phases peuvent catalyser plusieurs types de réaction comme des réactions d'hydrogénation, d'hydrogénolyse et de déshydration.

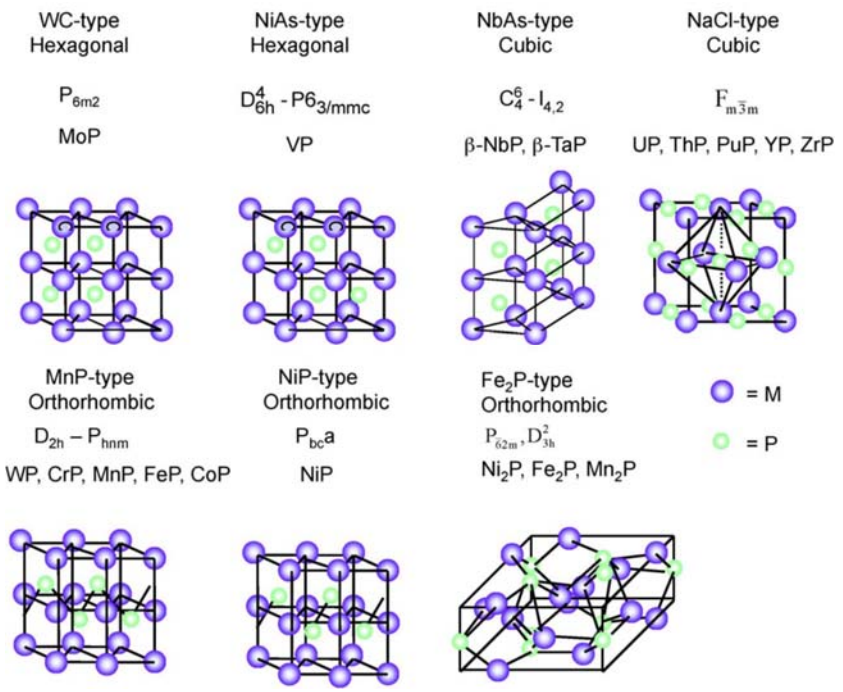

Figure 1-30 : Structures cristallines de différentes phases phosphures [96].

Récemment, plusieurs études sur la désoxygénation de divers composés phénoliques tels que le phénol [97], le guaiacol [98] et le p-crésol [99] ont montré que les catalyseurs à base de phosphure de nickel sont des catalyseurs efficaces en HDO. Zhao et al. [98] ont étudié l'HDO du guaiacol à pression atmosphérique à 300 ºC. Les résultats montrent que le catalyseur Ni_2P/SiO_2 est plus actif en désoxygénation que Pd/Al_2O_3 et que $CoMoS/Al_2O_3$. De plus, les mêmes auteurs ont rapporté que l'activité en HDO pour différentes phases phosphures suit l'ordre : $Ni_2P/SiO_2 > Co_2P/SiO_2 > Fe_2P/SiO_2 > WP/SiO_2 > MoP/SiO_2$.

La contribution de chaque voie de désoxygénation des composés phénoliques (DDO vs. HYD) dépend également de la nature de la phase M_xP phosphure (Ni_2P, MoP, Fe_2P…) et des conditions expérimentales utilisées [97,99–102]. Par exemple, en ce qui concerne la phase phosphure la plus active, c'est-à-dire Ni_2P, il a été observé que le Ni_2P massique produit du toluène comme principal produit désoxygéné à partir du p-crésol [102], tandis que le méthylcyclohexane apparait comme le produit désoxygéné majoritaire en utilisant le même

réactif et dans des conditions expérimentales similaires (325-350 ° C, 4-4,4 MPa) [99]. Il est donc intéressant d'évaluer et de comprendre l'influence des paramètres expérimentaux qui jouent un rôle dans les propriétés catalytiques de ces matériaux.

7. Conclusion

La biomasse lignocellulosique est une source très prometteuse pour la production de carburants et de produits chimiques à haute valeur ajoutée. Cette matière première est facilement accessible à partir de cultures dédiés mais aussi à partir de déchets.

L'intégration des différents procédés technologiques tels quels des procédés thermiques (pyrolyse ou gazéification), des procédés chimiques (hydrolyse, hydrotraitement, reformage à la vapeur et synthèse Fisher-Tropsh), des précédés biochimiques (fermentation, digestion anaérobique) conduit au concept de bioraffinerie.

Les travaux de cette thèse sont plus particulièrement axés sur la valorisation de biohuiles issues de procédés de pyrolyse et/ou de la dépolymérisation de la lignine, ces charges contenant des composés phénoliques. Le traitement de ces charges par le procédé d'hydrodésoxygénation est indispensable pour leur valorisation. Les composés phénoliques sont ainsi couramment utilisés comme molécules modèles afin d'étudier et de comprendre le rôle du catalyseur lors du traitement de ces charges.

Depuis quelques années, de nombreux travaux portant sur l'hydrodésoxygénation de composés phénoliques en présence de différentes phases catalytiques ont été rapportés dans la littérature. Néanmoins, ces travaux montrent que les propriétés des différents solides testés sont fortement dépendantes des conditions opératoires utilisées. Il est donc souvent difficile de les comparer d'une étude à une autre. Par ailleurs, les résultats présentés sont parfois contradictoires, notamment en termes d'activité et de sélectivité.

Ainsi, ces travaux de thèse se sont particulièrement intéressés à la mesure des propriétés catalytiques (activité, sélectivité et stabilité) des matériaux qui pourraient être mis en œuvre

dans un procédé d'hydrodésoxygénation intégré dans une bioraffinerie. Pour cela, des catalyseurs présentant des phases sulfures (MoS_2 et CoMoS), des phases oxydes (MoO_x), des phases métalliques (Ni) et phosphures (Ni_2P) ont été évalués en HDO de molécules phénoliques (o-, m- et p-crésol). L'influence de différents supports catalytiques (Al_2O_3, SiO_2, SBA-15, ZrO_2) a également été examinée.

Les objectifs de ces travaux sont donc de déterminer les principaux paramètres qui gouvernent la désoxygénation des composés phénoliques (type de phase active, support catalytique et conditions opératoires utilisées,…) et également de permettre une meilleure description des sites actifs et des mécanismes réactionnels impliqués pour chaque phase catalytique étudiée.

8. Références

[1] S. Fernando, S. Adhikari, C. Chandrapal, N. Murali, Energy Fuels. 20 (2006) 1727–1737.

[2] S.K. Maity, Energy Rev. 43 (2015) 1427–1445.

[3] J.R. Rostrup-Nielsen, Science. 308 (2005) 1421–1422.

[4] P. Venturi, G. Venturi, Biomass Bioenergy. 25 (2003) 235–255.

[5] R. Adib, Renewables 2015 Global Status Report (2015).

[6] M. Balat, H. Balat, Appl. Energy. 86 (2009) 2273–2282.

[7] G. Sorda, M. Banse, C. Kemfert, Energy Policy. 38 (2010) 6977–6988.

[8] P. Weiland, Appl. Microbiol. Biotechnol. 85 (2010) 849–860.

[9] C. Lu, J.A. Napier, T.E. Clemente, E.B. Cahoon, Curr. Opin. Biotechnol. 22 (2011) 252–259.

[10] F. Cherubini, Energy Convers. Manag. 51 (2010) 1412–1421.

[11] M. Stöcker, Angew. Chem. Int. Ed. 47 (2008) 9200–9211.

[12] J.S. Fleming, S. Habibi, H.L. MacLean, Transp. Res. Part Transp. Environ. 11 (2006) 146–159.

[13] E. Searcy, P.C. Flynn, Int. J. Green Energy. 5 (2008) 423–437.

[14] J.K. Kurian, G.R. Nair, A. Hussain, G.V. Raghavan, Renew. Sustain. Energy Rev. 25 (2013) 205–219.

[15] H. Ohara, Biorefinery, Appl. Microbiol. Biotechnol. 62 (2003) 474–477.

[16] B. Kamm, M. Kamm, Appl. Microbiol. Biotechnol. 64 (2004) 137–145.

[17] J. Gravitis, M. Suzuki, Biomass refinery–A way to produce value added products and base for agricultural zero emissions system, in: Citeseer, 1999.

[18] F. Cherubini, N.D. Bird, A. Cowie, G. Jungmeier, B. Schlamadinger, S. Woess-Gallasch, Resour. Conserv. Recycl. 53 (2009) 434–447.

[19] S. Hunt, R. Drigo, A review of the current state of bioenergy development in G8+ 5 countries, (2008).

[20] T. Browne, R. Gilsenan, Bio-energy and bio-chemicals synthesis report, FPInnovations, 2011.

[21] S.N. Naik, V.V. Goud, P.K. Rout, A.K. Dalai, Energy Rev. 14 (2010) 578–597.

[22] D. Hoornweg, P. Bhada-Tata, C. Kennedy, Nature. 502 (2013) 615–617.

[23] A.J. Ragauskas, C.K. Williams, B.H. Davison, G. Britovsek, J. Cairney, C.A. Eckert, W.J. Frederick, J.P. Hallett, D.J. Leak, C.L. Liotta, Science. 311 (2006) 484–489.

[24] S.R. Smith, Environ. Int. 35 (2009) 142–156.

[25] S.V. Mohan, G. Nikhil, P. Chiranjeevi, C.N. Reddy, M. Rohit, A.N. Kumar, O. Sarkar, Bioresour. Technol. 215 (2016) 2–12.

[26] P. Mondal, M. Basu, N. Balasubramanian, Biofuels Bioprod. Biorefining. 2 (2008) 155–174.

[27] A. Srivastava, R. Prasad, Renew. Sustain. Energy Rev. 4 (2000) 111–133.

[28] W.M. Achten, E. Mathijs, L. Verchot, V.P. Singh, R. Aerts, B. Muys, Biofuels Bioprod. Biorefining. 1 (2007) 283–291.

[29] W.-T. Tsai, C.-C. Lin, C.-W. Yeh, Renew. Sustain. Energy Rev. 11 (2007) 838–857.

[30] A. Ahmad, N.M. Yasin, C. Derek, J. Lim, Renew. Sustain. Energy Rev. 15 (2011) 584–593.

[31] S.K. Maity, Renew. Sustain. Energy Rev. 43 (2015) 1427–1445.

[32] D.M. Alonso, J.Q. Bond, J.A. Dumesic, Green Chem. 12 (2010) 1493–1513.

[33] P. Kumar, D.M. Barrett, M.J. Delwiche, P. Stroeve, Ind. Eng. Chem. Res. 48 (2009) 3713–3729.

[34] N. Mosier, C. Wyman, B. Dale, R. Elander, Y. Lee, M. Holtzapple, M. LadischBioresour. Technol. 96 (2005) 673–686.

[35] N. Eloutassi, B. Louaste, L. Boudine, A. Remmal, Rev. Energ. Renouvelables. 17 (2014) 600–609.

[36] J. Kim, S. Yun, Z. Ounaies, Macromolecules. 39 (2006) 5583–5583.

[37] Y. Li, S.S. Sheyko, Topics in current chemistry. 369 (2015) 1-36.

[38] A.J. Ragauskas, G.T. Beckham, M.J. Biddy, R. Chandra, F. Chen, M.F. Davis, B.H. Davison, R.A. Dixon, P. Gilna, M. Keller, Science. 344 (2014) 1246843.

[39] J.H. Lora, W.G. Glasser, J. Polym. Environ. 10 (2002) 39–48.

[40] M. Hoogwijk, A. Faaij, R. Van Den Broek, G. Berndes, D. Gielen, W. Turkenburg, Biomass Bioenergy. 25 (2003) 119–133.

[41] B. Kamm, P.R. Gruber, M. Kamm, Biorefineries–industrial processes and products, Wiley Online Library (2006).

[42] A.V. Bridgwater, Chem. Eng. J. 91 (2003) 87–102.

[43] K. Raveendran, A. Ganesh, K.C. Khilar, Fuel. 75 (1996) 987–998.

[44] T. Kan, V. Strezov, T.J. Evans, Renew. Sustain. Energy Rev. 57 (2016) 1126–1140.

[45] A. Bridgwater, S. Czernik, J. Piskorz, Fast Pyrolysis Biomass Handb. Newbury UK CPL Press Lib. House. 2 (2008) 1–22.

[46] V. Kirubakaran, Renew. Sustain. Energy Rev. 13 (2009) 179–186.

[47] T. Nussbaumer, Energy Fuels. 17 (2003) 1510–1521.

[48] Y. Sun, J. Cheng, Bioresour. Technol. 83 (2002) 1–11.

[49] J.B. Holm-Nielsen, T. Al Seadi, P. Oleskowicz-Popiel, Bioresour. Technol. 100 (2009) 5478–5484.

[50] J. Van Dyk, B. Pletschke, Biotechnol. Adv. 30 (2012) 1458–1480.

[51] H. Lange, S. Decina, C. Crestini, Eur. Polym. J. 49 (2013) 1151–1173.

[52] R. Behling, S. Valange, G. Chatel, Green Chem. 18 (2016) 1839–1854.

[53] B. Joffres, C. Lorentz, M. Vidalie, D. Laurenti, A.-A. Quoineaud, N. Charon, A. Daudin, A. Quignard, C. Geantet, Appl. Catal. B Environ. 145 (2014) 167–176.

[54] B. Joffres, M. Nguyen, D. Laurenti, C. Lorentz, V. Souchon, N. Charon, A. Daudin, A. Quignard, C. Geantet, Appl. Catal. B Environ. 184 (2016) 153–162.

[55] M. Saidi, F. Samimi, D. Karimipourfard, T. Nimmanwudipong, B.C. Gates, M.R. Rahimpour, Energy Environ. Sci. 7 (2014) 103–129.

[56] F. Cherubini, G. Jungmeier, M. Wellisch, T. Willke, I. Skiadas, R. Van Ree, E. de Jong, Biofuels Bioprod. Biorefining. 3 (2009) 534–546.

[57] J.-L. Wertz, A. Richel, P. Gérin, ValBiom. (2015) 1–37.

[58] E. Furimsky, Appl. Catal. Gen. 199 (2000) 147–190.

[59] G.W. Huber, A. Corma, Angew. Chem. Int. Ed. 46 (2007) 7184–7201.

[60] J. Zakzeski, P.C. Bruijnincx, A.L. Jongerius, B.M. Weckhuysen, Chem. Rev. 110 (2010) 3552–3599.

[61] P. Grange, E. Laurent, R. Maggi, A. Centeno, B. Delmon, Catal. Today. 29 (1996) 297–301.

[62] A. Walton, J.V. Lauritsen, H. Topsøe, F. Besenbacher, J. Catal. 308 (2013) 306–318.

[63] H. Topsøe, B.S. Clausen, F.E. Massoth, Catalysis 11 (1996) 1–269.

[64] P. Raybaud, Appl. Catal. Gen. 322 (2007) 76–91.

[65] O.İ. Şenol, Hydrodeoxygenation of aliphatic and aromatic oxygenates on sulphided catalysts for production of second generation biofuels (2007).

[66] R. Chianelli, Catal. Rev. Sci. Eng. 26 (1984) 361–393.

[67] H. Shafaghat, P.S. Rezaei, W.M.A.W. Daud, RSC Adv. 5 (2015) 103999–104042.

[68] C. Sepúlveda, K. Leiva, R. García, L. Radovic, I. Ghampson, W. DeSisto, Catal. Today. 172 (2011) 232–239.

[69] F. Massoth, P. Politzer, M. Concha, J. Murray, J. Jakowski, J. Simons, J. Phys. Chem. B. 110 (2006) 14283–14291.

[70] Y. Romero, F. Richard, S. Brunet, Appl. Catal. B Environ. 98 (2010) 213–223.

[71] E. Furimsky, Catal. Today. 217 (2013) 13–56.

[72] H. Wang, J. Male, Y. Wang, ACS Catal. 3 (2013) 1047–1070.

[73] D.A. Ruddy, J.A. Schaidle, J.R. Ferrell III, J. Wang, L. Moens, J.E. Hensley, Green Chem. 16 (2014) 454–490.

[74] R. Wandas, J. Surygala, E. Śliwka, Fuel. 75 (1996) 687–694.

[75] O. Şenol, E.-M. Ryymin, T.-R. Viljava, A. Krause, J. Mol. Catal. Chem. 277 (2007) 107–112.

[76] S. Echeandia, P. Arias, V. Barrio, B. Pawelec, J. Fierro, Appl. Catal. B Environ. 101 (2010) 1–12.

[77] M. Badawi, J.-F. Paul, E. Payen, Y. Romero, F. Richard, S. Brunet, A. Popov, E. Kondratieva, J.-P. Gilson, L. Mariey, Oil Gas Sci. Technol. D'IFP Energ. Nouv. 68 (2013) 829–840.

[78] E.O. Odebunmi, D.F. Ollis, J. Catal. 80 (1983) 56–64.

[79] E. Laurent, B. Delmon, Ind. Eng. Chem. Res. 32 (1993) 2516–2524.

[80] C. Bouvier, Y. Romero, F. Richard, S. Brunet, Green Chem. 13 (2011) 2441–2451.

[81] E.-M. Ryymin, M.L. Honkela, T.-R. Viljava, A.O.I. KrauseAppl. Catal. Gen. 389 (2010) 114–121.

[82] E.-M. Ryymin, M.L. Honkela, T.-R. Viljava, A.O.I. Krause, Appl. Catal. Gen. 358 (2009) 42–48.

[83] S. Brillouet, E. Baltag, S. Brunet, F. Richard, Appl. Catal. B Environ. 148–149 (2014) 201–211.

[84] P.M. Mortensen, J.-D. Grunwaldt, P.A. Jensen, A.D. Jensen, Acs Catal. 3 (2013) 1774–1785.

[85] C. Zhao, J.A. Lercher, ChemCatChem. 4 (2012) 64–68.

[86] G. Neri, A. Visco, A. Donato, C. Milone, M. Malentacchi, G. Gubitosa, Appl. Catal. Gen. 110 (1994) 49–59.

[87] P.M. de Souza, L. Nie, L.E. Borges, F.B. Noronha, D.E. Resasco, Catal. Lett. 144 (2014) 2005–2011.

[88] P.M. de Souza, R.C. Rabelo-Neto, L.E. Borges, G. Jacobs, B.H. Davis, U.M. Graham, D.E. Resasco, F.B. Noronha, ACS Catal. 5 (2015) 7385–7398.

[89] T. Mochizuki, S.-Y. Chen, M. Toba, Y. Yoshimura, Appl. Catal. B Environ. 146 (2014) 237–243.

[90] R. Olcese, M. Bettahar, D. Petitjean, B. Malaman, F. Giovanella, A. Dufour, Appl. Catal. B Environ. 115 (2012) 63–73.

[91] C.R. Lee, J.S. Yoon, Y.-W. Suh, J.-W. Choi, J.-M. Ha, D.J. Suh, Y.-K. Park, Catal. Commun. 17 (2012) 54–58.

[92] P.M. de Souza, R.C. Rabelo-Neto, L.E. P. Borges, G. Jacobs, B.H. Davis, D.E. Resasco, F.B. Noronha, ACS Catal. (2017).

[93] S.T. Oyama, T. Gott, H. Zhao, Y.-K. Lee, Catal. Today. 143 (2009) 94–107.

[94] R. Prins, M.E. Bussell, Catal. Lett. 142 (2012) 1413–1436.

[95] Q. Yuan, H. Ariga, K. Asakura, Top. Catal. 58 (2015) 194–200.

[96] S. Carenco, D. Portehault, C. Boissiere, N. Mezailles, C. Sanchez, Chem. Rev. 113 (2013) 7981–8065.

[97] Y. Li, X. Yang, L. Zhu, H. Zhang, B. Chen, RSC Adv. 5 (2015) 80388–80396.

[98] H. Zhao, D. Li, P. Bui, S. Oyama, Appl. Catal. Gen. 391 (2011) 305–310.

[99] W. Wang, K. Zhang, H. Liu, Z. Qiao, Y. Yang, K. Ren, Catal. Commun. 41 (2013) 41–46.

[100] A. Berenguer, T. Sankaranarayanan, G. Gómez, I. Moreno, J. Coronado, P. Pizarro, D. Serrano, Green Chem. 18 (2016) 1938–1951.

[101] V.M. Whiffen, K.J. Smith, S.K. Straus, Appl. Catal. Gen. 419 (2012) 111–125.

[102] V.M. Whiffen, K.J. Smith, Top. Catal. 55 (2012) 981–990.

Chapitre 2 : Partie expérimentale

Ce chapitre présente les méthodes expérimentales et les produits chimiques employés pendant ces travaux de thèse. Il comprend une présentation détaillée des techniques utilisées pour caractériser les différents catalyseurs, une description de l'appareillage expérimental (réacteur sous pression en échelle micro pilote) permettant de mesurer les propriétés catalytiques des différents solides en HDO des composés phénoliques modèles (crésols), ainsi que les méthodes analytiques utilisées au cours de ce travail de thèse.

1. Préparation des différents catalyseurs

1.1. Catalyseurs sulfures

Dans l'étude des phases sulfures en HDO, deux catalyseurs à base de molybdène supportés fournis par la société Total sous forme oxyde ont été étudiés, un catalyseur non promu ($Mo/\gamma\text{-}Al_2O_3$) et un catalyseur promu par du cobalt ($CoMo/\gamma\text{-}Al_2O_3$).

Le catalyseur est d'abord prétraité pour obtenir la phase sulfure. Cette procédure est réalisée *in situ* à 350 ºC sous 4 MPa de pression d'hydrogène en injectant une charge composée de 5,8 % pds. de DMDS dilué dans le dodecane. En effet, ce composé soufré se décompose en présence d'hydrogène en sulfure d'hydrogène et en méthane (Eq. (1)). Cette molécule soufrée (H_2S) est l'agent responsable de la sulfuration du catalyseur.

$$C_2H_3S_2 + 3H_2 \longrightarrow 2H_2S + 2CH_4 \qquad (1)$$

La charge de sulfuration est d'abord injectée à 150 °C pendant 1 h. Les débits en charge sulfurante et en hydrogène sont égaux à 8 mL h^{-1} et 4,7 NL h^{-1}, respectivement. Le rapport H_2/charge est égal à 587 NL L^{-1}. Ensuite, la température du réacteur est portée à 350 °C avec une rampe de chauffage de 5 °C min^{-1}. Le débit de charge est maintenu pendant 14 h à 350 ºC.

1.2. Catalyseurs oxydes

Trois catalyseurs supportés à base d'oxyde de molybdène ont été synthétisés et étudiés en HDO. Trois supports ont été choisis, une silice (SiO_2) mésoporeuse non ordonnée fournie par la société Degussa, une alumine (Al_2O_3) mésoporeuse fournie par la société Total et une silice mésoporeuse ordonnée de grande surface spécifique (SBA-15) synthétisée au laboratoire.

Pour la préparation de la SBA-15, 4 g de Pluronic P123 ($PEO_{20}PPO_{70}PEO_{20}$, M = 5.800 g mol^{-1}) a été dissous dans 150 ml d'une solution d'HCl (1,6 M) à 40 ° C jusqu'à dissolution complète du template. Ensuite, l'orthosilicate de tétraéthyle (9,6 g) est ajouté goutte à goutte sous agitation continue pendant 24 h. Le gel résultant a été soumis à un traitement hydrothermal pendant 48 heures à 100 °C. Après, le solide obtenu a été séché à 80 ºC pendant 24h. Finalement, le support SBA-15 a été obtenu après calcination à 550 °C pendant 6 h dans un four à moufle (rampe de chauffage de 1,5 °C min^{-1}).

L'oxyde de molybdène a été imprégné sur les différents supports en utilisant comme sel précurseur l'heptamolybdate d'ammonium ($(NH_4)_6.Mo_7O_{24},4H_2O$). Les solutions de précurseurs ont été préparées pour obtenir 10 pds% de Mo. Les imprégnations ont été réalisées en utilisant la méthode dite d'imprégnation par humidité naissante (IWI pour incipient wetness impregnation). Après imprégnation, les catalyseurs ont été placés dans une étuve à 25 ºC pendant 5 jours. Les catalyseurs à base d'oxyde de molybdène ont été obtenus après calcination à 400ºC (1,5 ºC min^{-1}) pendant 6 h dans un four à moufle. Avant leur utilisation, ces catalyseurs sont prétraités sous 4 MPa d'hydrogène (4,7 L h^{-1}) à 340 ºC pendant 30 min.

1.3. Catalyseurs métalliques

Deux catalyseurs à base de nickel (Ni/SiO_2 et Ni/ZrO_2) ont également été préparés. Les deux supports utilisés sont la SiO_2 fournie par Sigma-Aldrich et la ZrO_2 fournie par Saint-Gobain. L'oxyde de nickel a été introduit sur le support en utilisant la même technique que pour les catalyseurs à base de Mo (méthode IWI), à partir de solutions préparées à partir du nitrate de nickel ($Ni(NO_3)_2$) comme sel précurseur. Les solutions ont été préparées pour obtenir 10 pds

% de Ni. Après imprégnation, les échantillons ont été séchés à 100 °C pendant 24 heures puis calcinés sous air (60 mL min^{-1}) à 500 °C pendant 3 h. La phase métallique Ni^0 est préparée par réduction de l'oxyde de nickel supporté sous 4 MPa avec un débit d'H_2 de 4,7 L h^{-1} à 450 ºC (5 ºC min^{-1}) pendant 2 h.

1.4. Catalyseurs phosphures

Deux catalyseurs à base de phosphure de nickel (Ni_2P/SiO_2 et Ni_2P/ZrO_2) ont été préparés en utilisant les mêmes supports que pour le nickel métallique. Tout d'abord, une solution contenant du nitrate de nickel ($Ni(NO_3)_2.6H_2O$) a été préparée afin d'obtenir un taux de chargement de 10 pds % de Ni. Ensuite, le phosphate de diammonium ($(NH_4)_2HPO_4$) a été solubilisé dans un deuxième bécher. La solution contenant la source de phosphore est alors additionnée goutte à goutte dans le bécher contenant le nitrate de nickel, ceci sous agitation constante. Dans le bécher contenant la solution résultante, un précipité est observé. Sa dissolution complète est obtenue après ajout d'une faible quantité d'acide nitrique (HNO_3). Ensuite, les supports sont imprégnés par cette solution, en utilisant toujours la méthode IWI. Après imprégnation, les échantillons ont été séchés dans un four à 100 °C pendant 24 heures, puis calcinés sous air (60 mL min^{-1}) à 500 °C pendant 3 h. La phase de phosphure de nickel (Ni_2P) est obtenue après traitement sous 4 MPa d'hydrogène (4,7 L h^{-1}) à 450 ºC (5 ºC min^{-1}) pendant 2 h. Cette procédure d'activation est celle utilisée pour les catalyseurs à base de nickel.

2. Techniques de caractérisation des catalyseurs

Les caractérisations des différents matériaux catalytiques ont été principalement réalisées à l'aide des techniques disponibles au sein de l'Institut de Chimie des Milieux et Matériaux de Poitiers (IC2MP) à l'Université de Poitiers. Certaines caractérisations ont également été effectuées dans l'Instituto Nacional de Pesquisa (INT) à Rio de Janeiro (Brésil).

Les catalyseurs frais, après activation et après réaction, ont été caractérisés par différentes méthodes. Ainsi les teneurs en métaux ont été déterminées soit par fluorescence X, soit par absorption atomique. Les propriétés texturales ont été mesurées par adsorption/désorption d'azote. Les phases cristallines présentes dans les catalyseurs ont été identifiées par diffraction des rayons X (DRX). Certains catalyseurs ont été analysés par microscopie électronique en transmission (MET) afin notamment d'évaluer la taille des particules supportées. La réductibilité des espèces oxydes présentes dans les catalyseurs a été mesurée par réduction à température programmée (TPR). L'acidité des solides a été mesurée par thermodésorption programmée d'ammoniac (TPD-NH_3). Le nombre des sites actifs, notamment des phases phosphures, a été déterminé par chimisorption de CO. Les catalyseurs après réaction ont été analysés par analyse élémentaire via combustion du solide (CHNS).

L'ensemble de ces techniques est présenté plus en détails dans les paragraphes suivants.

2.1. Fluorescence X (FX)

L'échantillon est irradié par un rayonnement X d'une source incidente d'un spectromètre Bruker S4 Explorer dispersif en longueur d'onde. Les intensités des rayons X caractéristiques des atomes de métaux présents dans l´échantillon sont mesurées et comparées à celles obtenues sur des références, ce qui permet de quantifier les éléments présents dans le solide.

2.2. Absorption atomique

La teneur en molybdène des catalyseurs à base d'oxydes de molybdène a été déterminée à l'aide d'un instrument AA200 Perkin Elmer. Avant cette analyse, les solides sont solubilisés dans une solution aqueuse d'acide chlorhydrique et nitrique.

2.3. Adsorption/désorption d'azote

À partir des isothermes d'adsorption d'azote, il est possible d'obtenir les propriétés texturales des solides (surface spécifique, volume poreux, taille moyenne des pores). Pour cette mesure, un appareil Micromeritics ASAP 2000 a été utilisé. Avant analyse, les échantillons sous forme de poudre sont dégazés pendant une nuit sous vide secondaire à 200 °C. La surface spécifique (en $m^2\ g^{-1}$) est calculée à partir de l'isotherme d'adsorption (P/P_0 compris entre 0,05 et 0,20) en utilisant la méthode de Brunauer-Emmett-Teller (BET). Le volume total des pores est calculé à partir du volume d'azote adsorbé à P/P_0 égal à 0,99. Le volume mésoporeux est déterminé selon la méthode du t-plot. La distribution moyenne des mésopores est calculée à partir de la branche d'adsorption de l'isotherme en utilisant la méthode Barret-Joyner-Halenda (BJH).

2.4. Analyse élémentaire (C. H. N. S.)

Les teneurs en carbone et en soufre des différents solides obtenus après test catalytique sont déterminées à l'aide d'un analyseur élémentaire NA2100 Protein Thermoquest. Pour cela, l'échantillon est pesé précisément (1 à 1,5 mg) et placé dans une nacelle en étain. Ensuite, il est chauffé à 1020 °C en présence d'oxygène dilué dans l'hélium, les différents éléments chimiques (C. H. N. S.) sous forme de gaz de combustion du solide (CO_2, H_2O, N_2 et SO_2) sont séparés par une colonne chromatographique remplie avant d'être détectés à l'aide d'un catharomètre. Afin de vérifier les résultats analytiques, trois échantillons de référence sont également placés dans l'appareil, l'un correspondant au « blanc » et les deux autres avec des teneurs connues en carbone et en soufre. Les données sont exploitées à l'aide du logiciel Eager 2000.

2.5. Microscopie électronique à transmission (MET)

La microscopie électronique à transmission (MET) permet de visualiser les particules présentes dans les catalyseurs afin de vérifier leur morphologie et de déterminer leur taille. Les

études MET sont réalisées avec un microscope JEOL 2100 UHR 200 kV équipé d'un scanner Gatan Ultra. Les échantillons à analyser sont tout d'abord dispersés par ultrasons dans de l'éthanol et déposés sur une grille de cuivre supportant un film de carbone perforé.

2.6. Diffraction des rayons X (DRX)

La technique de diffraction des rayons X (DRX) permet d'obtenir des informations sur les phases cristallines présentes dans les solides étudiés. Les diffractogrammes ont été obtenus à l'aide d'un diffractomètre PAN-alytical Empyrean à poudre en utilisant une source au cuivre. L'identification des phases a été réalisée par comparaison avec les fichiers de la base de données de référence présente dans le logiciel PAN-alytical HighScore Plus.

Après avoir obtenus les diffractogrammes, il est possible de calculer la taille des cristallites par l'équation de Scherrer (Eq. (2)) :

$$Dc = \frac{K\,\lambda}{\beta\,\cos\theta} \qquad (2)$$

avec :

Dc : taille moyenne des cristallites suivant une raie

K : facteur de forme, égal à 0,9

λ : longueur d'onde (1,54059 Å pour un rayonnement au cuivre)

β : Largeur à mi-hauteur

Dans certains cas, notamment pour les phases Ni et Ni_2P supportées, un affinement des diffractogrammes a été réalisé par la méthode de Rietveld.

2.7. Réduction en température programmée (RTP-H_2)

La technique de réduction en température programmée (TPR) permet d'identifier les différentes espèces réductibles présentes dans le solide à partir de la consommation

d'hydrogène pendant l'expérience. L'échantillon solide (environ 100 mg) est placé dans un réacteur tubulaire en quartz en forme de U, puis chauffé par un four électrique. L'appareil utilisé est un Micromeritics AutoChem II. Avant l'étape de réduction, le solide est prétraité sous He (20 mL min^{-1}) à 200 °C pendant 30 min avec une rampe de chauffage de 10 °C min^{-1}. Le catalyseur est ensuite refroidi à 50 °C. Le gaz utilisé est un mélange de 10% de H_2 dilué dans de l'argon (20 mL min^{-1}). La température est augmentée progressivement jusqu'à 1000 °C (5 °C min^{-1}), le solide est maintenu pendant 90 min à cette température. La consommation d'hydrogène est mesurée à l'aide du détecteur TCD.

2.8. Thermodésorption de l'ammoniac (TPD-NH_3)

La technique de thermodésorption d'ammoniac (TPD-NH_3) permet d'obtenir des informations sur les propriétés acides des solides étudiés. Le catalyseur (environ 150 mg) est tout d'abord prétraité jusqu'à 450 °C (montée en température utilisée : 5 ºC min^{-1}) pendant 2 h sous débit d'H_2 pur (60 mL min^{-1}). Après cette étape de réduction, un rinçage par de l'hélium a lieu pendant 30 minutes et l'échantillon est ensuite refroidi à 100 °C. Le solide est traversé par un mélange de 20% de NH_3 dans He (30 mL min^{-1}) à un débit de 30 ml min^{-1} pendant 30 min. L'ammoniac physisorbé est alors éliminé par rinçage avec de l'hélium (30 ml min^{-1}) pendant 1 h. La désorption de NH_3 est mesurée à partir de 100 ºC (montée en température : 10 °C min^{-1}) jusqu'à 600 ºC sous He. Les effluents gazeux sont analysés en continu par TCD.

2.9. Chimisorption de CO

Afin d'estimer le nombre de sites actifs des phases métalliques et phosphures et donc accéder aux valeurs de TOF (de l'anglais *TurnOver Frequency*), la chimisorption de CO est réalisée à 30 °C. Les catalyseurs ont été prétraités au préalable sous 4 MPa d'H_2 à 450 ºC (5 ºC min^{-1}) pendant 2 h. Le solide (100 mg) est introduit dans le réacteur en quartz. Tout d'abord, l'échantillon solide est prétraité à 200 °C sous atmosphère d'hélium (30 mL min^{-1}) pendant 30 minutes et refroidi à 50 °C. Ensuite, une étape de réduction du solide est réalisée sous hydrogène

(60 mL min^{-1}), la température étant augmentée progressivement jusqu'à 700°C (vitesse de chauffage de 5°C min^{-1}), la température finale est maintenue pendant 2 h. Le réacteur est refroidi à la température d'adsorption (30 °C) sous atmosphère d'hélium (30 ml min^{-1}). Des pulses successifs de CO pur sont injectés successivement toutes les 2 min à l'aide d'une boucle de volume égal à 0,25 mL. La consommation de CO est analysée par un chromatographe en phase gazeuse équipée d'un détecteur TCD et d'une colonne Porapak Q, cette dernière permet d'analyser la quantité de CO_2 pouvant être produite pendant la réaction.

2.10. Chimisorption d'oxygène

Similairement à la mesure des sites actifs des phases métalliques et phosphures obtenue par chimisorption de CO, la chimisorption d'oxygène est utilisé afin de déterminer la quantité de sites actifs (lacunes en oxygène) présents sur les catalyseurs à base d'oxydes de molybdène. Les catalyseurs ont été prétraités au préalable sous 4 MPa d'H_2 à 340 ºC (5 ºC min^{-1}) pendant 30 min. Pour ces mesures, des pulses successifs de O_2 pur sont injectées toutes les 2 min à l'aide d'une boucle de volume 0,25 mL à 340 ºC. La consommation d'oxygène est déterminée par un chromatographe en phase gazeuse équipée d'un détecteur TCD et d'une colonne Porapak Q.

2.11. Raman

Les solides à base d'oxydes de molybdène ont été caractérisés par Raman. L'appareil utilisé est un HORIBA JOBIN YVON Labram HR800UV équipé d'un laser à ions d'argon (Melles Griot) avec une longueur d'onde d'excitation de 514,5 nm. La puissance du laser choisie est de 0,4 mW.

3. Mesure des propriétés catalytiques

3.1. Appareillage utilisé

Les tests catalytiques sont réalisés dans un réacteur à lit fixe traversé en flux descendant. Trois parties principales sur le montage expérimental sont facilement identifiables : le réacteur et son système de chauffage, l'alimentation dans la partie supérieure du réacteur composé de l'alimentation en hydrogène et en charge liquide réactionnelle, ainsi que le système d'obtention des échantillons en sortie du réacteur (Figure 2-1).

Le réacteur est de forme cylindrique en acier inoxydable (pression d'essai = 25 MPa) positionné en vertical (longueur = 40 cm, $d_{extérieur}$ = 1,72 cm et $d_{intérieur}$ = 1,26 cm). La pression à l'entrée du système est contrôlée à l'aide d'un contrôleur de pression Brooks 5866 (0-5 MPa). La charge liquide réactionnelle est maintenue dans des burettes réservoirs à une légère pression (< 50 kPa). Le débit de la charge liquide réactionnelle est contrôlé par une pompe Gilson 307 (avec une tête de pompe de 5 cm^3 et des débits compris entre 10 µL/min jusqu'à 10 mL/min). La source d'hydrogène pur est une bouteille à 20 MPa, le débit d'H_2 étant contrôlé par un débitmètre volumique Brooks 5850 (étalonné pour avoir des débits compris entre 0 NL/h et 30 NL/h).

L'ensemble des appareillages du montage expérimental est schématisé dans la Figure 2-1 et il est composé :

(1) d'un réacteur à lit fixe en position verticale,

(2) de l'arrivée en gaz contrôlé par le débitmètre Brooks 5850,

(3) de l'arrivée en charge liquide réactionnelle,

(4) de la pompe Gilson 307,

(5) du condenseur Minichiller-Huber cryostat maintenu à 10 ºC,

(6) et du système de neutralisation et d'évacuation des gaz.

La régulation de la température se fait à l'aide d'un thermocouple situé au cœur du lit catalytique afin de mesurer la température la plus exacte au sein du catalyseur. Ce thermocouple est introduit dans un puits thermométrique localisé à l'extrémité inferieure du réacteur.

Trois coquilles SOTELEM permettent de chauffer le réacteur à la température désirée. Des thermocouples sont placés dans chaque coquille afin de mesurer leur température. Ils sont reliés à des régulateurs électroniques, qui gèrent la température de consigne et permettent, en cas d'écarts trop importants, de couper l'alimentation du montage. La puissance de chaque coquille est de 500 W (sous 220 V) et elles peuvent atteindre une température maximale de 600 °C.

En sortie du réacteur, les effluents gazeux sont condensés à 10 ºC à l'aide d'un cryostat Minichiller Huber. Les effluents liquides sont prélevés périodiquement à l'aide d'une vanne de purge. Avant chaque prélèvement d'échantillon liquide, le condenseur est isolé de l'ensemble du système réactionnel afin d'éviter des modifications de pression trop importantes dans le réacteur lors de la prise d'échantillon. Après l'obtention de cet échantillon, la pression est alors réajustée à la pression de travail avant que le condenseur ne soit reconnecté au système expérimental. Les échantillons sont obtenus à intervalles de temps réguliers (environ toutes les heures) et analysés par chromatographie en phase gazeuse (caractéristiques données ci-après), pour l'identification et la quantification des produits.

Les effluents non condensables (majoritairement H_2 et H_2S pour les catalyseurs sulfures) sont détendus à pression atmosphérique avant barbotage dans une solution saturée d'hydroxyde de sodium (permettant l'élimination de l'hydrogène sulfuré, si besoin), puis évacués. Le contrôle du débit de gaz en sortie du réacteur est assuré à l'aide d'un débitmètre à aiguille (Ritter, modèle TG 05) couplé à un compteur à gaz (Ritter, modèle EDU 32 FP). Un débitmètre à bulle permet aussi, lorsque cela s'avère nécessaire, de vérifier le débit de gaz en sortie du réacteur.

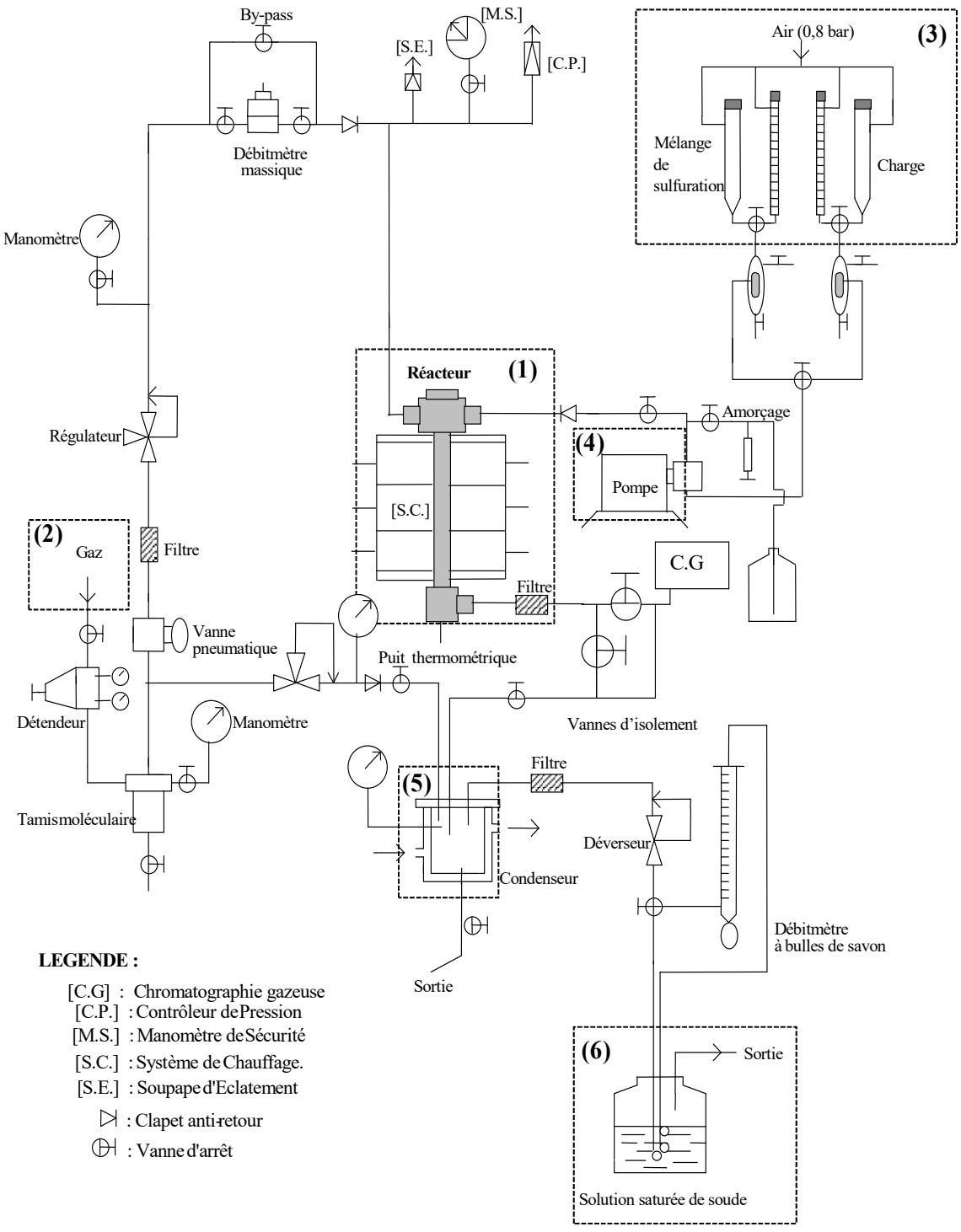

Figure 2-1 : Schéma du micro pilote sous pression pour réalisation des tests catalytiques

3.2. Chargement du réacteur

Les catalyseurs utilisés dans cette étude ont été broyés et tamisés au préalable afin d'obtenir une poudre dans une gamme de granulométrie comprise entre 250 µm et 315 µm. Le catalyseur (de masse comprise entre 30 mg et 120 mg) est dilué dans du carborundum (SiC ou carbure de silicium, un solide inerte) de granulométrie comprise entre 400 µm et 500 µm, afin de maintenir un volume de lit catalytique constant (hauteur de 58 mm), quelle que soit la masse de catalyseur. La quantité de carborundum est mesurée à l'aide d'une éprouvette de 2 ml. Tout d'abord, la quantité de catalyseur est introduite dans le réacteur, puis le carborundum est rajouté. Le lit catalytique est placé entre des billes de verre de 2 mm de diamètre et du carborundum (> 500 µm), afin d'éviter la présence de chemins préférentiels pour la charge réactionnelle. Le coton de verre permet de séparer chaque section. Un schéma représentatif du réacteur chargé est présenté dans la Figure 2-2. La flèche indique le sens de la charge réactionnelle.

Il a été vérifié que l'écoulement au sein du réacteur est bien de type piston, c'est-à-dire que les relations $L/d_{particules} > 50$ et $d_{intérieur}/d_{particules} > 10$ sont vérifiés (où L est la hauteur du lit catalytique, $d_{intérieur}$ est le diamètre interne du réacteur et $d_{particules}$ le diamètre des particules de catalyseur).

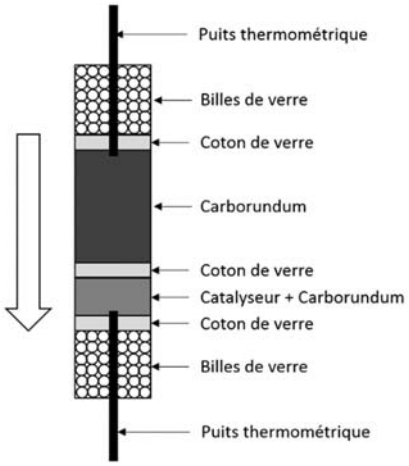

Figure 2-2 : Vue de coupe du réacteur après son chargement

3.3. Conditions de réaction

Les mesures d'activités de catalyseurs et de sélectivités effectuées lors de la transformation des différents composés phénoliques modèles (o-crésol, m-crésol et p-crésol) dilués dans le dodecane ont été obtenues à 340 ºC, sous une pression totale de 4 MPa et avec un rapport H_2/charge constant et égal à 486 NL L^{-1}. Les composés étudiés sont présentés dans la Figure 2-3.

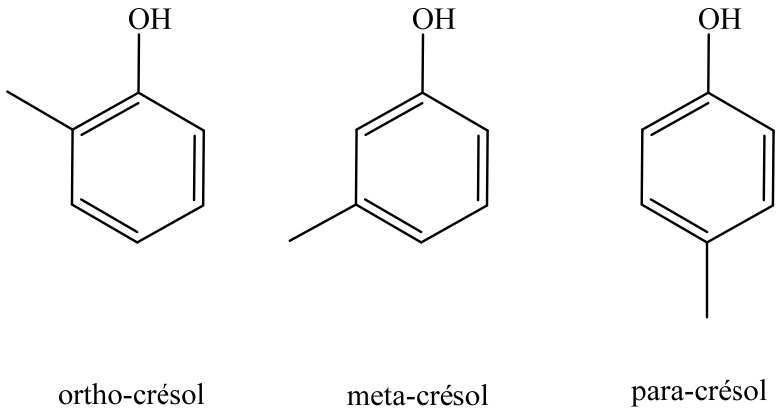

Figure 2-3 : Isomères de crésol étudiés

Différentes charges réactionnelles ont été utilisées lors de ce travail de thèse suivant le catalyseur étudié. Pour les catalyseurs sulfures, la charge liquide a été préparée en ajoutant du DMDS (diméthyldisulfure) afin de générer 1000 ppm de soufre dans la charge. En effet, le DMDS dans ces conditions opératoires se décompose en méthane et en hydrogène sulfuré, comme indiqué dans le paragraphe suivant. Pour les autres types de catalyseurs étudiés (oxydes de molybdène, nickel et phosphures de nickel), cet additif soufré n'est pas utilisé. Dans tous les cas, la pression en réactif oxygéné est constante et égale à 53 kPa (Tableau 2-1).

La charge réactionnelle contient aussi du n-heptane (étalon interne pour l'analyse chromatographique) et du dodecane (solvant de réaction). La composition en poids ainsi que les pressions partielles générées dans le milieu réactionnel sont regroupées dans le Tableau 2-1.

Pour une expérience standard, c'est à dire pour une pression totale égale à 4 MPa, la pression partielle en hydrogène est fixée à 3,24 MPa.

Tableau 2-1 : Composition chimique des charges réactionnelles utilisées (en $\%_{mol.}$) avec les pressions partielles de leurs composés dans le réacteur (kPa)

	Composition de la charge liquide (% pds.)		Pressions partielles générées dans le réacteur (kPa)	
Charge	Avec DMDS	Sans DMDS	Avec DMDS	Sans DMDS
Dodecane	92,6	92,8	668	676
Crésol	4,7	4,7	53	53
n-heptane	2,5	2,5	31	31
DMDS	0,2	-	-	-
CH_4	-	-	4	-
H_2S	-	-	4	-

A titre d'exemple, la préparation d'une charge de 150 g (égal à 198,1 mL) nécessite 139,0 g de dodecane, 6,98 g de crésol, 3,78 g de n-heptane et 0,22 g de DMDS. Dans le cas de la charge ne contenant pas l'additif soufré, la quantité de DMDS quantité est remplacée par du dodecane.

Les expériences ont été effectuées sur des durées entre 5 et 20 h. Dans certains cas, des taux de conversion différents ont été obtenus en modifiant le temps de contact (τ) défini par l'Eq (3). Pour une expérience donnée, la valeur du τ a été modifiée en changeant le débit du réactif et le débit d'hydrogène tout en maintenant constant le rapport H_2/charge égal à 486 NL L^{-1}.

$$\tau = \frac{m_{catalyseur}}{F_{charge}} \quad (3)$$

où :

τ : temps de contact (g h mol^{-1}) ;

$m_{catalyseur}$: masse de catalyseur (g) ;

F_{mol} : débit molaire du réactif (mol h^{-1}) ;

Ainsi, pour obtenir un temps de contact de 5,0 g h mol^{-1} pour un catalyseur donné, dans la transformation d'un composé phénolique sous 4 MPa de pression totale et à une température de 340 °C, il faut placer dans le lit catalytique 40 mg de catalyseur, utiliser un débit de charge liquide égal à 24,5 mL h^{-1}, et un débit en hydrogène de 12,0 L h^{-1}.

4. Méthodes analytiques

4.1. Analyses chromatographiques

Les mélanges réactionnels issus de la transformation des molécules phénoliques modèles ont été analysés par un système chromatographique en phase gaz Varian 430. Un volume de 0,8 µl est introduit dans un injecteur relié à une colonne DB1 capillaire (longueur : 30 m, diamètre interne : 0,320 mm, épaisseur du film : 5 µm) permettant la séparation des différents produits. Ce chromatographe est équipé d'un détecteur à ionisation de flamme (FID). Le gaz vecteur est l'hydrogène et cette colonne opère en mode isobare à 9 psi. Les températures de l'injecteur et du détecteur sont fixées respectivement à 250 et 280ºC. La programmation de température de l'analyse est reportée dans la Figure 2-4. Tous les produits ont été identifiés à l'aide d'un spectromètre de masse 1200 TQ couplée à un chromatographe Varian 3800 et par co-injection de composés commerciaux.

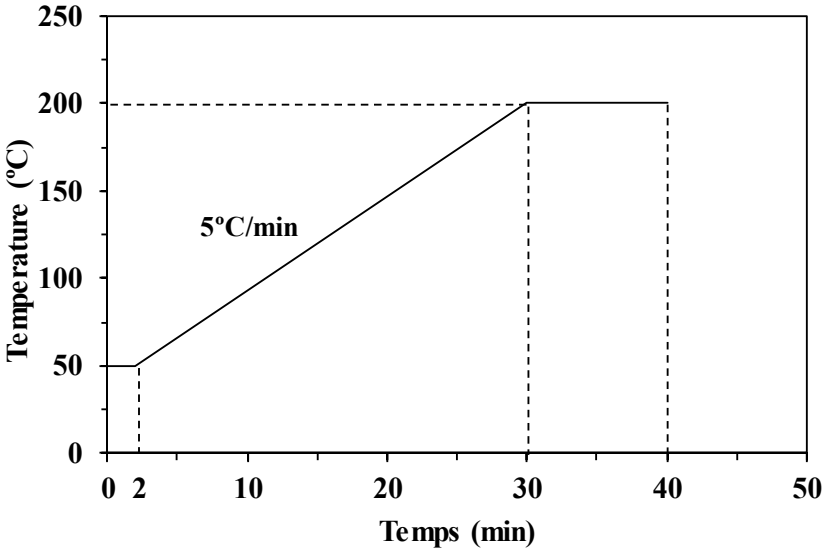

Figure 2-4 : Programme de température pour séparer les produits issus de la transformation des composés phénoliques.

La quantification des différentes molécules issues de la transformation des isomères de crésol a été réalisée en utilisant le n-heptane comme étalon interne. Tout d'abord, le coefficient de réponse (K_i) de chaque composé chimique i par rapport au n-heptane est déterminé en reportant le rapport molaire entre le composé à étalonner et l'étalon en fonction du rapport entre l'aire du pic du composé à étalonner et l'aire du pic du n-heptane (Eq. (4)) :

$$\frac{n_i}{n_{n-heptane}} = K_i \frac{A_i}{A_{n-heptane}} \quad (4)$$

Les coefficients de réponse sont déterminés à l'aide de droites d'étalonnage, comme illustré en Figure 2-5 pour le toluène et le méthylcyclohexane, ces deux composés étant des produits issus de la transformation des crésols.

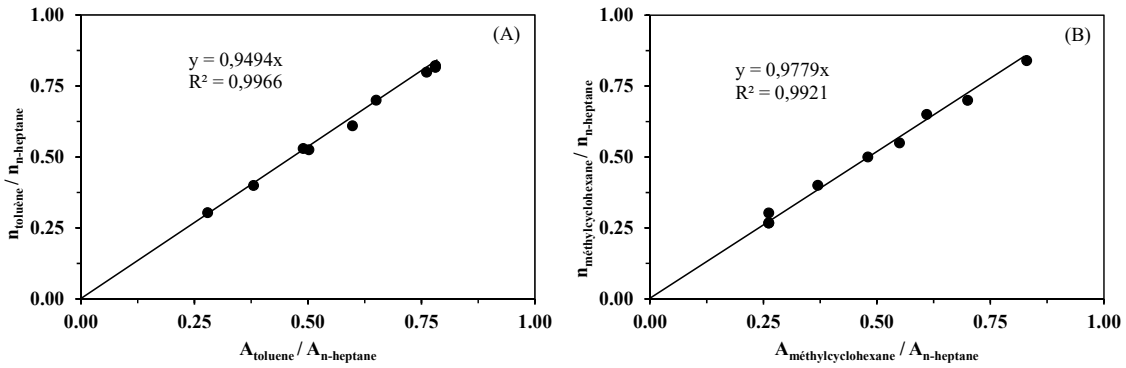

Figure 2-5 : Droites d'étalonnage des produits de transformation des crésols. (A) toluène et (B) méthylcyclohexane.

Toutefois pour les composés non commerciaux, leur coefficient a été déduit par rapport à leur nombre de carbone, en fixant celui du n-heptane arbitrairement égal à 1. L'ensemble des coefficients de réponse et des temps de rétention obtenus sont indiqués dans le Tableau II-2.

Tableau 2-2 : Temps de rétention et coefficients de réponse des composés observés lors de la transformation des crésols.

n°	$t_{rétention}$ (min)	Composé chimique	Coefficient de réponse
1	7,77	n-heptane	1,00[(a)]
	8,60	Diméthyldisulfure[(*)]	-
2	8,73	Methylcyclohexane	0,98[(b)]
3	9,15	Ethylcyclopentane	0,98[(c)]
4	9,23	3-methylcyclohexène	0,98[(b)]
4	9,23	4-methylcyclohexène	0,98[(b)]
5	9,94	Toluène	0,95[(b)]
6	10,34	1-methylcyclohexène	0,98[(b)]
7a	16,29	2-Methylcyclohexanone	0,99[(c)]
8a	16,53	2-Methylcyclohexanols	0,99[(c)]
7b	16,55	3-Methylcyclohexanone	0,99[(b)]
8b	16,55	3-Methylcyclohexanols	0,99[(b)]
7c	16,62	4-Methylcyclohexanone	0,99[(c)]
8c	16,82	4-Methylcyclohexanols	0,99[(c)]
13	20,63	3-methylcyclohexanol silylé	n. d.
9a	20,22	o-crésol	1,00[(b)]
9b	20,88	m-crésol	1,00[(b)]
9c	20,93	p-crésol	1,00[(b)]
14	21,64	3-methylcyclohexanol silylé	n. d.
10	22,89	Undécane (Impureté solvant)	n. d.
11	26,71	Dodécane	Solvant
12	29,54	Tridécane (Impureté solvant)	n. d.

[(*)] : non montré sur les chromatogrammes

[(a)] : coefficient déterminé par étalonnage

[(b)] : coefficient déterminé par étalonnage

[(c)] : coefficient estimé

Trois chromatogrammes obtenus après transformation des différentes charges réactionnelles, contenant soit l'o-crésol, le m-crésol ou le p-crésol, sont présentés dans la Figure 2-6.

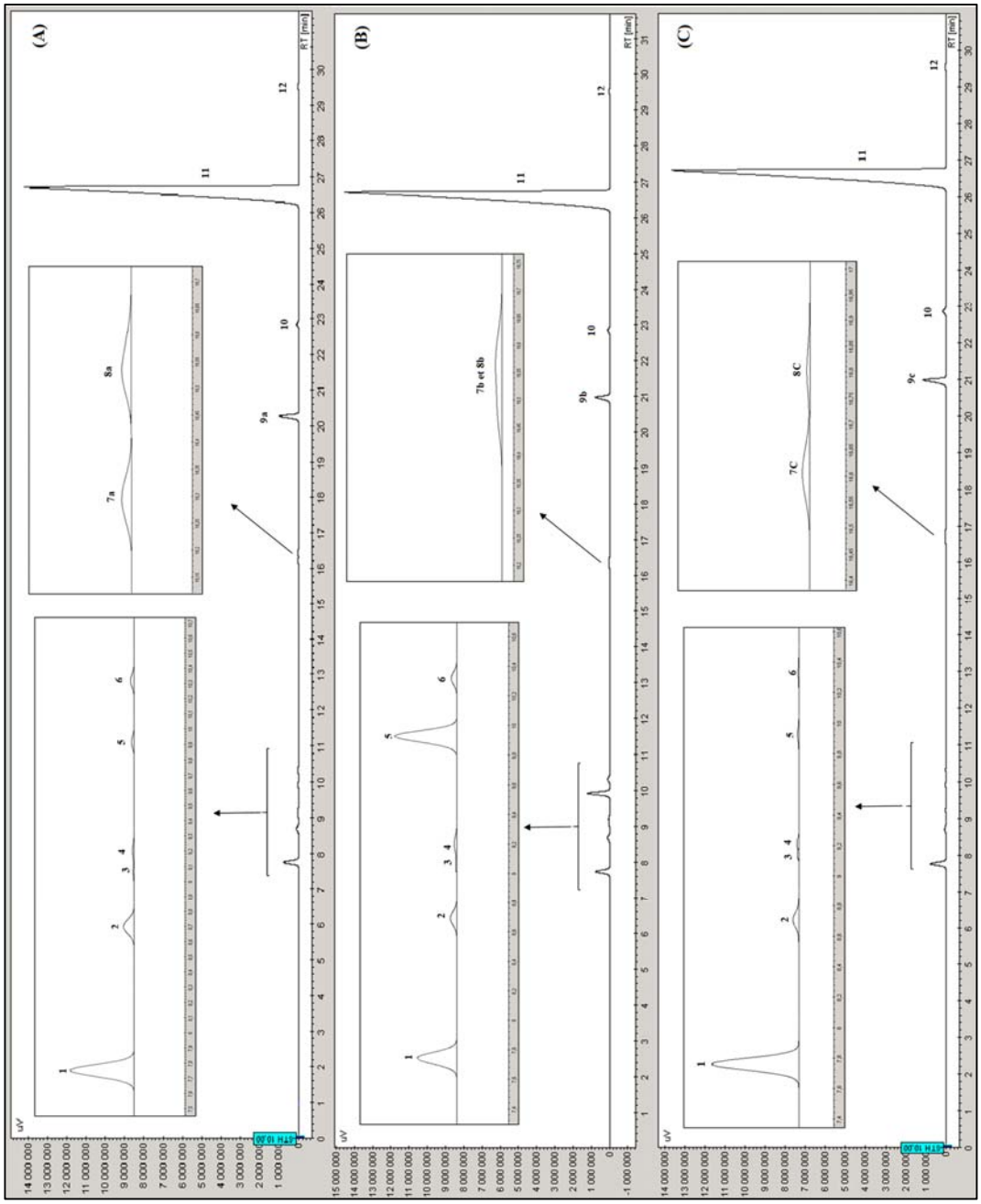

Figure 2-6 : Exemple de chromatogrammes obtenus après transformation de l'o-crésol (A), du m-crésol (B) et du p-crésol (C) ; (P = 4 MPa, T = 340 ºC, H_2/Charge = 486 NL/L).

Avec la programmation et la colonne utilisée, il n'est pas possible de séparer les produits 7b (3-methylcyclohexanol cis- et trans-) et 8b (3-methylcyclohexanone) issus de la transformation du m-crésol, comme observé dans la Figure 2-6 (B). En revanche, dans les mêmes conditions chromatographiques, il est possible de séparer les isomères analogues provenant de la transformation des deux autres crésols (o-crésol et p-crésol).

Afin de chiffrer les quantités d'alcools (3-methylcyclohexanol cis- et trans-) et de cétone (3-methylcyclohexanone) obtenus à partir du m-crésol, l'addition d'un agent de silylation, le BSTFA (N,O-Bis(triméthylsilyl)trifluoroacétamide), dans le milieu réactionnel est effectuée. Il est à noter que cette technique est couramment utilisée pour la dérivation des sucres comme des fructoses et glucoses afin de permettre leur analyse en chromatographie. Les alcools sont sélectivement transformés par silylation alors que les cétones ne sont pas réactives dans ces conditions. La réaction observée en présence de l'alcool est une substitution de l'hydrogène du groupe polaire -OH par le groupe silyle du BSTFA, comme illustré dans le Schéma 2-1. Ainsi, après l'ajout de l'agent silylant, deux pics d'alcools silylés apparaissent (provenant de la réaction avec les methylcyclohexanols cis- et trans-). La 3-methylcyclohexanone n'étant pas transformée, son pic chromatographique n'est évidemment pas modifié.

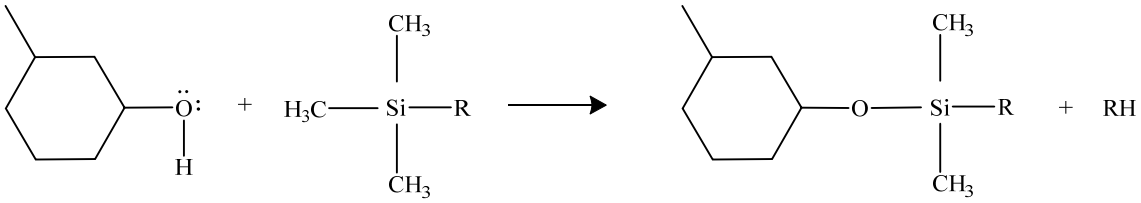

Schéma 2-1 : Réaction de silylation pour le 3-methylcyclohexanol en utilisant un agent de silylation arbitraire.

Il est donc possible de vérifier qu'avant introduction du BSTFA les 3 composés oxygénés ne sont pas séparés (Figure 2-7 (A)), alors que l'addition de l'agent silylant permet la séparation de ces 3 composés (Figure 2-7 (B)).

Pour quantifier la 3-méthylcyclohexanone présent dans le mélange réactionnel obtenu après silylation, il est indispensable de tenir compte de la dilution due à l'introduction de BSTFA. En effet, ces produits sont présents à l'état de traces dans le milieu réactionnel et une faible modification du volume entraîne une répercussion relativement importante sur la concentration de cette molécule. Ainsi, l'aire obtenue à partir du chromatogramme de la Figure 2-7 (B), notée A_{8b} dans l'Eq. (5), est corrigée grâce aux pics chromatographiques du n-heptane (étalon) obtenus avant et après l'addition de l'agent silylant.

$$A_{8b,récalculé} = A_{8b} \frac{A_{n-heptane,BSTFA}}{A_{n-heptane}} \quad (5)$$

L'aire des isomères de l'alcool peut être alors calculée en appliquant l'Eq. (6).

$$A_{7b} = A_{7b+8b} - A_{8b,récalculé} \quad (6)$$

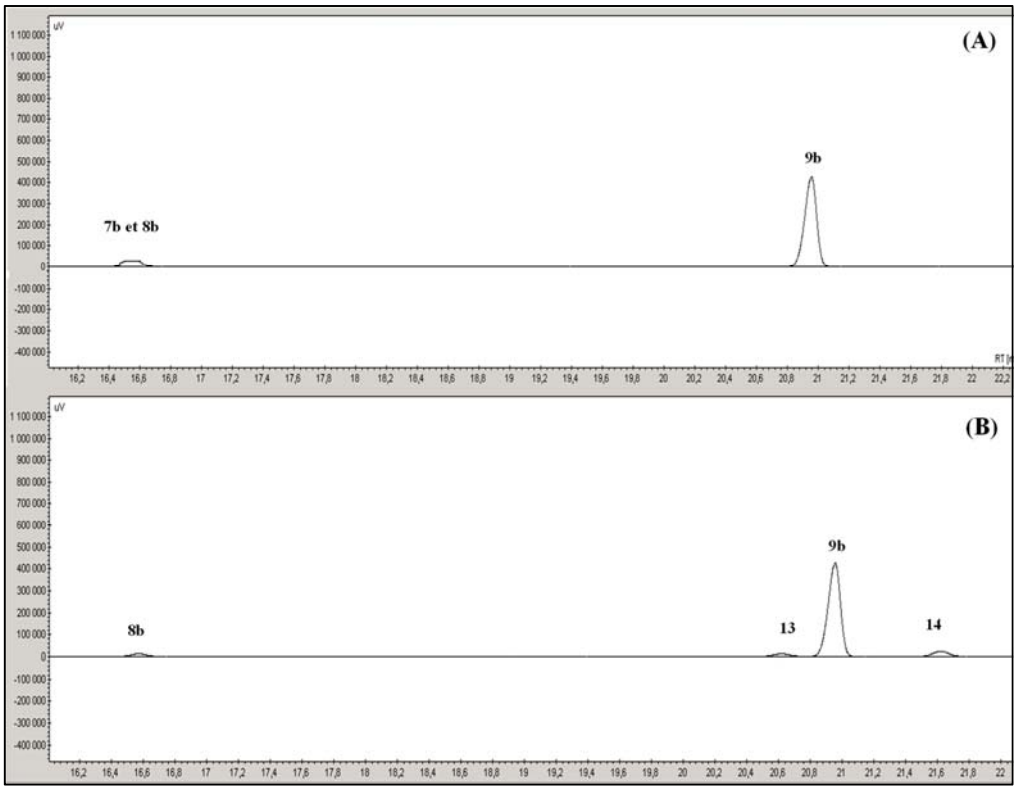

Figure 2-7 : Chromatogramme d'un échantillon obtenu pour la transformation de la charge avec le m-crésol comme molécule modèle (P = 4 MPa, T = 340 ºC, H_2/Charge = 486 NL L^{-1}). (A) sans BSTFA et (B) avec du BSTFA

4.2. Exploitation des résultats

Les conversions des molécules phénoliques modèles sont calculées en utilisant les chromatogrammes obtenus lors de la transformation des différentes charges modèles. A partir des aires des pics correspondants aux produits issus de la réaction chimique, l'aire du réactif et l'aire de l'étalon, la proportion d'un composé peut être calculé selon l'Eq. (7) :

$$\gamma_i = \frac{A_i}{A_{n-heptane}} \times K_i \times \%_{n-heptane} \quad (7)$$

Où :

γ_i : proportion du composé i (%mol.) ;

A_i : Aire obtenue pour le pic du composé i (µV min) ;

$A_{n\text{-heptane}}$: Aire obtenue pour le pic de l'étalon (µV min) ;

K_i : Coefficient de réponse du composé i ;

$\%_{n\text{-heptane}}$: Proportion de l'étalon (%mol.) ;

Le rendement molaire de chaque produit (notés par Y_i et exprimés en %mol.) est alors déterminé à partir de l'Eq. (8) :

$$Y_i = \frac{\gamma_i}{\gamma_{crésol,0}} \tag{8}$$

La conversion de l'isomère de crésol (notée par $X_{crésol}$ et exprimée en %) est calculée en utilisant l'Eq. (9) :

$$X_{crésol} = \frac{\gamma_{crésol,0} - \gamma_{crésol}}{\gamma_{crésol,0}} \tag{9}$$

La sélectivité d'un produit donné (notée par S_i et exprimée en %mol.) est calculée en utilisant l'Eq. (10) :

$$S_i = X_{crésol} Y_i \tag{10}$$

5. Produits chimiques

Les composés chimiques utilisés au cours de cette thèse, c'est-à-dire dans la préparation des différents matériaux, dans les tests catalytiques, et dans l'identification des commerciaux, avec leur fournisseur et pureté ont été listés ci-dessous.

Solides :

Heptamolybdate d'ammonium (Sigma-Aldrich, pureté > 99,9%) ;

Nitrate de nickel hexahydraté (Sigma-Aldrich, pureté > 98,5%) ;

Nitrate de cobalt hexahydraté (Sigma-Aldrich, pureté > 98%) ;

Phosphate de diammonium (Vetec, pureté > 99%) ;

Chlorure de cobalt (Sigma-Aldrich, pureté > 98%) ;

Borohydrure de sodium (Sigma-Aldrich, pureté > 99%) ;

Chlorure de lithium/clorure de potassium (Sigma-Aldrich, pureté > 99,9%) ;

p-crésol (Sigma-Aldrich, pureté > 99%) ;

Liquides :

Acétone (Fluka, pureté > 99,8%) ;

Isopropanol (Fluka, pureté > 99,8%) ;

Acide nitrique (Merk, pureté > 100%) ;

Diméthyldisulfure (Sigma-Aldrich, pureté > 99%) ;

Toluène (Sigma-Aldrich, pureté > 99,8%) ;

n-heptane (Sigma-Aldrich, pureté > 99,9%) ;

2-methylcyclohexanol (Sigma-Aldrich, pureté > 99%) ;

2-methylcyclohexanone (Sigma-Aldrich, pureté > 98%) ;

3-methylcyclohexanol (TCI, pureté > 98) ;

3-methylcyclohexanone (Sigma-Aldrich, pureté > 97%) ;

4-methylcyclohexanol (Sigma-Aldrich, pureté > 98%) ;

4-methylcyclohexanone (Sigma-Aldrich, pureté > 99,9%) ;

Éthylcyclopentane (TCI, pureté > 99%) ;

Méthylcyclohexane (Sigma-Aldrich, pureté > 99%);

4-methylcyclohexène (Sigma-Aldrich, pureté > 99%) ;

1-methylcyclohexène (Sigma-Aldrich, pureté > 97%) ;

o-crésol (Sigma-Aldrich, pureté > 99%);

m-crésol (Sigma-Aldrich, pureté > 98%) ;

Dodecane (Sigma-Aldrich, pureté > 99%) ;

BSTFA (Supelco, pureté > 99,6%) ;

Gaz :

H_2 (Air Liquide, pureté > 99,99%) ;

Ar (Air Liquide, pureté > 99,99%) ;

N_2 (Air Liquide, pureté > 99,99%) ;

10% O_2 dans He (Air Liquide, pureté > 99,99%) ;

O_2 (Air Liquide, pureté > 99,99%) ;

Chapitre 3 :

Hydrodeoxygenation of cresols over Mo/Al_2O_3 and $CoMo/Al_2O_3$ sulfided catalysts

Chapitre 3 : Hydrodeoxygenation of cresols over Mo/Al_2O_3 and $CoMo/Al_2O_3$ sulfided catalysts

1. Introduction

The depletion of non-renewable resources and their environmental problems have attracted much attention to the need of research and development of clean and sustainable new resources, especially for the production of aromatics [1–3]. Nowadays, the BTX (Benzene, Toluene and Xylene) platform is largely used to produce chemicals as plastics, components in gasoline, solvents, dyes, detergents [4]. BTX are conventionally produced by catalytic reforming of naphtha in a petroleum refinery or by extracting aromatics from naphtha feed to ethylene [5]. In both cases, the BTX production is tied to non-renewable crude oil.

With a goal to reduce the dependence of petroleum, the use of lignocellulose materials emerged as a new source of aromatics displaying economical and technical advantages of being plentiful, renewable, sustainable and free of CO_2 emissions source [6–9]. For example, Brazil and the U.S.A. are the leaders in bioethanol production (about 50 million tons per year) leading to a production of a large amount of wood waste containing lignin (25–35% of total biomass) [8]. The research of new valorization routes of the widely available lignin, a highly branched three-dimensional phenolic structure, will attract much interest, particularly in regard to the replacement of petro-chemical-based routes for the production of aromatic compounds.

The valorization of lignin as a source of aromatics requires first a depolymerization step, which can be performed by several processes reviewed recently in [6, 9], such as pyrolysis [10], catalytic oxidation [11, 12], hydroconversion [13, 14]. Depolymerization produces a large amount of aromatic oxygenates. Thus, to produce simple aromatics, the removal of oxygen atoms is mandatory and can be obtained by so-called hydrodeoxygenation (HDO) process using sulfided solids as efficient HDO catalysts [15–20]. Over sulfided catalysts, phenolic reactants are known to either produce aromatics by hydrogenolysis of the C-O bond (DDO pathway) or naphthenic compounds mainly involving hydrogenation properties of the sulfide phase (HYD pathway). The activity and selectivity of such solids during HDO of phenolic compounds are very dependent on the nature of the sulfide phase (MoS_2, CoMoS or NiMoS) and the experimental conditions (temperature, pressure, presence of H_2S in the feed,…). Interestingly,

it was reported that the DDO route was favored over a CoMoS phase and in presence of a reduced amount of H_2S [21–23].

It is of great interest to investigate the HDO of phenolic substituted compounds to understand how these oxygenated molecules react in HDO conditions. Concerning only the influence on the alkyl position, there are relatively few studies provided in literature regarding their differences in reactivity of cresol isomers over sulfide catalysts, and those reported were only carried out over $CoMo/Al_2O_3$ catalysts [24–26]. Moreover, the differences in reactivity between these three isomers varied substantially according to each study. For example, a reactivity order of the HDO of cresols measured at 350°C under 6.8 MPa of H_2 was meta > para > ortho [24]. On the contrary, under similar conditions ($CoMo/Al_2O_3$, 360°C and 7 MPa of H_2), Wandas et al. reported the following sequence: para > meta > ortho [25]. Under less severe experimental conditions (300°C and 2.85 MPa), the same order of reactivity over a $CoMo/Al_2O_3$ catalyst was pointed out, i.e. para > meta > ortho [26].

In this spirit, to clarify the effect of the position of the alkyl group on the reactivity of phenolic compounds, the deoxygenation of the cresol isomers was investigated independently over both Mo/Al_2O_3 and $CoMo/Al_2O_3$ sulfided solids under 3.2 MPa of H_2 and at 340°C using a fixed bed reactor. The main aim of this work consisted particularly in achieve useful information on the nature of HDO active sites by measuring the role of cobalt on the HDO of the three cresols, which allowed proposals of deoxygenation mechanisms.

2. Experimental

2.1. Materials

Both catalysts used (Mo/Al_2O_3 and $CoMo/Al_2O_3$) were provided by Total, their characteristics were already reported [22]. All catalysts exhibited a specific surface area close to 250 $m^2\ g^{-1}$. The Mo content of Mo/Al_2O_3 and $CoMo/Al_2O_3$ was 9.9 wt% and 9.2 wt%, respectively. $CoMo/Al_2O_3$ contained 4.2 wt% of Co. The oxygenated reactants (o-cresol, p-

cresol and m-cresol), n-heptane, dodecane, dimethyl disulfide (DMDS) were purchased from Sigma-Aldrich. H_2 was provided by Air Liquide.

2.2. Catalytic tests

The sulfidation process of the catalyst (particle size between 250 and 315 μm) was carried out under 4 MPa by DMDS (5.8 wt%) in dodecane using a continuous flow fixed-bed reactor (length: 40 cm; inner diameter: 1.26 cm). The sulfiding mixture was firstly injected at 150°C during 1 h, the temperature of the reactor was raised at 5°C min^{-1} to 350ºC and kept for 14 h. Then the temperature of the reactor was lowered to 340°C.

The deoxygenation of each cresol isomers was studied at 340 °C under 4 MPa, using a liquid model feed composed by the phenolic reactant (4.65 wt%), n-heptane (2.52 wt%) used as an internal standard and diluted with dodecane. DMDS (1000 ppm of S, 0.15 wt%) was also added in the feed to generate 3.8 kPa of H_2S. The H_2 partial pressure set to 3.24 MPa. The ratio H_2/model feed was kept constant and equal to 486 NL/L for all catalytic tests. All experiments were performed during 7 h on stream. In order to obtain similar conversion rates, experiments were carried out at different space times (τ, in g h mol^{-1}) defined as:

$$\tau = \frac{w}{F_{CRE,0}}$$

where w is the weight of catalyst (120 mg for Mo/Al_2O_3 and 30 mg for $CoMo/Al_2O_3$) and $F_{CRE,0}$ the molar flow of cresol fed into the reactor (between 2.3 and 9.8 mmol h^{-1}).

2.3. Activity measurements

Liquid samples were collected every hour by using a Minichiller-Huber cryostat and analyzed with a Varian 430 chromatograph equipped with a DB1 capillary column and a FID

detector. The products of reaction were identified both by co-injection of commercial compounds and by using a 1200 TQ mass spectrometer coupled with a Varian 3800 chromatograph.

The conversion of cresol (X_{CRE} in %) to oxygen-free products was calculated according to Eq. (1):

$$X_{CRE} = \frac{C_{CRE,0} - C_{CRE}}{C_{CRE,0}} . 100 \quad (1)$$

$C_{CRE,0}$ being the initial molar concentration of cresol and C_{CRE} as the molar concentration of cresol in the liquid sample collected at the studied space time τ.

The selectivity of a HDO product i (S_i in mol%) was given by Eq. (2):

$$S_i = \frac{C_i}{C_{CRE,0} - C_{CRE}} . 100 \quad (2)$$

where C_i represents the molar concentration of a HDO product in the liquid sample analyzed.

3. Results and discussion

3.1. Hydrodeoxygenation of m-cresol over Mo/Al_2O_3 and $CoMo/Al_2O_3$ catalysts

The HDO of m-cresol was carried out at 340 ºC under 4 MPa during 7 h over Mo/Al_2O_3 and $CoMo/Al_2O_3$. Figure 3-1 exhibits the conversion and the distribution of products as function of time on stream. Both experiments were carried out at different space times (τ = 15.8 g h mol^{-1} for Mo/Al_2O_3 and τ = 3.1 g h mol^{-1} for $CoMo/Al_2O_3$) to obtain similar conversion levels (close to 20%). The space time used for $CoMo/Al_2O_3$ was lower than the one of Mo/Al_2O_3 highlighting a promoting effect of Co, this particular point will be discussed further

in this manuscript. Both catalysts were relatively stable since their residual conversions measured after 7 h were 82% and 88% for $CoMo/Al_2O_3$ and Mo/Al_2O_3, respectively.

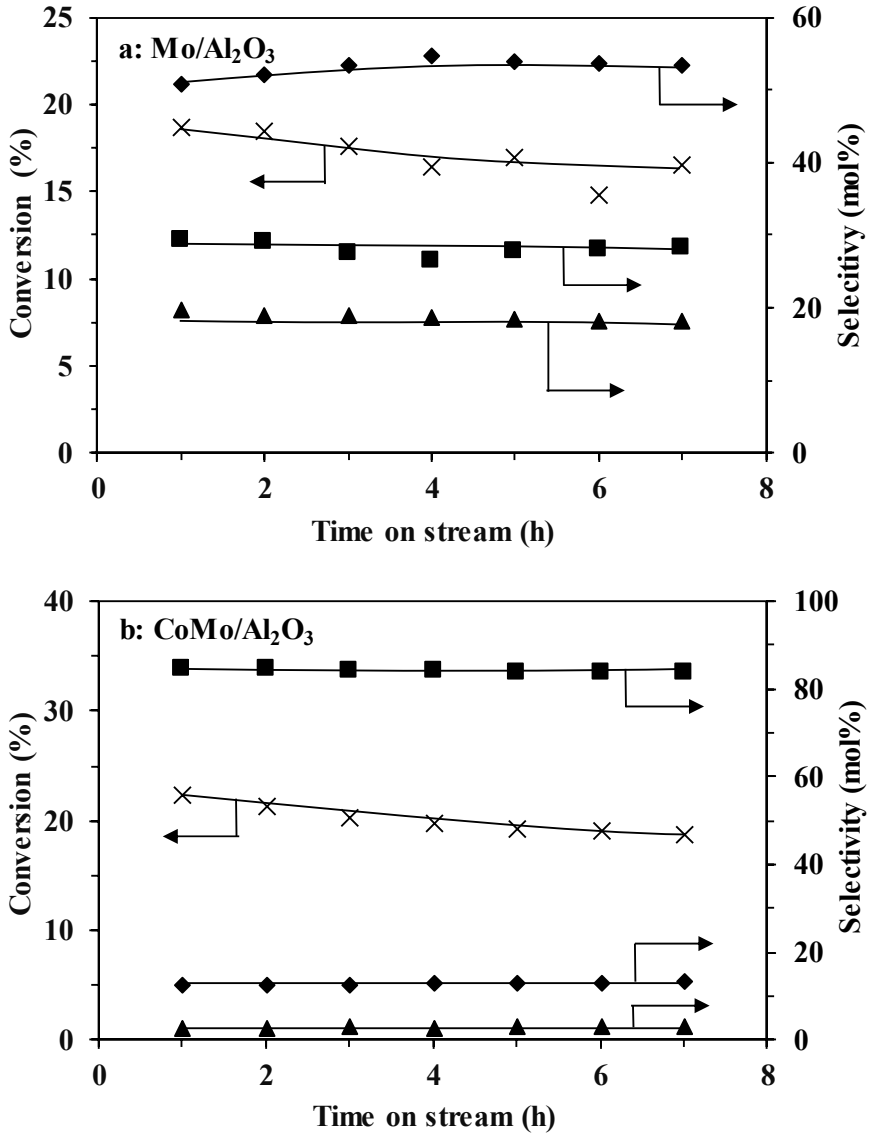

Figure 3-1 : HDO of m-cresol at 340 ºC under 4 MPa over a: Mo/Al_2O_3 (τ = 15.8 g h mol^{-1}) and b: $CoMo/Al_2O_3$ (τ = 3.1 g h mol^{-1}). Effect of time on stream on conversion (×) and selectivity into toluene (■), methylcyclohexenes (◆) and methylcyclohexane (▲).

All products analyzed in the liquid samples from the transformation of m-cresol carried out over sulfided catalysts were deoxygenated: toluene, methylcyclohexenes and methylcyclohexane. Figure 3-1 shows that the distribution of these products is independent of the time on stream. It can be assumed that the formation of those deoxygenated compounds proceeds through two routes (Scheme 3-1). Toluene was produced by the Direct DeOxygenation (DDO) pathway, involving a direct C-O bond scission. Methylcyclohexane and methylcyclohexene isomers were formed by the so-called "HYD" route, proceeding by ring hydrogenation of m-cresol followed by dehydration of 3-methylcyclohexanol. This alcohol was never observed under these experimental conditions due to its high reactivity, in accordance with results already reported using 2-ethylcyclohexanol as reactant [22]. Over both catalysts, 1-methylcyclohexene was always the main methylcyclohexene isomer observed. This result can be explained by the greater thermodynamic stability of 1-methylcyclohexene compared with the other two isomers. Indeed, this alkene represented 65 mol% and 61 mol% of all methyclcyclohexenes over Mo/Al_2O_3 and $CoMo/Al_2O_3$, respectively. These values are very close to the thermodynamic value (equal to 65 mol%) calculated from data reported by Peereboom et al. [27]. Finally, methylcyclohexane can be obtained by hydrogenation of methylcyclohexenes.

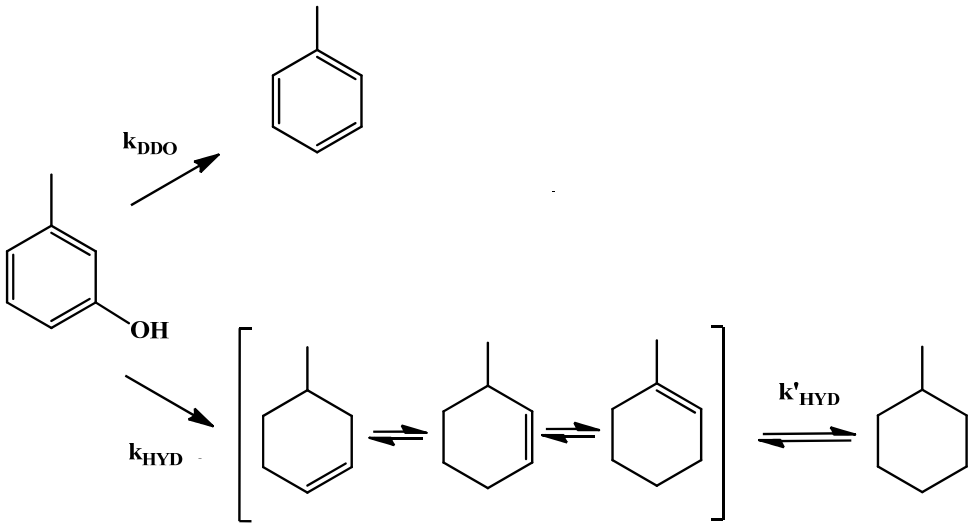

Scheme 3-1 : Reaction network of the deoxygenation of m-cresol over sulfided catalysts.

The kinetic analysis of the m-cresol HDO was performed at 340°C under 4 MPa over both sulfided catalysts. The conversion rates were varied by changing the space time, defined previously in the experimental part. Kinetics could be described by a general rate law kinetic expression:

$$r = -\frac{dC_{CRE}}{d\tau} = k.C_{CRE}^{n}.C_{H_2}^{m} \quad (2)$$

where r is the reaction rate of m-cresol transformation, k the rate constant, τ the space time, n and m the reaction order of m-cresol and H_2, respectively.

As H_2 was used in a large excess compared to m-cresol, its quantity can be considered as constant and included in the rate constant. Moreover, a pseudo-first order kinetics was assumed with respect to the oxygenated reactant, as often proposed for HDO reactions [15, 16, 18, 19]. Consequently, Eq. (2) can be simplified into:

$$r = -\frac{dC_{CRE}}{d\tau} = k_{HDO}.C_{CRE} \quad (3)$$

where k_{HDO} is the HDO apparent rate constant

After integration, Eq. (3) leads to:

$$C_{CRE} = C_{CRE,0}.e^{-k_{HDO}\cdot\tau} \quad (4)$$

After introducing of X, the conversion of m-cresol, Eq. (4) becomes:

$$-Ln\,(1-X) = k_{HDO}.\tau \quad (5)$$

The linear relationship between –Ln (1-X) and τ, shown in Figure 3-2, confirms that the overall reaction is pseudo-first order. Considering the global reaction network depicted in Scheme 3-1, several differential equations can be written (Eqs. 6-9) assuming all reaction steps following pseudo-first-order kinetics. In such model, the hydrogenation of toluene into methylcyclohexane has been neglected. Indeed, in an additional experiment, toluene was found

unreactive under these experimental conditions. This result indicates that DDO and HYD routes are parallel deoxygenation routes, as already proposed by several authors [22, 28].

$$-\frac{dC_{CRE}}{d\tau} = (k_{DDO}+k_{HYD})\, C_{CRE} \quad (6)$$

$$\frac{dC_{TOL}}{d\tau} = k_{DDO}.C_{CRE} \quad (7)$$

$$\frac{dC_{MCHe}}{d\tau} = k_{HYD}.C_{CRE} - k'_{HYD}.C_{MCH} \quad (8)$$

$$\frac{dC_{MCH}}{d\tau} = k'_{HYD}.C_{MCHe} \quad (9)$$

with k_{DDO} and k_{HYD} being the intrinsic kinetic rate constants of the DDO and HYD pathways, respectively; k'_{HYD} the intrinsic rate constant of the hydrogenation of methylcyclohexenes into methylcyclohexane; C_{TOL}, C_{MCHe} and C_{MCH} the molar concentrations of toluene, methylcyclohexenes and methylcyclohexane.

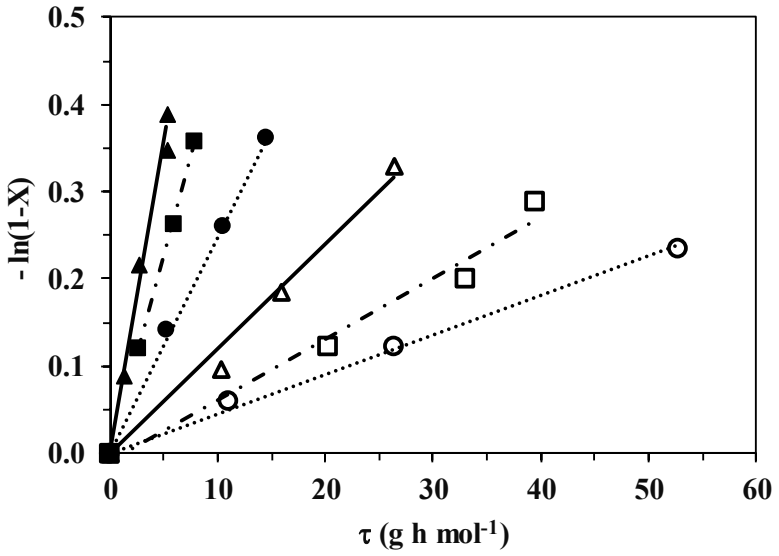

Figure 3-2 : Pseudo-first order plots of the HDO of cresol isomers at 340ºC under 4 MPa over Mo/Al_2O_3 (empty symbols) and $CoMo/Al_2O_3$ (full symbols): o-cresol (○; ●); m-cresol (△; ▲); p-cresol (□; ■).

It is noteworthy to mention that similar models have been already used to estimate kinetic data from the HDS of dibenzothiophenic compounds [29] and the HDN of propylaniline [30], these compounds being converted over sulfide catalysts by similar reaction schemes.

The algebraic solutions of Eqs. 6-9 are:

$$C_{CRE} = C_{CRE,0}.e^{-k_{HDO}.\tau} \quad (10)$$

$$C_{TOL} = \frac{C_{CRE,0}.k_{DDO}}{k_{HDO}}(1 - e^{-k_{HDO}.\tau}) \quad (11)$$

$$C_{MCHe} = \frac{C_{CRE,0}.k_{HYD}}{k_{HDO}-k'_{HYD}}\left(e^{-k'_{HYD}.\tau} - e^{-k_{HDO}.\tau}\right) \quad (12)$$

$$C_{MCH} = C_{CRE,0}\left(1 - e^{-k_{HDO}.\tau} - \frac{k_{DDO}}{k_{HDO}}\left(1 - e^{-k_{HDO}.\tau}\right) - \frac{k_{HYD}}{k_{HDO}-k'_{HYD}}\left(e^{-k'_{HYD}.\tau} - e^{-k_{HDO}.\tau}\right)\right) \quad (13)$$

From Eq. (10) to (13), the selectivity in each product i (in mol%) can be calculated by Eq. 14:

$$S_i = \frac{C_i}{C_{CRE,0}-C_{CRE}}.100 \quad (14)$$

Using the overall apparent constant k_{HDO} determined above, Eq. (11) to (13) can be used to fit the experimental data and achieve an accurate estimation of the individual apparent rate constants, given in Table 3-1. Their estimation was performed with a nonlinear method by minimizing the residual concentration sum of squares (RSS, Eq. 15) between the experimental data and calculated concentrations of the components in liquid samples collected:

$$RSS = \sum(C_{i,exp}, - C_{i,cal})^2 \quad (15)$$

where $C_{i,exp}$ and $C_{i,cal}$ are the experimental and calculated concentrations of component i in the liquid sample.

Table 3-1 : Individual apparent rate constants determined during the transformation of m-cresol over Mo/Al_2O_3 and $CoMo/Al_2O_3$ at 340 ◦C under 4 MPa of total pressure.

	Rate constants (in mmol g^{-1} h^{-1})			
	k_{HDO}	k_{DDO}	k_{HYD}	k'_{HYD}
Mo/Al_2O_3	11.7	3.2	8.4	37.1
$CoMo/Al_2O_3$	67.0	55.0	12.1	106.9

Figure 3-3 exhibits a good fitting between the experimental data and the simulated results for the HDO product distribution as function of conversion of m-cresol over both catalysts, allowing the validation of such a model. As expected, toluene and methylcyclohexenes appeared as primary products whereas methylcyclohexane was a secondary product obtained from hydrogenation of methylcyclohexenes, regardless of the catalyst. In addition, methylcyclohexenes and methylcyclohexane were the main products (more than 70 mol%) observed over Mo/Al_2O_3 (Figure 3-3a), whereas toluene was favored over $CoMo/Al_2O_3$, accounting for 82 mol% of all deoxygenated products (Figure 3-3b), indicating a strong effect of cobalt on the product distribution. These results can be explained by different values of the deoxygenation rate constants: k_{DDO} was lower than k_{HYD} over Mo/Al_2O_3 (k_{DDO}/k_{HYD} = 0.4) whereas the reverse was observed over $CoMo/Al_2O_3$ (k_{DDO}/k_{HYD} = 4.5).

Interestingly, the estimated value of the individual rate constant (k'_{HYD}) for the sequential reactions in the HYD route, i.e. the hydrogenation of methylcyclohexenes into methylcyclohexane, was about 2.9 times higher over $CoMo/Al_2O_3$ than that measured over Mo/Al_2O_3, showing that the presence of cobalt also allowed to improve the hydrogenating properties of the molybdenum sulfide phase. This result is in agreement with the promoting effect of cobalt (equal to 2.2) determined during the hydrogenation of cyclopentene over Mo/Al_2O_3 and $CoMo/Al_2O_3$ carried out at 150°C under atmospheric pressure [31].

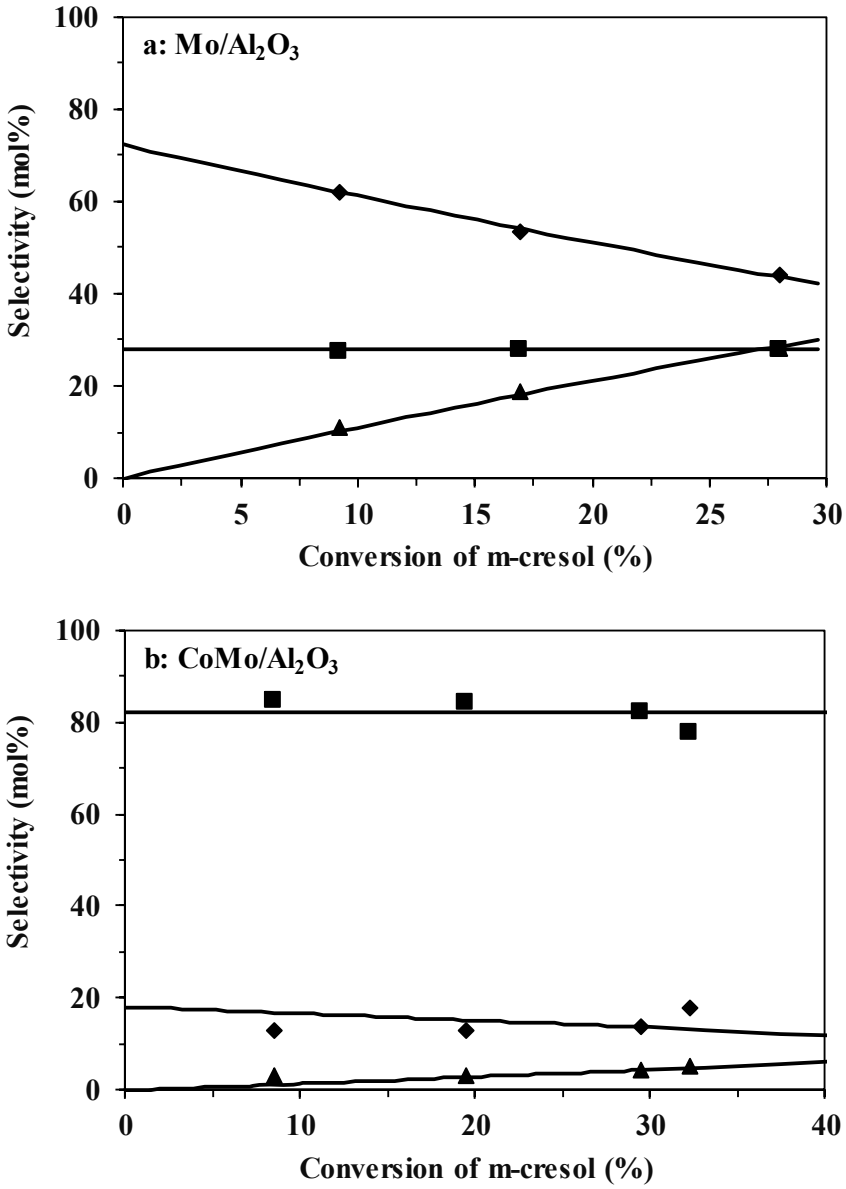

Figure 3-3 : Selectivity of Mo/Al_2O_3 (a) and $CoMo/Al_2O_3$ (b) during the transformation of m-cresol (340 °C, 4 MPa). Experimental points: toluene (■), methylcyclohexenes (◆) and methylcyclohexane (▲); lines: calculated from the first-order kinetics model (Eq. (10) to (13))

3.2. Comparison of the reactivity of cresols over (Co)Mo/Al_2O_3 sulfided catalysts.

The catalytic properties in HDO of Mo/Al_2O_3 and $CoMo/Al_2O_3$ sulfides catalysts were determined at 340ºC under 4 MPa using the three cresol isomers as model phenolic reactants. The kinetic apparent rate constants of HDO (k_{HDO}) have also been calculated for o-cresol and p-cresol cresol assuming a first order reaction, as shown in Figure 3-2. The HDO rate constants (k_{HDO}) measured over $CoMo/Al_2O_3$ for all phenolic isomers (ranging from 25 and 67 mmol h^{-1} g^{-1}, Figure 3-4b), were found to be higher than the values determined over Mo/Al_2O_3 (ranging from 5 and 12 mmol h^{-1} g^{-1}, Figure 3-4a), highlighting the promoting effect of cobalt.

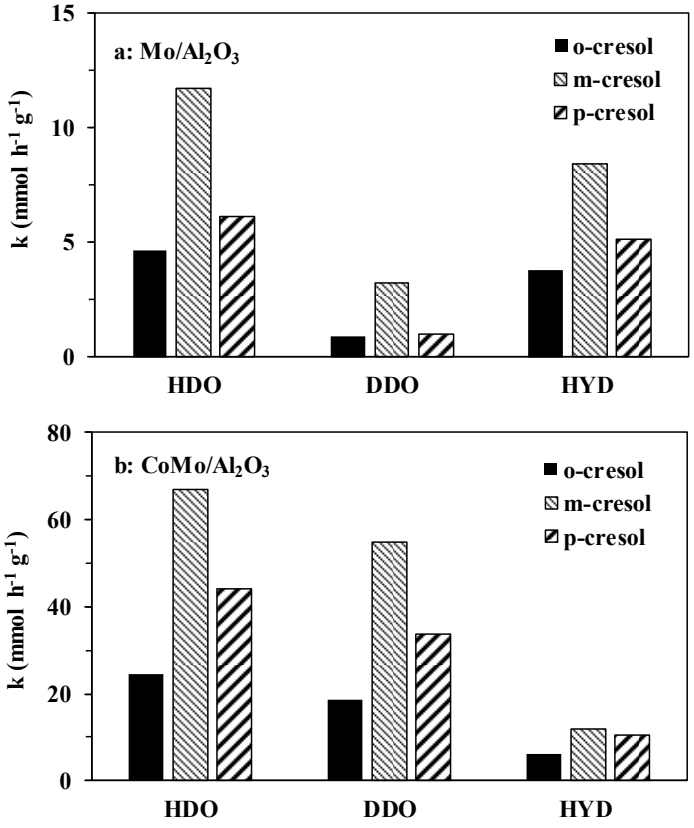

Figure 3-4 : Influence of the cresol isomer on the activity of Mo/Al2O3 (a) and CoMo/Al2O3 (b) at 340°C under 4 MPa.

The promoting effect can be quantified by the ratio between the k_{HDO} values determined over $CoMo/Al_2O_3$ and Mo/Al_2O_3 for each cresol isomer. Figure 3-5 shows that the overall promoting effect of cobalt was of the same order of magnitude (between 5 and 7) for the three phenolic isomers. Such promoting effect was also reported for HDO of various oxygenated aromatics as o-ethylphenol [22, 23], guaiacol [28] and p-cresol [32].

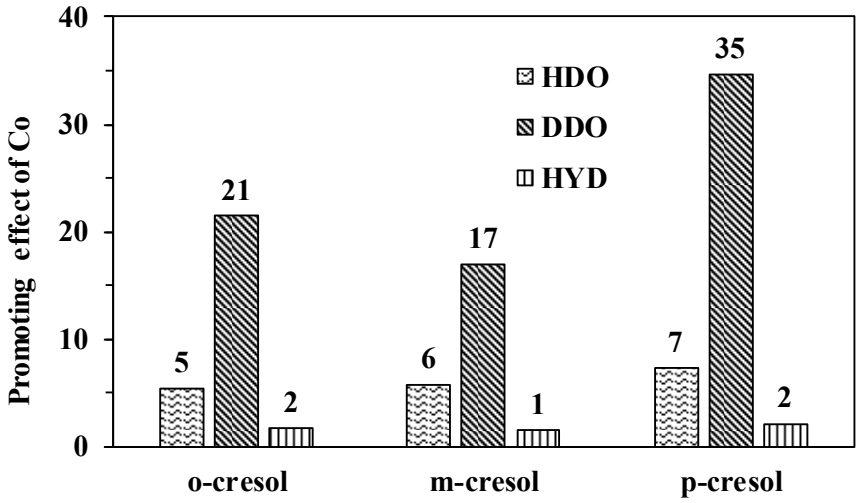

Figure 3-5 : Influence of the cresol isomer on the promoting effect of cobalt (calculated as the ratio between the activity of $CoMo/Al_2O_3$ and the activity of Mo/Al_2O_3) measured at 340°C under 4 MPa.

It can be pointed out that the order of cresol reactivity in HDO was the same for both catalysts and followed m-cresol > p-cresol > o-cresol. The same reactivity scale was already reported by Odebunmi et al. using a $CoMo/Al_2O_3$ catalyst [24]. The highest reactivity of m-cresol could be explained by a better stabilization of the reaction intermediates involved, due to electronic effects of the alkyl group located at the meta-position. This particular point will be covered in the next section. In addition, it is important to emphasize that o-cresol was always the less reactive isomer, suggesting a possible steric effect of the methyl group in alpha position

with respect to the OH group, as already proposed by several authors but only over $CoMo/Al_2O_3$ catalysts [25, 26, 33].

The role of cobalt was highly dependent on the deoxygenation pathway concerned. Indeed, in the case of Mo/Al_2O_3, the k_{HYD} values determined for cresol isomers were higher than the k_{DDO} values (Figure 3-4a). The reverse was observed over $CoMo/Al_2O_3$ (Figure 3-4b). Consequently, the promoting effect of cobalt (calculated as the ratio between the kinetic rate constants measured over $CoMo/Al_2O_3$ and Mo/Al_2O_3) on the DDO route was much more significant than on the HYD route. Indeed, it varied between 17 and 35 for the DDO pathway and was 2 or less for the HYD pathway (Figure 3-5). These results are in agreement with previous works demonstrating that the CoMoS phase is more active into the DDO route compared to the MoS_2 phase [22, 23, 28, 32], and underline that the presence of cobalt in the sulfide phase favors the direct C-O bond scission. The promoting effect can be explained by a strong activation of the C-O bond of cresol, probably due to its adsorption through its oxygen atom on an active site involving cobalt, as discussed in the last part of this present paper.

The distribution of deoxygenated products from the transformation of all cresol isomers was dependent on the type of catalyst (promoted vs unpromoted) but not much on the positon of methyl group, as indicated in Table 3-2. Over $CoMo/Al_2O_3$, toluene was the main product accounting for more than 75 mol% of all deoxygenated products for all cresols. On the contrary, methylcyclohexane and methylcyclohexene isomers were always found as the main products over Mo/Al_2O_3. As a result, the DDO/HYD selectivity was the highest over $CoMo/Al_2O_3$ (ranging from 3.0 to 5.3) and the lowest over Mo/Al_2O_3 (close to 0.2), which confirms that CoMoS phase is more selective into DDO, being irrespective of the cresol isomer.

Table 3-2 : Distribution of products obtained for deoxygenation of cresols over Mo/Al_2O_3 and $CoMo/Al_2O_3$ at 340 ◦C under 4 MPa of total pressure.

	Mo/Al_2O_3			$CoMo/Al_2O_3$		
	o-cresol	m-cresol	p-cresol	o-cresol	m-cresol	p-cresol
Conversion (%)	11.5	16.9	18.2	22.8	20.1	23.0
τ (g h mol^{-1})	26.4	15.8	32.9	10.5	3.1	5.9
Product distribution (mol%)						
Toluene	19	28	16	76	84	76
Methylcyclohexenes	42	53	50	14	13	18
Methylcyclohexane	36	19	32	9	3	5
Ethylcyclopentane	3	0	2	1	0	0
DDO/HYD selectivity	0.2	0.4	0.2	3.0	5.3	3.2

3.3. Proposals concerning the nature of deoxygenation active sites and reaction mechanisms

As shown in Figure 3-5, the promoting effect of cobalt is strongly dependent on the deoxygenation route (DDO vs HYD), this seems to indicate that different kinds of active sites are involved throughout the deoxygenation process of cresols, as illustrated in Scheme 3-2. Based on DFT studies [35–37], it was proposed that sulfur vacancies located on the edges of the sulfide phases could act as deoxygenation active sites. Indeed, it is known that cobalt in the sulfided phase donates electrons to molybdenum, which leads to a weakening metal-sulfur bond [38]. This weakening promotes an easier elimination of sulfur atoms and increases the number

of active sites compared to the MoS_2 phase. The important promoting effect of cobalt on the DDO route observed experimentally (Figure 3-5) can be reasonably explained by an increase of sulfur vacancies. Regarding the increase of k_{DDO} values between $CoMo/Al_2O_3$ and Mo/Al_2O_3 (Figure 3-4), these sulfur vacancies favored by the presence of cobalt acts most likely as DDO active sites. Thus, in order to react through DDO, the phenolic compound must be adsorbed by its oxygen atom through η_1 adsorption atom onto a sulfur vacancy. As indicated in Scheme 3-2, a dihydrophenol intermediate can be formed after a first hydrogenation step, as already suggested by several authors [26, 39, 40]. Obviously, such species was never observed due to its very high reactivity and it can lead to toluene, the DDO product, after C-O bond scission. A detailed mechanism, shown in Scheme 3-3, will be discussed below.

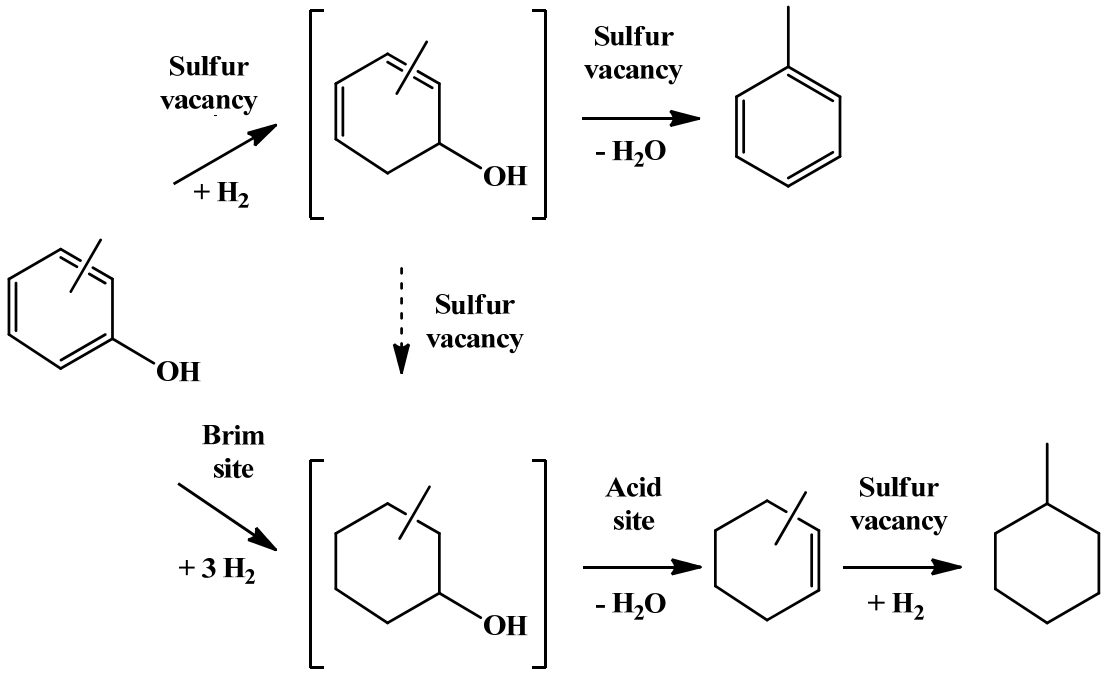

Scheme 3-2 : Proposals of the different active sites likely to occur during the deoxygenation of cresols.

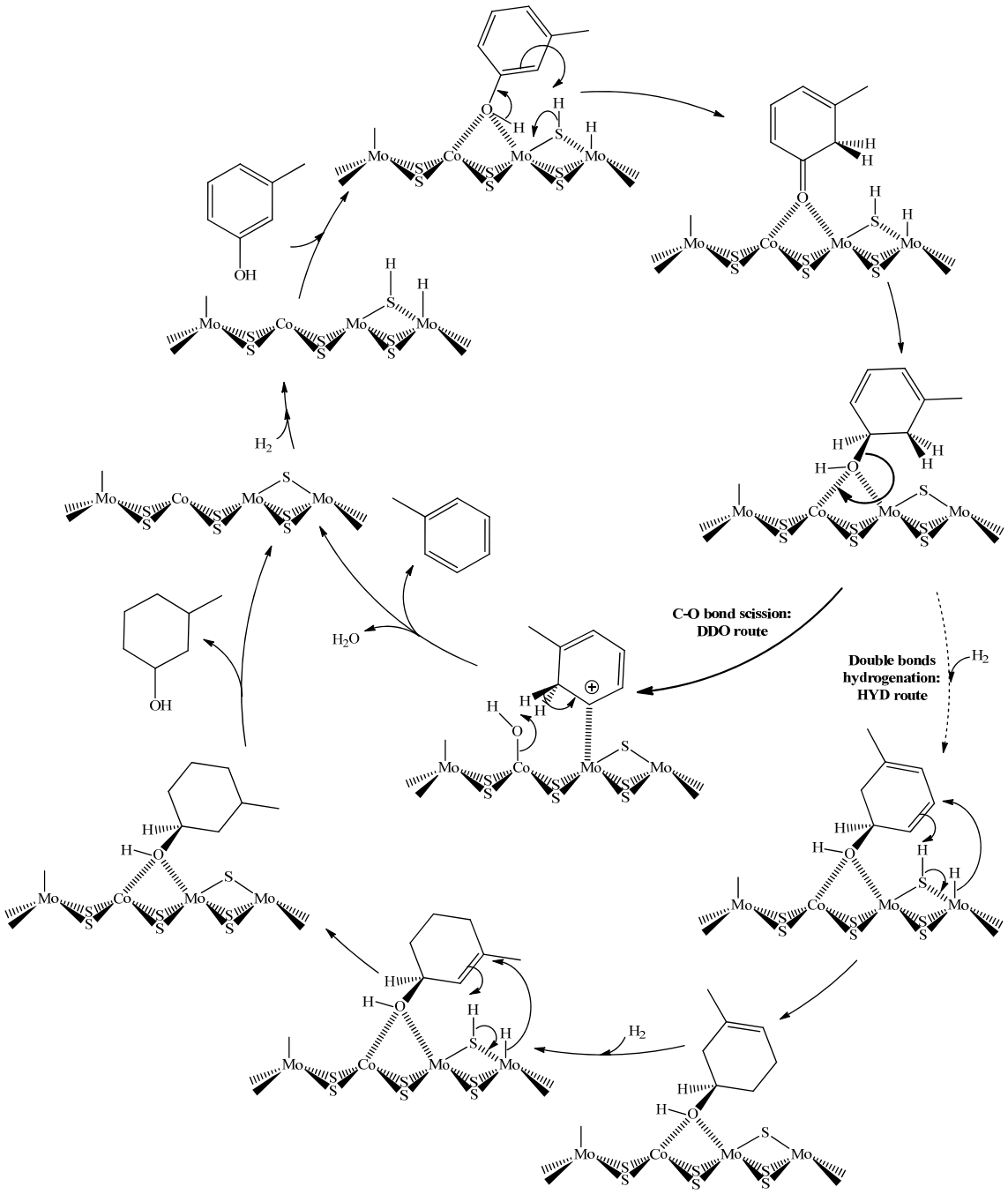

Scheme 3-3 : Mechanism of deoxygenation of m-cresol over a schematic CoMoS site.

Concerning the HYD route, which leads methylcyclohexenes and methylcyclohexane, its first step is also the formation of a dihydrophenol intermediate by hydrogenation. As it is

shown in Figure 3-5, this route was practically not affected by the presence of cobalt. This result suggests that the active sites in aromatic hydrogenation are probably not of the same nature as those involved in DDO. In order to explain the reactions involving dibenzothiophenic compounds over MoS_2 and CoMoS phases, it has been proposed that the so-called "brim sites" located near the edge of the basal planes of the sulfide phases could be responsible for hydrogenation reactions [41, 42]. The involvement of such sites to explain the formation of HYD products from cresols can also be proposed. However, differently of the adsorption mode proposed to explain the production of toluene by the DDO route, a η_6 adsorption of cresols is probably required on "brim sites" in order to favor the hydrogenation of the aromatic ring (HYD pathway). Moreover, it was observed that toluene was unreactive under these conditions, indicating that the presence of oxygen atom is mandatory to activate the hydrogenation of the aromatic ring. After the hydrogenation of cresols, an alcohol is expected but never detected. The dehydration of such oxygenate probably occurs on an acid site present on the catalytic support. Nevertheless, the participation of the acidity of the sulfide phase, through the SH groups, cannot be ruled out.

A promoting effect of cobalt on the hydrogenation of methylcyclohexenes into methylcyclohexane was also highlighted. Indeed, it was close to 3 when m-cresol was used as a reactant (compare values of k'_{HYD} reported in Table 3-1 for Mo/Al_2O_3 and $CoMo/Al_2O_3$). Such effect could be explained by the involvement of sulfur vacancies as hydrogenating sites of alkenes. Their activation on the so-called "Brim sites" should be probably too low to ensure their hydrogenation, explaining why methylcyclohexenes were observed in higher amounts compared to methylcyclohexane over Mo/Al_2O_3 from the three cresol isomers (Table 3-2). This result is in line with the very low hydrogenation reactivity of decenes into decane observed during the deoxygenation of decanoic acid over the same unpromoted catalyst [43] indicating that such catalyst contains a low quantity of sites able to hydrogenate alkenes.

A proposal for the reaction mechanism of m-cresol deoxygenation is depicted in Scheme 3-3, using a schematic CoMoS site already described by DFT studies [37, 44–48]. The first step of the deoxygenation mechanism requires heterolytic dissociation of hydrogen [49]. Subsequently, the cresol isomer can be adsorbed on cobalt and molybdenum, acting as the sulfur

vacancy, through its oxygen atom via σ-bonding (η_1 adsorption). Methylcyclohexadienone can be obtained by tautomerization involving a SH group of the sulfided phase. The participation of such oxygenated species has been recently suggested by de Souza et al. during the deoxygenation process of phenol over Pd-based catalysts [50] and Ni-Fe-based catalysts [51]. The methyl group in ortho position might reduce the formation of keto form in tautomeric equilibrium due to steric effect, which would explain the lowest reactivity of o-cresol compared to other cresols observed experimentally over both catalysts (Figure 3-4).

The next step is proposed to be the hydrogenation of its carbonyl group leading to 3-methyl-3,5-cyclohexanedienol, which could be proposed to be a common intermediate between both deoxygenation routes, as suggested in Scheme 3-2. As the $C(sp^3)$-O bond cleavage of this intermediate is much easier than the direct $C(sp^2)$-O bond scission of m-cresol [15], we propose the formation of an intermediate arenium ion (cationic species) after $C(sp^3)$-O bond scission (DDO route). The reactivity of cresols would depend on the relative stabilities of such intermediates. Thus, the highest DDO reactivity of m-cresol (as shown in Figure 3-4) can be explained by the highest relative stability of its arenium ion since only a tertiary carbenium ion can be written in this case, i.e. after the C-O bond scission of 3-methyl-3,5-cyclohexanedienol, as shown in Scheme 3-4. The two other isomers, o-cresol and p-cresol, should have presented similar reactivity, having the same electronic structure for their derived cationic species (Scheme 3-4). However, the lowest reactivity of o-cresol is probably attributed to steric hindrance, as discussed above.

Moreover, the great promoting effects of cobalt for all cresol isomers in DDO pathway (Figure 3-5) suggest a strong interaction between cobalt located in the sulfide phase and oxygen of the enol intermediate facilitating the cleavage of the C-O bond. Finally, the formation of toluene may occur by deprotonation and the active site is regenerated by the release of water from the catalytic surface.

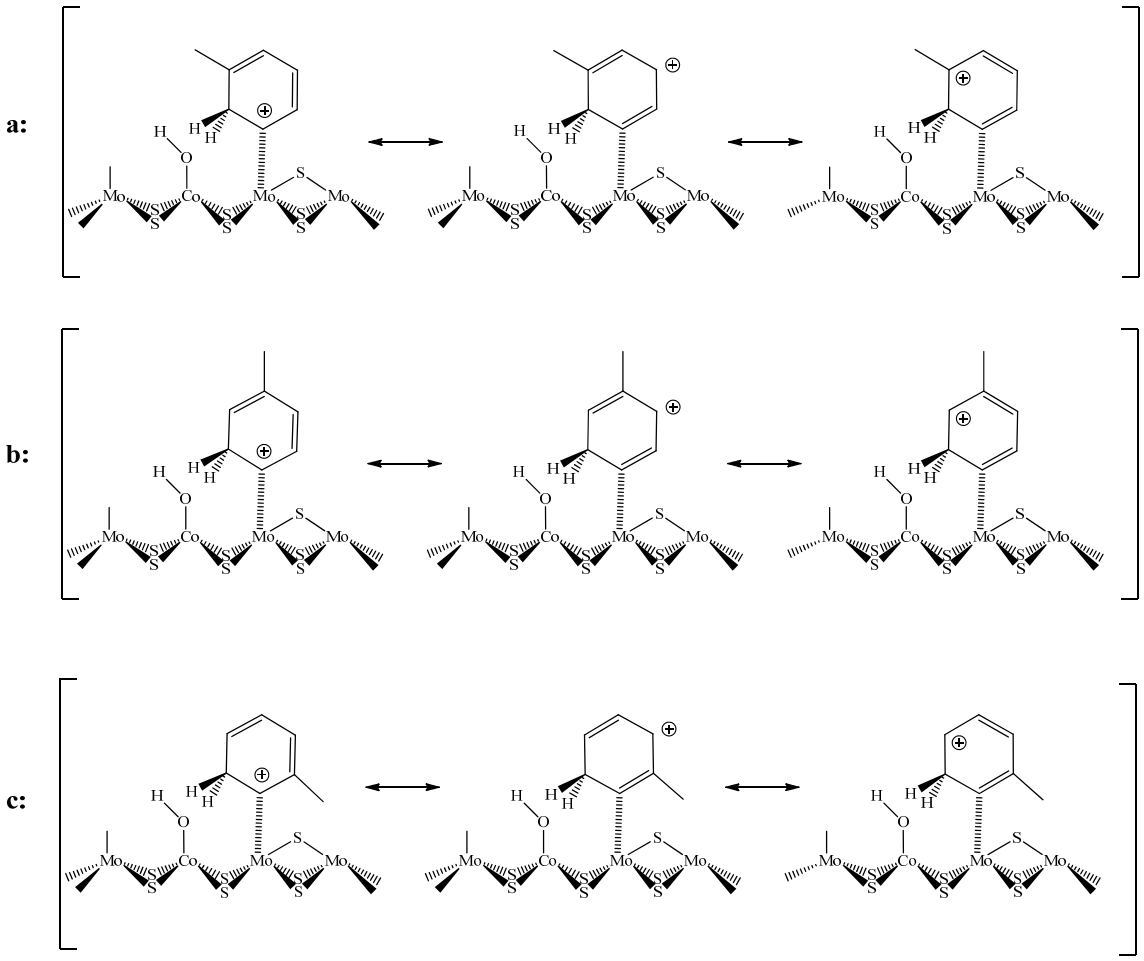

Scheme 3-4 : Arenium ions likely to be involved during the DDO route of o-cresol (a), m-cresol (b) and p-cresol (c).

The formation of the HYD products can be explained by successive hydrogenation of the adsorbed 3-methyl-3,5-cyclohexanedienol leading to 3-methylcyclohexanol, which is in the end of the catalytic cycle desorbed regenerating the active site. This alcohol was never observed in reaction mixture due to its easily dehydration over alumina into methylcyclohexenes. The presence of cobalt hardly influences this route since its promoting effect is very low (less than 2) compared to the effect on the DDO route (Figure 3-5) indicating that the hydrogenation steps of 3-methyl-3,5-cyclohexanedienol are probably disfavored compared to its C-O bond scission.

As the DDO/HYD selectivity was lower than 1 over Mo/Al_2O_3 (Table 3-2), it seems easier to hydrogenate the aromatic ring than to break the C-O bond over this kind of catalyst. Therefore, it suggests that the C-O bond is not enough activated probably due to a weak interaction between molybdenum of the unpromoted site and the oxygen atom of the intermediate. Hence, over the unpromoted catalyst, it could be assumed that the participation of the so-called brim sites becomes predominant to explain its activity and selectivity.

4. Conclusion

The present study demonstrated that $CoMo/Al_2O_3$ is a very efficient catalyst to produce aromatics from all cresol isomers. The differences in reactivity of cresols over Mo/Al_2O_3 and $CoMo/Al_2O_3$ were explained by different factors, including nature of active sites and reaction mechanisms. Toluene was produced by the so-called DirectDeOxygenation route involving sulfur vacancy as active site, the formation of such site was favored by the presence of cobalt in the sulfide phase. On the other hand, the formation of methylcyclohexenes and methylcyclohexane, the main products observed over Mo/Al_2O_3, implied several active sites including the so-called “brim sites”, acid sites and sulfur vacancies, the latter being active in hydrogenation of alkenes.

The highest reactivity of m-cresol was attributed to the involvement of a more stable cationic species. On the contrary, the lowest reactivity of o-cresol could be due to a steric hindrance limiting the initial tautomerization step involved in the proposed reaction mechanism. In addition, the high selectivity in toluene of $CoMo/Al_2O_3$ may be due to a great affinity between cobalt on the sulfided phase and the adsorbed oxygen atom of the oxygenated intermediates.

5. References

[1] G.W. Huber, A. Corma, Angew. Chem. Int. Ed. 46 (2007) 7184–7201.

[2] B. Valle, A.G. Gayubo, A.T. Aguayo, M. Olazar, J. Bilbao, Energy Fuels. 24 (2010) 2060–2070.

[3] H.J. Park, K.-H. Park, J.-K. Jeon, J. Kim, R. Ryoo, K.-E. Jeong, S.H. Park, Y.-K. Park, Fuel. 97 (2012) 379–384.

[4] S.J. Gerssen-Gondelach, D. Saygin, B. Wicke, M.K. Patel, A.P.C. Faaij, Renew. Sustain. Energy Rev. 40 (2014) 964–998.

[5] C. Marcilly, Acido-basic catalysis: application to refining and petrochemistry, Editions Technip, 2006.

[6] J. Zakzeski, P.C.A. Bruijnincx, A.L. Jongerius, B.M. Weckhuysen, Chem. Rev. 110 (2010) 3552–3599.

[7] F.G. Calvo-Flores, J.A. Dobado, ChemSusChem. 3 (2010) 1227–1235.

[8] P. Sannigrahi, Y. Pu, A. Ragauskas, Curr. Opin. Environ. Sustain. 2 (2010) 383–393.

[9] C. Li, X. Zhao, A. Wang, G.W. Huber, T. Zhang, Chem. Rev. 115 (2015) 11559–11624.

[10] M. Brebu, C. Vasile, Cellul. Chem. Technol. 44 (2010) 353.

[11] H. Lange, S. Decina, C. Crestini, Eur. Polym. J. 49 (2013) 1151–1173.

[12] R. Behling, S. Valange, G. Chatel, Green Chem. (2016).

[13] B. Joffres, C. Lorentz, M. Vidalie, D. Laurenti, A.-A. Quoineaud, N. Charon, A. Daudin, A. Quignard, C. Geantet, Appl. Catal. B Environ. 145 (2014) 167–176.

[14] B. Joffres, M.T. Nguyen, D. Laurenti, C. Lorentz, V. Souchon, N. Charon, A. Daudin, A. Quignard, C. Geantet, Appl. Catal. B Environ. 184 (2016) 153–162.

[15] E. Furimsky, Appl. Catal. Gen. 199 (2000) 147–190.

[16] Q. Bu, H. Lei, A.H. Zacher, L. Wang, S. Ren, J. Liang, Y. Wei, Y. Liu, J. Tang, Q. Zhang, R. Ruan, Bioresour. Technol. 124 (2012) 470–477.

[17] M. Saidi, F. Samimi, D. Karimipourfard, T. Nimmanwudipong, B.C. Gates, M.R. Rahimpour, Energy Environ. Sci. 7 (2013) 103–129.

[18] E. Furimsky, Catal. Today. 217 (2013) 13–56.

[19] H. Wang, J. Male, Y. Wang, ACS Catal. 3 (2013) 1047–1070.

[20] D.A. Ruddy, J.A. Schaidle, J.R.F. Iii, J. Wang, L. Moens, J.E. Hensley, Green Chem. 16 (2014) 454–490. doi:10.1039/C3GC41354C.

[21] E. Laurent, B. Delmon, Ind. Eng. Chem. Res. 32 (1993) 2516–2524.

[22] Y. Romero, F. Richard, S. Brunet, Appl. Catal. B Environ. 98 (2010) 213–223.

[23] C. Bouvier, Y. Romero, F. Richard, S. Brunet, Green Chem. 13 (2011) 2441–2451.

[24] E.O. Odebunmi, D.F. Ollis, J. Catal. 80 (1983) 56–64.

[25] R. Wandas, J. Surygala, E. Śliwka, Fuel. 75 (1996) 687–694.

[26] F.E. Massoth, P. Politzer, M.C. Concha, J.S. Murray, J. Jakowski, J. Simons, J. Phys. Chem. B. 110 (2006) 14283–14291.

[27] M. Peereboom, B. Van de Graaf, J.M.A. Baas, Recl. Trav. Chim. Pays-Bas. 101 (1982) 336–338.

[28] V.N. Bui, D. Laurenti, P. Afanasiev, C. Geantet, Appl. Catal. B Environ. 101 (2011) 239–245.

[29] H. Farag, J. Colloid Interface Sci. 348 (2010) 219–226.

[30] A. Hrabar, J. Hein, O.Y. Gutiérrez, J.A. Lercher, J. Catal. 281 (2011) 325–338.

[31] M. Badawi, L. Vivier, G. Pérot, D. Duprez, J. Mol. Catal. Chem. 293 (2008) 53–58.

[32] W. Wang, G. Zhu, L. Li, S. Tan, K. Wu, X. Zhang, Y. Yang, Fuel. 174 (2016) 1–8.

[33] B.S. Gevert, J.E. Otterstedt, F.E. Massoth, Appl. Catal. 31 (1987) 119–131.

[34] B.S. Gevert, J.E. Otterstedt, F.E. Massoth, Appl. Catal. 31 (1987) 119–131.

[35] M. Badawi, S. Cristol, J.-F. Paul, E. Payen, Comptes Rendus Chim. 12 (2009) 754–761.

[36] M. Badawi, J.F. Paul, S. Cristol, E. Payen, Y. Romero, F. Richard, S. Brunet, D. Lambert, X. Portier, A. Popov, J. Catal. 282 (2011) 155–164.

[37] M. Badawi, J.-F. Paul, S. Cristol, E. Payen, Catal. Commun. 12 (2011) 901–905.

[38] R.R. Chianelli, Catal. Rev. 26 (1984) 361–393.

[39] A.Y. Bunch, U.S. Ozkan, J. Catal. 206 (2002) 177–187.

[40] Y. Romero, F. Richard, Y. Renème, S. Brunet, Appl. Catal. Gen. 353 (2009) 46–53.

[41] A.K. Tuxen, H.G. Füchtbauer, B. Temel, B. Hinnemann, H. Topsøe, K.G. Knudsen, F. Besenbacher, J.V. Lauritsen, J. Catal. 295 (2012) 146–154.

[42] J.V. Lauritsen, F. Besenbacher, J. Catal. 328 (2015) 49–58.

[43] S. Brillouet, E. Baltag, S. Brunet, F. Richard, Appl. Catal. B Environ. 148 (2014) 201–211.

[44] A. Travert, C. Dujardin, F. Maugé, E. Veilly, S. Cristol, J.-F. Paul, E. Payen, J. Phys. Chem. B. 110 (2006) 1261–1270.

[45] J.V. Lauritsen, J. Kibsgaard, G.H. Olesen, P.G. Moses, B. Hinnemann, S. Helveg, J.K. Nørskov, B.S. Clausen, H. Topsøe, E. Lægsgaard, F. Besenbacher, J. Catal. 249 (2007) 220–233.

[46] P. Raybaud, Appl. Catal. Gen. 322 (2007) 76–91.

[47] E. Krebs, B. Silvi, P. Raybaud, Catal. Today. 130 (2008) 160–169.

[48] J.-F. Paul, S. Cristol, E. Payen, Catal. Today. 130 (2008) 139–148.

[49] M. Sun, A.E. Nelson, J. Adjaye, J. Catal. 233 (2005) 411–421.

[50] P.M. de Souza, R.C. Rabelo-Neto, L.E.P. Borges, G. Jacobs, B.H. Davis, T. Sooknoi, D.E. Resasco, F.B. Noronha, ACS Catal. 5 (2015) 1318–1329. doi:10.1021/cs501853t.

[51] L. Nie, P.M. de Souza, F.B. Noronha, W. An, T. Sooknoi, D.E. Resasco, J. Mol. Catal. Chem. 388–389 (2014) 47–55.

Chapitre 4 :

Effect of the support on the hydrodeoxygenation of m-cresol over molybdenum oxide based catalysts

Chapitre 4 : Effect of the support on the hydrodeoxygenation of m-cresol over molybdenum oxide based catalysts

1. Introduction

The phenolic fraction issued from biomass pyrolysis has attracted attention due to its potential as a source of several biosourced products such as resins, carbon fibers, biofuels, additives, and aromatic chemicals (Benzene, Toluene and Xylene or BTX) [1–3]. Regarding the composition of biomass, an important part is constituted of lignin which is the most widely available renewable source of aromatics [4]. Nowadays, the majority of the bulk BTX are produced from fossil resources, mostly by the catalytic reforming of naphtha in a petroleum refinery, which is tied to the traditional petro-based platform [5]. The replacement of the fossil resources by biosourced raw materials has been continuously developed in biorefineries [6].

Hydrodeoxygenation (HDO) process is a promising technology to produce value-added products from oxygenated compounds. This process allows to upgrade the phenolic pyrolysis fraction through the elimination of oxygen atoms as water and/or carbon oxides (CO and CO_2). In this process, aromatic oxygenates are exposed to a H_2 atmosphere, at temperatures between 250-500 ºC, in the presence of a solid catalyst [7,8]. It is noteworthy that to produce aromatics from phenolic compounds, it is a requirement during HDO to remove oxygen atoms while limiting the hydrogen consumption [9].

Many efforts have been made to design efficient catalyst formulations for the hydrotreatment of oxygenated compounds. Sulfided Mo-based catalysts were first studied for the HDO reactions since they were already used in hydrotreatment processes implemented in conventional oil refineries to decrease the sulfur content from petroleum [10]. Their uses for the treatment of bio-oils from biomass is rather not preferable due to environmental concerns relative to the possible contamination of HDO products by sulfur [11,12].

Recently, molybdenum oxide (MoO_x) was evaluated as catalyst for the HDO of both model molecules [9,13–15] and pyrolysis bio-oils [16,17]. Interestingly, molybdenum oxide, which can be considered as an environment-friendly and also a cost-effective material, showed the highest activity in HDO among a series of metal oxides (MoO_3, V_2O_5, Fe_2O_3, CuO and WO_3) [9]. At 320°C under atmospheric pressure, Shetty et al. [14] reported that several supported MoO_x catalysts (MoO_x/SiO_2, MoO_x/Al_2O_3, MoO_x/TiO_2 and MoO_x/ZrO_2) can

selectively cleave the C-O bond of m-cresol without hydrogenate the aromatic ring. Toluene was obtained at high selectivities, from 76 and 99 mol%. The authors proposed that the catalytic activity was dependent on the reducibility of Mo species but also on the electronegativity of the support cation. Prasomsri and co-workers [9,13] only observed aromatic production (mainly benzene and toluene) during the HDO of anisole over unsupported MoO_3 catalyst, under similar experimental conditions (320-350 ºC, under atmospheric pressure). These results show that such molybdenum oxide is an attractive catalyst to selectively produce aromatics from oxygenated phenolic compounds. Unfortunately, a strong deactivation of Mo-based catalysts occurred during HDO reactions at atmospheric pressure [9,13,14,18]. For example, the conversion of m-cresol decreased about 25% in 7 hours when reaction was performed at 350°C under atmospheric pressure with unsupported MoO_x catalyst [13]. In the same way and under similar experimental conditions (320°C, atmospheric pressure), supported MoO_x catalysts presented a significant deactivation (close to 50% after 14 h on stream when using MoO_x/TiO_2 catalyst) [14]. Such deactivation was attributed to coke deposition and/or over reduction of Mo leading to less or inactive Mo species. However, Prasomsri et al. [9] observed a significant enhancement in the stability of MoO_x-based catalysts during the HDO of 2-hexanone by increasing the partial pressure of H_2, all experiments were carried out under atmospheric pressure. The beneficial effect of the increase of hydrogen partial pressure was attributed to both regeneration of oxygen vacancies, considered as active sites, and decrease in coke formation. From these results, performing HDO reactions under high hydrogen pressure can be an attractive approach to limit catalyst deactivation.

The present study concerns the evaluation of the deoxygenation catalytic properties (activity, selectivity and stability in reaction) of supported MoO_x catalysts under high pressure. The HDO of m-cresol used as a model oxygenated molecule was carried out at 340°C under 4 MPa as total pressure over molybdenum oxides supported on different solids (commercial SiO_2, synthetized SBA-15 and commercial γ-Al_2O_3). The impact of some characteristics of the support used on catalytic properties can then be considered.

2. Experimental

2.1. Catalyst preparation

Molybdenum oxide was obtained by incipient wetness impregnation (IWI), over both commercial supports (SiO_2 and γ-Al_2O_3) and ordered type silica (SBA-15). Active phase loading was fixed at 10 wt.% of Mo. SBA-15 was prepared under classical acidic conditions as initially proposed by Zhao et al. [19]. The detailed synthesis procedure can be found elsewhere [20]. For the IWI step, the calculated weight of the Mo precursor (ammonium molybdate tetrahydrate, $(NH_4)_6Mo_7O_{24}\cdot 4H_2O$, Sigma-Aldrich) was dissolved in known volumes, corresponding to measured water pore volume of the support. Thereafter, the prepared solution was added dropwise to the corresponding support. After adding, the mixture was aged during 5 days at 25 ºC. After drying, the samples were calcined at 400 ºC (1.5 ºC min^{-1}) for 5 h. Afterwards, the obtained catalysts were pelleted, crushed and sieved (250–315 μm).

2.2. Reaction setup

The hydrodeoxygenation of m-cresol was chosen to evaluate the influence of the support (nature and textural properties) on the catalytic properties of supported MoO_x catalyst. The catalytic test was performed in a down flow tubular inox fixed-bed reactor (length: 40 cm; inner diameter: 1.26 cm) operating at 4 MPa of total pressure. Prior to reaction, the catalysts (120 mg) were pretreated with pure H_2 (4.7 NL h^{-1}) at 340 ºC for 30 min under 4 MPa as total pressure. The reaction was carried out at this temperature. The feed was composed by m-cresol as reactant (53 kPa), n-heptane as an internal standard (31 kPa) in dodecane. The H_2/m-cresol ratio was set to 486 NL/L. The H_2 partial pressure is equal to 3.2 MPa in reaction conditions. The line at the bottom of the reactor was maintained at 10 ºC using a Minichiller-Huber condenser. Thus, liquid samples were collected every hour and analyzed using a Varian 430 chromatograph equipped with a DB1 capillary column (length: 30 m; inside diameter: 0.320 mm; film thickness: 5 μm) and a FID detector.

Conversion and selectivity were calculated by Eqs. (1) and (2) as follows:

$$X_{CRE}\ (\%) = \frac{C_{CRE,0} - C_{CRE}}{C_{CRE,0}} . 100 \quad (1)$$

$$S_i\ (mol\%) = \frac{C_i}{C_{CRE,0} - C_{CRE}} . 100 \quad (2)$$

where $C_{CRE,0}$ and C_{CRE} are the molar fractions of m-cresol in the feed and in the collected liquid sample; C_i is the molar fraction of a given *i* product.

Space times (τ in g $hmol^{-1}$) were calculated from the catalyst weights and the m-cresol flow as defined in Eq. (3):

$$\tau = \frac{w}{F_{CRE}} \quad (3)$$

with w as the weight of catalyst (120 mg), and F_{CRE}, the molar flow of m-cresol.

A first-order model was used to evaluate the rate constant of the transformation of m-cresol. Thus, the overall apparent rate constant (k_{HDO}) was calculated by Eq. (4):

$$k_{HDO} = \frac{1}{\tau} \ln(1 - X_{CRE}) \quad (4)$$

where k_{HDO} is the reaction rate constant (mmol g^{-1} h^{-1}).

2.3. Catalyst characterization

The molybdenum loading in catalysts was determined by atomic absorption AA200 Perkin Elmer. The wavelength used was 313.26 nm. Before analysis, the catalysts were solubilized in an acidic aqueous solution containing both hydrochloric and nitric acids.

The textural properties (surface areas, pore volume and pore size) of the support and as-prepared catalysts were obtained by N_2 physisorption at -196 ºC. Surface areas (using the B.E.T.

method) and pore size (B.J.H. method) were issued from adsorption-desorption isotherms. Prior to the analysis, samples were outgassed at 200 ºC overnight to remove any surface adsorbed residual moisture.

The XRD patterns of the bare supports and Mo supported catalysts were obtained on a PAN-alytical EMPYREAN powder diffractometer in Bragg-Brentano (θ-θ) configuration with a copper tube powered at 45 kV and 40 mA (Cu Kα1 = 1.54060 Å and Cu Kα2 = 1.54443 Å). A nickel filter was installed in the secondary optic in order to eliminate the K β component. Analysis is performed for 2θ values from 20° to 80°, with steps of 0.1° and fixed acquisition time of 20 min per step. Low angles diffractions were also collected from 0.5° to 5° for SBA-15 and derived catalyst. Obtained diffractograms were analyzed with HighScore Plus software. Before analysis, a pretreatment was performed at 340 ºC (5 ºC min^{-1}) under 4 MPa of hydrogen for 30 min (flow of H_2 = 4.7 NL h^{-1}).

The H_2-TPR profiles of the Mo-based catalysts were collected on a Micromeritics AutoChem 2910 from 100 °C to 1000 °C using a ramp of 5 ºC min^{-1}, under 10 vol.% H_2 in Ar flow (total flow rate of 20 mL min^{-1}). Prior to the experiments, samples were pretreated with pure He (20 mL min^{-1}) at 200 ºC during 1 h. The hydrogen consumption was continuously monitored using TCD.

NH_3-TPD was performed for each supported MoO_x. Experiments were performed on a Micromeritics Autochem 2910 equipment. Prior to the experiments, samples were pretreated with pure He at 200 ºC for 1 h. After treatment, the temperature was lowered to 100 ºC and the sample was saturated with anhydrous NH_3 (10 vol.% in He) for 1 h. Subsequently, the samples were purged under He flow, and the temperature was raised to 600 ºC applying a temperature gradient rate of 5 °C min^{-1}. The desorbed NH_3 was continuously monitored by TCD.

Raman spectra were recorded using HORIBA JOBIN YVON Labram HR800UV and an argon ion laser (Melles Griot) with an excitation wavelength of 514.5 nm. A laser power of 0.4 mW at the sample was applied.

The TEM studies were performed on a JEOL 2100 UHR 200 kV microscope equipped with a Gatan Ultra scan camera. Samples were dispersed ultrasonically in ethanol and deposited on a copper grid supporting a perforated carbon film.

Oxygen chemisorption was performed for each solid. Before analysis, the materials were activated using the following standard procedure: 340°C under 4 MPa of hydrogen during 30 min. The solid was inserted in a quartz U-shaped tube reactor. Successive pulses of pure O_2 at 340 ºC were then injected until saturation of the sample. The O_2 uptake (oxygen adsorbed) was used to calculate the number of redox active Mo species (Eq. (5)) and the TOF (Turn over Frequency, in h^{-1} - Eq. (6)), as proposed by Shetty and co-workers [14]:

$$\%\, Redox\ Mo = \frac{2\,.\,Oxygen\ uptake}{Mo\ loading}\,.100 \quad (5)$$

$$TOF = \frac{k_{HDO}}{2\,.\,Oxygen\ uptake}\,.100 \quad (6)$$

2.4. Catalyst characterization

Chemical analysis of carbon and hydrogen were carried out after reaction test by using an elemental analyzer (NA2100 analyzer, CE instruments). DRX analysis were also performed over all spent catalysts. These catalysts were characterized without chemical treatment.

3. Results and discussion

3.1. Catalyst characterization

As indicated in Table 4-1, the experimental molybdenum loadings, determined by atomic absorption, were close to the set value of the preparation, i.e. 10 wt.%. Figure 4-1 shows

the N_2 adsorption-desorption isotherms for the bare supports and MoO_x derived catalysts. Both MoO_x/SBA-15 and MoO_x/Al_2O_3 catalysts presented similar profiles (type IV isotherms) compared to their respective supports, indicating porosity developed in the domains of the mesopores. In addition, the hysteresis shapes did not evolve after the impregnation-activation step. This result indicates that the pore characteristics remains unchanged for the supported molybdenum materials. However, the N_2 physisorption isotherms obtained for bare SiO_2 and MoO_x/SiO_2 were quite different, evolving from type II to type IV. In addition, the hysteresis is also evolving due to a modification of pore shape from aggregate-type porosity to ink-bottle shaped porosity. Such important modification of the pore characteristics, upon aqueous impregnation, was already reported by Sydorchuk et al. [21] over commercial silica.

Table 4-1: Chemical composition and textural properties of bare supports and impregnated MoO_x catalysts.

Solid	Mo[a] (wt. %)	S_{BET}[b] (m^2g^{-1})	Pore volume[c] ($cm^3\ g^{-1}$)	Average pore diameter[d] (nm)
SiO_2	-	271	0.40	9
MoO_x/SiO_2	10.2	253 (299)[e]	0.62 (0.73)[e]	14
SBA-15	-	797	1.00	7
MoO_x/SBA-15	9.1	586 (678)[e]	0.72 (0.83)[e]	6
Al_2O_3	-	251	0.77	12
MoO_x/Al_2O_3	10.5	216 (256)[e]	0.62 (0.73)[e]	12

a: Deduced from atomic atomic absorption
b: Specific surface area calculated by the BET method
c: Total pore volume determined at $P/P_0 = 0.99$
d: Calculated using the adsorption branch from the N_2 isotherm
e: In brackets are values determined after correction due to the contribution of the weight gain consecutive to the introduction of MoO_3.

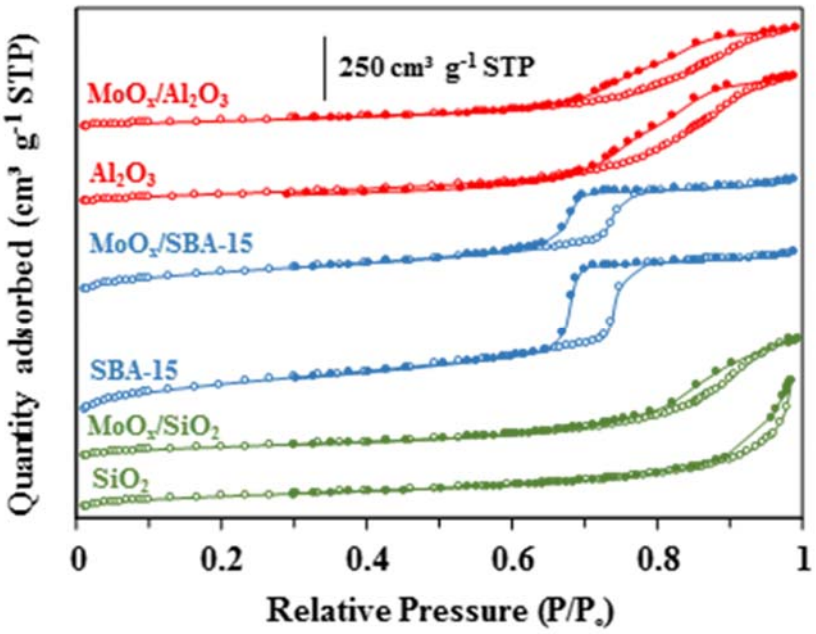

Figure 4-1 : N_2 adsorption and desorption isotherms of supports and the as-prepared supported MoO_x catalysts. (○) Adsorption (●) Desorption.

Calculated values of specific surface area, pore volume, and pore diameter issued from physisorption isotherms, are gathered in Table 4-1. As expected, the surface specific area of MoO_x/SBA-15 was the highest (equal to 586 m^2 g^{-1}). For supported molybdenum materials, raw values were recalculated to remove the contribution of MoO_3 weight on textural properties (values in parenthesis in Table 4-1) and to access information on the stability of the support during impregnation-calcination steps [22]. The corrected surface areas obtained for MoO_x/SiO_2 and MoO_x/Al_2O_3 were close to those displayed by the parent support, and range around 250-300 m^2 g^{-1}. No notable modification of the surface area between the support and the catalyst indicates, for these two materials, a satisfying stability of the support was observed, even for the silica derived catalyst for which important modification of the isotherm shape. On the contrary, the corrected surface area of MoO_x/SBA-15 was lower than the surface area of SBA-15 (decreased by 15%). The decrease can originate from possible pore plugging occurring

when confined particles forms during the calcination steps [23,24]. Considering the pore volume values, the corrected value of MoO_x/Al_2O_3 was close to the one measured on the parent support (around 0.7 $cm^3\ g^{-1}$), whereas the corrected value of MoO_x/SBA-15 was lower compared to its bare support (decreased by 15%). This result is always in favor of the formation of mesopore confined particles in the SBA-15 channel type porosity. On the contrary, the presence of MoO_x phase allowed to increase the pore volume (by about 80%) of SiO_2. Finally, the catalysts pore size average is only slightly modified by the impregnation-activation process except for the SiO_2 materials for which significant modification of the isotherm shape was observed.

XRD patterns of calcined supports and catalysts activated at 340°C under 4 MPa of H_2, are presented in Figure 4-2. Over silica-based catalysts, only a broad reflection was observed, at 2θ~22º, characteristic of amorphous silica. For alumina based support, only reflections ascribed to γ-Al_2O_3 were detected [25]. Regardless of the support used, reflections attributed to MoO_x phase were never observed, which suggests that molybdenum oxide forms small particles (< 3-4 nm, detection limit of the X-ray diffraction), and/or remains in an amorphous state. For SBA-15 loaded molybdenum oxide, low angle XRD was performed (Figure 4-3). The presence of three reflections at 2θ > 2° is a clear indication of the maintaining of the hexagonal pore structure in the catalyst, as awaited from N_2 physisorption result interpretation (Figure 4-1). Decrease in intensity and small variation in peak position, over the MoO_x/SBA-15, is originated from reduction of contrast and strong X-ray absorption from heavier molybdenum atoms [26].

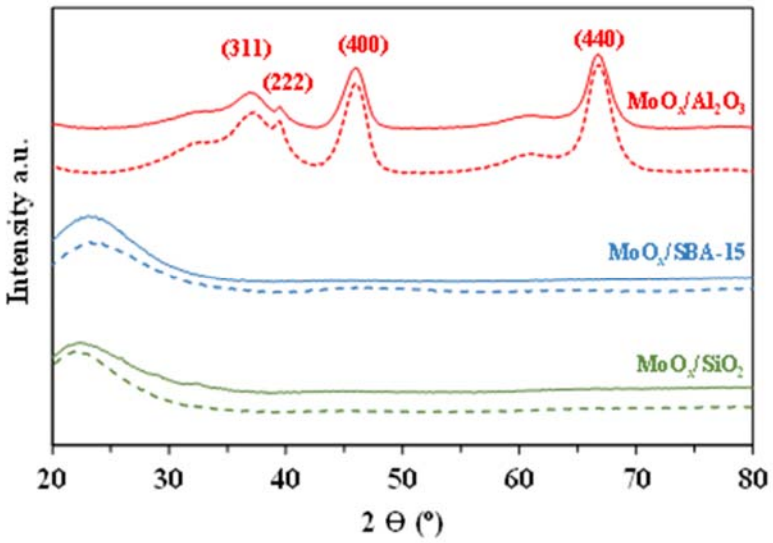

Figure 4-2 :Wide-Angle XRD Patterns of the bare supports and supported MoO_x catalysts. The hkl indices of Al_2O_3 are reported in brackets. Supports (---); Catalysts (—)

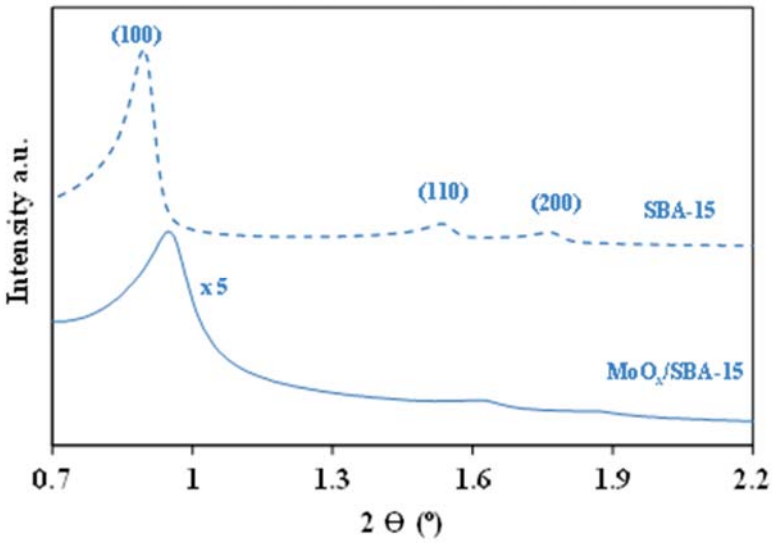

Figure 4-3 : Small-angle XRD patterns for SBA-15 and MoO_x/SBA-15. The hkl indices of SBA-15 structure are reported in brackets. Supports (---); Catalysts (—)

In order to obtain supplementary information concerning the size of molybdenum oxide particles, representative images obtained for the three Mo-containing catalysts are presented in Figure 4-4 to 4-6. On SiO_2, molybdenum oxide particles were observed as both microparticles (diameter close to 1 µm) and nanoparticules (1-2 nm) as shown in Figure 4-4. On SBA-15 (Figure 4-5) and Al_2O_3 (Figure 4-6), only pseudo-spherical MoO_x particles of very small sizes (1-2 nm for MoO_x/SBA-15 and lower than 1 nm for MoO_x/Al_2O_3) located on the support surfaces were observed. Thus, the use of either an ordered silica (SBA-15), or an acidic support (alumina) instead of SiO_2 favored the dispersion of molybdenum oxide species, preventing the formation of very large particles of MoO_x. In addition, EDX analysis confirms a molybdenum loading on local analysis zone comparable to this awaited from chemical analysis.

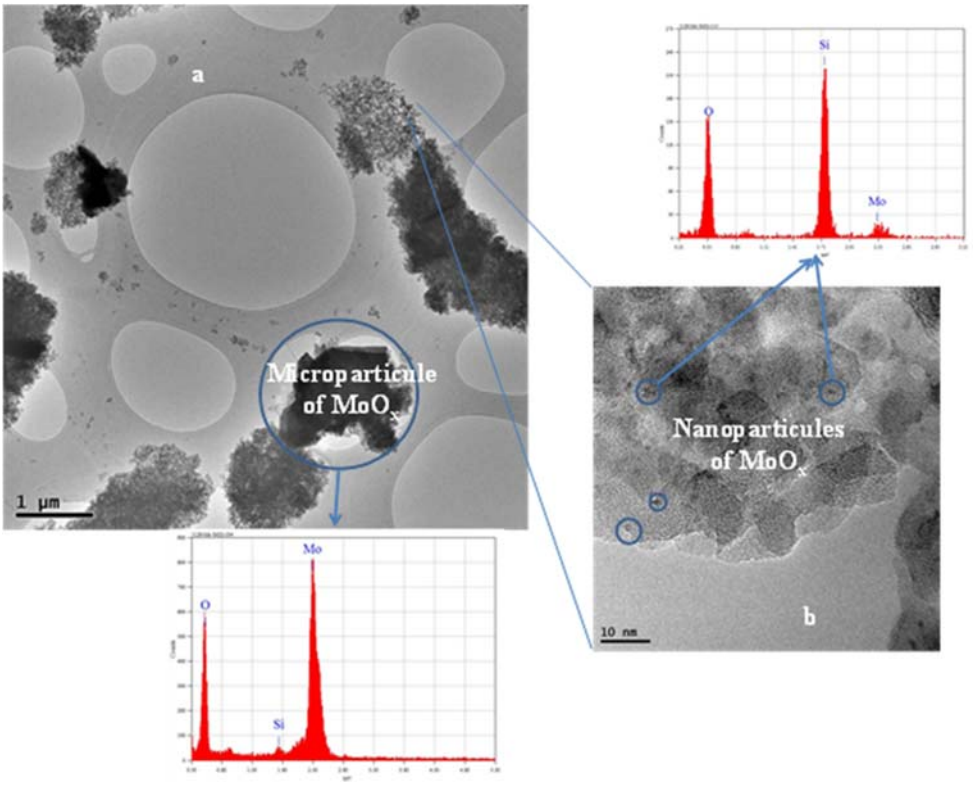

Figure 4-4 : TEM images and EDX analysis of MoO_x/SiO_2 at low (a) and high (b) magnification.

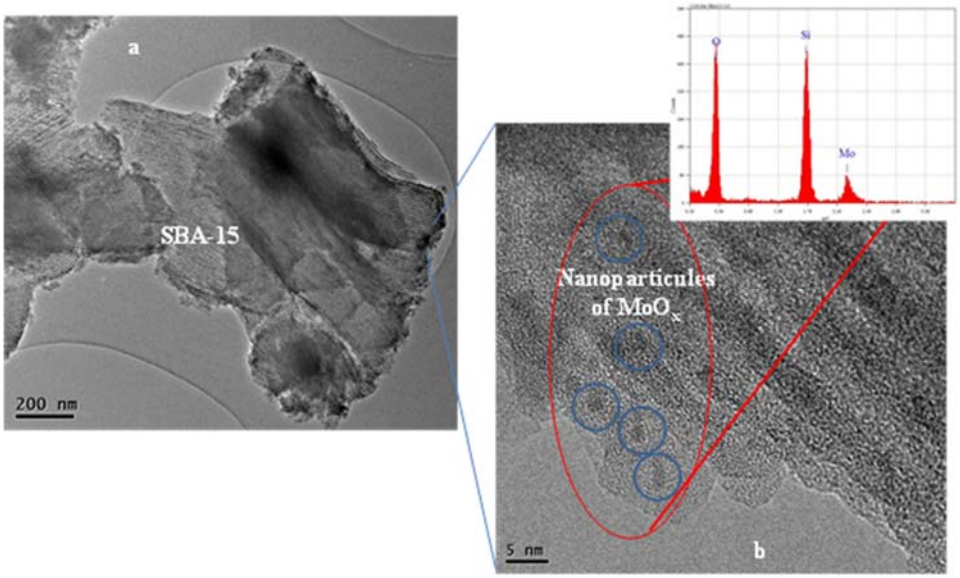

Figure 4-5 : TEM images and EDX analysis of MoO_x/SBA-15 at low (a) and high (b) magnification.

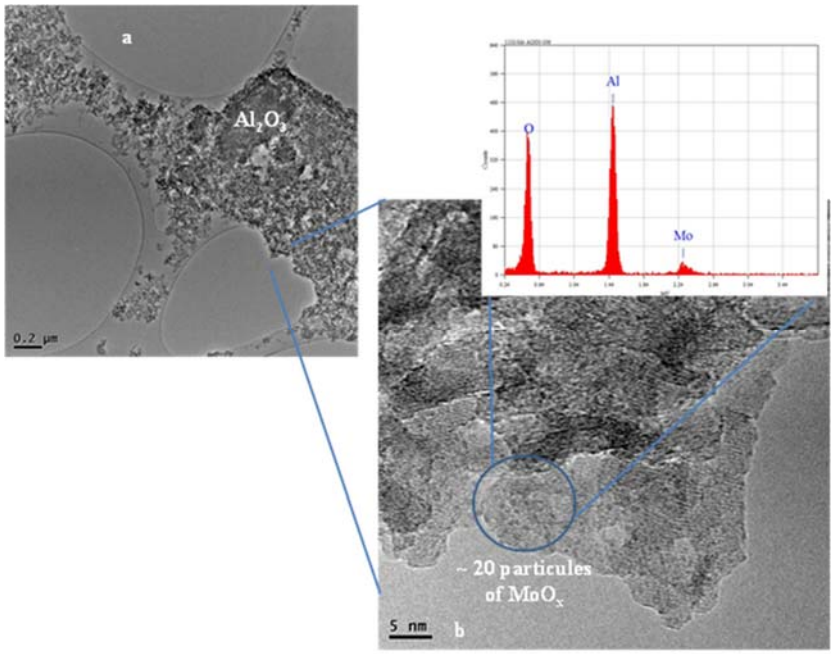

Figure 4-6 : TEM images and EDX analysis of MoO_x/Al_2O_3 at low (a) and high (b) magnification.

TPR profiles of MoO_x based catalysts are presented in Figure 4-7. Reducibility of molybdenum was strongly dependent on the support nature and morphology. First, over silica and alumina, Mo(VI) can be present in both octahedral (Mo_O) and tetrahedral (Mo_T) forms [27]. Reduction of MoO_3 phase proceeds in two steps, with a first reduction of MoO_3 into MoO_2 (in the range of 450-650 °C) followed by the reduction of MoO_2 into molybdenum metal (up to 700 °C) [28]. For the three samples, the observed low temperature (LT) reduction is assigned to the partial reduction of octahedrally coordinated Mo(VI) into Mo(IV) [29]. The temperature of the LT reduction of supported molybdenum oxides followed: MoO_x/Al_2O_3 (~475 °C) < MoO_x/SBA-15 (~540 °C) < MoO_x/SiO_2 (~560 °C). This indicates that Mo(VI) species are more easily reducible on Al_2O_3 than on silica based supports, probably due to the smaller oxide particles as observed by TEM (Figure 4-4 to 4-6). A second reduction peak was also observed at higher temperatures, particularly for molybdenum oxides supported on Al_2O_3 and SiO_2. These peaks can be ascribed to a deep reduction of residual Mo(VI) and Mo(IV) into Mo^0, including highly dispersed Mo_T from MoO_3 phase [29].

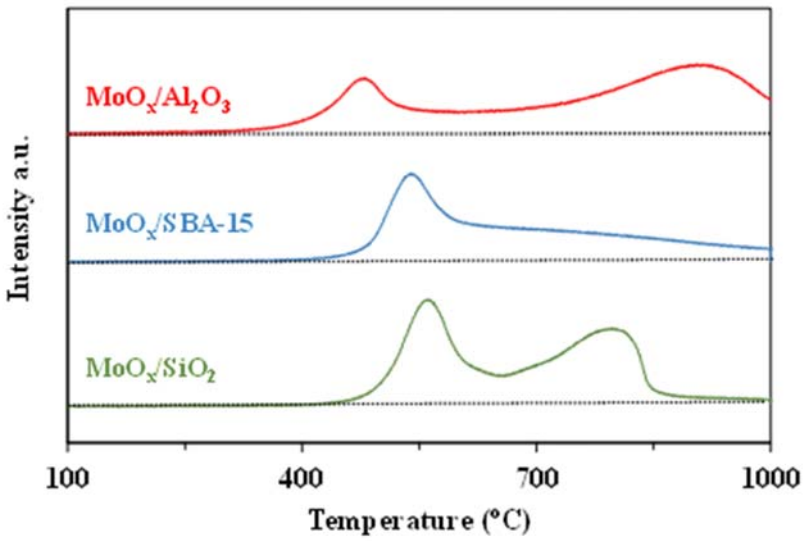

Figure 4-7 : H_2-TPR profiles of supported MoO_x catalysts.

Table 4-2 shows the values hydrogen consumed obtained by H_2-TPR experiments, and theoretical hydrogen consumption to reduce all Mo(VI) to metal. Over silica, a reduction degree of about 80% was calculated, showing an incomplete reduction of molybdenum cation, even at 1000°C, which could be related to the presence of oxide microparticles (Figure 4-4). Higher molybdenum reduction degree (higher than 90%) was determined when molybdenum oxides were supported over alumina. In addition, the molybdenum oxide species were less reducible to metallic Mo on alumina, since TPR experiments showed that the complete reduction occurred at the higher temperature (above 1000°C). This phenomena can be explained by smaller oxide particles on this support, as observed by TEM.

Table 4-2 : Physico-chemical characterizations of bare supports and impregnated MoO_x catalysts

Solid	H_2 uptake ($mmolg^{-1}$)		MoO_x Reducibility (%)	Total acidity[c] ($\mu mol\ g^{-1}$)	O_2 uptake[d] ($\mu mol\ g^{-1}$)	Redox Mo[e] (%)
	Exp[a].	Cal.[b]				
SiO_2	n.d.	n.d.		0	0	n.d.
MoO_x/SiO_2	2.7	3.2	84	860	115	22.1
SBA-15	n.d.	n.d.		0	0	n.d.
MoO_x/SBA-15	2.3	2.9	79	708	163	31.3
Al_2O_3	n.d.	n.d.		1044	0	n.d.
MoO_x/Al_2O_3	3.1	3.3	94	1702	181	34.7

a: Quantity of H_2 determined from TPR experiments
b: Quantity of H_2 calculated according the nominal composition according the following reaction: $MoO_3 + 3\ H_2 \rightarrow Mo + 3\ H_2O$
c: Deduced from NH_3-TPD
d: Deduced from chemisorption of O_2
e: Calculated using Eq. (5)

The acid properties of the MoO_x-based catalysts were probed using NH_3 thermodesorption experiments (NH_3-TPD). Although ammonia thermodesorption does not allow to discriminate Brønsted and Lewis acid sites, the amount of NH_3 desorbed is an indirect measure of the material global acidity. Acidity of the molybdenum oxide phase was issued from the difference in global acidity between catalyst and support. Profiles for bare and impregnated supports are presented in Figure 4-8. As expected, both SiO_2 and SBA-15 did not present any significant NH_3 desorption. Al_2O_3 support exhibited both weak (< 300 °C) and intermediate/strong (> 300 °C) acidity. NH_3-TPD experiments performed over Mo-containing catalysts display an increase of the acidity for all solids, which can be attributed to the presence of the molybdenum oxide phase. Over these materials, the amount of ammonia desorbed ranges between 658 µmol g^{-1} and 860 µmol g^{-1} (Table 4-2). As proposed by several authors [30,31], the MoO_x phase exhibits mainly Brønsted acid sites caused by the formation of hydroxyl groups on the molybdenum oxide layers.

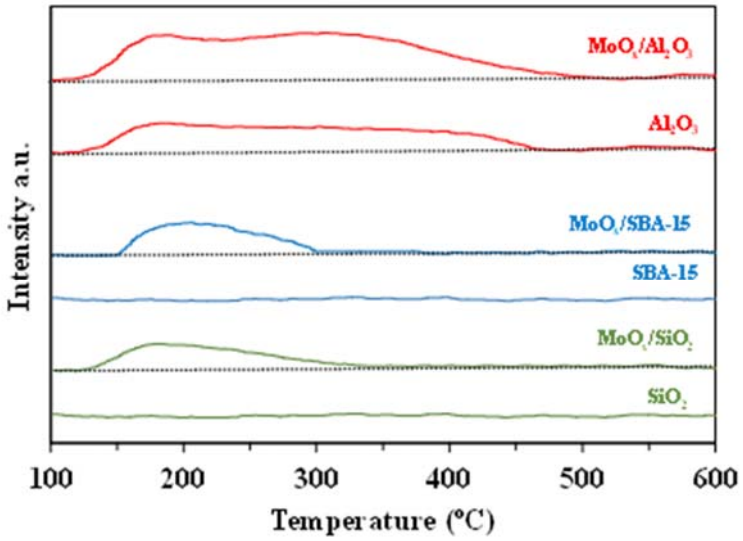

Figure 4-8 : NH_3-TPD profiles of bare supports and supported MoO_x catalysts

Oxygen uptake measurement was used to determine the number of active Mo species. Shetty et al. [14] demonstrated that the oxygen chemisorption experiments was an efficient technique to evaluate the number of oxygen vacancies, coordinately unsaturated sites (CUS) involved in HDO. Active site number thereafter allows to calculate TOF values of different MoO_x-based catalysts. Oxygen uptake values, issued from oxygen chemisorption experiments are gathered in Table 4-2, and the following order of uptake is obtained: MoO_x/Al_2O_3 > MoO_x/SBA-15 > MoO_x/SiO_2. This order is identical to the order of Mo(VI) reducibility, as observed from TPR experiments (Figure 4-7), and seems to be related to the difference in molybdenum oxide particle size on the three catalysts. No oxygen uptake was observed over bare supports.

Raman spectra of the catalysts, recorded in the 750-1050 cm^{-1} domain, are presented in Figure 4-9. Two main signals were observed: (1) at 968-981 cm^{-1}, characterizing Mo=O terminal stretching vibration, and (2) a broad band at ~ 830 cm^{-1} located in the region to Mo-O-Mo functionalities [32–35]. A variation of the band position ascribed to the Mo=O stretching vibration is observed depending on the support. For MoO_x/Al_2O_3, the band was positioned at 968 cm^{-1}. For MoO_x/SiO_2, its position was at 981 cm^{-1}, while an intermediate value was obtained for MoO_x/SBA-15 (974 cm^{-1}). The shift could be linked to the differences in vacancy densities in the MoO_x clusters. Regarding the results of H_2-TPR and oxygen chemisorption measurements, it seems that when Raman signal of Mo=O terminal stretching vibration appears at lower position, the vacancy densities increases and a higher Mo(VI) reducibility can be expected.

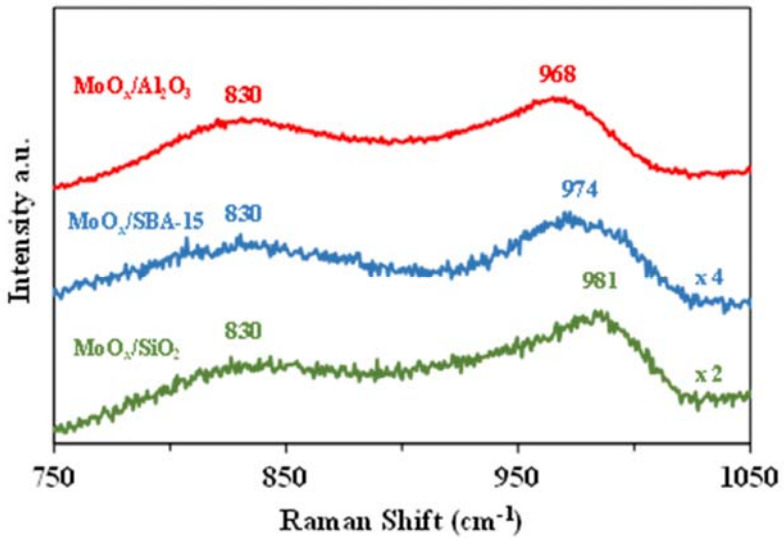

Figure 4-9 : Raman spectra of supported MoOx catalysts in the Raman shift ranges of 750–1050 cm^{-1}.

3.2. Catalytic properties of MoO_x-based catalysts on the hydrodeoxygenation of m-cresol.

The hydrodeoxygenation of m-cresol was studied at 340 ºC under 4 MPa as total pressure over the three MoO_x supported catalysts. A blank test was performed showing that m-cresol was unreactive in absence of catalyst. Similarly, the bare supports appeared to be inactive even at high τ values, with no measureable conversion of m-cresol. All experiments were carried out during 20 h on stream and τ (space time, as defined in Eq. (3)) was changed every 5 h to obtain different levels of conversion (Figure 4-10). For all catalysts, it can be observed that the conversions obtained in the first 5 h were very close to those measured during the last 5 h on stream when τ remains constant (equal to 26 g h mol^{-1}), experiments being carried out under high pressure, i.e. 3.2 MPa of H_2. This indicates an absence of catalyst deactivation/poisoning during reaction for at least 20 h, which reflects a satisfying stability for the molybdenum active sites. The amounts of carbon contained in the used catalysts was

relatively high (between 4.7 and 6.9 wt%, as indicated in Table 3). Carbon can be related to adsorbed molecules on the catalyst surface. The nature of organic molecules can be identified, based on the measured C/H ratio in weight basis [36]. For all catalysts, these values were close to 10.5, which is the C/H ratio of m-cresol. Consequently, carbon in the spent catalysts is preferably attributed to the presence of adsorbed phenolic reactant on the catalyst surface. The presence of coke formed during reaction cannot however be completely excluded. However, if carbon massively formed during reaction, the C/H experimental ratio should have been significantly higher than 10. Such stability was clearly not the case when the HDO reaction using molybdenum oxide was performed under atmospheric pressure, where MoO_x based catalysts exhibited poor stability [14]. Such beneficial effect of H_2 pressure on the catalyst stability was recently highlighted over a phosphide catalyst (Ni_2P) for HDO reaction [36]. The observed deactivation of MoO_x based catalysts was attributed both to the over reduction of Mo(VI) into less active species and to coke deposition on catalyst surface [9,14]. In our case, it seems that the use of high pressure results in several beneficial effects: (i) there is no induction period for reaction, as observed by Prasomsri et al. [13], and (ii) the stability of catalysts is improved.

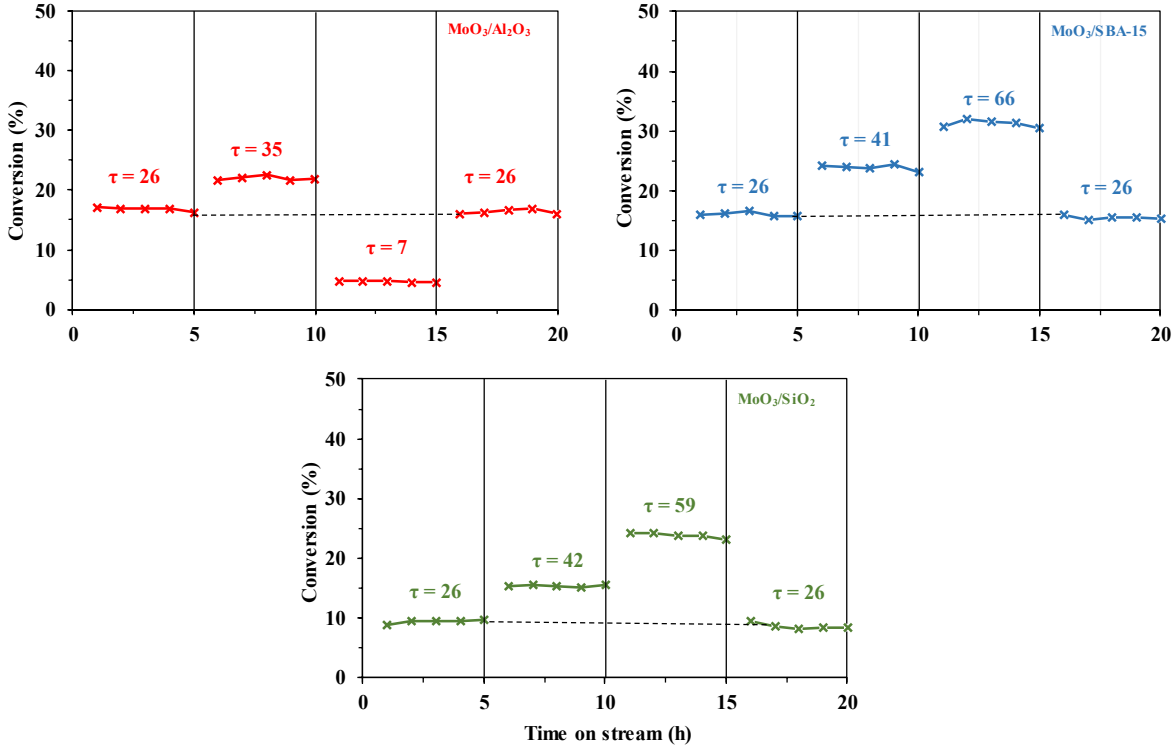

Figure 4-10 : Conversion as function of time on stream for the HDO of m-cresol at 4 MPa and 340 ºC. MoO_x/SiO_2 (x);MoO_x/SBA-15 (x); MoO_x/Al_2O_3 (x);τ in mol g h^{-1}.

Figure 4-11 shows a linear relationship between ln(1-X_{CRE}) and τ, which indicates a first order reaction for HDO of m-cresol over supported molybdenum oxides. The k_{HDO} values obtained using Eq. (9) showed the following order of activity for materials: MoO_x/Al_2O_3 > MoO_x/SBA-15 > MoO_x/SiO_2 (Table 4-3). The nature of the support for MoO_x acted positively on the active sites numbers, which are proposed to be coordinatively unsaturated sites (CUS) [9,14]. Such increase in CUS density in material was demonstrated by O_2 chemisorption. The O_2 uptake (Table 4-2) followed the same order as the deoxygenation activity. In addition, the fact that MoO_x/SiO_2 was less active than MoO_x/SBA-15 can be explained by the presence of large microparticles of MoO_x over the former which were probably less active than MoO_x nanoparticles for the HDO reaction.

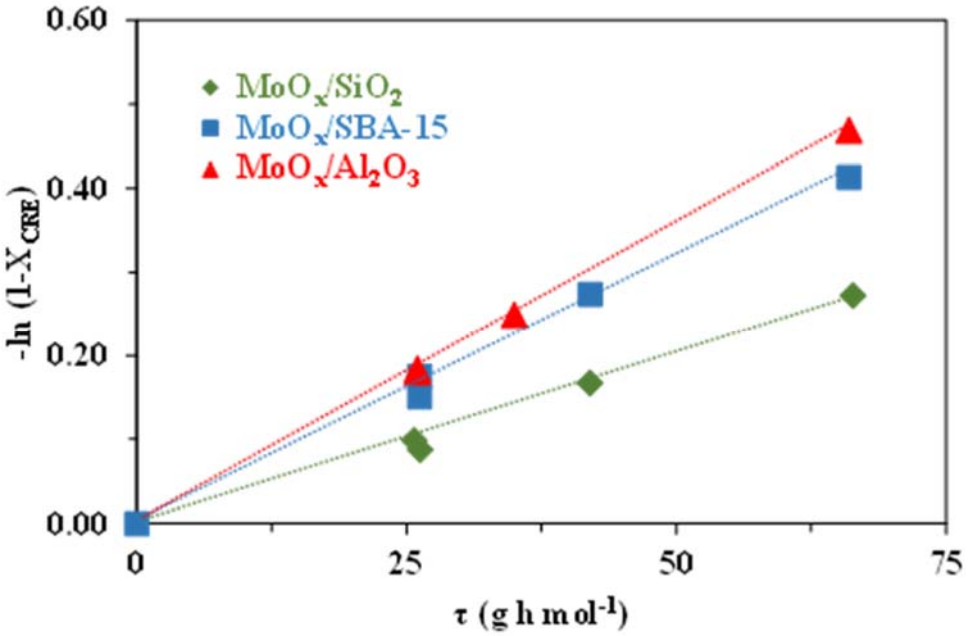

Figure 4-11 : Plots of -ln (1- X_{CRE}) as function of τ obtained from the HDO of m-cresol at 4 MPa and 340 ºC. MoO_x/SiO_2 (♦); $MoO_x/SBA\text{-}15$ (●); MoO_x/Al_2O_3 (▲).

Table 4-3 : Individual apparent rate constants and TOF values (standard deviation of values close to 5%) determined during the transformation of m-cresol over molybdenum oxides based catalysts at 340 °C under 4 MPa of total pressure.

	Rate constants (in mmol g^{-1} h^{-1})				TOF
	k_{HDO}	k_{DDO}	k_{HYD}	k'_{HYD}	(h^{-1})
MoO_x/SiO_2	4.1 ± 0.2	3.4 ± 0.2	0.70 ± 0.03	12.3 ± 0.6	19 ± 1
$MoO_x/SBA\text{-}15$	6.5 ± 0.3	5.4 ± 0.3	0.90 ± 0.04	8.6 ± 0.4	20 ± 1
MoO_x/Al_2O_3	7.1 ± 0.3	6.1 ± 0.3	1.00 ± 0.05	6.9 ± 0.3	20 ± 1
MoS_2/Al_2O_3 [37]	11.6 ± 0.6	3.2 ± 0.2	8.4 ± 0.4	37.1± 1.8	n.d.

It is noteworthy that molybdenum in sulfide phase was about 1.6 times more active than in oxide phase [37], demonstrating a higher activity of MoS_2 compared to the MoO_x. This fact may be explained by either an easier formation of a sulfur vacancy than an oxygen vacancy on molybdenum or differences in strength between these two CUS. Nevertheless, it must be emphasized that a sulfur source (dimethyldisulfure) was added in the model feed to keep the catalytic activity of MoS_2/Al_2O_3 stable, preventing the oxidation of the sulfide phase [38]. Since sulfur is present at very low contents in biomass feedstocks, sulfide catalysts are likely to deactivate during HDO. Moreover, the strategy of adding sulfur to a biomass feedstock would lead to the eventual contamination of the products [11,12], which is indeed not desired.

Table 4-4 shows the distribution of products obtained from m-cresol HDO over the three MoO_x based catalysts at comparable levels of conversion (about 20%). Interestingly, all detected products were deoxygenated, which point out that MoO_x based catalysts are efficient catalysts for deoxygenation reactions. It was reported that alcohols and ketones, as oxygenated intermediates from m-cresol HDO, were observed over Ni_2P/SiO_2 catalysts under comparable experimental conditions [36]. In addition, these intermediates were usually observed when noble (i.e. Pd, Pt) or non-noble catalysts (i.e. Ni, Co) were used for the HDO of phenolic molecules [39,40].

Table 4-4 : Product distribution from the HDO of m-cresol at 340°C under 4 MPa of total pressure over supported molybdenum oxides and sulfide catalysts.

Catalyst	τ	Conversion	Selectivity (mol %)			1-MCHe/
	(g h mol^{-1})	(%)	Tol	MCHes	MCH	MCHes
MoO_x/SiO_2	66.0	23.8	81.9	14.9	3.2	60
MoO_x/SBA-15	42.0	23.9	82.8	14.3	2.9	60
MoO_x/Al_2O_3	35.0	22.1	85.5	12.8	1.7	65
MoS_2/Al_2O_3 [37]	15.8	16.9	27.8	53.6	18.6	65

Regardless of the support nature, toluene was the main deoxygenated product, accounting for more than 80 mol% of all deoxygenated products. Similarly, Shetty et al [14] previously reported that the use of MoO_x based catalysts led only to aromatics production during the HDO of m-cresol under atmospheric pressure. It is noteworthy to mention that the relative high pressure of H_2 used in our work allowed to maintain high selectivity into aromatics, while methylcyclohexenes were also observed at low selectivity and methylcyclohexane appeared as trace. Indeed, methylcyclohexenes selectivity ranged between 11-15 mol% and methylcyclohexane was clearly the minor product, its selectivity being always below 5 mol%. As presented in Table 4-4, the 1-MCHe/MCHes ratio ranged between 60 and 65 mol%, showing that 1-methylcyclohexene was always the main alkene isomer observed from m-cresol HDO, in accordance with results reported over sulfide [37] and phosphide [36] catalysts. From a thermodynamic point of view, at 340 °C, the ratio of 1-methylcyclohexene/methylcyclohexenes, is expected to be equal to 65 mol% [41]. It is noteworthy to mention that 1-methylcyclohexene is not directly expected from m-cresol. Indeed, it can be assumed that the total hydrogenation of the aromatic ring of m-cresol leads only to 3-methylcyclohexanol. This alcohol was never detected during reaction. TPD-NH_3 experiments (Figure 4-8) highlighted the formation of acid sites attributed to the molybdenum oxide species, which can dehydrate this alcohol into either 3- or 4-methylcyclohexenes. The fact that 1-methylcyclohexene appeared as the main alkene isomer, implies that an isomerization step occurred, involving the acid properties of the MoO_x phase. In the case of MoO_x/Al_2O_3, isomerization might also occur on alumina acid sites.

Table 4-4 also presents the product distribution determined over MoS_2/Al_2O_3 [37]. Over such phase, the deoxygenation of m-cresol mainly led to hydrogenated products, methylcyclohexenes being the main products. This indicates a completely different behavior between molybdenum oxide and sulfide phases, the former being very selective to aromatic whereas the latter was selective into cycloalkenes and cycloalkanes. Consequently, the nature of a sulfur vacancy and an oxygen vacancy could be different in nature, the former favoring the hydrogenation of aromatic ring whereas the latter favoring the direct C-O bond scission.

Based on the distribution of the products, a reaction scheme for the HDO of m-cresol over molybdenum oxides supported catalysts, under high H_2 pressure, is depicted in Scheme 4-1. The same reaction scheme was also proposed to explain the formation of deoxygenated products over sulfide phases [37]. Thus, two reaction routes were proposed: Direct DeOxygenation (DDO route) and ring HYDrogenation (HYD route). The main pathway involves the direct cleavage of the C-O bond of m-cresol leading to toluene production. The HYD route is responsible for the formation of methylcyclohexenes and methylcyclohexane. This latter and minor pathway was never previously observed over such MoO_x catalysts [9,13,14], probably because these studies were carried out under atmospheric pressure.

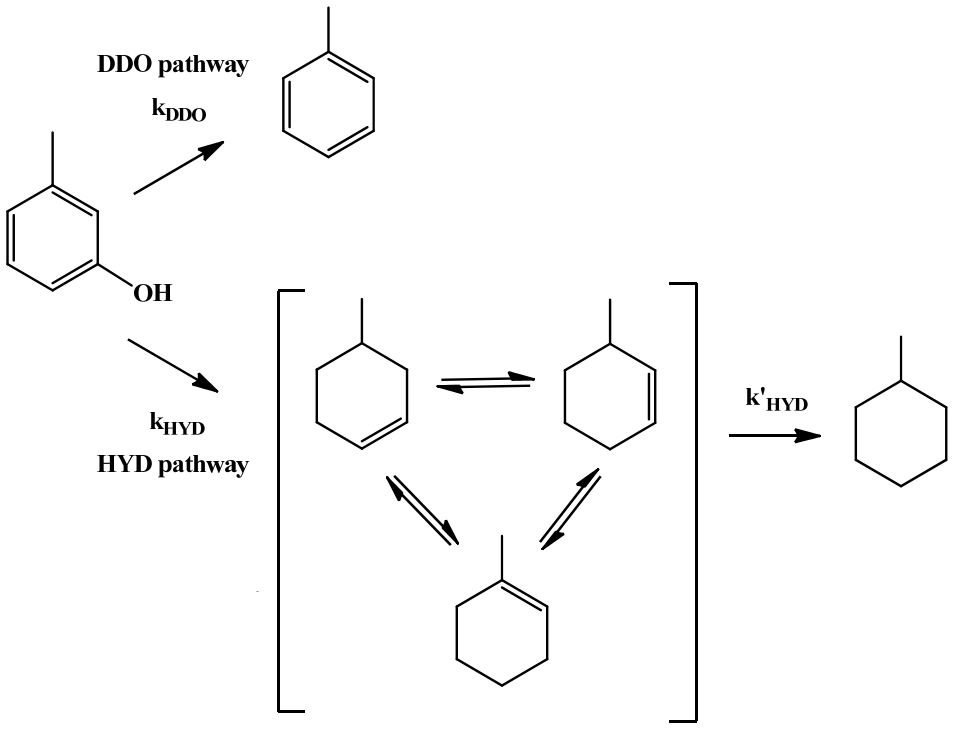

Scheme 4-1 : Reaction network of m-cresol transformation at 340 ºC and 4 MPa over supported MoO_x.

In turn, a kinetic modeling was performed in order to better evaluate the effect of supporting molybdenum on different solids. Such model was already used to determine the

kinetic values involved in the HDO of cresol isomers over sulfide catalysts [37]. The kinetic values determined (k_{DDO}, k_{HYD} and k'_{HYD}) are given in Table 4-3. For catalysts studied, k_{DDO} values (ranged from 3.4 to 6.1 mmol h^{-1} g^{-1}) were higher than k_{HYD} values (between 0.7 and 1.0 mmol h^{-1} g^{-1}), which is in accordance with the high selectivity to aromatics measured. In the model used, the hydrogenation of toluene into methylcyclohexane was not considered since the selectivity into toluene was independent of the conversion of m-cresol, irrespective to the catalyst as shown in Figure 4-12. This assumption was confirmed with an additional experiment using toluene as reactant which showed that this aromatic was unreactive under our experimental conditions over MoO_x catalysts.

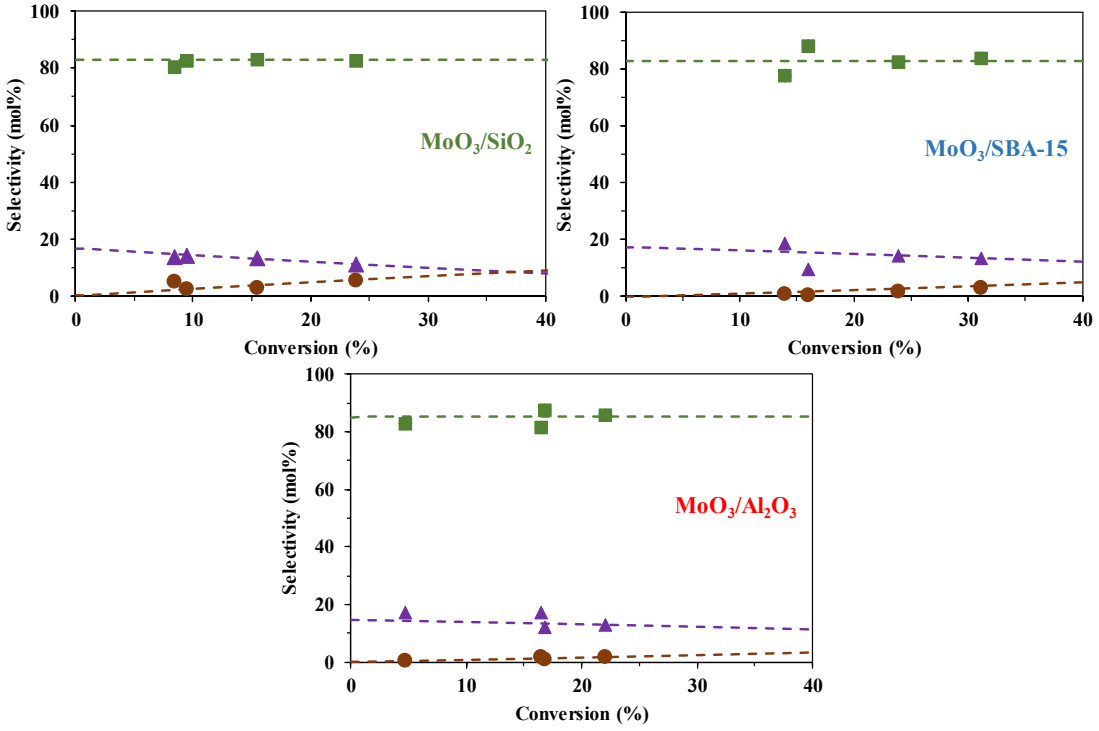

Figure 4-12 : Selectivity as function of m-cresol conversion. Experimental data obtained at 4 MPa and 340 ºC using MoO_x/SiO_2; MoO_x/SBA-15; MoO_x/Al_2O_3. Toluene (■); methylcyclohexenes (▲); methylcyclohexane (●). Calculated data (---).

The product distribution obtained experimentally from the HDO of m-cresol over supported molybdenum oxides as well as the calculated data are presented in Figure 4-12, which displays a good data fitting for all catalysts. Regardless of the catalyst used, toluene and methylcyclohexenes were found as primary products, whereas methylcyclohexane appeared as a secondary product, accordingly the reaction scheme proposed (Scheme 4-1). According to values reported in Table 4-3, k_{HDO}, k_{DDO} and k_{HYD} followed the same order: MoO_x/Al_2O_3 > MoO_x/SBA-15 > MoO_x/SiO_2. This might suggest that active sites in both deoxygenation routes could be similar in nature. However, the order of k'_{HYD} values, which measure the hydrogenation capability of alkenes, followed the inverse order: MoO_x/SiO_2 > MoO_xSBA-15 > MoO_x/Al_2O_3. This fact seems to indicate that active sites responsible for the hydrogenation of aromatic ring could be different in nature than those involved for the hydrogenation of alkenes.

An interesting difference in behavior between oxide and sulfide molybdenum phase is highlighted by the comparison between the rate constant values reported in Table 4-3. Indeed, the MoS_2 phase favors hydrogenation reactions in a large extend (compare k_{HYD} and k'_{HYD} values for both catalysts supported on alumina), whereas the rate of the C-O bond scission (k_{DDO}) determined on MoO_x/Al_2O_3 was about twice higher than the one measured over MoS_2/Al_2O_3. Such different results obtained over molybdenum sulfide catalysts compared to oxide shows an opposite trend which is in accordance to lower selectivity in aromatics measured over MoS_2/Al_2O_3. These results are in line with the assumption that the active sites on both phases may be different.

3.3. Proposals on the nature of active sites and on the reaction mechanism

Although the specific nature of the HDO active sites present in molybdenum oxide phase needs further clarification, it can be proposed that oxygen vacancies involving reduced Mo species (Mo^{5+} and Mo^{4+}) have a main role in deoxygenation reactions [9,13,14]. It was recently proposed that oxycarbide phase ($MoO_xC_yH_z$) could also participate as active site in HDO [13,14]. In our case, such species were only detected over the MoO_x/SiO_2 spent catalyst

(Fig. S7, Supplementary Information). As this catalyst exhibited the lowest activity, the involvement of such species as HDO active sites remains uncertain.

The formation of such site was estimated by DFT method using a Mo_3O_9 cluster model of the MoO_3 surface [9,42]. For example, it was proposed that the first step to create such vacancy is the adsorption of H_2, followed by a proton transfer and finally the release of water, the overall process being endothermic (about 90 kJ mol^{-1}) [9]. The beneficial role of H_2 was confirmed experimentally for HDO of 2-hexanone over MoO_3. Indeed, an increase of the partial pressure of H_2 resulted in better activity and stability of the catalyst, demonstrating that H_2 atmosphere allow to favor the creation of oxygen vacancies. According to the proposal of vacancies being the HDO active sites, it is hence necessary to remove an atom oxygen bonded to molybdenum. Therefore, it is expected that an easier reduction of Mo species provides a more available number of active sites due to an easier O-removal from the surface. From H_2-TPR and chemisorption experiments (Figure 4-7 and Table 4-2), it seems that the formation of such sites on molybdenum oxides is the most favored when Al_2O_3 is used as support and less favored when SiO_2 is the support. These proposals are in line with the experimental order of activity determined for the HDO of m-cresol: MoO_x/Al_2O_3 > MoO_x/SBA-15 > MoO_x/SiO_2 (Figure 4-11). Nevertheless, the turnover frequency values (TOF; Eq. (6)) of all catalysts were close to 20 h^{-1} (Table 4-3), which indicates that all catalysts displayed similar intrinsic activities per site and hence suggests that the active sites involved in HDO of phenolic compounds are very similar in nature irrespective to the support used.

In addition, the fact that MoO_x/SBA-15 was more active than MoO_x/SiO_2 could be attributed to a better dispersion of molybdenum oxides on SBA-15 than on SiO_2, as observed in TEM images (Figure 4-4 to 4-6), and supported by the highest O_2 uptake determined for MoO_x/SBA-15 compared to MoO_x/SiO_2 (Table 4-2). These differences between both catalysts could be related to their textural properties, including a specific surface area about twice higher for MoO_x/SBA-15 compared to MoO_x/SiO_2 (Table 4-1).

Scheme 4-2 presents a mechanism proposal concerning the formation of toluene (DDO product) from m-cresol, which is the main product obtained over molybdenum oxides catalysts

(Table 4-2). As proposed by several authors [9,35,43], Mo species can be present on the surface of MoO_x based catalysts. These species can react with H_2 and allow the creation of a vacancy after the release of H_2O, in accordance with proposals made by Prasomsri et al. [9]. The oxygenated reactant could be adsorbed through its oxygen atom on the oxygen vacancy to favor the cleavage of the C-O bond. The next step is the activation of H_2, which could occur by heterolytic dissociation. The addition of a hydride species on the carbon bearing the OH group could lead to the C-O bond scission and hence the formation of toluene. The vacancy is afterwards recovered by release of water.

The formation of HYD products (methylcyclohexenes and methylcyclohexane) firstly requires the total hydrogenation of the aromatic ring, probably involving a flat adsorption of m-cresol through its aromatic ring. In this case, the involvement of at least two neighboring vacancies could be proposed as active site. Such site seems unlikely over molybdenum oxides phase explaining the low quantity of HYD products compared to the DDO product, irrespective to the catalyst.

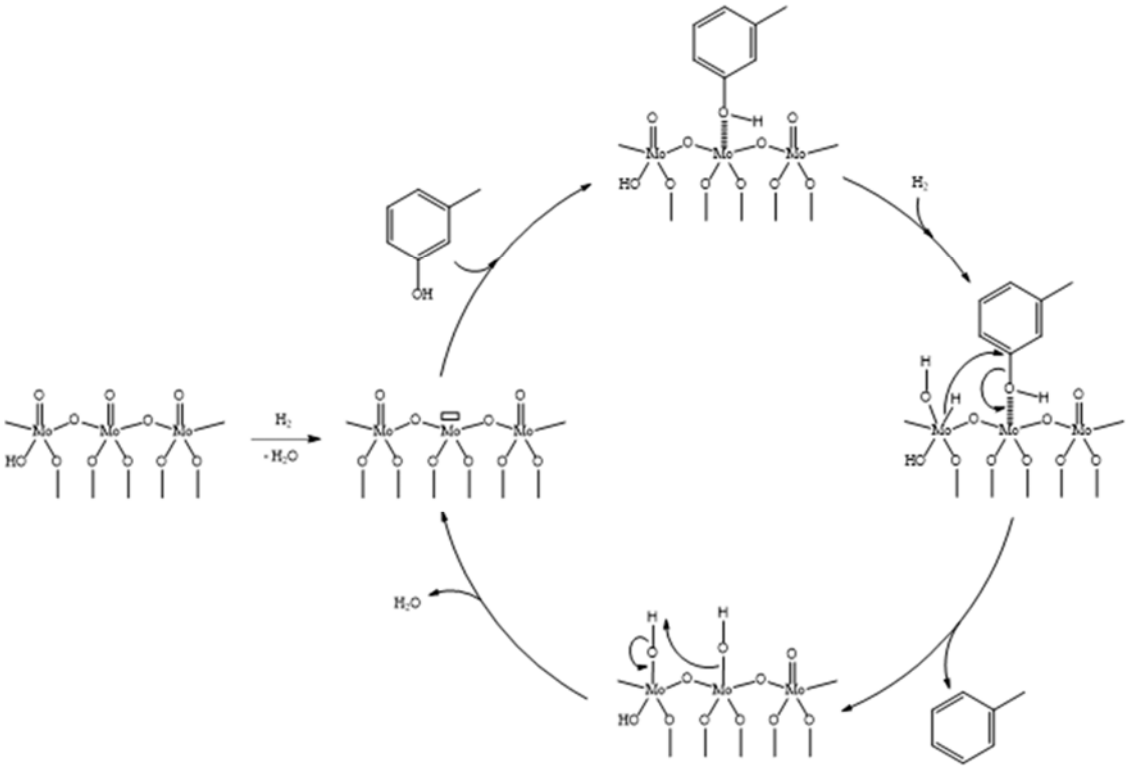

Scheme 4-2 : Mechanism of the direct deoxygenation (DDO) route of m-cresol on a schematic molybdenum oxide site species.

The HYD products being the main observed products on the sulfide phase might be explained by an easier creation of multiple sulfur vacancies compared to the creation of oxygen vacancies on molybdenum, leading to higher activity in hydrogenation. Nevertheless, compared to a sulfur vacancy, an oxygen vacancy could lead to a stronger molybdenum site for the DDO route, acting as Lewis acid site, favoring the C-O bond scission, which explains the high selectivity to aromatic of the oxide molybdenum phase compared to the sulfide phase.

4. Conclusion

The present study showed that supported molybdenum oxides are promising HDO catalysts to produce selectively aromatics from phenolic compounds, with a high degree of

deoxygenation. Regardless of the catalyst used, the selectivity into toluene from m-cresol was always higher than 80 mol%.

An influence of the nature of support was highlighted: the order of HDO activity being MoO_x/Al_2O_3 > MoO_x/SBA-15 > MoO_x/SiO_2. The effect of the support could be attributed to the difference in the reducibility of Mo(VI) species observed by H_2-TPR. Compared to a commercial silica, the reducibility of molybdenum oxides was improved either by the use of an acidic support (Al_2O_3), or by the use of a mesoporous nanoparticles support (SBA-15). These differences in behavior were related to the particle size of molybdenum oxide, being smaller and more reducible on alumina. Consequently, the number of active sites present on the oxide phase, measured by O_2 chemisorption, was a function of the support used: it was the highest on MoO_x/Al_2O_3 and the lowest on MoO_x/SiO_2. In addition, it can be assumed that in the case of existence of active sites affected by the support (i.e. monomeric site), these are probably exhibiting a weak activity with no significant contribution to the global activity as demonstrated by the constant TOF values obtained whatever the support.

It can be assumed that the nature of active sites was not affected by the support, the TOF values being independent on the type of catalyst. In addition, as all catalysts exhibited a remarkable stability under the experimental conditions used, the use of a high pressure of hydrogen (3.2 MPa) allowed to preserve these active sites.

Based on results presented in this study, in order to improve activity, further evolution of the catalyst consists in the control of the support functional and textural properties in order to adjust acidic site density, nature and strength while maintaining open porosity for efficient diffusion of reactants and products.

5. References

[1] A. Corma, S. Iborra, A. Velty, Chem. Rev. 107 (2007) 2411–2502.

[2] T.P. Vispute, H. Zhang, A. Sanna, R. Xiao, G.W. Huber, Science 330 (2010) 1222–1227.

[3] M. Hara, K. Nakajima, K. Kamata, Sci. Technol. Adv. Mater. (2016).

[4] J. van Haveren, E.L. Scott, J. Sanders, Biofuels Bioprod. Biorefining 2 (2008) 41–57.

[5] C. Marcilly, Acido-Basic Catalysis: Application to Refining and Petrochemistry, TECHNIP OPHRYS EDITIONS, 2006.

[6] F. Cherubini, Energy Convers. Manag. 51 (2010) 1412–1421.

[7] Z. He, X. Wang, Catal. Sustain. Energy 1 (2012) 28–52.

[8] K. Jacobson, K.C. Maheria, A.K. Dalai, Renew. Sustain. Energy Rev. 23 (2013) 91–106.

[9] T. Prasomsri, T. Nimmanwudipong, Y. Román-Leshkov, Energy Environ. Sci. 6 (2013) 1732–1738.

[10] E. Furimsky, Appl. Catal. Gen. 199 (2000) 147–190.

[11] E.-M. Ryymin, M.L. Honkela, T.-R. Viljava, A.O.I. Krause, Appl. Catal. Gen. 358 (2009) 42–48.

[12] S. Brillouet, E. Baltag, S. Brunet, F. Richard, Appl. Catal. B Environ. 148–149 (2014) 201–211.

[13] T. Prasomsri, M. Shetty, K. Murugappan, Y. Román-Leshkov, Energy Environ. Sci. 7 (2014) 2660–2669.

[14] M. Shetty, K. Murugappan, T. Prasomsri, W.H. Green, Y. Román-Leshkov, J. Catal. 331 (2015) 86–97.

[15] S. Boullosa-Eiras, R. Lødeng, H. Bergem, M. Stöcker, L. Hannevold, E.A. Blekkan, Catal. Today 223 (2014) 44–53.

[16] M.W. Nolte, J. Zhang, B.H. Shanks, Green Chem. 18 (2016) 134–138.

[17] G. Zhou, P.A. Jensen, D.M. Le, N.O. Knudsen, A.D. Jensen, ACS Sustain. Chem. Eng. (2016).

[18] S. Boullosa-Eiras, R. Lødeng, H. Bergem, M. Stöcker, L. Hannevold, E.A. Blekkan, Catal. Today 223 (2014) 44–53.

[19] D. Zhao, J. Feng, Q. Huo, N. Melosh, G.H. Fredrickson, B.F. Chmelka, G.D. Stucky, Science 279 (1998) 548–552.

[20] C. Ciotonea, B. Dragoi, A. Ungureanu, A. Chirieac, S. Petit, S. Royer, E. Dumitriu, Chem. Commun. 49 (2013) 7665–7667.

[21] V. Sydorchuk, S. Khalameida, V. Zazhigalov, J. Skubiszewska-Zięba, R. Leboda, K. Wieczorek-Ciurowa, Appl. Surf. Sci. 257 (2010) 446–450.

[22] N. Bejenaru, C. Lancelot, P. Blanchard, C. Lamonier, L. Rouleau, E. Payen, F. Dumeignil, S. Royer, Chem. Mater. 21 (2009) 522–533.

[23] B. Dragoi, A. Ungureanu, A. Chirieac, V. Hulea, S. Royer, E. Dumitriu, Catal. Sci. Technol. 3 (2013) 2319–2329.

[24] A. Ungureanu, B. Dragoi, A. Chirieac, C. Ciotonea, S. Royer, D. Duprez, A. Mamede, E. Dumitriu, ACS Appl. Mater. Interfaces 5 (2013) 3010–3025.

[25] R.H.R. Castro, D.V. Quach, J. Phys. Chem. C 116 (2012) 24726–24733.

[26] B.M.Q. Phan, Q.L.M. Ha, N.P. Le, P.T. Ngo, T.H. Nguyen, T.T. Dang, L.H. Nguyen, D.A. Nguyen, L.C. Luu, Catal. Lett. 145 (2015) 662–667.

[27] F.E. Massoth, in:, H.P. and P.B.W. D.D. Eley (Ed.), Adv. Catal., Academic Press, 1979, pp. 265–310.

[28] J.R. Regalbuto, J.-W. Ha, Catal. Lett. 29 (1994) 189–207.

[29] S. Rajagopal, H.J. Marini, J.A. Marzari, R. Miranda, J. Catal. 147 (1994) 417–428.

[30] M.L. Shozi, V.D.B.C. Dasireddy, S. Singh, P. Mohlala, D.J. Morgan, H.B. Friedrich, ACS Sustain. Chem. Eng. 4 (2016) 5752–5760.

[31] T. Kitano, S. Okazaki, T. Shishido, K. Teramura, T. Tanaka, J. Mol. Catal. Chem. 371 (2013) 21–28.

[32] R. Radhakrishnan, C. Reed, S.T. Oyama, M. Seman, J.N. Kondo, K. Domen, Y. Ohminami, K. Asakura, J. Phys. Chem. B 105 (2001) 8519–8530.

[33] E.L. Lee, I.E. Wachs, J. Phys. Chem. C 111 (2007) 14410–14425.

[34] A. Christodoulakis, E. Heracleous, A.A. Lemonidou, S. Boghosian, J. Catal. 242 (2006) 16–25.

[35] G. Tsilomelekis, S. Boghosian, Catal. Sci. Technol. 3 (2013) 1869–1888.

[36] V.O.O. Gonçalves, P.M. de Souza, V.T. da Silva, F.B. Noronha, F. Richard, Appl. Catal. B Environ. 205 (2017) 357–367.

[37] V.O.O. Gonçalves, S. Brunet, F. Richard, Catal. Lett. 146 (2016) 1562–1573.

[38] E. Furimsky, Catal. Today 217 (2013) 13–56.

[39] A. Gutierrez, R. Kaila, M. Honkela, R. Slioor, A. Krause, Catal. Today 147 (2009) 239–246.

[40] C.A. Teles, R.C. Rabelo-Neto, J.R. de Lima, L.V. Mattos, D.E. Resasco, F.B. Noronha, Catal. Lett. 146 (2016) 1848–1857.

[41] M. Peereboom, B. Van de Graaf, J.M.A. Baas, Recl. Trav. Chim. Pays-Bas 101 (1982) 336–338.

[42] D.R. Moberg, T.J. Thibodeau, F.G. Amar, B.G. Frederick, J. Phys. Chem. C 114 (2010) 13782–13795.

[43] A. Christodoulakis, S. Boghosian, J. Catal. 260 (2008) 178–187.

Chapitre 5 :

Kinetics of the hydrodeoxygenation of cresol isomers over Ni_2P/SiO_2: Proposals of nature of deoxygenation active sites based on an experimental study

Chapitre 5 : Kinetics of the hydrodeoxygenation of cresol isomers over Ni_2P/SiO_2: Proposals of nature of deoxygenation active sites based on an experimental study

1. Introduction

The use of lignocellulosic biomass as a renewable and sustainable source of energy is of growing importance due to the increasing attention on environmental concerns. Such raw materials could be transformed into chemicals and biofuels in a biorefinery [1–4]. The first step required is its depolymerization which can be carried out by several processes, including fast pyrolysis [3,5,6]. The bio-oil produced by fast pyrolysis has to be upgraded by hydrodeoxygenation (HDO) in order to reduce its oxygen content, leading to an oil with better physical and chemical properties such as higher heating values, lower viscosity, stability, pH values, and combustion properties compared to the crude bio-oil [7–11].

The type of catalyst play a key role on the HDO process. Conventional metal sulfides were extensively studied in such reactions due to their great importance in sulfur removal in oil processing [6,12–14]. Despite of their high activity in deoxygenation, sulfided catalysts have a drawback to process bio-oil since a sulfiding agent must be added to the reactant feed to keep the solid active and stable during the reaction, which could produce undesirable S-containing compounds in the final products [15–17]. Noble metal catalysts could be used as HDO catalyst due to their high activity in oxygen removal. [18–22]. Meanwhile, as they are highly expensive, their use for this purpose may be limited. Alternatively, the non-noble metal (e.g. Ni-based catalysts) are less costly than noble metal catalysts and also show acceptable deoxygenation performance [23–26]. However, Ni-based catalysts are known to promote secondary reactions like hydrogenolysis of C–C bond, methanation and decarbonylation, which results in a loss of carbon and a higher consumption of hydrogen. Transition metal phosphides have been proposed as catalysts for HDO of bio-oil [27–30]. The advantages of transition metal phosphides compared to other catalysts used in HDO are low cost when compared with noble metal catalysts, and the low selectivity for other reactions than deoxygenation with respect to non-noble metal catalysts [31–33].

Recent studies on deoxygenation of various phenolic model compounds such as phenol [34–36], guaiacol [37–41] and p-cresol [42,43] have shown that nickel phosphide based

catalysts are effective catalysts in HDO. Zhao et al. [37] investigated the HDO of guaiacol under atmospheric pressure and 300 ºC and found Ni_2P/SiO_2 to be more active to deoxygenation than a metallic phase (Pd/Al_2O_3) and a sulfide phase ($CoMo/Al_2O_3$). In addition, the same authors reported the HDO activity for different phosphide phases followed the order: Ni_2P/SiO_2 > Co_2P/SiO_2 > Fe_2P/SiO_2 > WP/SiO_2 > MoP/SiO_2. Indeed, nickel phosphide appeared as the most promising phosphide phase for HDO of various model oxygenated compounds [32,36,37,44,45], attributed to a higher d-electron density of the Ni_2P phase compared to other phosphide phases [45] but also to the presence of phosphorous that provides "ligand" (or electronic) and "ensemble" (or geometrical) effects on metal sites [39,45,46]. In fact, the ligand effect of P increases the electrophilicity of metal sites favoring the adsorption of oxygenated model compound, facilitating the C-O bond scission [31,45]. In general, catalytic behavior of different transition metal phosphides are interpreted in terms of the electron property of metal site, solid acidity or a combination of both [47]. Another interesting fact is the greater stability of phosphides compared to their parent metals. Indeed, during the HDO of anisole (1.5 MPa and 300 ºC), Li et al. [45] assigned the higher stability of Ni_2P/SiO_2 compared to Ni/SiO_2 to the ligand effect given by P species, which would inhibit the combination of Ni with O and makes nickel phosphide catalyst more stable.

There are different reaction routes proposed for the HDO of phenol and alkylated phenols: direct deoxygenation (DDO) route; hydrogenation followed by dehydration (HYD) and tautomerization. The contribution of each route in the distribution of products is highly dependent on the nature of the active phase, as highlighted in recent reviews [7,10,14]. Over sulfided molybdenum-based catalysts, aromatics were favored over CoMoS phase, whereas the products formed by the HYD route (cycloalkenes and cycloalkanes) were predominated over both MoS_2 and NiMoS phases (under 4-7 MPa, 250-340 °C) [48–51]. Using noble metal based-catalysts (i.e. Pd or Pt) under atmospheric pressure, aromatics appeared as the main deoxygenated products [20,21,52] meanwhile cycloalkanes were the main deoxygenated products under high pressure (10 MPa) [19]. In addition, oxophilic supports like ZrO_2 favored the selectivity to deoxygenated products due to the enhanced hydrogenation of the carbonyl function of the key intermediate suggested to be involved (phenolic tautomer) [20,21,52]. For the phosphide phases, the contribution of each deoxygenated route of phenolic compounds

depended on the nature of the M_xP catalyst (Ni_2P, MoP, Fe_2P,…) and the experimental conditions [34–36,42,43,53]. Regarding the most active phosphide phase (i.e Ni_2P), it was reported that bulk Ni_2P yielded toluene as the main deoxygenated products from p-cresol [42], while methylcyclohexane appeared as the main deoxygenated product using the same reactant and under similar experimental conditions (325-350 °C, 4-4.4 MPa) [43]. Using phenol as model oxygenated molecule, the HYD route was also found to be predominant over different supported Ni_2P catalysts at 220 °C under 4 MPa [36]. Nevertheless, using the same oxygenated substrate, a modification of the selectivity of Ni_2P/SiO_2 was highlighted depending on the preparation method to obtain the phosphide phase [35]. These results show that the parameters which govern the selectivity of the Ni_2P phase are not yet completely known and hence require further investigation.

Therefore, the goal of this work was to investigate the catalytic properties ofNi_2P/SiO_2 catalyst for the hydrodeoxygenation of cresol isomers as model oxygenated compounds under high pressures of hydrogen (between 1.6 and 3.2 MPa) at temperatures between 250 and 340 °C. The different pathways involved during the transformations of such model molecules were carefully considered, in particular by using a kinetic model. The nature of active sites present on the nickel phosphide phase and reaction mechanisms were also discussed.

2. Experimental

2.1. Materials and chemicals

Silica was provided by Sigma-Aldrich. $Ni(NO_3)_2.6H_2O$ (Merck), $(NH_4)_2HPO_4$ (Vetec) and HNO_3 (Merck) were used as precursors during the synthesis of the catalyst. The chemicals used ~~in~~ for the reaction study (o-cresol, p-cresol, m-cresol, n-heptane and n-dodecane) were also purchased from Sigma-Aldrich. All chemicals were used without further purification. H_2 was provided by Air Liquide.

2.2. Catalyst synthesis

Prior to impregnation, silica was calcined under air flow at 800 ºC for 5 h. The support was impregnated by nickel phosphide precursors using incipient wetness impregnation method (IWI), according to the procedure described by Yang et al. [31]. A solution containing the amounts of $(NH_4)_2.HPO_4$ and $Ni(NO_3)_2.6H_2O$ required to obtain a Ni/P molar ratio of 2/1.6 and a nickel loading of 10 wt% was used. After impregnation, the solid sample was calcined under air at 500 ºC for 3 h (2 ºC min^{-1}).

2.3. Catalyst characterization

The chemical composition of the solid sample containing Ni_2P precursors was determined by inductively coupled plasma optical emission spectrometry (ICP-OES) using an SPECTRO ARCOS ICP-OES instrument. For this analysis, the sample was digested with concentrated nitric acid and hydrofluoric acid using microwave heating system.

N_2 adsorption−desorption isotherms were measured on a Micromeritics ASAP 2000 analyzer at -196 ºC. Prior to N_2 adsorption, the solid solid samples containing oxide precursors were degassed overnight under secondary vacuum at 200°C. The specific surface area (S_{BET} in m^2 g^{-1}) was calculated from the adsorption isotherm (P/P_0 between 0.05 and 0.20) using the Brunauer-Emmett-Teller (BET) method. The total pore volume was calculated from the adsorbed volume of nitrogen at P/P_0 equal to 0.99. The mesoporous volume was determined using the t-plot method. The average mesopore-size distribution was calculated from the adsorption isotherm branch using the Barret-Joyner-Halenda (BJH) method.

X-ray diffraction (XRD) pattern of the catalyst was collected between 2θ = 20 and 80° using a PAN-alytical EMPYREAN powder diffractometer using Cu-Kα monochromatized radiation source (Kα = 1.54059 Å). Phase identification was performed by comparison with the ICDS database reference files. The crystallite size (Dc) of Ni_2P particles was estimated by the Scherrer equation (Eq. 1), as already reported [54]:

$$Dc = K\lambda/(\beta \cos\theta) \quad (1)$$

where K is the Scherrer constant (0.9), λ is the wavelength of the X-ray radiation (1.54059 Å), β is the width of the peak at half-maximum (FWHM) and θ is the Bragg angle. Prior to analysis, the nickel phosphide phase was obtained by performing the reduction of the catalyst in situ at 450 ºC (5 ºC min^{-1}) under 4 MPa as total pressure during 2 h using pure hydrogen (4.7 NL h^{-1}). After activation in situ, samples were cooled down under hydrogen until 25 ºC and passivated at this temperature under atmospheric pressure for 3 h by a flow of 5 vol.% O_2 in He (80 ml min^{-1}).

In order to estimate the number of active sites and hence to calculate TOF values, CO chemisorption was performed at 30 ºC. It was assumed that CO-metal ratio was equal to 1, accordingly to Zhao et al. [37]. The solid containing oxide precursors (100 mg) was pretreated at 200 ºC under helium (30 mL min^{-1}) for 30 min and cooled down to 50 ºC. Then, the reduction was carried out in order to obtain the phosphide nickel phase under pure hydrogen (60 mL min^{-1}) at 700 ºC (heating rate 5 ºC min^{-1}), the final temperature was kept for 2 h. A XRD analysis performed after such treatment confirmed the formation of Ni_2P phase. The reactor was cooled down to the adsorption temperature (30 °C) under helium (30 mL min^{-1}). Successive pulses of pure CO (0.25 mL) were injected every 2 min. Results were collected by a gas phase chromatograph equipped with a TCD detector and a Porapak Q column (used to verify the absence of formation of CO_2 from CO) allowing the determination of the CO uptake value.

Temperature programmed reduction (H_2-TPR) was performed in a Micromeritics AutoChem 2910. Prior to reduction, the sample (100 mg) was pretreated under He flow (20 mL min^{-1}) at 200 ºC (heating rate of 10 ºC min^{-1}) for 30 min. Then the catalyst was cooled down to 50 ºC. The reduction measurements started at this temperature using 10% H_2 in Ar (20 mL min^{-1}). The temperature was progressively increased until 1000 ºC (heating rate 5 ºC min^{-1}) and held for 90 min. The hydrogen consumption was estimated using a TCD detector.

In order to determine the acidity of the phosphide phase, NH_3-TPD was carried out using 150 mg of solid samples: the bare SiO_2 and the nickel phosphide catalyst obtained after the

activation procedure (450 ºC under 4 MPa of H_2) and then passivated (details in the XRD analysis description). The samples were pretreated with He (30 mL min^{-1}) at 200 °C for 30 min, and cooled down to 100 ºC. The solids were then exposed to a flow containing 5% NH_3 in He (30 mL min^{-1}) for 30 min. The physisorbed ammonia was purged with He (30 mL min^{-1}) for 1 h. Desorption was measured under a heating of 5 ºC min^{-1} under He to 600 ºC with a plateau at this temperature for 1 h. The measurements of desorbed NH_3 quantities were continuously monitored by a TCD detector.

The nickel phosphide phase was obtained by performing the reduction of the catalyst in situ under 4 MPa of H_2 at 450 ºC for 2 h. After activation in situ, samples were cooled down under hydrogen until 25 ºC and passivated at this temperature under atmospheric pressure for 3 h by a flow of 5 vol.% O_2 in He (80 ml min^{-1}).

2.4. Catalytic experiments

The HDO of cresol (o-, m- and p-cresol) was performed in a fixed-bed reactor (length: 40 cm; inner diameter: 1.26 cm) at 340 °C under 4 MPa. Prior to reaction, the catalyst (pelleted, crushed and sieved to 250–315 μm) were reduced in situ at 450 ºC (5 ºC min^{-1}) under 4 MPa as total pressure for 2 h using pure hydrogen (4.7 NL h^{-1}). The reactor was continuously fed by a liquid model feed prepared to obtain 53 kPa of the oxygenated reactant and 31 kPa of n-heptane used as an internal standard diluted with n-dodecane. The hydrogen to oxygenate molar ratio was kept as 486 NL L^{-1}.

Experiments were performed during 20 h on stream (TOS). Different conversion levels (conversions lower than 25%) were obtained varying the space time (τ in g h mol^{-1}, defined in Eq. 2) every 5 h on stream. For a single experiment, space times were varied by changing the reactant flow.

$$\tau = \frac{w}{F_{CRE}} \quad (2)$$

where w is the weight of catalyst and F_{cresol} the molar flow rate of the oxygenated model compound fed into the reactor. For all experiments, the mass balances were always between 95 and 100%, in accordance with study carried out with the same type of reactant [42]. The absence of internal mass-transfer effect was confirmed by the calculation of the Weisz-Prater criteria (Supplementary Information, Table S5-1) [44,55,56]. In addition, it was verified the absence of external diffusion. Indeed, the conversion of cresols remained constant when a variation of the molar flow rate at the reactor entrance was compensated by a proportional variation of the catalyst weight. Moreover, it was previously verified that n-heptane and n-dodecane were unreactive in presence of Ni_2P/SiO_2.

The reaction products were periodically collected from the condenser (Minichiller-Huber cryostat) and analyzed by a Varian 430 chromatograph equipped with a DB1 capillary column (length: 30 m, inside diameter: 0.320 mm, film thickness: 5 µm) and a flame ionization detector (FID). All products were identified by using a 1200 TQ mass spectrometer coupled with a Varian 3800 chromatograph and by co-injection of commercial compounds.

The reactant conversion (X_{cresol} in %) was calculated according to Eq. (3):

$$X_{CRE} = \frac{C_{CRE,0} - C_{CRE}}{C_{CRE,0}} . 100 \quad (3)$$

$C_{CRE,0}$ being the initial molar concentration of the cresol isomer and C_{CRE} as the molar concentration of the corresponding reactant in the liquid sample collected at the studied space time τ.

The selectivity and the yield of a product i (S_i in mol%) are given by Eqs. (4) and (5), respectively:

$$S_i = \frac{C_i}{C_{CRE,0} - C_{CRE}} . 100 \quad (4)$$

$$Y_i = S_i . X_{CRE}/100 \quad (5)$$

where C_i represents the molar concentration of a product "i" in the liquid sample analyzed.

Assuming the reaction as pseudo-first order, the total apparent rate constant (k_{TOT}, in mmol h^{-1} g^{-1}) and the turnover frequency (TOF, in h^{-1}) values can be calculated using Eqs. (6) and (7), respectively:

$$k_{TOT} = {}^{1}/_{\tau} . \ln(1 - X_{CRE}) \quad (6)$$

$$TOF = k_{TOT} \, / \, M \quad (7)$$

where M is the CO uptake (in mmol g^{-1}) obtained from chemisorption measurement.

2.5. Elemental analysis of spent catalysts

Chemical analysis of carbon and hydrogen were carried out after reaction test by using an elemental analyzer (NA2100 analyzer, CE instruments). The spent catalysts were characterized without chemical treatment.

3. Results and discussion

3.1. Catalyst characterization

From ICP analysis, the catalyst after the reduction procedure contained 9.0 wt% of nickel which corresponds to 11.3 wt% of Ni_2P. Figure 5-1 shows the XRD pattern of the catalyst after the reduction at 450 °C under 4 MPa of hydrogen. A broad peak was observed at $2\Theta \approx 22°$ characteristic of the amorphous silica. All characteristic diffraction peaks of the Ni_2P phase were observed (ICDS 98-064-6102) indicating that the reduction procedure allowed to obtain the desired nickel phosphide phase (Ni_2P). Interestingly, using the same Ni/P ratio, it was observed in the literature that $Ni_{12}P_5$ was favored at reduction temperatures lower than 550 °C when the activation procedure was carried out under atmospheric pressure [57]. It should be mentioned that $Ni_{12}P_5$ phase is known to be less active for HDO than Ni_2P [37]. Consequently,

the activation procedure carried out under 4 MPa of H_2 allowed to decrease significantly the reduction temperature required to achieve the formation of Ni_2P phase, which usually ranged between 600–700 °C, as reported in the literature [29]. In addition, the average crystallite size of Ni_2P calculated by the Scherrer equation was about 12 nm, close to values already reported using a similar loading (7.91%) of the same phosphide phase [58].

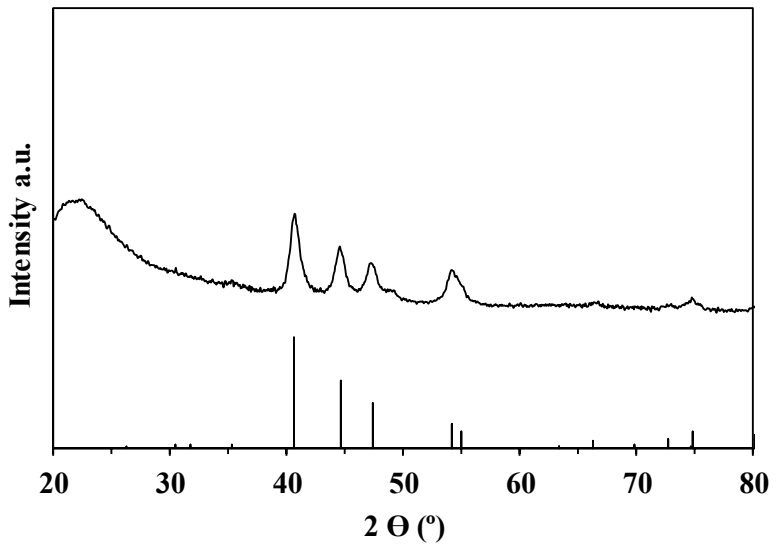

Figure 5-1 : XRD diffraction pattern for Ni_2P/SiO_2 obtained after reduction procedure carried out at 450 °C under 4 MPa of H2 (ICDS 98-064-6102 file appears at the bottom of the figure).

Figure 5-2 displays the adsorption-desorption isotherms of different materials: the bare silica, the silica containing oxide precursors ($Ni_xP_yO_z$) and the silica containing Ni_2P phase obtained after reduction under 4 MPa of H_2 and 450 ºC. According to the IUPAC classification, all isotherms were typical of mesoporous materials (type IV), and exhibited H_2 type hysteresis due to the presence of "ink-bottle" pore [59].

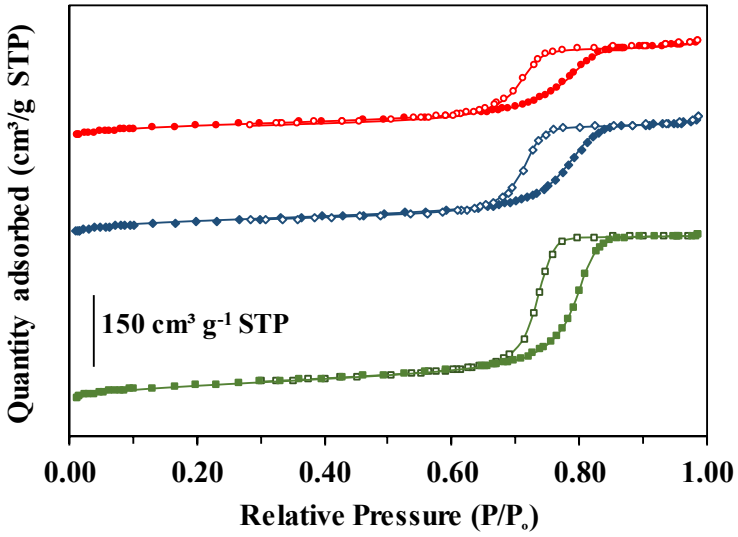

Figure 5-2 : Nitrogen adsorption-desorption isotherms of bare silica (■), silica containing oxide precursors (♦), silica containing Ni_2P phase after reduction at 450 ºC under 4 MPa of H_2 (●). Full symbols for adsorption branch and empty symbols for desorption branch.

As shown in Table 5-1, the impregnation of oxides on silica led to a decrease in the specific surface area (15%) and pore volume (39%). This trend can be mainly explained by introduction of both precursors leading to a partial blockage of the porous system. The reduction step required to obtain the Ni_2P phase had practically no effect on the specific surface area but led to a further decrease in the pore volume (15%) and a small reduction of the pore diameter of silica. These results seem to indicate that the formation of the nickel phosphide phase impact only slightly on the porosity of the support used.

Table 5-1 : Textural properties of pure silica (SiO_2), supported nickel phosphide precursors ($Ni_xP_yO_z/SiO_2$) and supported nickel phosphide (Ni_2P/SiO_2) solids determined by adsorption-desorption of nitrogen.

	S_{BET} ($m^2\ g^{-1}$)	Pore volume[a] ($cm^3\ g^{-1}$)	Mesoporous volume[b] ($cm^3\ g^{-1}$)	Average pore diameter[c] (nm)
SiO_2	208	0.57	0.54	9
$(NiO + P_2O_5)/SiO_2$	176	0.40	0.33	8
Ni_2P/SiO_2	172	0.34	0.27	7

a: calculated at P/P_0 equal to 0.98
b: deduced from the t-plot method
c: deduced from the BJH method using the adsorption branch.

The CO uptake measurement is often used to provide an estimation of the number of active sites presents on nickel phosphide phase [29]. Using FT-IR analysis, it was proposed that CO was bounded to the Ni sites on Ni_2P [60], such sites were probably involved for adsorption of cresol isomers, and will be discussed in the next part of the present manuscript. The value measured in our case (M = 33 μmol g^{-1}) was close to values reported for similar loading of Ni_2P phase [61,62].

Figure 5-3 shows the TPR profile of the oxyphosphate precursors ($Ni_xP_yO_z$) which reveals several peaks in the range of 400-1000 °C. Since this sample was prepared from the mixture of nickel and phosphorus precursors, nickel is likely to be in the form of phosphate ($Ni_xP_yO_z$), as proposed by several authors [40,58]. This may explain why the reduction occurred at higher temperature than observed for nickel oxide samples, usually at lower temperatures than 550 °C [19,26]. As expected, no consumption of H_2 was observed during the analysis of bare SiO_2. The value of H_2 uptake obtained for Ni_2P/SiO_2 was equal to 4.10 mmol g^{-1}, this value is about 16% higher than the theoretical value (equal to 3.45 mmol g^{-1}) calculated to form Ni_2P from the quantity of NiO present on silica (9.0 % of Ni). Thus, the excess of hydrogen consumed (about 0.65 mmol g^{-1}) could correspond to the reduction of P-O bond leading to the formation

of PH_3, centered at 800 °C. In the same way, Oyama and co-workers [63], demonstrated that some phosphorus present in the support can be release in the TPR step as PH_3.

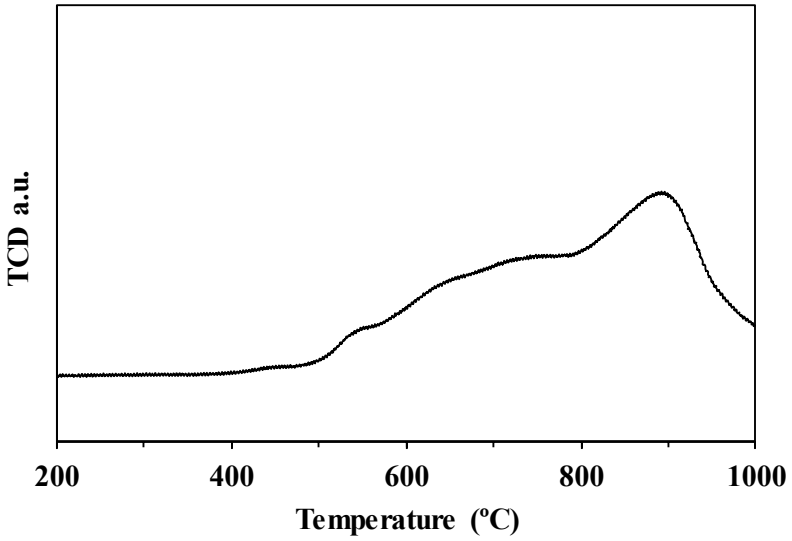

Figure 5-3 : H_2-TPR profile of Ni_2P/SiO_2.

The acid properties of the Ni_2P/SiO_2 catalyst were determined using a NH_3 thermodesorption experiment (NH_3-TPD). Figure 5-4 shows a broad peak centred at around 235-ºC indicating that its acidity (123 µmol/g) is quite weak and only attributed to the phosphide phase since bare SiO_2 did not exhibit any NH_3 adsorption. Similar profile was already reported by Wu et al for the same type of catalyst [40]. In addition, using pyridine as a probe molecule, it was proposed that nickel phosphide phase exhibited both Lewis acid sites (attributed to $Ni^{\delta+}$ species) and Brønsted acid sites (ascribed to PO-H groups) [54,55].

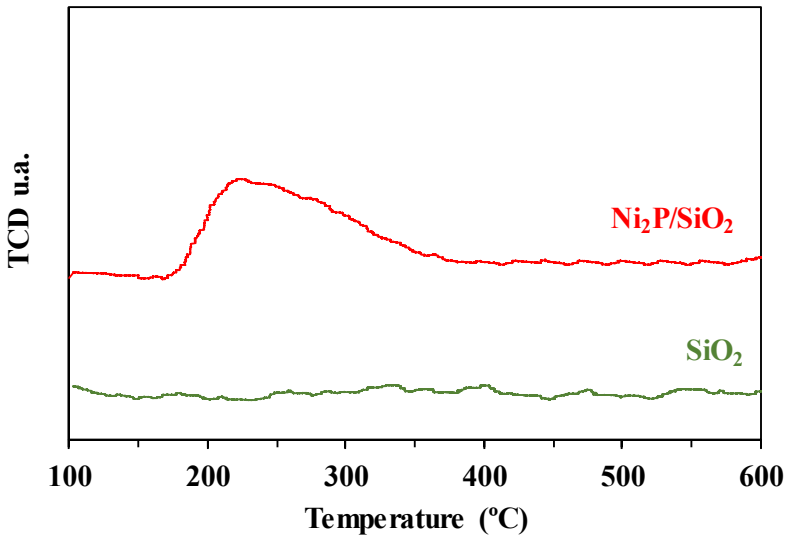

Figure 5-4 : NH_3-TPD profile of Ni_2P/SiO_2 and bare SiO_2.

3.2. Catalytic properties of Ni_2P/SiO_2 during HDO of cresol isomers

The hydrodeoxygenation of cresol isomers was studied at 340 ºC under 4 MPa of total pressure over Ni_2P/SiO_2 during 20 h time on stream. As shown in Figure 5-5, the conversions of m-cresol obtained at the beginning and after 20 h on stream at the same τ (5.0 g h mol^{-1}) were quite similar, which indicates that Ni_2P/SiO_2 was quite stable under these experimental conditions, in spite of amount of carbon measured on this catalyst after reaction (between 6 and 7 wt.%, Table 5-2). As no deactivation was observed, the amount of carbon deposited can be attributed to the presence of adsorbed oxygenated reactants rather than heavy molecules explaining why the catalyst exhibited a good stability. Indeed, the C/H ratios determined on the spent catalysts (close to 11) were of the same order of magnitude than the corresponding ratio calculated for cresol isomers (C_7H_8O, which C/H is equal to 10.5). Therefore, the use of a high pressure of hydrogen (3.2 MPa) prevented the deactivation of the nickel phosphide phase. On the contrary, a strong deactivation rate was observed during HDO of guaiacol carried out under atmospheric pressure over Ni_2P/SiO_2 [38,40]. This deactivation was mainly attributed to coke

accumulation. Li et al. [45] also reported a significant deactivation of Ni_2P/SiO_2 studying the deoxygenation of anisole at 300 °C under mild pressure (1.5 MPa). This result was assigned to a modification of the phosphide phase leading to the formation of inactive phosphate species. Such modification does not occur in our case, confirming the beneficial role of a high pressure of H_2 on the stability of nickel phosphide phase. These results are in accordance with the positive effect of pressure in the pyrolysis bio-oil upgrading steps proposed by Koike et al. [65].

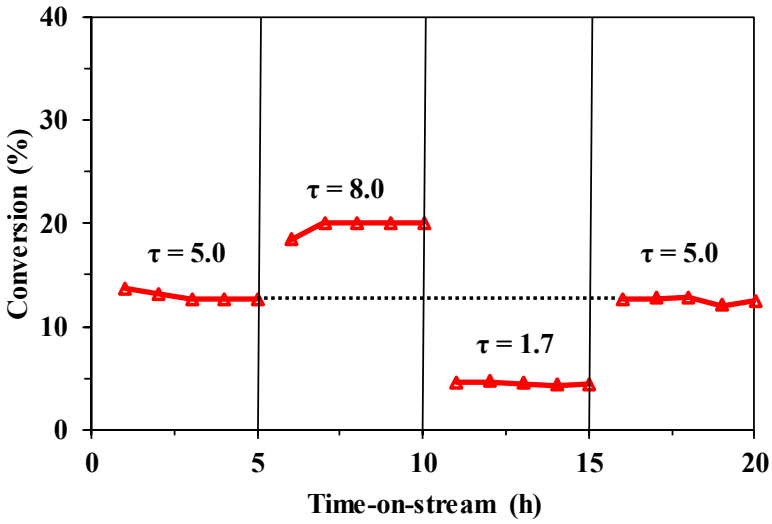

Figure 5-5 : Conversion of m-cresol under 4 MPa and 340 ºC over Ni_2P/SiO_2 as function of time-on-stream (τ in g h mol^{-1}).

Table 5-2 : Chemical composition in carbon and hydrogen of spent catalysts, obtained after 20 h on stream at 340 °C under 4 MPa as total pressure

Model molecule	C (wt%)	H (wt%)	C/H
o-cresol	6.4	0.6	11
m-cresol	6.7	0.6	11
p-cresol	6.0	0.5	12

Various products were detected during the transformation of cresols under 4 MPa at 340 °C: aromatic (toluene), oxygenates (methylcyclohexanol and methylcyclohexanone isomers), alkenes (1-, 3- and 4-methylcyclohexene) and naphthenic (methylcyclohexane and ethylcyclopentane) compounds. Their quantities varied depending on the reactant, the operating conditions and the conversion (Table 5-3 and Figure 5-6). Regardless of the cresol isomer, the selectivity into deoxygenated products was higher than 79% and methylcyclohexane was the main deoxygenated product at about 20% of conversion, its selectivity varying from 56 to 65 mol% (Table 5-3). Figure 5-6 shows that the yield into toluene increased linearly with the conversion of cresol isomers indicating that toluene was unreactive under these experimental conditions. This is in line with the fact that anisole and phenol were converted into either benzene or cyclohexane, the former being favored under atmospheric pressure, whereas the latter was favored at higher pressure (0.8 MPa) [39]. Thus, in this study, the hydrogenation of benzene was never observed. In addition, toluene was favored when m-cresol was used as reactant, its selectivity being close to 20 mol% while only half of this amount was obtained from the other two isomers (Table 5-3).

Table 5-3 : Transformation of cresol isomers at 340 °C under 4 MPa of total pressure over Ni_2P/SiO_2 (conversion close to 20%).

Model molecule	τ (g h mol^{-1})	Conv. (%)	Selectivity (mol%)						1-MCHe/ MCHes
			Tol	MCHnone	MCHols	MCHes	MCH	ECP	
o-cresol	11.0	18.7	8.2	13.6	7.4	14.4	55.7	0.7	65
m-cresol	8.0	20.2	20.6	1.6	0.0	13.8	62.9	1.1	65
p-cresol	9.0	19.4	10.2	4.1	7.1	10.0	64.8	3.8	63

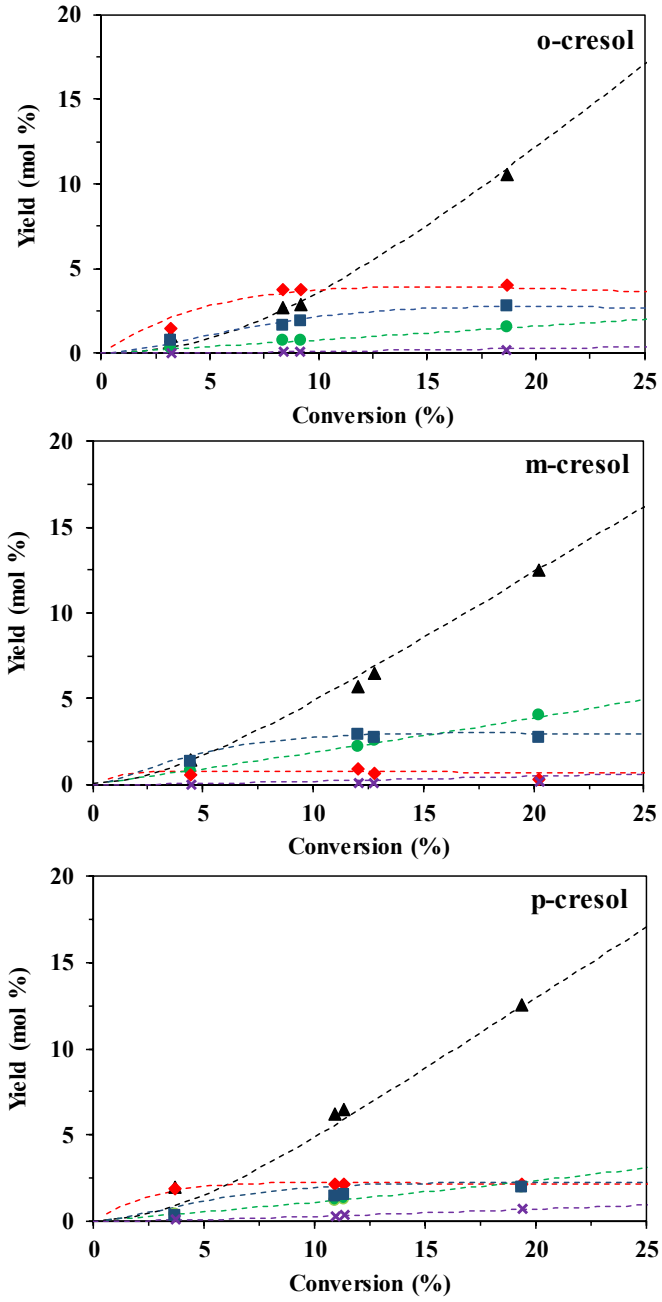

Figure 5-6 : Experimental (symbols) and calculated (lines) yields into products from the transformation of o-cresol (a), m-cresol (b) and p-cresol (c) over Ni_2P/SiO_2 at 4 MPa and 340 ºC; methylcyclohexane (▲); methylcylohexenes (■); oxygenates (◆); toluene (●); ethylcyclopentane (×).

Oxygenates and alkenes appeared as intermediates since their yield reached a maximum and then decreased (Figure 5-6). It can be pointed out that the amount of oxygenates were highly dependent on the reactant. As indicated in Table 5-3, o-cresol led to the highest quantity of oxygenates and m-cresol the lowest, 21.0 and 1.6 mol%, respectively. These results indicate an important effect of the position of the methyl group on the reactivity of these compounds. Indeed, the selectivity into ketone varied according to the followed order: o-cresol > p-cresol > m-cresol. This result demonstrates that the methyl group in ortho position limit the hydrogenation of the ketone function. The selectivity into methylcyclohexene isomers were similar for all cresols, ranging 10–15 mol%. Interestingly, 1-methylcyclohexene was always the main alkene isomer. Based on thermodynamics, the percentage of this isomer is expected to be equal to 65 mol% [66], and very close to the experimental values reported in Table 5-3 (between 63 and 65 mol%). This indicates that the methylcyclohexene isomers were observed in thermodynamic equilibrium. From m-cresol and p-cresol, 1-methylcyclohexene was not expected. Its formation can be explained by the double-bond migration due to the acidity of the phosphide phase. Moreover, ethylcyclopentane was also detected in trace amounts. Its appearance is also linked to the acidic properties of Ni_2P/SiO_2, resulting in an isomerization of methylcyclohexane.

From our experimental results, and accordingly to the literature data obtained from the HDO of cresol isomers on Ni_2P phase [42,43], it can be considered that the formation of those products proceeded via two parallel reaction pathways as described in Scheme 5-1. Toluene was produced by direct cleavage of C-O bond (DDO pathway) whereas the other products were obtained by hydrogenation, hydrogenolysis and dehydration reactions (HYD pathway) leading to naphthenic compounds (methylcyclohexane and ethylcyclopentane) as final products. It is noteworthy to mention that methylcyclohexane can be either produced by hydrogenolysis of methylcyclohexanol (estimated by k_1) or by hydrogenation of methylcyclohexenes isomers, which can be obtained by dehydration the alcohol (estimated by k_2).

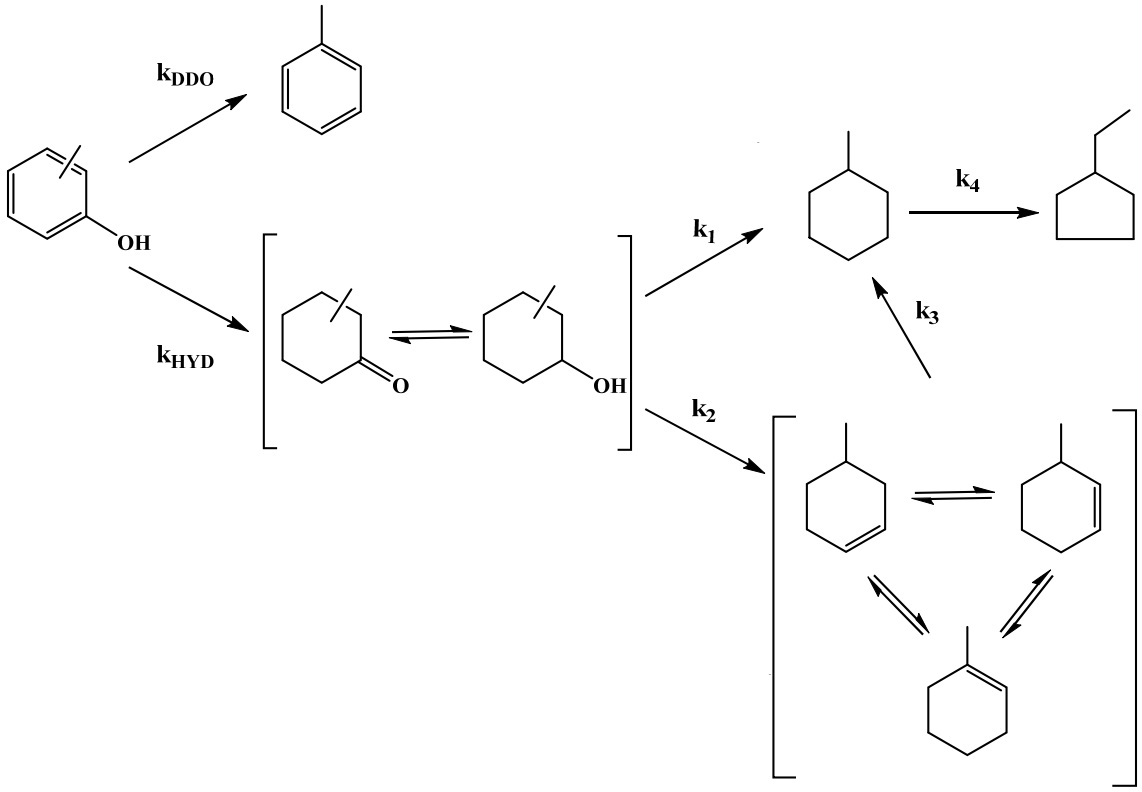

Scheme 5-1 : Reaction scheme for the transformation of cresol isomers over Ni_2P/SiO_2.

In order to obtain more information about the transformation of all cresol isomers, a kinetic analysis was employed using an adequate power law model, similar to the equation already used to model the HDO of cresols over sulfide catalysts [51]. In this case, a proper equation can be written:

$$-r_{Tot} = \frac{dC_{CRE}}{d\tau} = -k\, {C_{CRE}}^{\alpha}\, {P_{H_2}}^{\beta} \qquad (8)$$

where r_{Tot} is the total rate of the transformation of cresols, k is the reaction rate constant, C_{CRE} the molar concentration of a given cresol, P_{H_2} the partial pressure of hydrogen, τ the space time defined previously, α the reaction order in the cresol isomer, and β the reaction order in H_2.

As hydrogen was used in a large excess compared to cresols, the hydrogen partial pressure was assumed to be constant. In addition, according to Figure 5-7, the plot of -ln (1-

X_{CRE}) as function of space times displays a pseudo-first order behavior for the three cresol isomers, as proposed to describe kinetics from the HDO of p-cresol [42]. Consequently, Eq. (8) can be simplified as follows:

$$-r_{Tot} = \frac{dC_{CRE}}{d\tau} = -k_{Tot}\, C_{CRE} \qquad (9)$$

where k_{Tot} is the global apparent constant.

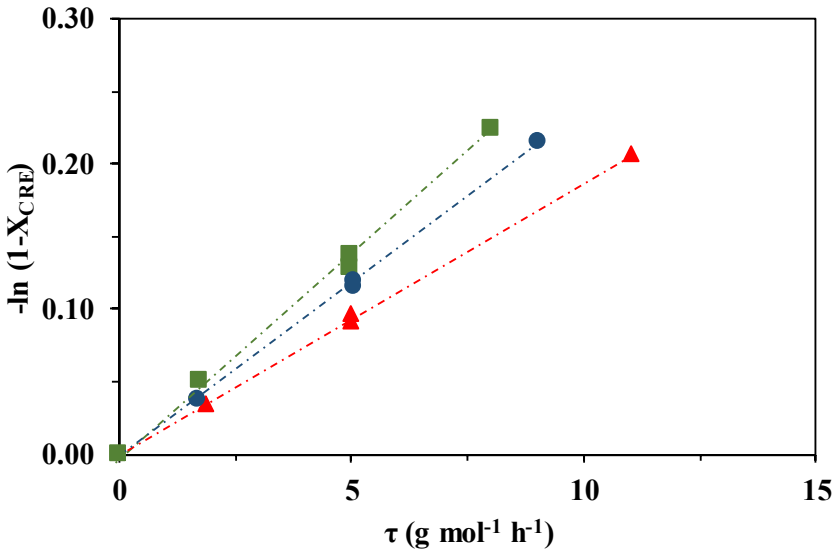

Figure 5-7 : Pseudo-first order plots obtained from the HDO of cresol isomers over Ni_2P/SiO_2 under 4 MPa at 340 ºC; o-cresol (▲), m-cresol (■) and p-cresol (●).

The total kinetic apparent rate constants (k_{Tot}) measured for the three cresol isomers are given in Table 5-4 and followed the order m-cresol > p-cresol > o-cresol, indicating that the reactivity of cresols was dependent on the position of the methyl group. The same reactivity scale was reported over sulfide catalysts under the same experimental conditions (340 °C, 4 MPa) [51]. In addition, it was observed that the total rate constant using o-cresol as reactant (equal to 18.8 mmol g^{-1} h^{-1}) was close to the one determined for a sulfided $CoMo/Al_2O_3$ catalyst (25 mmol g^{-1} h^{-1}, value reported in [51]). Nevertheless, this sulfide phase was about twice as

active as the phosphide phase for the HDO of m-cresol. As expected, the TOF values followed the same order as k_{Tot}, in the range of 570 and 858 h^{-1}. These values were considerably higher than those reported in the literature for several phenolic compounds at 300°C under mild and atmospheric pressures [37,40,45]. As an example, using guaiacol as model reactant, Wu et al. found that the TOF value was 220 h^{-1} under atmospheric conditions using Ni_2P/SiO_2 as catalyst [40]. Due to the mesoporosity of the support (as shown in Table 5-1), it can be assumed that all active sites were accessible to the cresol isomers.

Table 5-4 : Individual apparent rate constants determined during the transformation of cresol isomers at 340 °C under 4 MPa of total pressure over Ni_2P/SiO_2 (standard deviation of rate constants close to 5%).

Model molecule	Rate constants (in mmol h^{-1} g^{-1})							TOF (h^{-1})
	k_{Tot}	k_{DDO}	k_{HYD}	k_1	k_2	k_3	k_4	
o-cresol	18.8 ± 0.9	1.5 ± 0.1	17.3 ± 0.9	345 ± 17	31 ± 2	482 ± 24	23 ± 1	570 ± 29
m-cresol	28.3 ± 1.4	5.8 ± 0.3	22.5 ± 1.1	2254 ± 113	166 ± 8	552 ± 30	39 ± 3	858 ± 43
p-cresol	24.0 ± 1.2	2.5 ± 0.1	21.5 ± 1.1	605 ± 30	318 ± 16	599 ± 28	54 ± 2	727 ± 36

The kinetic modeling based on the proposed reaction network can be performed using an integral method. In this case, following Scheme 5-1, several differential equations related to the transformation of cresols can be written. For a shake of simplicity, the concentrations of oxygenated compounds have been put together and named C_{oxy}.

$$\frac{dC_{CRE}}{d\tau} = -(k_{DDO} + k_{HYD})\, C_{CRE} \quad (10)$$

$$\frac{dC_{Tol}}{d\tau} = k_{DDO}\, C_{CRE} \quad (11)$$

$$\frac{dC_{Oxy}}{d\tau} = k_{HYD}\, C_{CRE} - k_1\, C_{Oxy} - k_2\, C_{Oxy} \quad (12)$$

$$\frac{dC_{MCHes}}{d\tau} = k_2\, C_{Oxy} - k_3\, C_{MCHes} \quad (13)$$

$$\frac{dC_{MCH}}{d\tau} = k_1\, C_{Oxy} + k_3\, C_{MCHes} - k_4\, C_{MCH} \quad (14)$$

$$\frac{dC_{ECP}}{d\tau} = k_4\, C_{MCH} \quad (15)$$

where k_{DDO}, k_{HYD}, k_1, k_2, k_3, k_4 are the intrinsic rate constants involved in the transformation of cresol isomers. C_{Tol}, C_{Oxy}, C_{MCHes}, C_{MCH} and C_{ECP} are the molar concentration of toluene, oxygenates, methylcyclohexenes, methylcyclohexane and ethylcyclopentane, respectively.

The system of equations above (Eqs. (10) to (15)) was solved applying Runge–Kutta 4th order numerical integration algorithm. Data fitting was performed by minimizing the residual sum of squares (RSS, Eq. (16)) between the molar concentration of each product obtained experimentally and the calculated values. The results of modeling for Ni_2P/SiO_2 are presented in Figure 5-6, which shows the yield of each product as function of conversion.

$$RSS = \sum\left(C_{i,exp} - C_{\mathrm{i,cal}}\right)^2 \quad (16)$$

where $C_{i,exp}$ and $C_{i,cal}$ are the experimental and calculated partial pressure of component

The kinetic rates obtained from data fitting, presented in Table 5-4, showed that the reaction proceeds mainly toward the HYD route (k_{HYD}/k_{DDO} between 4 and 12, depending on the cresol isomer). According to the data, it appears that the influence of the position of the methyl group is more important on the DDO route than on the HYD route. Indeed, k_{DDO} measured from m-cresol was more than twice as high as this rate constant for p-cresol, whereas the values of k_{HYD} for both reactants were very close. In addition, o-cresol was the less reactive isomer regardless of the deoxygenation route, which is likely due to a steric hindrance attributed to the methyl group in the vicinity of the OH group. Such steric effect was already described for the HDO reaction of cresols but only over CoMoS catalysts [51,67].

For all reactants, the k_1 values were always higher than k_2, showing that alcohols were mainly deoxygenated by hydrogenolysis of the C-O bond to methylcyclohexane (estimated by

k_1) rather than by dehydration yielding methylcyclohexenes (estimated by k_2). This result can be explained by a weak acidity of the phosphide phase leading to a low rate of the alcohol dehydration. In addition, the order of reactivity of alcohol intermediates was dependent on the type of reaction involved. Thus, the sequence of reactivity followed 3-MCHols > 4-MCHols > 2-MCHols for hydrogenolysis (k_1 values), while the sequence was 4-MCHols > 3-MCHols > 2-MCHols for dehydration (k_2 values). Moreover, the sequence of reactivity determined previously for C-O hydrogenolysis of alcohols isomers (estimated by k_1 values) was the same than the one determined for the direct C-O bond scission of cresols (estimated by k_{DDO}). These results seem to indicate that the effect of the position of the methyl group was the same for both C-O bond scissions, suggesting that active sites involved in both reactions could be similar in nature. In addition, k_1 values were much higher than k_{DDO} values since the C-O bond strength of a phenolic compound is about 80 kJ mol^{-1} greater compared to an aliphatic alcohol [12].

As for the dehydration rate of methylcyclohexanols (k_2), the isomerization of methylcyclohexane into ethylcyclopentane (measured by k_4) is related to the acidic properties of Ni_2P/SiO_2. The k_4 values should not be very dependent on the cresol isomer used. Moreover, as expected, the k_3 rate constants were practically not dependent on the starting cresol, since these values estimated the hydrogenation rate of methylcyclohexenes which were obtained in thermodynamic quantities. However, the mixture of methylcyclohexenes was found in thermodynamic equilibriums which might explain why these values were close for all cresol isomers (Table 5-4).

The influence of temperature was also investigated between 250 ºC and 340 ºC for the conversion of m-cresol under 4 MPa as total pressure (Table 5-5). As expected, an increase of the temperature led to an increase in the activity of Ni_2P/SiO_2 as shown in Figure 5-8. The apparent activation energy (E_a) can be calculated by the Arrhenius equation (Eq. (17)):

$$\ln k_{Tot} = \ln A - \frac{E_a}{R\,T} \qquad (17)$$

where k_{Tot} is the total rate constant at a given reaction temperature, A corresponds to the frequency factor, E_a is the apparent activation energy, R is the universal gas constant, and T is the reaction temperature (K).

Table 5-5 : Effect of temperature and partial pressure of H_2 on the HDO of m-cresol over Ni_2P/SiO_2 (conversion close to 10%).

Entry	Reaction temp. (°C)	H_2 pressure (MPa)	τ (g h mol^{-1})	Conv. (%)	Selectivity (mol%)						1-MCHe /MCHes
					Tol	3-MCHnone	3-MCHols	MCHes	MCH	ECP	
1	250	3.2	90.0	8.9	5.2	13.8	8.4	38.5	33.8	0.3	69
2	300	3.2	15.0	10.0	13.9	11.4	4.3	26.8	42.9	0.7	67
3	340	3.2	5.0	12.8	20.7	5.3	0.0	22.0	51.2	0.8	64
4	340	2.4	6.0	10.8	24.5	22.8	0.0	8.5	43.6	0.6	64
5	340	1.6	7.0	10.5	26.2	25.4	0.0	7.8	40.2	0.4	64

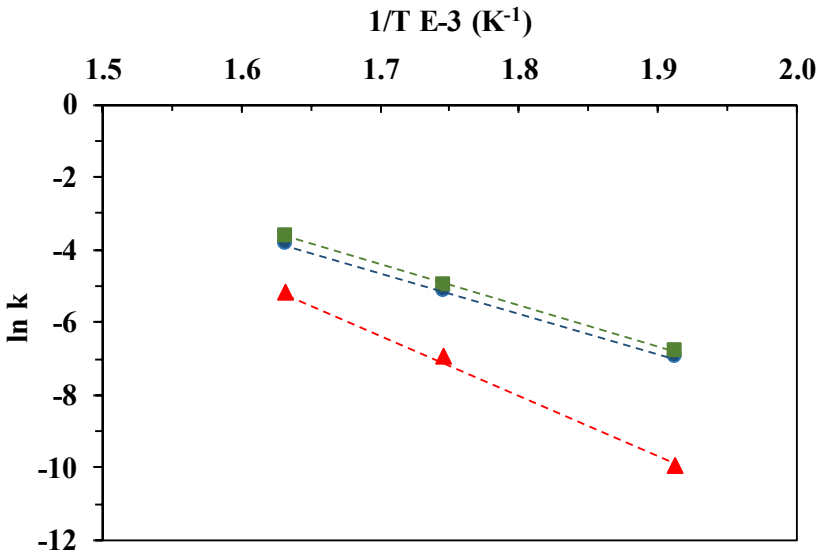

Figure 5-8 : Influence of the temperature on the kinetic rate constants (k_{Tot}: ■; k_{DDO}: ▲ and k_{HYD}: ●) determined during the transformation of m-cresol over Ni_2P/SiO_2. Ln k as function of 1/T.

In order to calculate the apparent activation energy of both deoxygenation routes, $E_{a,HYD}$ and $E_{a,DDO}$, k_{Tot} was replaced by k_{HYD} and k_{DDO} in Eq. (17), respectively. The calculated activation energy for hydrodeoxygenation of m-cresol was 95 kJ mol^{-1}. Regarding the different pathways, the E_a of the HYD pathway was close to the overall reaction (90 kJ mol^{-1}) since it was the main pathway for the transformation of m-cresol. The E_a of the DDO route was higher, close to 138 kJ mol^{-1}. Consequently, an increase of the temperature favors the DDO route over the HYD route, explaining the decrease of the k_{HYD}/k_{DDO} ratio with increasing temperature. Thus, the k_{HYD}/k_{DDO} ratio was equal to 10 at 250 °C and close to 4 at 340 °C. These results seem to confirm that active sites involved in the direct C-O bond scission (DDO route) and in hydrogenation of the aromatic ring (the initial step of the HYD route) could be different in nature. This particular point will be further discussed.

Increasing the temperature decreased the selectivity to 3-MCHnone and 3-MCHols indicating a beneficial effect of the temperature on the deoxygenation degree of m-cresol (see entries 1 to 3 in Table 5-5). As a result, the oxygenated products accounted for approximately 22 mol% of all products at 250 °C and only 5 mol% at 340 °C. The increase of temperature favored the production of toluene; its selectivity increased by almost four-fold between 250 and 340 °C. This increase can be explained both by kinetics (as shown in Figure 5-8), but also by thermodynamics, aromatic being favored compared to naphthenic compounds at higher temperatures [14]. The increase of temperature increased the selectivity to methylcyclohexane whereas the formation of methylcyclohexene decreased. Indeed, the alkane/alkenes ratio was equal to 0.9 at 250 °C and it rose to 2.4 at 340 °C. However, the total amount of methylcyclohexane and methylcyclohexene remained constant for all reaction temperatures. These results suggest that an increase of the temperature favors both the hydrogenolysis of methylcyclohexanols and the hydrogenation of methylcyclohexenes. In addition, as shown in Table 5-5, the slight decrease of the 1-methylcyclohexene/methylcyclohexenes ratio with temperature can be attributed to thermodynamics [66].

The effect of H_2 pressure was also evaluated for the HDO of m-cresol over Ni_2P/SiO_2, the temperature being kept constant at 340 °C. Figure 5-9 shows that an increase of the partial pressure of H_2 resulted in a significant increase of k_{Tot} indicating a benefit for the catalytic

activity of Ni_2P/SiO_2. It is observed that the k_{Tot} value practically doubled when partial pressure of hydrogen increased from 1.6 MPa to 3.2 MPa, the apparent global kinetic order of H_2 being close to 1. It can also be noted that the HYD pathway was promoted by increasing hydrogen pressure, whereas the DDO pathway was only slightly improved. The kinetic partial order of H_2 was dependent on the deoxygenation route: 0.8 for HYD route and 0.5 for DDO route. Therefore, the k_{HYD}/k_{DDO} ratio increased with the pressure of H_2, being 2.8 under 1.6 MPa and close to 4 under 3.2 MPa. These results clearly indicated that an increase in the pressure of H_2 was beneficial for the HDO of phenolic compounds, in agreement with results reported by Moon et al. [39]. Nevertheless, the effect of pressure was dependent on the deoxygenation route involved. The positive effect of hydrogen was higher on the HYD route than on the DDO route. This fact can be easily explained since the HYD route needs a higher quantity of hydrogen to be performed than the DDO route.

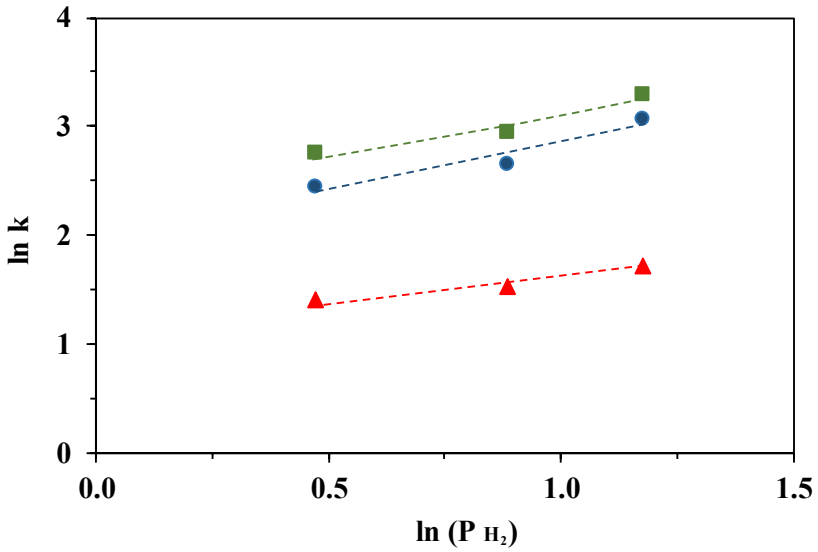

Figure 5-9 : Influence of the pressure of H_2 on the kinetic rate constants (k_{Tot}: ■; k_{DDO}: ▲ and k_{HYD}: ●) determined during the transformation of m-cresol over Ni_2P/SiO_2. Ln k as function of ln (P_{H2}).

The product distribution from the HDO of m-cresol at different H_2 pressure obtained at similar conversion levels are given in Figure 5-8 (entries 3 to 5). It is important to mention that an increase of partial pressure of H_2 decreased the selectivity into oxygenated products, hence favoring the deoxygenation degree of m-cresol. However, the selectivity to toluene decreased from 26.2 mol% to 20.7 mol% when the partial pressure of H_2 increased from 1.6 MPa to 3.2 MPa. This trend can also be explained by both thermodynamics and kinetics. Indeed, it is known that the thermodynamic equilibrium between cyclohexane and benzene can shift in favor of alkane with an increase of the pressure of H_2 [39]. From kinetics point of view, as k_{HYD} was more affected by pressure than k_{DDO}, toluene (DDO product) must be less favored than deoxygenated products (methylcyclohexenes and methylcyclohexane) obtained by the HYD route, as shown in Figure 5-8. In addition, the selectivity to methylcyclohexane increased only slightly compared to methylcyclohexenes when the partial pressure of H_2 increased. This result may be attributed to the competition between hydrogenolysis and dehydration reactions, the former could be less favored by H_2 than the dehydration of alcohols.

A crystal of Ni_2P presents an orthorhombic structure constituted by two kinds of P atoms, P(1) and P(2), and two types of Ni, Ni(1) and Ni(2) [29,39,68,69]. Ni(1) atoms exhibit a near tetrahedral structure whereas Ni(2) atoms have a square pyramidal structure. Along the (0001) direction of Ni_2P bulk, two stacked structures, Ni_3P and Ni_3P_2 are alternatively placed. The former is composed by Ni(2) and P(1) and the latter by Ni(1) and P(2). Based on DFT studies, it was proposed that the termination of the crystal with Ni_3P_2 was more stable than the Ni_3P [68,70]. However, both surface terminations were observed by photoemission electron microscopy [71].

For the HDS of 4,6-dimethyldibenzothiophene, it was proposed that Ni(1), which has a lower coordination number, was likely to be involved in the DDS route leading to dimethylbiphenyl, while Ni(2) could be responsible of the HYD route yielding methylcyclohexyltoluenes [72,73]. These results indicate that the Ni_3P surface, composed by Ni(2) atoms, could exhibit high hydrogenation properties whereas the Ni_3P_2, composed by Ni(1), allows the direct C-S bond scission. Similarly to HDS, Feitosa et al. proposed that DDO active sites for the HDO of guaiacol involves Ni(1) [74]. According to theoretical calculations

[39,68], it was suggested the existence of an hollow site on the Ni_3P_2 surface involving three Ni(1) neighbor atoms. Such site was proposed as an active site for the DDO route of guaiacol since it allowed a strong adsorption of the OH group by the oxygen atom [39]. Similarly, it was proposed that Ni(1) could act as an adsorption site for 2-methyltetrahydropyran through its oxygen atom [75].

In turn, based on our experimental results, several types of active sites present on the nickel phosphide phase can be considered to explain the reactivity of cresols (Scheme 2). It can then be suggested that the C-O bond scission leading to toluene from the cresol isomers and to methylcyclohexane from methylcyclohexanols took place on the same kind of active site, which could involve the participation of three neighboring Ni(1) on the Ni_3P_2 surface, as already proposed for other oxygenated compounds [39,74,75].

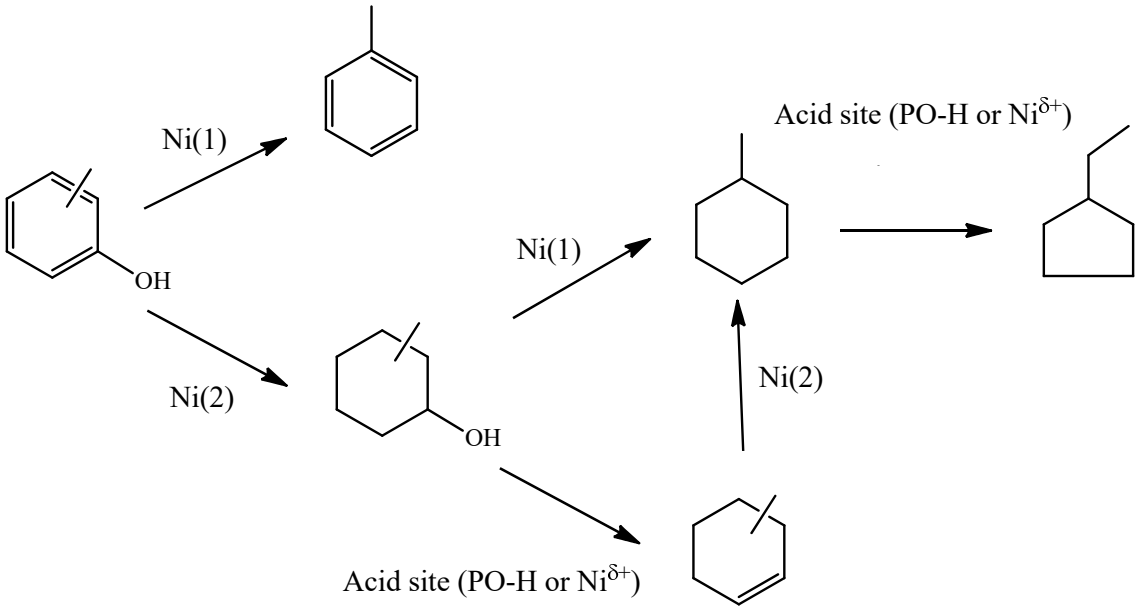

Scheme 5-2 : Proposals of the different active sites likely to occur transformation of cresols over Ni_2P phase.

After the dissociation of H_2 on Ni(1) atoms, the adsorption of cresol through its oxygen atom could take place on a schematic hollow site presented in Scheme 5-3. The C-O bond scission can occur by a nucleophilic attack of a hydride species on the carbon bearing the OH

group, which results in the formation of toluene. The same type of mechanism can be assumed to explain the formation of methylcyclohexane from methylcyclohexanols. As already discussed above, the rates of these reactions are estimated by the values of k_{DDO} and k_1 for the formation of toluene and methylcyclohexane, respectively. The fact that these values were the lowest when o-cresol was used as reactant can be explained by a steric effect due to the presence of methyl group on the α-carbon (Table 5-4). In addition, as m-cresol and the alcohols obtained by hydrogenation of this cresol isomer exhibits the highest reactivity, the presence of the methyl group on the carbon in β position seems to better activate the C-O bond scission compared to the other isomers, which may be related to electronic effects.

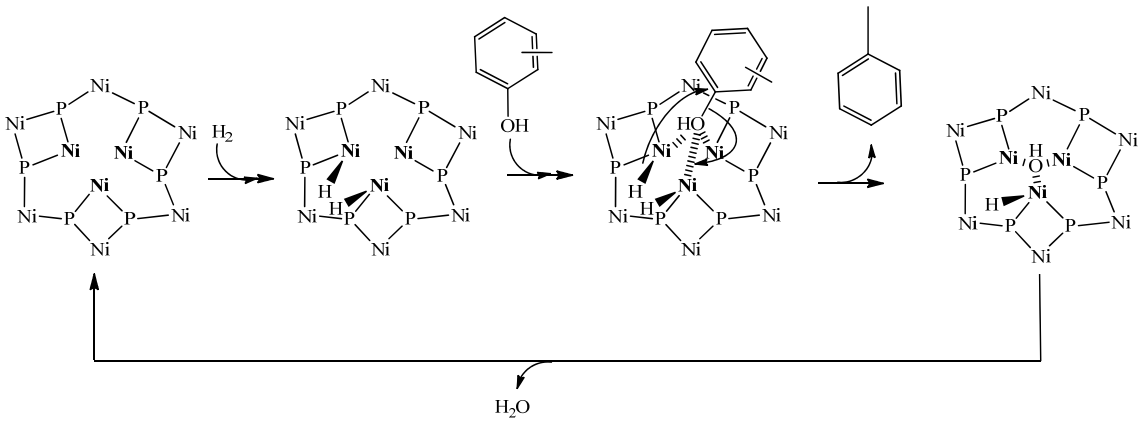

Scheme 5-3 : Proposals for the formation of toluene from cresol on a schematic hollow site composed by three neiboring Ni(1) on the Ni_3P_2 termination (adapted from [69]).

Concerning the HYD route, as proposed recently [72,73], we suggest that the initial steps of this deoxygenation route could be performed on Ni_3P termination, involving Ni(2) species, as indicated in Scheme 5-4. Differently to the DDO route, a flat adsorption through the aromatic ring could be considered in this case. Such adsorption mode may explain why the position of the methyl group has little effect on the k_{HYD} values, as shown in Table 5-4. Indeed, theoretical calculation would be needed to prove this assumption. However, this proposition related to the experimental data seem reasonable. The presence of PO-H sites as Brønsted acid sites on the phosphide phase can explain the presence of products obtained by dehydration (methylcyclohexenes) and isomerization (mixture of alkenes in thermodynamic equilibrium

and ethylcyclopentane) as indicated in Scheme 5-2. Nevertheless, the participation of the Lewis acidity, due to $Ni^{\delta+}$, cannot be ruled out. To confirm such proposals concerning the adsorption modes and reaction mechanisms further investigations are required, especially by using DFT methods.

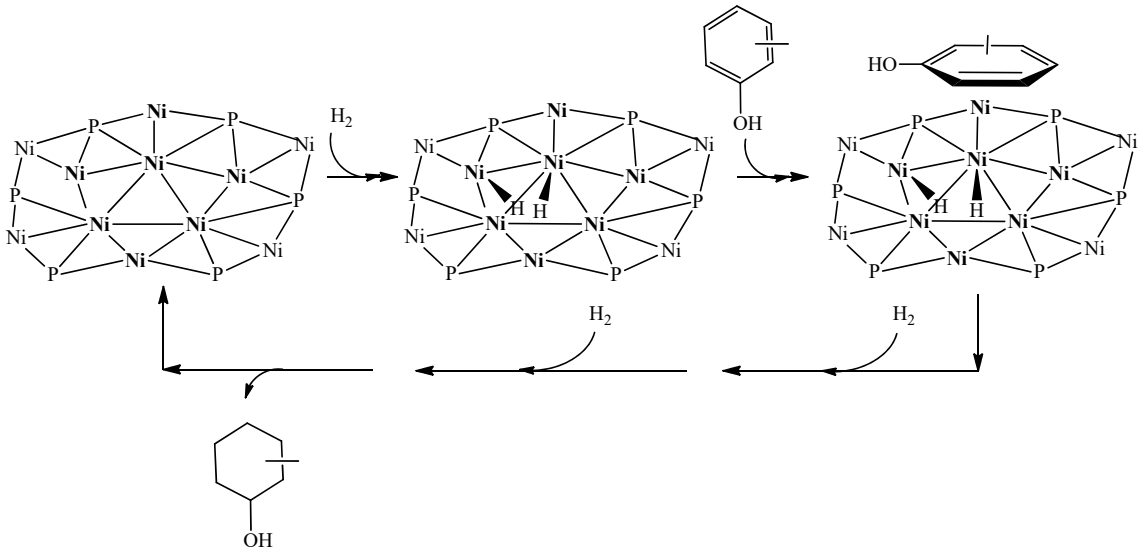

Scheme 5-4 : Proposal mechanism for the formation of methylcyclohexanol from cresol on a schematic Ni_3P termination (adapted from [69]).

4. Conclusion

The present study investigated the HDO of cresols isomers over Ni_2P/SiO_2 catalyst, which involved two parallel deoxygenation routes. Different reactions such as hydrogenolysis, hydrogenation, dehydration and isomerization took place on this catalyst leading to several products. The main pathway (so-called HYD) led to oxygenated (ketones and alcohols) and deoxygenated products (cycloalkenes and cycloalkane), whereas the DDO route yielded only toluene by hydrogenolysis of the C-O bond. The use of a relative high pressure of hydrogen (3.2 MPa) allowed to ensure a remarkable stability of the nickel phosphide phase. An effect of the position of the methyl group was highlighted, depending on the pathway considered. The

reactivity of cresols followed: m-cresol > p-cresol > o-cresol, the DDO route being more affected by the position of the methyl group than the HYD route. This result suggests that active sites involved in both deoxygenation routes could be different. The effect of temperature and hydrogen pressure was also dependent on the deoxygenation route: temperature favored more the DDO route whereas an increase of the hydrogen pressure was more beneficial for the HYD route. Nevertheless, it is important to underline that an increase of both experimental parameters allowed a higher deoxygenation degree of m-cresol (close to 100%), in spite of low conversion rates (lower than 20%).

Based on these experimental results, several kinds of active sites and adsorption modes were proposed to explain the formation of the products observed experimentally. The Ni(1) sites present on the Ni_3P_2 termination seem to be associated to hydrogenolysis reactions which take place in the transformation of cresols into toluene and methylcyclohexanols into methylcyclohexane. These reactions probably need an activation of the C-O bond through the adsorption by the oxygen atom. On the opposite, Ni(2) sites, presents on the Ni_3P termination, are likely to be active for hydrogenation of aromatic ring, probably suggesting a flat adsorption of cresols. In addition, Brønsted acid sites (probably PO-H groups) as well as Lewis acid sites ($Ni^{\delta+}$ species) were involved in dehydration and isomerization reactions.

5. References

[1] G.W. Huber, A. Corma, Angew. Chem. Int. Ed. 46 (2007) 7184–7201.

[2] D.M. Alonso, J.Q. Bond, J.A. Dumesic, Green Chem. 12 (2010) 1493–1513.

[3] J. Zakzeski, P.C.A. Bruijnincx, A.L. Jongerius, B.M. Weckhuysen, Chem. Rev. 110 (2010) 3552–3599.

[4] S.K. Maity, Renew. Sustain. Energy Rev. 43 (2015) 1427–1445.

[5] G.W. Huber, S. Iborra, A. Corma, Chem. Rev. 106 (2006) 4044–4098.

[6] C. Li, X. Zhao, A. Wang, G.W. Huber, T. Zhang, Chem. Rev. 115 (2015) 11559–11624.

[7] E. Furimsky, Catal. Today 217 (2013) 13–56.

[8] N. Arun, R.V. Sharma, A.K. Dalai, Renew. Sustain. Energy Rev. 48 (2015) 240–255.

[9] M. Patel, A. Kumar, Renew. Sustain. Energy Rev. 58 (2016) 1293–1307.

[10] H. Wang, J. Male, Y. Wang, ACS Catal. 3 (2013) 1047–1070.

[11] S. De, B. Saha, R. Luque, Bioresour. Technol. 178 (2015) 108–118.

[12] E. Furimsky, Appl. Catal. Gen. 199 (2000) 147–190.

[13] M. Saidi, F. Samimi, D. Karimipourfard, T. Nimmanwudipong, B.C. Gates, M.R. Rahimpour, Energy Environ. Sci. 7 (2014) 103–129.

[14] D.A. Ruddy, J.A. Schaidle, J.R.F. Iii, J. Wang, L. Moens, J.E. Hensley, Green Chem. 16 (2014) 454–490.

[15] O. Şenol, T.-R. Viljava, A. Krause, Appl. Catal. Gen. 326 (2007) 236–244.

[16] E.-M. Ryymin, M.L. Honkela, T.-R. Viljava, A.O.I. Krause, Appl. Catal. Gen. 358 (2009) 42–48.

[17] S. Brillouet, E. Baltag, S. Brunet, F. Richard, Appl. Catal. B Environ. 148–149 (2014) 201–211.

[18] C. Zhao, Y. Kou, A.A. Lemonidou, X. Li, J.A. Lercher, Angew. Chem. 121 (2009) 4047–4050.

[19] P.M. Mortensen, J.-D. Grunwaldt, P.A. Jensen, A.D. Jensen, ACS Catal. 3 (2013) 1774–1785.

[20] P.M. de Souza, L. Nie, L.E.P. Borges, F.B. Noronha, D.E. Resasco, Catal. Lett. 144 (2014) 2005–2011.

[21] P.M. de Souza, R.C. Rabelo-Neto, L.E.P. Borges, G. Jacobs, B.H. Davis, T. Sooknoi, D.E. Resasco, F.B. Noronha, ACS Catal. 5 (2015) 1318–1329.

[22] M.B. Griffin, G.A. Ferguson, D.A. Ruddy, M.J. Biddy, G.T. Beckham, J.A. Schaidle, ACS Catal. (2016) 2715–2727.

[23] M.V. Bykova, D.Y. Ermakov, V.V. Kaichev, O.A. Bulavchenko, A.A. Saraev, M.Y. Lebedev, V.A. Yakovlev, Appl. Catal. B Environ. 113–114 (2012) 296–307.

[24] I. Rossetti, C. Biffi, C.L. Bianchi, V. Nichele, M. Signoretto, F. Menegazzo, E. Finocchio, G. Ramis, A. Di Michele, Appl. Catal. B Environ. 117–118 (2012) 384–396.

[25] L. Nie, P.M. de Souza, F.B. Noronha, W. An, T. Sooknoi, D.E. Resasco, J. Mol. Catal. Chem. 388–389 (2014) 47–55.

[26] C.A. Teles, R.C. Rabelo-Neto, J.R. de Lima, L.V. Mattos, D.E. Resasco, F.B. Noronha, Catal. Lett. 146 (2016) 1848–1857.

[27] S.T. Oyama, T. Gott, H. Zhao, Y.-K. Lee, Catal. Today 143 (2009) 94–107.

[28] A.-M. Alexander, J.S.J. Hargreaves, Chem. Soc. Rev. 39 (2010) 4388–4401.

[29] R. Prins, M.E. Bussell, Catal. Lett. 142 (2012) 1413–1436.

[30] S. Carenco, D. Portehault, C. Boissière, N. Mézailles, C. Sanchez, Chem. Rev. 113 (2013) 7981–8065.

[31] Y. Yang, J. Chen, H. Shi, Energy Fuels 27 (2013) 3400–3409.

[32] J. Chen, H. Shi, L. Li, K. Li, Appl. Catal. B Environ. 144 (2014) 870–884.

[33] Z. Zhang, M. Tang, J. Chen, Appl. Surf. Sci. 360 (2016) 353–364.

[34] Y. Li, X. Yang, L. Zhu, H. Zhang, B. Chen, RSC Adv. 5 (2015) 80388–80396.

[35] K. Yan, Y. Li, X. Zhang, X. Yang, N. Zhang, J. Zheng, B. Chen, K.J. Smith, Int. J. Hydrog. Energy 40 (2015) 16137–16146.

[36] A. Berenguer, T.M. Sankaranarayanan, G. Gómez, I. Moreno, J.M. Coronado, P. Pizarro, D.P. Serrano, Green Chem. 18 (2016) 1938–1951.

[37] H. Zhao, D. Li, P. Bui, S. Oyama, Appl. Catal. Gen. 391 (2011) 305–310.

[38] S.-K. Wu, P.-C. Lai, Y.-C. Lin, H.-P. Wan, H.-T. Lee, Y.-H. Chang, ACS Sustain. Chem. Eng. 1 (2013) 349–358.

[39] J.-S. Moon, E.-G. Kim, Y.-K. Lee, J. Catal. 311 (2014) 144–152.

[40] S.-K. Wu, P.-C. Lai, Y.-C. Lin, Catal. Lett. 144 (2014) 878–889.

[41] M.B. Griffin, F.G. Baddour, S.E. Habas, D.A. Ruddy, J.A. Schaidle, Top. Catal. 59 (2016) 124–137.

[42] V.M.L. Whiffen, K.J. Smith, Top. Catal. 55 (2012) 981–990.

[43] W. Wang, K. Zhang, H. Liu, Z. Qiao, Y. Yang, K. Ren, Catal. Commun. 41 (2013) 41–46.

[44] A. Infantes-Molina, E. Gralberg, J.A. Cecilia, E. Finocchio, E. Rodríguez-Castellón, Catal. Sci. Technol. 5 (2015) 3403–3415.

[45] K. Li, R. Wang, J. Chen, Energy Fuels 25 (2011) 854–863.

[46] J. Cecilia, A. Infantes-Molina, E. Rodríguez-Castellón, A. Jiménez-López, S. Oyama, Appl. Catal. B Environ. 136 (2013) 140–149.

[47] C. Kordulis, K. Bourikas, M. Gousi, E. Kordouli, A. Lycourghiotis, Appl. Catal. B Environ. 181 (2016) 156–196.

[48] E. Laurent, B. Delmon, Ind. Eng. Chem. Res. 32 (1993) 2516–2524.

[49] O.İ. Şenol, E.-M. Ryymin, T.-R. Viljava, A.O.I. Krause, J. Mol. Catal. Chem. 277 (2007) 107–112.

[50] C. Bouvier, Y. Romero, F. Richard, S. Brunet, Green Chem. 13 (2011) 2441–2451.

[51] V.O.O. Gonçalves, S. Brunet, F. Richard, Catal. Lett. 146 (2016) 1562–1573.

[52] L. Nie, D.E. Resasco, J. Catal. 317 (2014) 22–29.

[53] V.M.L. Whiffen, K.J. Smith, S.K. Straus, Appl. Catal. Gen. 419–420 (2012) 111–125.

[54] S. Oyama, X. Wang, F. Requejo, T. Sato, Y. Yoshimura, J. Catal. 209 (2002) 1–5.

[55] G.F. Froment, K.B. Bischoff, J.D. Wilde, Chemical Reactor Analysis and Design, 3 edition, Wiley, Hoboken, N.J, 2010.

[56] P.M. Mortensen, D. Gardini, H.W.P. de Carvalho, C.D. Damsgaard, J.-D. Grunwaldt, P.A. Jensen, J.B. Wagner, A.D. Jensen, Catal. Sci. Technol. 4 (2014) 3672–3686.

[57] Q. Guan, X. Cheng, R. Li, W. Li, J. Catal. 299 (2013) 1–9.

[58] S.T. Oyama, X. Wang, Y.-K. Lee, K. Bando, F.G. Requejo, J. Catal. 210 (2002) 207–217.

[59] G. Leofanti, M. Padovan, G. Tozzola, B. Venturelli, Catal. Today 41 (1998) 207–219.

[60] Y.-K. Lee, S.T. Oyama, J. Catal. 239 (2006) 376–389.

[61] S.T. Oyama, X. Wang, Y.-K. Lee, W.-J. Chun, J. Catal. 221 (2004) 263–273.

[62] J.A. Cecilia, A. Infantes-Molina, E. Rodríguez-Castellón, A. Jiménez-López, J. Phys. Chem. C 113 (2009) 17032–17044.

[63] A. Iino, A. Cho, A. Takagaki, R. Kikuchi, S.T. Oyama, J. Catal. 311 (2014) 17–27.

[64] D. Li, P. Bui, H.Y. Zhao, S.T. Oyama, T. Dou, Z.H. Shen, J. Catal. 290 (2012) 1–12.

[65] N. Koike, S. Hosokai, A. Takagaki, S. Nishimura, R. Kikuchi, K. Ebitani, Y. Suzuki, S.T. Oyama, J. Catal. 333 (2016) 115–126.

[66] M. Peereboom, B. Van de Graaf, J.M.A. Baas, Recl. Trav. Chim. Pays-Bas 101 (1982) 336–338.

[67] F. Massoth, P. Politzer, M. Concha, J. Murray, J. Jakowski, J. Simons, J. Phys. Chem. B 110 (2006) 14283–14291.

[68] A.E. Nelson, M. Sun, A.S.M. Junaid, J. Catal. 241 (2006) 180–188.

[69] Q. Yuan, H. Ariga, K. Asakura, Top. Catal. 58 (2015) 194–200.

[70] P. Liu, J.A. Rodriguez, T. Asakura, J. Gomes, K. Nakamura, J. Phys. Chem. B 109 (2005) 4575–4583.

[71] S. Suzuki, G.M. Moula, T. Miyamoto, Y. Nakagawa, K. Kinosthita, K. Asakura, S.T. Oyama, S. Otani, J. Nanosci. Nanotechnol. 9 (2009) 195–201.

[72] S.T. Oyama, Y.-K. Lee, J. Catal. 258 (2008) 393–400.

[73] H. Zhao, S.T. Oyama, H.-J. Freund, R. Włodarczyk, M. Sierka, Appl. Catal. B Environ. 164 (2015) 204–216.

[74] L.F. Feitosa, G. Berhault, D. Laurenti, T.E. Davies, V. Teixeira da Silva, J. Catal. 340 (2016) 154–165.

[75] P.P. Bui, S.T. Oyama, A. Takagaki, B.P. Carrow, K. Nozaki, ACS Catal. 6 (2016) 4549–4558.

6. Supplementary Information

Transport Limitations

The Weisz-Prater criteria (C_{wp}) can be calculated to evaluate if internal diffusion can be neglected. In this case, the calculated value of C_{wp} should be lower than 1 [1]. The criteria is given by Eq. S1 according to [2,3]:

$$C_{wp} = \frac{r_{Tot}\,\rho_C R^2}{D_e C_{CRE-S}} \quad \text{(S1)}$$

With:

r_{Tot} as the experimental rate expressed in mol s^{-1} g^{-1} calculated from Eq. 9 of the manuscript;

ρ_C is the catalyst density, equal to 0.62 g. cm^{-3};

R is the particle radius of the catalyst, equal to 0.0315 cm;

De is the effective diffusivity, equal to 0.014 cm^2 s^{-1} according to Infantes-Molina et al. [2];

C_{CRE-S} is the gas concentration of cresol isomer at the catalyst surface expressed in mol cm^{-3} assuming no external diffusion limitation (equal to 1.039 10^{-5} mol cm^{-3});

From the the calculated C_{wp} values, given in Table S5-1, it can be concluded that internal mass transfer effects can be neglected, since all values are much smaller than 1.

Table S5-1 : The calculated Weisz-Prater criterion (C_{wp}) for all experiments.

Model molecule	Temperature (°C)	Total pressure (MPa)	r_{Tot} (mol s^{-1} g^{-1})	C_{wp}
o-cresol	340	4	3.65 E-7	0.0015
m-cresol	340	4	5.50 E-7	0.0023
p-cresol	340	4	4.67 E-7	0.0020
m-cresol	340	2	4.39 E-7	0.0018
m-cresol	340	3	4.88 E-7	0.0021
m-cresol	250	4	2.14 E-8	9 E-5
m-cresol	300	4	1.39 E-7	0.0006

[1] G.F. Froment, K.B. Bischoff, J.D. Wilde, Chemical Reactor Analysis and Design, 3 edition, Wiley, Hoboken, N.J, 2010.

[2] A. Infantes-Molina, E. Gralberg, J. Cecilia, E. Finocchio, E. Rodríguez-Castellón, Catal. Sci. Technol. 5 (2015) 3403–3415.

[3] P.M. Mortensen, D. Gardini, H.W.P. de Carvalho, C.D. Damsgaard, J.-D. Grunwaldt, P.A. Jensen, J.B. Wagner, A.D. Jensen, Catal. Sci. Technol. 4 (2014) 3672–3686.

Chapitre 6 :

Hydrodeoxygenation of m-cresol over nickel and nickel phosphide based catalysts. Influence of the nature of the active phase and the support

Chapitre 6 : Hydrodeoxygenation of m-cresol over nickel and nickel phosphide based catalysts. Influence of the nature of the active phase and the support

1. Introduction

Hydrodeoxygenation (HDO) is an important process to upgrade pyrolysis bio-oil to produce suitable biofuels or blendings to be add into existing fuels [1–4]. Most of the undesired properties of bio-oil (chemical instability, corrosivity, low heating value, high viscosity and immiscibility with petroleum) should be eliminated by oxygen removal by reacting its oxygenated molecules with H_2 using a specific catalyst [5,6].

In the research of an appropriate catalyst for the HDO process, metal sulfides catalysts, conventionally used in petroleum refining (e.g., NiMoS and CoMoS), were the first catalysts tested in such reaction. Although sulfides catalysts are active for HDO with a high selectivity to deoxygenated products [7,8], their main disadvantage is the need for sulfur addition to the feed to maintain the catalytic activity, which can eventually lead to the formation of sulfur compounds [9,10].

Noble metal catalysts also exhibit high activity toward deoxygenation products [11–13], but they are very expensive, which limits their commercial application. The non-noble metal catalysts are more cost effective than noble metal catalysts and show acceptable catalytic performance [14,15]. In particular, Ni-based catalysts have been extensively studied for hydrodeoxygenation of different bio-oil model compounds [14–22]. The improvement of HDO activity for Ni catalysts was observed with the use of oxophilic supports like zirconia [13,14,16,20,21]. For example, Ni/ZrO_2 and Pd/ZrO_2 catalysts were more selective to benzene than Pd/SiO_2 and Ni/SiO_2 for HDO of phenol at 300 °C under atmospheric pressure [13]. Mortensen et al. [14] also reported the best performance for Ni/ZrO_2 among a series of catalysts (Ni/Al_2O_3, Ni/SiO_2, $Ni/MgAl_2O_4$, Ni/CeO_2-ZrO_2, Ni/CeO_2, Ni/C, Ru/C and Pd/C) for the deoxygenation of phenol (275 °C, 10 MPa). In summary, the striking difference in selectivity toward deoxygenated products for these catalysts could be related to the adsorption mode of oxygenated compounds. On Ni/ZrO_2, the HDO activity was facilitated by preferential interaction between Zr cations (oxophilic sites) and oxygen atom of model compound, as confirmed by Foraita et al. [21].

Chapitre 6 : Hydrodeoxygenation of m-cresol over nickel and nickel phosphide based catalysts. Influence of the nature of the active phase and the support

Recently, transition metal phosphides (M_xP_y) have been studied for HDO reactions of different model compounds of bio-oil [23–34]. There are several interesting features in the use of such solids, they are more economical than noble metal catalysts and less susceptible to secondary reactions (hydrogenolysis of C–C bond, methanation and decarbonylation) than non-noble metal catalysts. The high performance of transition metal phosphides has been attributed to the presence of phosphorous that provides "ligand" (or electronic) and "ensemble" (or geometrical) effects on metal sites [29,30]. Overall, phosphide catalysts show bifunctional properties (acid/metal function) and the presence of P species may lead to the formation of P-OH groups, increasing their acidity [31]. Among a series of metal phosphides (Ni_2P, Co_2P, Fe_2P, WP, MoP), Ni_2P revealed superior activity for deoxygenation and higher stability than others catalysts [23–25,28]. Infantes-Molina et al. [28] attributed the best performance of Ni_2P in the hydrodeoxygenation of dibenzofuran to the higher amount of P-OH species on the catalyst, which can prevent the oxidation of Ni_2P phase and also act as H-donors (weak acid sites), hydrogenating C species on surface and reducing coke formation. Therefore, phosphide catalysts can present high stability for HDO reactions. However, water produced in the reaction may lead to catalyst deactivation depending on the type of the phosphide catalyst. Li et al. [23] observed that MoP/SiO_2 was more susceptible to oxidation and less active for HDO of anisole (300 °C, 1.5 MPa) than the Ni_2P/SiO_2 due to higher affinity of Mo with oxygen from water compared to Ni. Recently, our group also reported that Ni_2P/SiO_2 remained quite stable during the HDO of cresols isomers for at least 20 h of reaction using high pressure of H_2 [27]. In the same study, the product distribution was explained by the presence of different active sites on Ni_2P phase (Ni(1) and Ni(2)) and adsorption modes on the catalyst. Ni(1) sites present on the Ni_3P_2 termination interact with the oxygen atom of C-OH bond and facilitate the hydrogenolysis reactions of cresols into toluene and methylcyclohexanols into methylcyclohexane whereas Ni(2) sites of Ni_3P termination promote a flat adsorption of cresols, favoring the hydrogenation of aromatic ring.

Although it is well known that the nature of support influences the product distribution and the extent of the HDO reaction, only a few studies investigated the effect of the type of support on the performance of phosphide catalysts in HDO of model molecules [26,32–34],

which appears fairly complex. The type of support can affect the nature of phosphide phase formed and it may lead to the formation of phosphate species with the support upon calcination (like $AlPO_4$ when Al_2O_3 is used as support) [26]. Moon and Lee [34] showed that the support can protect the Ni_2P phase during the HDO of guaiacol (300°C, 3 MPa). Indeed, under these conditions, the Ni_2P/SiO_2 catalyst was oxidized to nickel phosphate by water whereas the Ni_2P phase supported on zirconia and active carbon was resistant to oxidation. Using fresh catalysts, the order of activity was the following: Ni_2P/SiO_2 > Ni_2P/ZrO_2 > Ni_2P/AC (AC = active carbon). Wu et al. [33] also investigated the HDO of guaiacol at the same temperature (300°C) but under atmospheric pressure over the same nickel phosphide phase (Ni_2P) supported on alumina, zirconia and silica. The intrinsic activity decreased in the following order: Ni_2P/ZrO_2 > Ni_2P/Al_2O_3 > Ni_2P/SiO_2. As a result, the order of activity between Ni_2P/SiO_2 and Ni_2P/ZrO_2 is still controversial.

In order to investigate the effect of the active phase and the support, this work investigated the effect use of SiO_2 and tetragonal ZrO_2 as supports for metallic nickel and nickel phosphide for HDO of m-cresol (340 °C, 4 MPa). The evaluation of the catalytic properties (activity, selectivity and stability) was performed and discussed. The use of a kinetic modeling also grounded the discussions.

2. Experimental

2.1. Catalyst synthesis

Silica (Hi-Sil 915, PPG Industries) and ZrO_2 (Saint-Gobain NorPro) were used as supports. Prior to impregnation, silica was calcined under air flow at 800 ºC for 5 h. No previous treatment was performed on zirconia. Ni/SiO_2 and Ni/ZrO_2 samples were prepared by incipient wetness impregnation of the supports (IWI method) using an aqueous solution of nickel nitrate hexahydrate ($Ni(NO_3)_2.6H_2O$, Merck) to obtain 10 wt.% of Ni. Both solids were then dried under air flow (60 ml min^{-1}) at 120 ºC for 24 h and then calcined in air at 500ºC for 3 h (2 ºC

min^{-1}). Nickel phosphide catalysts (NiP/SiO_2 and NiP/ZrO_2) were also synthesized by IWI method to obtain the oxide precursors of the phosphide phase ($Ni_xP_yO_z$). In the first step, the nickel nitrate hexahydrate ($Ni(NO_3)_2.6H_2O$, Merck) and ammonium hydrogen phosphate ($(NH_4)_2HPO_4$, Vetec) salts were solubilized separately in distilled water. The solution of $(NH_4)_2HPO_4$ was added dropwise to an aqueous solution containing $Ni(NO_3)_2{\cdot}H_2O$ under magnetic stirring and a precipitate was formed. Then, the nitric acid (HNO_3, Vetec) was added dropwise until the solubilization of the precipitate. The concentration of the precursor solutions was adjusted to obtain catalysts with 10 wt.% of nickel. According to previous reports, an excess of phosphorus is required when an acid support is used due to the formation of a phosphate phase with the support [32]. Thus, the P/Ni molar ratio for Ni_2P/SiO_2 and Ni_2P/ZrO_2 catalysts was 0.8 and 3.0, respectively, in order to guarantee the formation of the Ni_2P phase. The resultant solution was impregnated onto both ZrO_2 and SiO_2 supports for Ni-based catalysts. Afterwards, these solids were also dried and calcined as previous described. Both nickel and phosphide phases were finally prepared after in situ reduction treatment as further discussed. Prior to use, all catalysts were pelleted, crushed and sieved with 250–315 µm

2.2. Catalyst characterization

The chemical composition of nickel oxide and the oxidic precursors of nickel phosphides over SiO_2 and ZrO_2 were determined by inductively coupled plasma optical emission spectrometry (ICP-OES) using an SPECTRO ARCOS ICP-OES instrument. Prior to analysis, the samples were digested with concentrated nitric acid and hydrofluoric acid using microwave heating system.

Textural properties of the solids were obtained using the N_2 adsorption−desorption isotherms were measured on a Micromeritics ASAP 2000 analyzer at -196 ºC. Prior to N_2 adsorption, the solid samples were degassed overnight under secondary vacuum at 200 °C. The specific surface area (S_{BET} in $m^2\ g^{-1}$) was calculated from the adsorption isotherm (P/P_0 between 0.05 and 0.20) using the Brunauer-Emmett-Teller (B.E.T.) method. The total pore volume was

calculated from the adsorbed volume of nitrogen at P/P_0 equal to 0.99. The mesoporous volume was determined using the t-plot method. The average mesopore-size distribution was calculated from the adsorption isotherm branch using the Barret-Joyner-Halenda (BJH) method.

X-ray diffraction (XRD) diagrams were obtained the Cu Kα radiations of a Bruker D8 advance diffractometer in a Bragg-Brentano geometry in the range 20-90° for 2q. The instrument was operating at 40 kV and 40 mA. Steps interval of 0.04° or 0.06° for 2θ and counting time varying between 10 and 20 s for each step were used with a LYNX EYE rapid detector. The pattern of a Cr_2O_3 powder (Standard NIST 674b) was collected at the same geometrical conditions to generate an instrumental resolution function to account for the experimental broadening. Rietveld refinements of the diffractograms were performed using the Materials Analysis Using Diffraction (MAUD) software [35]. Prior to analysis, the catalysts were reduced at 450 ºC (5 ºC min^{-1}) under 4 MPa as total pressure during 2 h using pure hydrogen (4.7 NL h^{-1}). After activation in situ, samples were cooled down under hydrogen to 25 ºC and passivated at this temperature under atmospheric pressure for 3 h by a flow of 5 vol.% O_2 in He (80 ml min^{-1}).

The reducibility of the supported oxide precursors of Ni and $Ni_xP_yO_z$ were characterized by the H_2 temperature-programmed reduction (H_2-TPR) using a Micromeritics AutoChem 2910. Prior to reduction, each sample (100 mg) was pretreated under He flow (20 mL min^{-1}) at 200 ºC (heating rate of 10 ºC min^{-1}) for 30 min. Then, the catalyst was cooled down to 50 ºC. The reduction measurements started at this temperature using 10% H_2 in Ar (20 mL min^{-1}). The temperature was progressively increased until 1000 ºC (heating rate of 5 ºC min^{-1}) and held for 90 min. The hydrogen consumption was estimated using a TCD detector. The reduction of phosphide catalyst was also carried out in a system coupled to a VC 40 Thermo quadrupole mass-spectrometer. The signal due to water (m/z= 18), H_2 (m/z= 2), N (m/z= 14), CO and N_2 (m/z= 28), P (m/z= 31), O_2 (m/z= 32), PH_3 (m/z= 34), CO_2 (m/z= 44), and P_2 (m/z= 62) were recorded during TPR.

The measure of acid sites on the catalyst was performed NH_3-TPD technique using 150 mg of sample. Prior to the measurement, the samples were reduced in situ with pure hydrogen

(60 mL min^{-1}) at 450ºC. The heating rate was 5 ºC min^{-1} and the final temperature was kept for 2 h. The system was then purged with He (30 mL min^{-1}) for 30 min and then the sample was cooled down to 100 ºC. The feed composition was switched to a mixture containing 20% NH_3 in He (30 mL min^{-1}) for 30 min. Afterwards, the physisorbed ammonia was flushed out with flowing He (30 mL min^{-1}) for 1 h. Desorption was measured under a heating of 10 ºC min^{-1} under He to 600 ºC. The reactor effluent was continuously monitored by mass spectrometry.

2.3. Activity measurements

A vertical continuous fixed-bed reactor (length: 40 cm; inner diameter: 1.26 cm) was used to study the transformation of m-cresol at 340°C under 4 MPa. Prior to reaction, all catalysts were reduced in-situ at 450ºC under 4 MPa for 2 h using pure hydrogen (4.7 NL h^{-1}). A liquid model feed was prepared to obtain 53 kPa oxygenated reactant, 31 kPa n-heptane as internal standard and dodecane as solvent. The top inlet of the reactor was continuously fed by the liquid model feed c using a HPLC Gilson pump and H_2 flow with a ratio hydrogen to oxygenate molar ratio of 486 NL L^{-1}. In the reaction conditions the H_2 partial pressure was set to 3.24 MPa.

Liquid samples were collected each hour from a condenser (Minichiller-Huber cryostat set to 10 ºC located in the outlet line of the reactor). The samples were analyzed by a Varian 430 chromatograph with a DB1 capillary column (length: 30m, inside diameter: 0.320 mm, film thickness: 5µm) equipped with a flame ionization detector (FID). All products were identified by using a 1200 TQ mass spectrometer coupled with a Varian 3800 chromatograph and by co-injection of commercial compounds.

For each catalyst, experiments lasted 20 h on stream. During a single experiment set, the liquid inlet flow was varied to obtain different levels of conversion, keeping the ratio H_2/oxygenate constant. The ratio between the catalyst weight and the oxygenated model compounds can be defined as space time (τ, in g h mol^{-1}) in Eq. (1):

$$\tau = \frac{W}{F_{CRE}} \quad (1)$$

The reactant conversion of oxygenate (X_{CRE} in %) was calculated according to Eq. (2):

$$X_{CRE} = \frac{C_{CRE,0} - C_{CRE}}{C_{CRE,0}} . 100 \quad (2)$$

$C_{CRE,0}$ being the initial molar fraction of m-cresol and C_{CRE} as the molar fraction of the corresponding reactant in the liquid sample collected at the studied space time τ.

The selectivity of a product i (S_i in mol%) was given by Eq. (3):

$$S_i = \frac{C_i}{C_{CRE,0} - C_{CRE}} . 100 \quad (3)$$

where C_i represents the molar fraction of a product i in the liquid sample analyzed.

Assuming a pseudo-first-order model, the global activity of catalyst (k_{Tot} in mmol h^{-1} g^{-1})) can be calculated using Eq. (4):

$$\ln(1 - X_{CRE}) = k_{Tot} . \tau \quad (4)$$

For all experiments, the mass balances were always between 95 and 100%. The reaction was carried out in the absence of internal and external mass-transfer effect as previously demonstrated [27].

3. Results and discussion

3.1. Catalyst characterization

Table 6-1 lists the Ni and P loading of the materials obtained by ICP analysis. The Ni loading was around 9 wt.%. The Ni_2P/SiO_2 and Ni_2P/ZrO_2 samples showed a P/Ni molar ratio very close to the values set in the synthesis, being equal to 0.8 and 2.8, respectively.

Table 6-1 : Chemical composition and textural properties of the fresh[⊥] and reduced/passived[∓] samples.

Solid	(wt. %)		Specific surface area ($m^2\ g^{-1}$)		Mesoporous volume[a] ($cm^3\ g^{-1}$)		Average pore diameter[b] (nm)	
	Ni	P	fresh	red./pass.	fresh	red./pass.	fresh	red./pass.
SiO_2	-	-	208	-	0.57	-	9	-
ZrO_2	-	-	142	-	0.21	-	6	-
Ni/SiO_2	9.7	-	183	176	0.39	0.28	8	8
Ni/ZrO_2	10.1	-	128	125	0.17	0.17	6	5
Ni_2P/SiO_2	9.0	3.9	176	172	0.40	0.34	8	7
Ni_2P/ZrO_2	7.4	10.8	103	98	0.11	0.11	5	5

[⊥] fresh = dried and calcined samples.

[∓] red./pass. = reduced at 450 ºC (5 ºC min^{-1}) under 4 MPa as total pressure during 2 h using pure H_2 (4.7 NL h^{-1}).

[a] deduced from the t-plot method

[b] deduced from the BJH method using the adsorption branch.

The adsorption-desorption isotherms of supports and catalysts before and after reduction/passivation step (450 ºC, 4 MPa) are shown in Figure 6-1. All the materials showed typical isotherms IV-type profile, according to the IUPAC classification. However, the type of hysteresis was different between SiO_2 and ZrO_2 materials. The hysteresis loop of pure silica

and silica supported catalysts was H_2 type, characteristic of "ink-bottle" pore [36]. In contrast, the zirconia samples exhibited isotherms with type-H4 desorption hysteresis, associated with the slit-like pores [36].

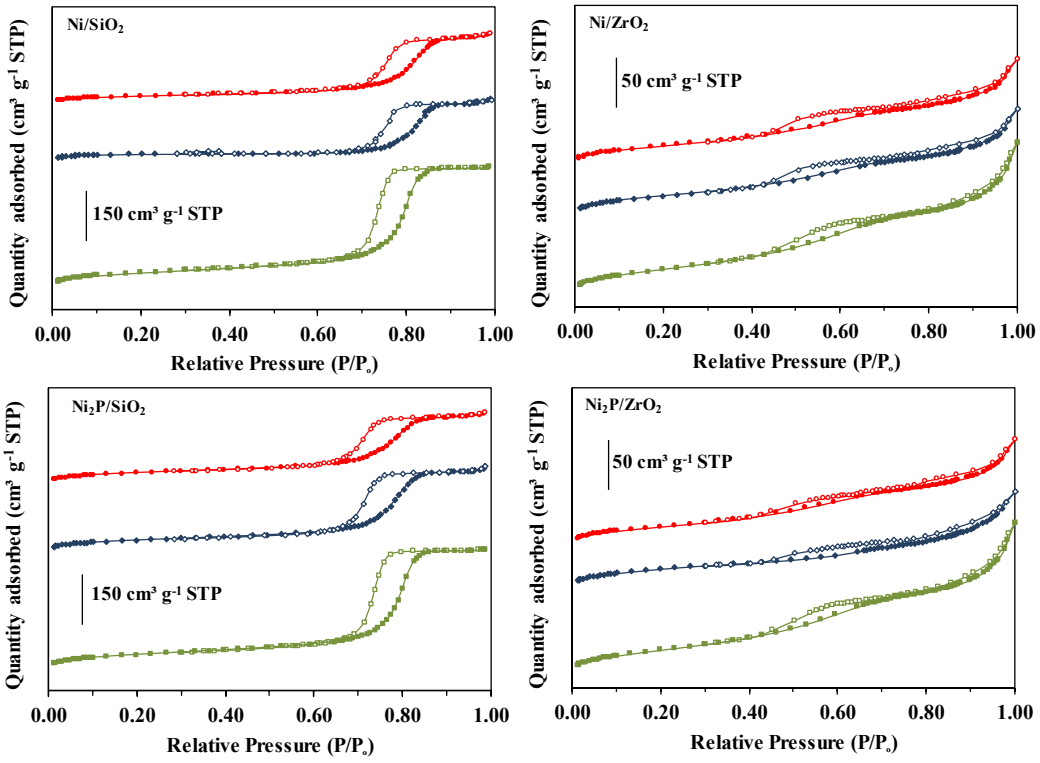

Figure 6-1 : Nitrogen adsorption-desorption isotherms of base support (■), supported oxide precursors (♦), active phase after pre-treatment at 450 °C and 4 MPa of H_2 (●). Full symbols for adsorption and empty symbols for desorption. (a) Ni/SiO_2; (b) Ni/ZrO_2; (c) Ni_2P/SiO_2; (d) Ni_2P/ZrO_2.

Table 6-1 summarizes the values of specific area, average pore volume and size for fresh and after being activated at 4 MPa of H_2 at 450 ºC. Comparing the bare SiO_2 and ZrO_2 supports, the former exhibited higher specific surface area (208 $m^2\ g^{-1}$) and pore volume (0.57 $cm^3\ g^{-1}$) than the latter (142 $m^2\ g^{-1}$ and 0.21 $cm^3\ g^{-1}$, respectively). The addition of Ni and P decreased

the specific surface area and pore volume could be explained by a possible pore blocking. The contribution of the weight gain consecutive to the introduction of Ni based phases can also explain the modification of the textural properties of these solids. However, these properties were practically not affected by the reduction/passivation treatment.

The XRD patterns of all catalysts after reduction (450 ºC, 4 MPa) and passivation procedure are shown in Figure 6-2. Rietveld refinement of the XRD diagrams were performed to determine the grain size of the different catalysts with an isotropic model for the grain shape and for the microstrain. Excellent refinement of all the diffractograms were obtained (factor of goodness varying between 1.5 and 1.9) allowing a precise determination of the crystallite size (the uncertainty for the the crystallite size is typically ± 1 nm). The XRD pattern of Ni/SiO_2 and Ni/ZrO_2 catalysts exhibited the lines characteristic of Ni^0 (ICDS 98-064-6090; 2θ = 45.5, 51.9 and 76.5 º) and the lines corresponding to the respective supports; amorphous silica (a broad line between 2θ = 20 – 30º) and tetragonal ZrO_2 (2θ = 30.2, 35.3, 50.5 and 60.2 º) with an additional line at 2θ = 28.3º (low intensity) corresponding to presence of monoclinic ZrO_2 phase. The diffractograms of supported nickel phosphide catalysts showed the diffraction lines corresponding to the supports, indicating that the crystalline structure of silica and zirconium is not altered even under a large amount of P. Both catalysts showed only the diffraction lines typical of the Ni_2P phase (ICDS 98-064-6102; 2θ = 40.6, 44.5, 47.3 and 54°). The diffraction lines corresponding to metallic Ni phase or oxyphosphates were not observed, demonstrating that the reduction procedure used (450 °C, 4 MPa) allowed to obtain the desired nickel phosphide phase (Ni_2P).

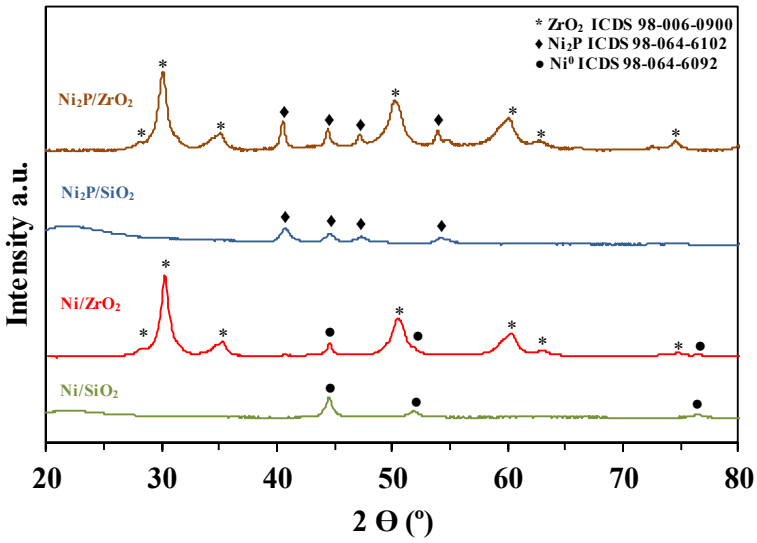

Figure 6-2 : XRD patterns of nickel and nickel phosphide supported catalysts.

The particle size, the theoretical metal site concentration and the dispersion were calculated for all catalysts, assuming uniform spherical particles (Table 6-2). These values were close to the values reported in the literature for the same type of catalyst [31,33,37]. The crystallite size depended on both the nature of the phase (Ni vs Ni_2P) and the support used (SiO_2 vs ZrO_2). Metallic nickel and phosphide nickel particles were about 1.6-1.8 times higher when ZrO_2 was used as support instead of SiO_2. Consequently, the dispersion of active phases was favored over silica, as already reported by several authors considering the Ni_2P phase [33,34]. This result agrees very well with the BET surface area of the supports (Table 6-1): the higher surface area of SiO_2 (208 $m^2\ g^{-1}$) favored the formation of smaller particles compared to ZrO_2 (142 $m^2\ g^{-1}$). Indeed, it was already reported that an increase of surface area of silica favored the dispersion of Ni_2P particles [38]. The nature of the support could also explain, at least in part, the difference in dispersion due to different metal/support interaction [39].

Table 6-2 : Catalysts properties.

Catalyst	H_2 uptake (mmol g^{-1})		d_{XRD}[d]	n_{sites}[e]	Dispersion[f]	NH_3 uptake[g]
	Theoretical	Experimental[c]	(nm)	(µmol g^{-1})	(%)	(µmol g^{-1})
Ni/SiO_2	1.5[a]	1.6	10	157	9.2	0
Ni/ZrO_2	1.6[a]	1.7	17	92	5.4	179
Ni_2P/SiO_2	3.5[b]	4.1	16	117	6.8	299
Ni_2P/ZrO_2	2.9[b]	4.2	31	60	3.5	1020

[a] calculated to obtain Ni^0 calculated from Ni wt.% in the catalyst

[b] calculated to obtain Ni_2P calculated from Ni wt.% in the catalyst

[c] determined by H_2-TPR.

[d.] particle size (d_{XRD}) calculated from XRD.

[e] Ni site density (n_{sites}) estimated from d_{XRD} based on $n_{site} = S_{eff}$ x n x f [31]). S_{eff} being the effective surface area of an active site particle ($S_{eff} = 6/ (\rho \times d_{XRD})$; ρ is the density of an active site ($\rho_{NiO} = 6.67$ g.cm^{-3}; $\rho_{Ni2P} = 7.09$ g.cm^{-3}); n is the surface metal atom density ($n = 1.05 \times 10^{15}$ atoms/cm^2); f is the weight fraction of active site.

[f] dispersion estimated by n_{sites}/(mol of Ni/g of catalyst) x 100 %.

[g] determined by TPD-NH_3

Figure 6-3 shows the H_2-TPR profiles of the calcined samples. SiO_2 and ZrO_2 supports did not exhibit any hydrogen consumption (not shown). The TPR profiles of nickel oxide supported over silica or zirconia revealed the same onset reduction temperature (300 ºC). The presence of various peaks was observed, particularly in the case of Ni/ZrO_2 which exhibited a large zone of reduction (between 300 and 600 °C). This seems to indicate that there are different NiO species that interact differently with ZrO_2: the weak metal/support interaction leading to peaks at lower temperature. In addition, distinct maximum uptakes were observed for both solids, at 386 ºC for ZrO_2 and at 419 ºC for SiO_2. This shows that the reduction of some NiO particles were easier on ZrO_2. The nickel oxide particles were completely reduced below 600 ºC for both catalysts. The hydrogen consumption measured for both Ni/SiO_2 and Ni/ZrO_2 were very close to the theoretical values expected for the complete reduction of NiO to Ni^0, as shown in Table 6-2.

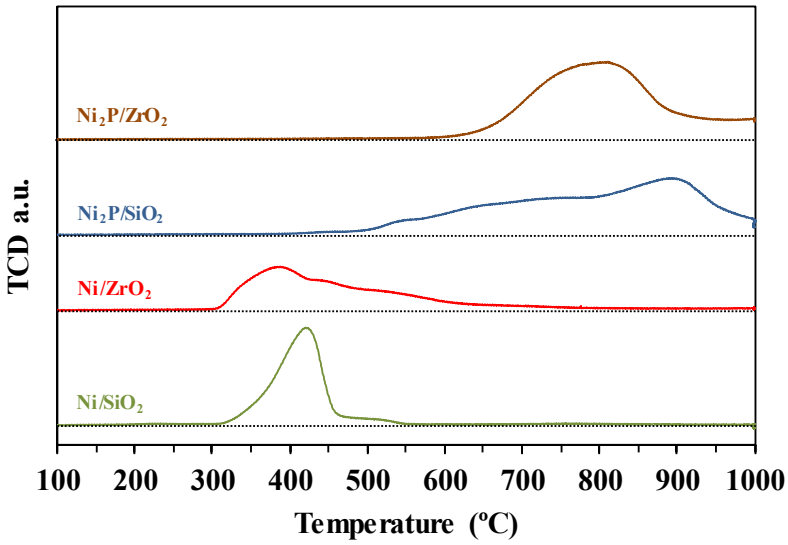

Figure 6-3 : H_2-TPR profiles of nickel and nickel phosphide supported catalysts. Reduction conditions: 20 ml min^{-1} 10% of H_2 in Ar with heating rate of 5°C min^{-1}.

Nickel phosphide catalysts were reduced at higher temperatures than nickel oxide catalysts, accordingly with several studies [33,37,38]. For them, initially occurs the reduction of nickel oxide and followed by the reduction of the phosphorus oxide, producing the metal phosphide [40]. In addition, catalysts with lower P contents tend to have multiple peaks associated the reduction of nickel oxy-phosphates species, while catalysts with higher P contents, a simple TPR profile with high reduction temperature is obtained due the presence of nickel only as nickel phosphate ($Ni_xP_yO_z$) [41].

Comparing the TPR profiles of Ni_2P/SiO_2 and Ni_2P/ZrO_2 catalysts, the reduction of Ni_2P/SiO_2 catalysts started at about 400 ºC and was almost complete at 1000 ºC. Several shoulders were observed, but the maximum H_2 consumption was achieved at 893 ºC. For Ni_2P/ZrO_2 catalysts, one large peak appeared at higher temperature compared to Ni_2P/SiO_2 (between 588-950 ºC), the maximum H_2 consumption being observed at about 795 °C.

The theoretical hydrogen consumption of each nickel phosphide catalyst, calculated considering the formation of Ni_2P phase from the quantity of Ni present in the catalysts [27], is also reported in Table 6-2. Despite of the different P content, the H_2 consumption was approximately the same for both nickel phosphide catalysts (4.1-4.2 mmol g^{-1}), which is 15% higher than the theoretical value for Ni_2P/SiO_2 and 31% for Ni_2P/ZrO_2. The higher gap between theoretical and experimental H_2 uptake for Ni_2P/ZrO_2 can be explain by the high amount of P in the synthesis of Ni_2P/ZrO_2 (P/Ni = 3) compared to Ni_2P/SiO_2 (P/Ni = 0.8). In fact, the excess of hydrogen consumed is likely due to the reduction of phosphates species (such as PO_4^{-3}, $P_2O_7^{2-}$ or PO_3^-) into PH_3 species [41]. Additional TPR experiments were performed to follow the phosphine (PH_3 – m/z = 34) signal during reduction of Ni_2P/SiO_2 and P/SiO_2 samples, which demonstrated the loss of P as PH_3 for both materials (Supplementary Information, Figure S6-1).

NH_3-TPD were carried out to determine the strength and the density of the acid sites of the catalysts. The profiles of the catalysts are shown in Figure 6-4. Ni/SiO_2 did not show any peak, indicating that this catalyst has negligible acidity. Ni/ZrO_2 exhibited a broad peak at around 270ºC, which is attributed to the Lewis acidity due to Zr surface sites [39]. In the same way, De Souza et al. [42] observed by DRIFTS of adsorbed pyridine that tetragonal zirconia revealed only the presence of Lewis acid sites. Comparing the NH_3-TPD profile and the amount of desorbed ammonia for Ni_2P/ZrO_2 and Ni/ZrO_2, it is noticed that the presence of phosphorus increased significantly the density of acid sites, which is mainly due to the Brønsted acid sites attributed to the presence of PO-H groups on the support surface. The density of acid sites of all catalysts was also calculated from NH_3-TPD profiles and the results are reported in Table 6-2. The density of acid sites followed the order: $Ni_2P/ZrO_2 > Ni_2P/SiO_2 > Ni/ZrO_2 >> Ni/SiO_2$.

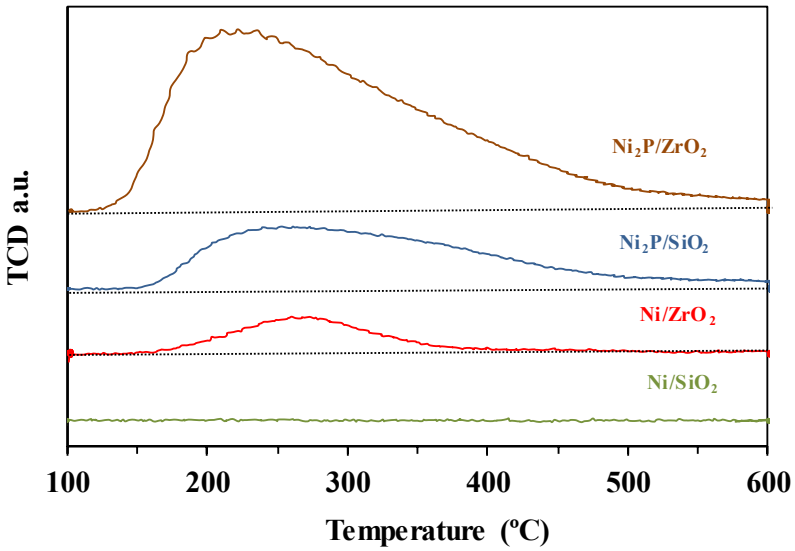

Figure 6-4 : NH_3-TPD profiles of nickel and nickel phosphide supported catalysts.

3.2. HDO of m-cresol

The hydrodeoxygenation of m-cresol was carried out under 4 MPa at 340 °C over Ni-based and Ni_2P-based catalysts. Figure 6-5 shows a linear relationship between -ln (1-X_{CRE}) and τ for all catalysts confirming that the overall reaction can be described as pseudo-first order, as previously proposed [27]. The deduced values of k_{Tot} are given in Table 6-3 and follow the order: Ni_2P/ZrO_2 > Ni_2P/SiO_2 > Ni/ZrO_2 > Ni/SiO_2. This trend shows that the Ni phosphide phase was much more active than the Ni metallic phase, irrespective the support used. Nevertheless, studies reporting comparison of the HDO activity between Ni and Ni_2P are still controversial. For example, Li et al. [23] showed that Ni/SiO_2 and Ni_2P/SiO_2 presented about the same activity for the HDO of anisole at 300 °C under 1.5 MPa. The same observation was made by Chen et al. [37] studying the HDO of methyl laurate under 2 MPa at 300 °C. On the contrary, Ni/SiO_2 was found 2.3 times more active than Ni_2P/SiO_2 for the HDO of guaiacol at 350 °C under a lower pressure (0.5 MPa). It was demonstrated that an increase of pressure was

more benefit for Ni_2P than for Ni for HDO of methyl oleate [43]. Indeed, the authors reported that Ni/SBA-15 was 3.5 times more active than Ni_2P/SBA-15 under 0.3 MPa, whereas both catalysts practically showed the same activity under 4 MPa. In our case, Ni_2P clearly exhibited much higher activity than Ni, which can be in part related to the high pressure used in the present study (4 MPa).

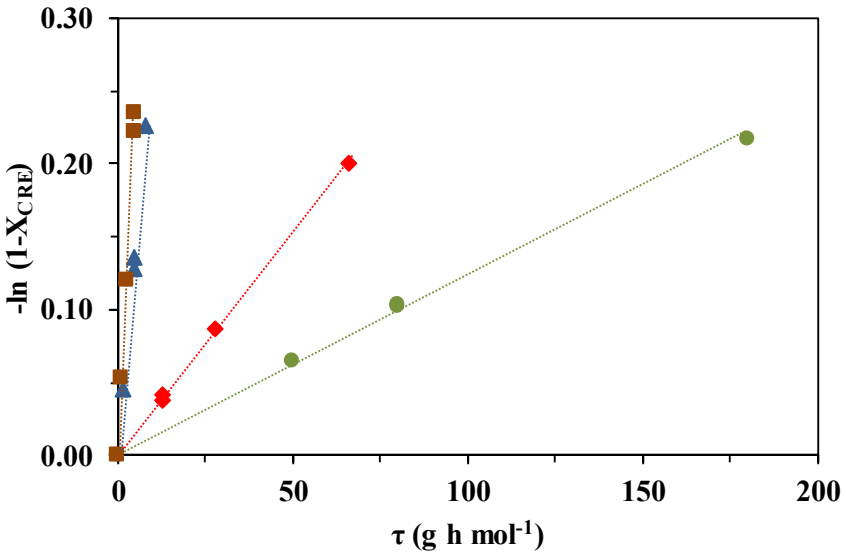

Figure 6-5 : Pseudo-first order plots of the HDO of m-cresol at 340ºC under 4 MPa; Ni/SiO_2 (●); Ni/ZrO_2 (◆); Ni_2P/SiO_2 (▲); Ni_2P/ZrO_2 (■).

The use of ZrO_2 as catalytic support allowed to increase both the activity of Ni and Ni_2P based catalysts compared to SiO_2. Regarding the influence of the support, the same result was observed by de Souza et al. [44] for HDO of m-cresol at 300 ºC under atmospheric pressure over SiO_2 and ZrO_2 supported Pd catalysts. The authors attributed this result to the presence of oxygen vacancies (oxiphilic sites) represented by completely coordinated Zr^{4+}/Zr^{3+} cations near the periphery of metal particles. This fact can be related to metal-oxygen bond strength of both supports: the metal-oxygen bond energy of ZrO_2 (14.2 eV) being more than twice lower than that of SiO_2 (34.2 eV) [45]. As a result, the number of oxygen vacancies is expected to be higher

on zirconia and thus favor the adsorption of oxygenated compounds, which explains the significant improvement of the hydrodeoxygenation activity of Ni/ZrO_2 compared to Ni/SiO_2.

Table 6-3 : Individual apparent rate constants determined during the transformation of m-cresol at 340 ºC under 4 MPa of total pressure (standard deviation of rate constants close to 5%).

Catalyst	Rate constants (in mmol g^{-1} h^{-1})						
	k_{Tot}	k_{DDO}	k_{HYD}	k_1	k_2	k_3	k_4
Ni/SiO_2	1.13 ± 0.06	0.05± 0.01	1.08 ± 0.05	35 ± 2	3.0 ± 0.2	127 ± 6	-
Ni/ZrO_2	3.00 ± 0.15	0.16 ± 0.01	2.84 ± 0.14	67 ± 3	108 ± 5	41 ± 3	32 ± 2
Ni_2P/SiO_2	28.3 ± 1.4	5.8 ± 0.3	22.5 ± 1.1	2254 ± 113	166 ± 8	552 ± 30	39 ± 3
Ni_2P/ZrO_2	47.0 ± 2.4	5.9 ± 0.3	41.0 ± 2.1	2385 ± 119	309 ± 15	835 ± 42	85 ± 4

In this present work, experiments were performed during 20 h on stream and space times were modified during the transformation of m-cresol to obtain different values of conversion. Regardless of the conversion obtained and the τ used, by recalculating the global apparent constant (k_{Tot}) using Eq. (4), it is observed that very close values are obtained for each hour of experiment and catalyst (Figure 6-6). Consequently, all catalysts exhibited a very good stability at least during 20 hours on stream, highlighting the beneficial use of high pressure, as previously reported [27]. On the contrary, Li et al [23] observed a deactivation profile of both Ni/SiO_2 and Ni_2P/SiO_2 by carrying out the hydrodeoxygenation of anisole at a lower pressure (1.5 MPa) at 300 ºC. Similarly, past studies reported Ni-based [19,23] and Ni_2P-based [31,33] catalysts tend to deactivate at low H_2 pressure.

To investigate the effect of the active phase and the support on the selectivity of catalysts, the product distribution determined at the same level of conversion (close to 20%) is given in Table 6-4. The transformation of m-cresol yielded 3-methylcyclohexanone (3-MCHnone) and 3-methylcyclohexanols (3-MCHols) as oxygenated products,

methylcyclohexenes (MCHes), methylcyclohexane (MCH), ethylcyclopentane (ECP) and toluene (Tol) as deoxygenated products.

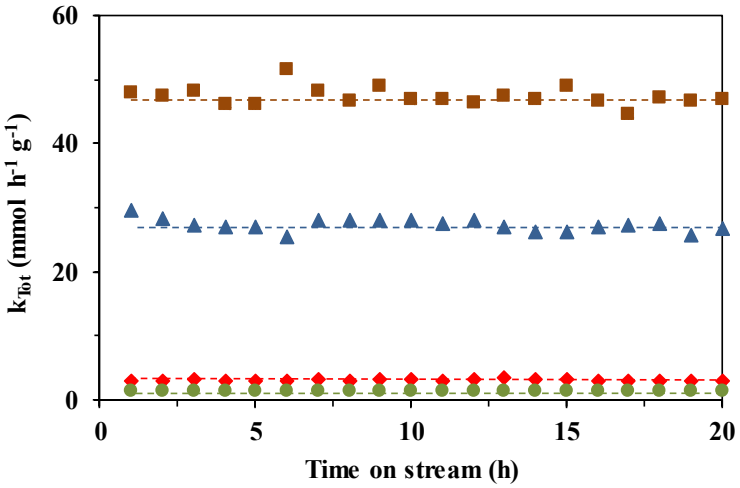

Figure 6-6 : k_{Tot} as function of time on stream for the HDO of m-cresol at 340ºC under 4 MPa. Ni/SiO_2 (●); Ni/ZrO_2 (◆); Ni_2P/SiO_2 (▲); Ni_2P/ZrO_2 (■).

Table 6-4 : Product distribution obtained from the transformation of m-cresol at 340 ◦C under 4 MPa of total pressure (conversion close to 20%).

Catalyst	τ (g h mol^{-1})	Conversion (%)	Selectivity (mol%)						1-MCHe/ MCHes
			Tol	3-MCHone	3-MCHols	MCHes	MCH	ECP	
Ni/SiO_2	180.0	19.6	4.0	6.6	12.6	13.2	63.6	0	18
Ni/ZrO_2	66.0	18.2	5.3	5.0	4.2	27.7	56.8	1.0	61
Ni_2P/SiO_2	8.0	20.2	20.6	1.6	0.0	13.8	62.9	1.1	65
Ni_2P/ZrO_2	5.0	20.9	12.7	0.0	0.0	9.9	74.3	3.1	65

MCH was always the main product over all catalysts, its amount varying between 57 mol% for Ni/ZrO_2 and 74 mol% for Ni_2P/ZrO_2. Concerning the Ni-based catalysts, the deoxygenation products (Tol + MCH + MCHes) were favored over Ni/ZrO_2 than over Ni/SiO_2. Zirconia promoted the production of MCHes, their selectivity being about twice higher for Ni/ZrO_2 compared to Ni/SiO_2. In addition, the composition of the methylcyclohexene isomers was dependent on the Ni-based catalyst (Table 6-4). Over Ni/ZrO_2, 1-methylcyclohexene was the main alkene isomer, which is not the case over Ni/SiO_2. From a thermodynamic point of view, the percentage of this isomer is expected to be equal to 65 mol% at 340 ºC [46], which is very close to the experimental value reported for Ni/ZrO_2 (Table 6-4). In turn, 3- and 4-MCHes are expected from dehydration of 3-MCHols: However, 1-methylcyclohexene cannot be directly produced. Its formation can be explained by the double-bond migration due to the presence of acid sites, which occurs in a high extent for Ni/ZrO_2 (acidic catalyst) reaching MCHes thermodynamic equilibrium. The Ni/SiO_2 catalyst does not features any acidity as demonstrated by NH_3-TPD, which explains the low 1-MCHe/MCHes ratio compared to Ni/ZrO_2. In the same way, it was demonstrated that ZrO_2 exhibited high activity for the dehydration of cyclohexanol to cyclohexene, which was also attributed to its high density of acid sites [42].

The selectivity into oxygenated products (3-MCHols and 3-MCHnone) was lower over the nickel phosphide based catalysts compared to metallic catalysts. Indeed, at 20 % of m-cresol conversion, no oxygenates were detected over Ni_2P/ZrO_2 and a small amount of 3-MCHone was observed over Ni_2P/SiO_2. Similarly to Ni/ZrO_2, the 1-MCHe/MCHes ratio for both Ni phosphide catalysts showed that the thermodynamic equilibrium of MCHes is also reached due to their acidic properties. The use of Ni_2P catalysts increased the selectivity into toluene compared to Ni catalysts: its selectivity was close to 5 mol% over both Ni/SiO_2 and Ni/ZrO_2 and equal to 12.7 and 21.6 mol% over Ni_2P/ZrO_2 and Ni_2P/SiO_2, respectively (Table 6-4).

The selectivity into Tol, oxygenates (3-MCHnone and 3-MCHol), MCHes, MCH as function of m-cresol conversion is shown in Figure 6-7. Oxygenates appeared as intermediates since their selectivity decreased by increasing conversion. Similarly, alkenes were also

observed as intermediates being hydrogenated into MCH at higher conversions. Since the selectivity into toluene was constant over all catalysts with the increase of conversion, it is considered that this aromatic was unreactive under these experimental conditions. In order to verify such assumption, additional sets of experiments were performed replacing m-cresol for toluene for each catalyst, which showed no hydrogenation of the aromatic for all catalysts.

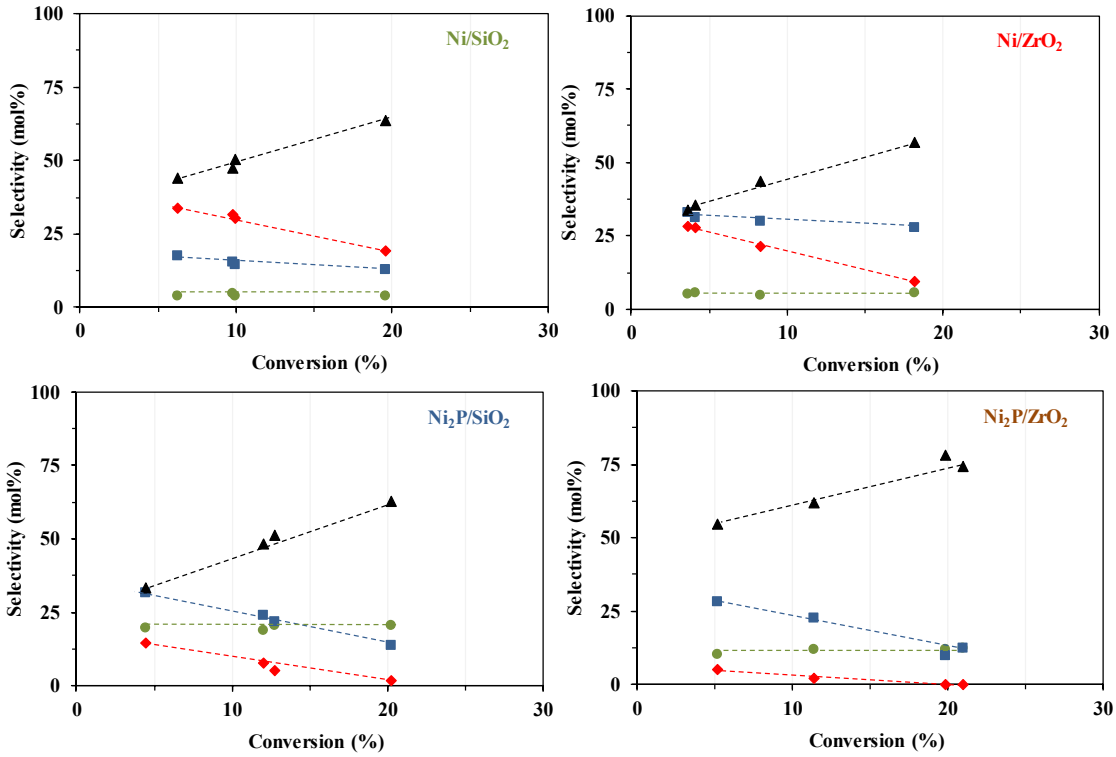

Figure 6-7 : Selectivity as function of conversion at 340ºC under 4 MPa. (▲) methylcyclohexane, (■) methylcyclohexenes; (◆) oxygenates (3-methylcyclohexanols and 3-methylcyclohexanone); (●) toluene; (- - -) Trend lines. (a) Ni/SiO_2; (b) Ni/ZrO_2; (c) Ni_2P/SiO_2; (d) Ni_2P/ZrO_2.

Considering the analysis of Figure 6-7, a plausible network for the transformation of m-cresol over Ni metallic and Ni phosphide phases, recently proposed in [27], is depicted in

Scheme 6-1. It is assumed that the transformation of such phenolic compound proceeds via two parallel pathways. Toluene can be directly produced by the cleavage of the C-O bond of m-cresol (DDO pathway) while hydrogenation, hydrogenolysis and dehydration reactions can take place for the formation of oxygenates, alkenes and alkanes (HYD pathway). For the latter pathway, 3-MCHnone is probably obtained by the hydrogenation of m-cresol aromatic ring, which can further lead to 3-MCHols. The alcohols can be either directly transformed into methylcyclohexane by hydrogenolysis or into 3- and 4-methylcyclohexene by dehydration, these alkenes can be isomerized into 1-methylcyclohexene. MCHes can be hydrogenated into MCH. The appearance of ECP is a result of isomerization of MCH which also occurs on acid sites.

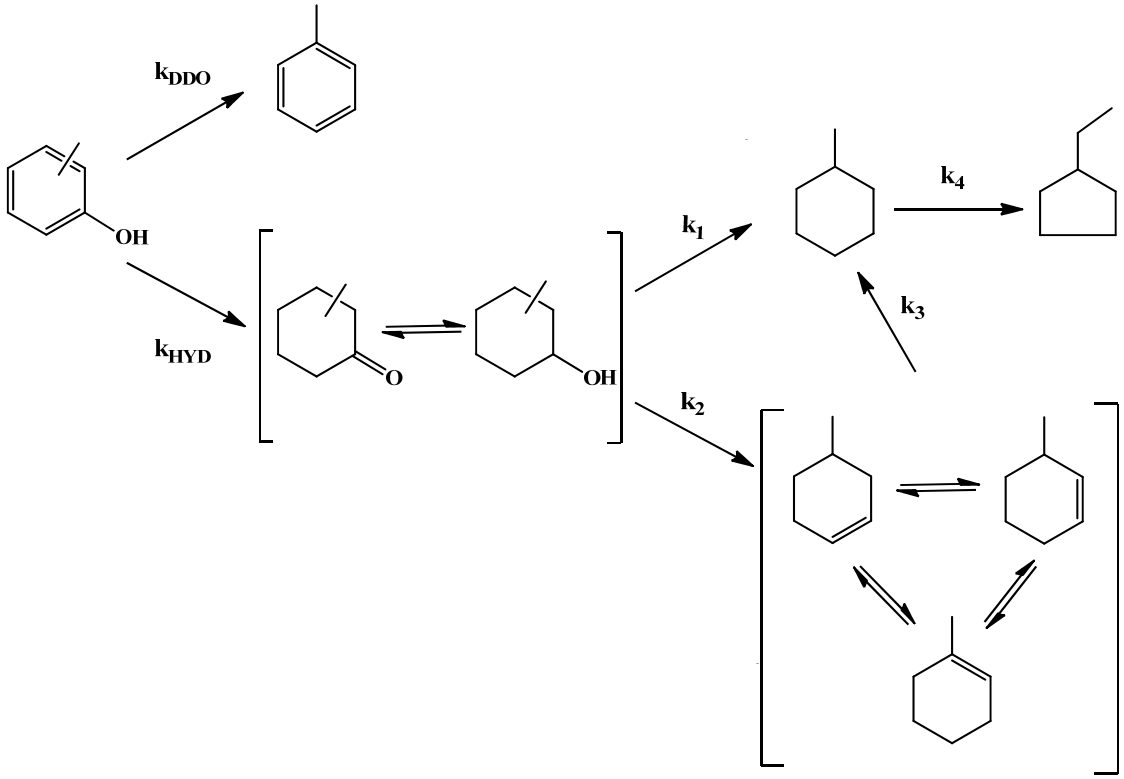

Scheme 6-1 : Reaction network of the deoxygenation of m-cresol isomers over Ni-based and Ni_2P-based catalysts.

In order to measure the rate of these different reactions involved over Ni-based and Ni_2P-based catalysts, a kinetic modeling based on the proposed reaction network (Scheme 6-1) was performed using an integral method. The same kinetic model was also used recently to determine the kinetic constants involved in the transformation of cresol isomers using Ni_2P/SiO_2 as catalyst [27]. This model is detailed in the supplementary information file, and the results of modeling for all catalysts are shown in Figure S6-2 (Supplementary Information). The kinetic values determined (k_{HDO}, k_{DDO}, k_{HYD}, k_1, k_2, k_3 and k_4) are given in Table 6-3.

Concerning the metallic Ni-based catalysts, Table 6-3 shows that k_{DDO} and k_{HYD} were about 3-fold higher for Ni/ZrO_2 than for Ni/SiO_2, highlighting the beneficial role of zirconia on the activation of oxygenated reactants, as already proposed in literature [14,22,47]. Indeed, the oxygen vacancies (oxophilic sites) present on zirconia can favor the adsorption of m-cresol through its oxygen atom on Zr cations, allowing the activation of the phenolic compound. In this case, hydrogen activated on metallic Ni particles participates on both hydrogenation and hydrogenolysis reactions. Such cooperative effect between metallic particles and ZrO_2 was already described to explain the HDO of phenol [14] and stearic acid [22]. A similar trend is observed for the transformation of 3-MCHols into MCH, k_1 value being two times higher for Ni/ZrO_2 compared to Ni/SiO_2. It can be assumed that the alcohol is also adsorbed on zirconia cations through its oxygen atom similarly as m-cresol. In the case of SiO_2, weak acid sites (silanol groups) may not allow an activation of oxygenated compounds, explaining the lower activity of Ni/SiO_2.

The rate of dehydration of alcohols was estimated by k_2 values. The irrelevant k_2 value of Ni/SiO_2 is an accordance with the fact that this catalyst does not feature any acidity, as observed by NH_3-TPD (Figure 6-4). On the contrary, the k_2 value was much higher over Ni/ZrO_2, showing that the dehydration of alcohols was favored over this catalyst due to the support acidity. As a consequence, the 3-methylcyclohexanol isomers were mainly deoxygenated by hydrogenolysis over Ni/SiO_2 and by dehydration over Ni/ZrO_2. Indeed, the k_1/k_2 ratio was high over the former (equal to 12) and low over the latter (equal to 0.6). As

expected, the k_4 values measuring the isomerization of MCH into ECP (an acid-catalyzed reaction) followed the same trend than k_2.

Among all kinetic values determined for nickel supported on SiO_2 and ZrO_2, only the k_3 value was higher on Ni/SiO_2. This result indicates that the hydrogenating properties related to the hydrogenation of alkenes into MCH was favored when SiO_2 was used as support. Actually, such observation may be explained by two main reasons: the difference in (i) particle sizes of nickel and/or (ii) the composition of alkenes mixture. Firstly, as the particles of Ni were smaller on SiO_2 (Table 6-2), it seems reasonable that the hydrogenation of alkenes is favored on Ni/SiO_2 compared to Ni/ZrO_2, as proposed in literature [48]. Secondly, the alkenes mixture was mainly composed by 3- and 4-methylcyclohexenes over Ni/SiO_2 (Table 6-4). As these isomers present a higher reactivity in hydrogenation than 1-methylcyclohexene [49], this also justifies the higher value of k_3 determined over Ni/SiO_2.

Irrespective to the support, it is clear that all kinetic constant values increased considerably when Ni_2P-based catalysts were used instead of Ni-based catalysts (Table 6-3). Nevertheless, the influence of the support seems not to be the same for metallic and phosphide phases. As discussed above, the k_{DDO} and k_1 values measure the rate of the C-O bond scission of m-cresol and methylcyclohexanols, respectively. These values were practically the same for Ni_2P/SiO_2 and Ni_2P/ZrO_2, showing that hydrogenolysis reaction was not impacted by the nature of the support. On the contrary, the steps involving hydrogenation of either aromatic ring (k_{HYD}) or double bond (k_3) were higher on Ni_2P/ZrO_2 than on Ni_2P/SiO_2. It can be noted that the increase of both k_2 (dehydration) and k_4 (isomerization) is in line with the modification of the acidic properties of catalyst (Figure 6-4).

It is well known that the Ni_2P phase is constituted by an orthorhombic crystalline structure that can present two different types of terminations along the (0001) direction, Ni_3P and Ni_3P_2 [30,50–52]. Recently, using cresol isomers as model molecules and Ni_2P/SiO_2 as catalyst, we proposed that the Ni_3P phase could be involved in the hydrogenation reactions and the Ni_3P_2 in hydrogenolysis of C-O bond [27]. These proposals are in line with various studies reported in literature concerning HDO and HDS reactions [38,47,53]. It was proposed that

cresol isomer can be adsorbed through their oxygen atom on three Ni neighbor atoms (hollow site), present on the Ni_3P_2 termination, leading to C-O bond cleavage. Consequently, no effect of support is expected in this case, explaining why similar k_{DDO} and k_1 values were obtained for Ni_2P/SiO_2 and Ni_2P/ZrO_2 (Table 6-3).

Considering the HYD route, we have already suggested that the initial step requires a flat adsorption of m-cresol through its aromatic ring on the Ni_3P termination allowing the complete hydrogenation of the aromatic ring leading to oxygenated intermediates (3-MCHnone and 3-MCHol) [27]. The fact that Ni_2P/ZrO_2 presented a higher k_{HYD} than Ni_2P/SiO_2 may be explained by several factors. As discussed above for Ni-based catalysts, ZrO_2 can contribute indirectly activating m-cresol through its oxygen atom on Zr cations. Another reason could be the difference in particle size of Ni_2P, being twice higher on ZrO_2 (Table 6-2). Mortensen et al. reported that the bigger Ni particles have higher activity for the hydrogenation of aromatic ring of phenol [54], which could also be the case for Ni phosphide catalysts.

4. Conclusion

The present study focused on the hydrodeoxygenation of m-cresol using both Ni and Ni_2P active phases supported either on silica or zirconia. It was clearly demonstrated that the phosphide nickel phase (Ni_2P) supported on zirconia was the more efficient catalyst used in deoxygenation of the model phenolic compound. This result was explained by the intrinsic deoxygenating properties of the Ni_2P active phase associated to the presence of oxygen vacancies (oxophilic sites) located on zirconia. Indeed, zirconia allow the activation of m-cresol through its oxygen atom adsorption on Zr cationic species facilitating deoxygenation. Such cooperative effect between the active phase and zirconia was highlighted for both Ni and Ni_2P. The lower textural properties (specific surface areas and porous volume) and dispersion of both active phases on zirconia seems to have a limited influence on the catalytic properties of Ni and Ni_2P based catalysts.

For all catalysts, m-cresol was deoxygenated through two parallel routes involving either C-O bond cleavage (Direct DeOxygenation route), or hydrogenation, dehydration, isomerization and hydrogenolysis steps (HYDrogenation route). The latter was always the major deoxygenation route and led mainly to methylcyclohexane. Toluene, the only DDO product, was more favored on Ni_2P than on Ni, even though this deoxygenation route remained relatively low over all catalysts used. It was highlighted that zirconia can promoted the HYD route over both active phases (Ni and Ni_2P) and the DDO route for Ni catalyst. The rate reaction of the DDO pathway of both Ni_2P catalysts was independent of the nature of support (silica or zirconia).

5. References

[1] T. Kan, V. Strezov, T.J. Evans, Renew. Sustain. Energy Rev. 57 (2016) 1126–1140.

[2] D.C. Elliott, Curr. Opin. Chem. Eng. 9 (2015) 59–65.

[3] C. Li, X. Zhao, A. Wang, G.W. Huber, T. Zhang, Chem. Rev. 115 (2015) 11559–11624.

[4] H. Shafaghat, P.S. Rezaei, W.M.A.W. Daud, RSC Adv. 5 (2015) 103999–104042.

[5] G. Yildiz, M. Pronk, M. Djokic, K.M. van Geem, F. Ronsse, R. Van Duren, W. Prins, J. Anal. Appl. Pyrolysis. 103 (2013) 343–351.

[6] H. Prajitno, R. Insyani, J. Park, C. Ryu, J. Kim, Appl. Energy. 172 (2016) 12–22.

[7] Y. Romero, F. Richard, S. Brunet, Appl. Catal. B Environ. 98 (2010) 213–223.

[8] V.O. Gonçalves, S. Brunet, F. Richard, Catal. Lett. 146 (2016) 1562–1573.

[9] O.İ. Şenol, T.-R. Viljava, A.O.I. Krause, Appl. Catal. Gen. 326 (2007) 236–244.

[10] S. Brillouet, E. Baltag, S. Brunet, F. Richard, Appl. Catal. B Environ. 148–149 (2014) 201–211.

[11] L. Nie, D.E. Resasco, J. Catal. 317 (2014) 22–29.

[12] L. Wang, H. Wan, S. Jin, X. Chen, C. Li, C. Liang, Catal. Sci. Technol. 5 (2014) 465–474.

[13] P.M. de Souza, R.C. Rabelo-Neto, L.E.P. Borges, G. Jacobs, B.H. Davis, T. Sooknoi, D.E. Resasco, F.B. Noronha, ACS Catal. 5 (2015) 1318–1329.

[14] P.M. Mortensen, J.-D. Grunwaldt, P.A. Jensen, A.D. Jensen, Acs Catal. 3 (2013) 1774–1785.

[15] C.A. Teles, R.C. Rabelo-Neto, J.R. de Lima, L.V. Mattos, D.E. Resasco, F.B. Noronha, Catal. Lett. 146 (2016) 1848–1857.

[16] X. Zhang, Q. Zhang, T. Wang, L. Ma, Y. Yu, L. Chen, Bioresour. Technol. 134 (2013) 73–80.

[17] C. Zhao, Y. Yu, A. Jentys, J.A. Lercher, Appl. Catal. B Environ. 132–133 (2013) 282–292.

[18] L. Nie, P.M. de Souza, F.B. Noronha, W. An, T. Sooknoi, D.E. Resasco, J. Mol. Catal. Chem. 388–389 (2014) 47–55.

[19] X. Zhang, T. Wang, L. Ma, Q. Zhang, T. Jiang, Bioresour. Technol. 127 (2013) 306–311.

[20] P.M. Mortensen, D. Gardini, H.W.P. de Carvalho, C.D. Damsgaard, J.-D. Grunwaldt, P.A. Jensen, J.B. Wagner, A.D. Jensen, Catal. Sci. Technol. 4 (2014) 3672–3686.

[21] S. Foraita, J.L. Fulton, Z.A. Chase, A. Vjunov, P. Xu, E. Baráth, D.M. Camaioni, C. Zhao, J.A. Lercher, Chem. – Eur. J. 21 (2015) 2423–2434.

[22] B. Peng, X. Yuan, C. Zhao, J.A. Lercher, J. Am. Chem. Soc. 134 (2012) 9400–9405.

[23] K. Li, R. Wang, J. Chen, Energy Fuels. 25 (2011) 854–863.

[24] H. Zhao, D. Li, P. Bui, S. Oyama, Appl. Catal. Gen. 391 (2011) 305–310.

[25] A. Berenguer, T. Sankaranarayanan, G. Gómez, I. Moreno, J. Coronado, P. Pizarro, D. Serrano, Green Chem. 18 (2016) 1938–1951.

[26] S.T. Oyama, T. Onkawa, A. Takagaki, R. Kikuchi, S. Hosokai, Y. Suzuki, K.K. Bando, Top. Catal. 58 (2015) 201–210.

[27] V.O. Gonçalves, P.M. de Souza, V.T. da Silva, F.B. Noronha, F. Richard, Appl. Catal. B Environ. 205 (2017) 357–367.

[28] A. Infantes-Molina, E. Gralberg, J. Cecilia, E. Finocchio, E. Rodríguez-Castellón, Catal. Sci. Technol. 5 (2015) 3403–3415.

[29] J.A. Cecilia, A. Infantes-Molina, E. Rodríguez-Castellón, A. Jiménez-López, S.T. Oyama, Appl. Catal. B Environ. 136–137 (2013) 140–149.

[30] J.-S. Moon, E.-G. Kim, Y.-K. Lee, J. Catal. 311 (2014) 144–152.

[31] S.-K. Wu, P.-C. Lai, Y.-C. Lin, Catal. Lett. 144 (2014) 878–889.

[32] H. Shi, J. Chen, Y. Yang, S. Tian, Fuel Process. Technol. 118 (2014) 161–170.

[33] S.-K. Wu, P.-C. Lai, Y.-C. Lin, H.-P. Wan, H.-T. Lee, Y.-H. Chang, ACS Sustain. Chem. Eng. 1 (2013) 349–358.

[34] J.-S. Moon, Y.-K. Lee, Top. Catal. 58 (2015) 211–218.

[35] L. Lutterotti, S. Matthies, H. Wenk, MAUD: a friendly Java program for material analysis using diffraction, IUCr Newsl. CPD. 21 (1999).

[36] G. Leofanti, M. Padovan, G. Tozzola, B. Venturelli, Catal. Today. 41 (1998) 207–219.

[37] J. Chen, H. Shi, L. Li, K. Li, Appl. Catal. B Environ. 144 (2014) 870–884.

[38] S.T. Oyama, Y.-K. Lee, J. Catal. 258 (2008) 393–400.

[39] I. Rossetti, C. Biffi, C.L. Bianchi, V. Nichele, M. Signoretto, F. Menegazzo, E. Finocchio, G. Ramis, A. Di Michele, Appl. Catal. B Environ. 117–118 (2012) 384–396.

[40] A. Wang, M. Qin, J. Guan, L. Wang, H. Guo, X. Li, Y. Wang, R. Prins, Y. Hu, Angew. Chem. 120 (2008) 6141–6143.

[41] S. Oyama, X. Wang, Y.-K. Lee, K. Bando, F. Requejo, J. Catal. 210 (2002) 207–217.

[42] P.M. de Souza, R.C. Rabelo-Neto, L.E. Borges, G. Jacobs, B.H. Davis, U.M. Graham, D.E. Resasco, F.B. Noronha, ACS Catal. 5 (2015) 7385–7398.

[43] Y. Yang, C. Ochoa-Hernández, V.A. de la Peña O'Shea, J.M. Coronado, D.P. Serrano, ACS Catal. 2 (2012) 592–598.

[44] P.M. de Souza, L. Nie, L.E. Borges, F.B. Noronha, D.E. Resasco, Catal. Lett. 144 (2014) 2005–2011.

[45] H. Idriss, M.A. Barteau, Adv. Catal. 45 (2000) 261–331.

[46] M. Peereboom, B. Van de Graaf, J. Baas, Recl. Trav. Chim. Pays-Bas. 101 (1982) 336–338.

[47] L.F. Feitosa, G. Berhault, D. Laurenti, T.E. Davies, V.T. da Silva, J. Catal. 340 (2016) 154–165.

[48] M. Che, C.O. Bennett, TAdv. Catal. 36 (1989) 55–172.

[49] R.A.W. Johnstone, J.-Y. Liu, L. Lu, D. Whittaker, J. Mol. Catal. Chem. 191 (2003) 289–294.

[50] R. Prins, M.E. Bussell, Catal. Lett. 142 (2012) 1413–1436.

[51] A.E. Nelson, M. Sun, A.S. Junaid, J. Catal. 241 (2006) 180–188.

[52] Q. Yuan, H. Ariga, K. Asakura, Top. Catal. 58 (2015) 194–200.

[53] H. Zhao, S.T. Oyama, H.-J. Freund, R. Włodarczyk, M. Sierka, Appl. Catal. B Environ. 164 (2015) 204–216.

[54] P.M. Mortensen, J.-D. Grunwaldt, P.A. Jensen, A.D. Jensen, Catal. Today. 259, Part 2 (2016) 277–284.

6. Supplementary Information

Kinetic model

In order to obtain more information about the transformation of m-cresol, a kinetic analysis was employed using an adequate power law model. A proper equation can be written:

$$r_{Tot} = -\frac{dC_{CRE}}{d\tau} = k\ {C_{CRE}}^{\alpha}\ {P_{H_2}}^{\beta} \quad (1)$$

where r_{Tot} is the total rate of the transformation of cresols, k is the reaction rate constant, C_{CRE} the molar fraction of a given cresol, P_{H_2} the partial pressure of hydrogen, τ the space time defined previously, α the reaction order in the cresol isomer, and β the reaction order in H_2.

As hydrogen was used in a large excess compared to cresols, the hydrogen partial pressure was assumed to be constant. In addition, a pseudo-first order behavior was used to describe HDO of m-cresol. Consequently, Eq. (1) can be simplified as follows:

$$r_{Tot} = -\frac{dC_{CRE}}{d\tau} = k_{Tot}\ C_{CRE} \quad (2)$$

where k_{Tot} is the global apparent constant.

Several differential equations related to the transformation of m-cresol can be written. For a shake of simplicity, the concentrations of oxygenated compounds have been put together and named C_{oxy}.

$$\frac{dC_{CRE}}{d\tau} = -(k_{DDO} + k_{HYD})\ C_{CRE} \quad (3)$$

$$\frac{dC_{Tol}}{d\tau} = k_{DDO}\ C_{CRE} \quad (4)$$

$$\frac{dC_{Oxy}}{d\tau} = k_{HYD}\ C_{CRE} - k_1\ C_{Oxy} - k_2\ C_{Oxy} \quad (5)$$

$$\frac{dC_{MCHes}}{d\tau} = k_2\ C_{Oxy} - k_3\ C_{MCHes} \quad (6)$$

$$\frac{dC_{MCH}}{d\tau} = k_1\, C_{Oxy} + k_3\, C_{MCHes} - k_4\, C_{MCH} \quad (7)$$

$$\frac{dC_{ECP}}{d\tau} = k_4\, C_{MCH} \quad (8)$$

where k_{DDO}, k_{HYD}, k_1, k_2, k_3, k_4 are the intrinsic rate constants involved in the transformation of m-cresol. C_{Tol}, C_{Oxy}, C_{MCHes}, C_{MCH} and C_{ECP} are the molar fraction of toluene, oxygenates, methylcyclohexenes, methylcyclohexane and ethylcyclopentane, respectively.

The system of equations above (Eqs. (3) to (8)) was solved applying Runge–Kutta 4th order numerical integration algorithm. Data fitting was performed by minimizing the residual sum of squares (RSS, Eq. (9)) between the molar fraction of each product obtained experimentally and the calculated values.

$$RSS = \sum\left(C_{i,exp} - C_{\mathrm{i,cal}}\right)^2 \quad (9)$$

where $C_{i,exp}$ and $C_{i,cal}$ are the experimental and calculated molar fraction of a component i.

Figure S6-1 : H_2-TPR following PH_3 formation (m/z = 34) for nickel phosphide catalysts.

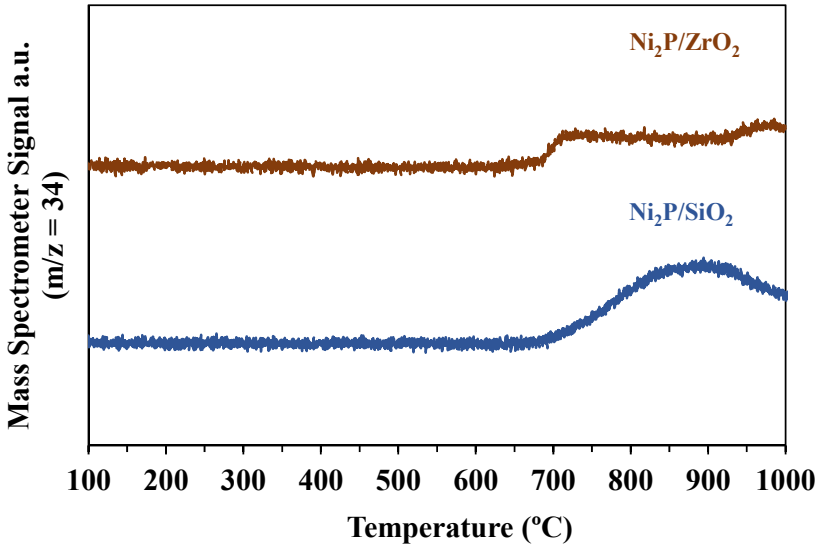

Figure S6-2 : Experimental (symbols) and calculated (dash lines) yields into products from the transformation of m-cresol at 4 MPa and 340 °C; toluene (●); oxygenates (◆); methylcyclohexenes (■); methylcyclohexane (▲); ethylcyclopentane (×).

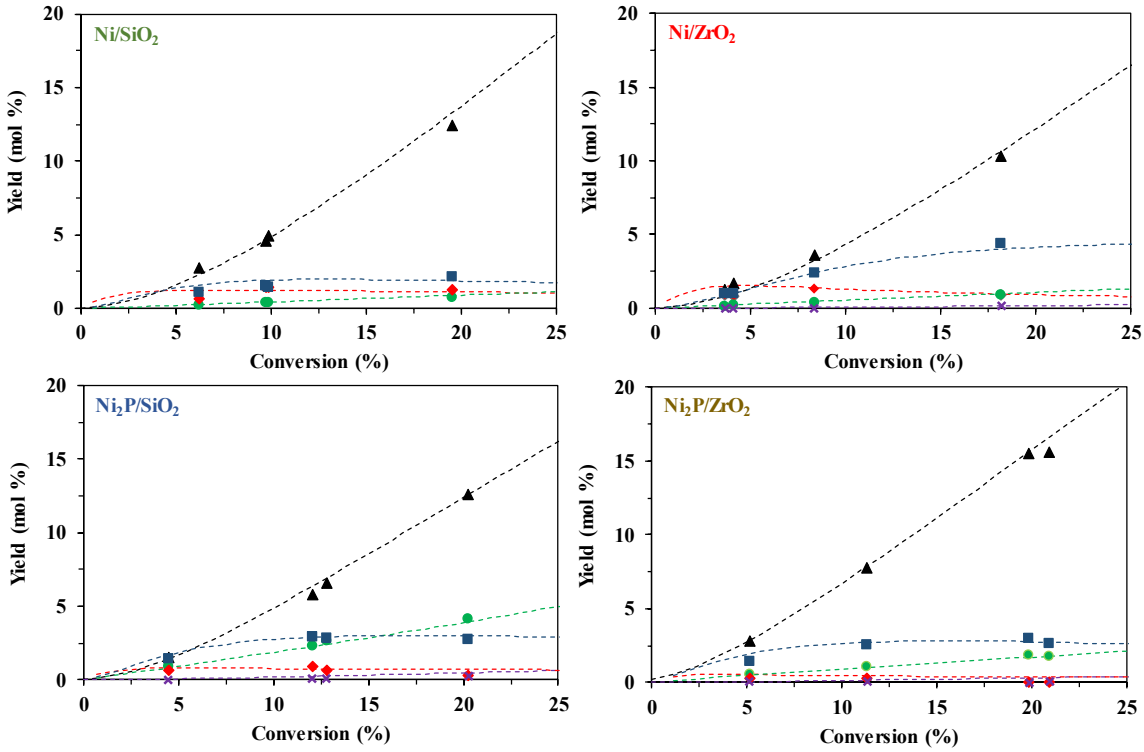

Conclusion générale

Conclusion générale

Les travaux présentés dans ce manuscrit de thèse ont montré que différentes phases catalytiques peuvent être utilisées en HDO de composés phénoliques : des phases soit à base de molybdène (sulfure ou oxyde), soit à base de nickel (métallique ou phosphure). Il a clairement été mis en évidence que les propriétés catalytiques, notamment en termes d'activité et de sélectivité, dépendent des phases actives utilisées. De plus, il a été montré que ces propriétés peuvent être impactées par le support catalytique utilisé.

Les composés phénoliques, notamment les crésols, sont des molécules modèles particulièrement intéressantes à utiliser pour caractériser des catalyseurs d'HDO car elles permettent de chiffrer aisément les éventuelles modifications des propriétés catalytiques de ces solides. En effet, la désoxygénation de ces composés phénoliques s'effectue selon deux voies de transformation. La première voie, impliquant la rupture directe de la liaison C-O, nommée voie DDO, conduit uniquement à la formation de toluène. La deuxième voie de désoxygénation, notée HYD, implique différentes réactions consécutives, notamment l'hydrogénation du noyau aromatique, le produit final attendu étant le méthylcyclohexane. Selon cette voie, d'autres produits peuvent également être formés, impliquant des réactions de déshydratation, d'isomérisation et d'hydrogénolyse. L'étude de la distribution de ces produits permet également d'obtenir des informations sur la présence ou non d'autres types de sites actifs, notamment des sites acides.

L'étude de la transformation des crésols (o-, m- p-crésol) sur les phases sulfures MoS_2 et CoMoS supportées sur alumine (Mo/Al_2O_3 et $CoMo/Al_2O_3$) a mis en évidence un fort effet promoteur du cobalt sur l'activité globale en HDO (Figure i). Cet effet promoteur du Co est important sur la voie DDO alors que la voie HYD est moins impactée, la sélectivité DDO/HYD est donc fortement dépendante de la phase sulfure utilisée, comme indiqué dans la Figure ii. Ainsi, quel que soit l'isomère étudié, le catalyseur $CoMo/Al_2O_3$ est particulièrement actif en formation du toluène. Par ailleurs, l'ordre de réactivité des trois isomères phénoliques est indépendant de la phase sulfure utilisée, et suit l'ordre : m-crésol > p-crésol > o-crésol. L'ensemble de ces résultats a permis de confirmer les principales hypothèses formulées dans la littérature concernant la nature des sites actifs impliqués lors de la désoxygénation des composés phénoliques. Ainsi, la voie DDO implique uniquement des lacunes anioniques (CUS) qui sont favorisées sur la phase CoMoS. En revanche, la voie HYD impliquerait, quant à elle,

différents sites actifs : des lacunes anioniques (également actives en DDO), des sites totalement soufrés situés sur les bords des feuillets des phases sulfures (nommés « Brim sites »), ainsi que des sites acides présents sur les phases sulfures et/ou sur le support catalytique (Alumine). Il a été mis en évidence une grande stabilité de ces phases sulfures, notamment grâce à l'introduction d'un agent soufré dans la charge réactionnelle, le diméthyldisulfure.

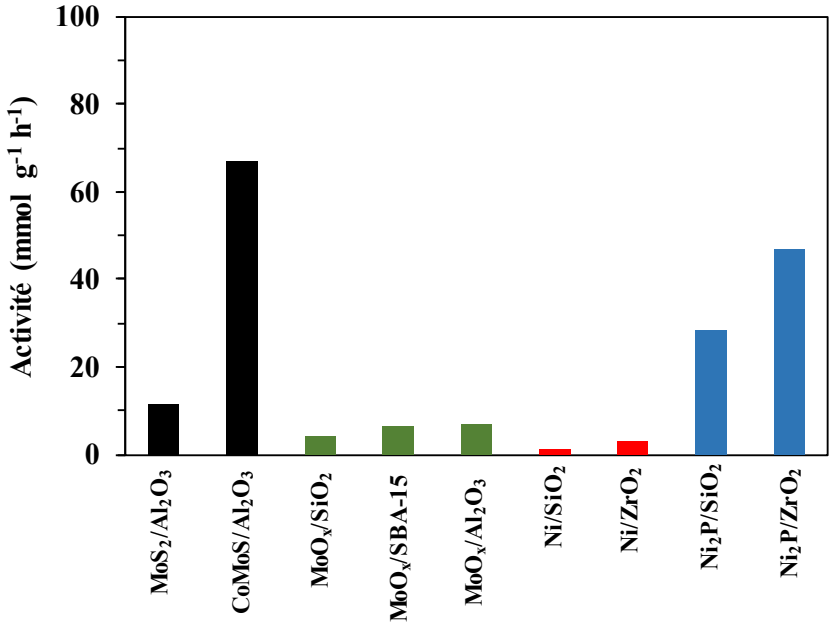

Figure i : Activité en HDO des catalyseurs sulfures, oxyde, métallique et phosphure.

Malgré des activités plus faibles comparées au catalyseur Mo/Al_2O_3 sulfuré (Figure i), les oxydes de molybdène supportés pourraient être des catalyseurs prometteurs en HDO, notamment pour produire sélectivement des composés aromatiques à partir de composés phénoliques (Figure ii). En effet, quel que soit le catalyseur utilisé, la sélectivité en toluène à partir du m-crésol est toujours supérieure à 80 %mol. Une influence de la nature du support sur l'activité en désoxygénation a été mise en évidence, l'ordre d'activité étant MoO_x/Al_2O_3 > MoO_x/SBA-15 > MoO_x/SiO_2. L'effet du support a pu être attribué en partie à la différence de réductibilité des oxydes de molybdène. Comparé à un support inerte (SiO_2), leur réductibilité a été améliorée soit par l'utilisation d'un support acide (Al_2O_3), soit par l'utilisation d'un support mésoporeux ordonné de haute surface spécifique (SBA-15). Ainsi, il a été proposé que le nombre de sites actifs présents, des lacunes en oxygène sur le molybdène, sont fonction du

support utilisé. Ce nombre est le plus élevé sur MoO_x/Al_2O_3 et le plus faible sur MoO_x/SiO_2. Néanmoins, la nature des sites actifs ne semble pas être affectée par le support catalytique. De plus, tous les catalyseurs ont présenté une stabilité remarquable dans les conditions expérimentales utilisées, probablement en raison de l'utilisation d'une pression élevée en hydrogène (3,2 MPa).

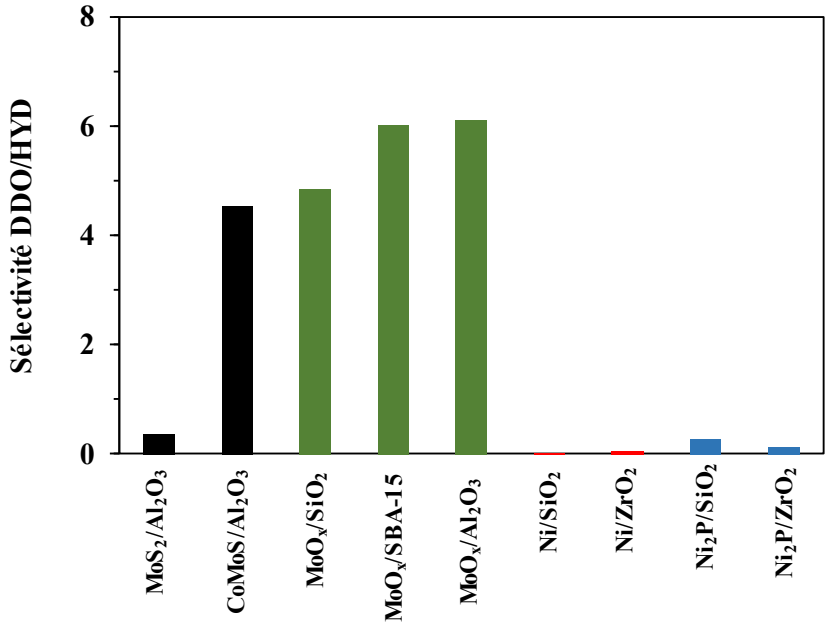

Figure ii : Sélectivité DDO/HYD des catalyseurs sulfures, oxyde, métallique et phosphure en transformation du m-crésol.

Les performances catalytiques d'une phase phosphure de nickel déposée sur silice (Ni_2P/SiO_2) ont également été évaluées en détails pour l'HDO des crésols. La transformation des composés phénoliques a impliqué des réactions d'hydrogénolyse, d'hydrogénation, de déshydration et d'isomérisation. Contrairement aux phases oxydes et sulfures à base de molybdène, des produits oxygénés ont été observés (cétones et alcools), indiquant donc que cette phase phosphure de nickel semble moins sélective en désoxygénation. Comme observé pour les phases sulfures, un effet de la position du groupe méthyle a été mis en évidence, dépendant de la voie de désoxygénation considérée. De plus, la température de réaction favorise plus la voie DDO alors qu'une augmentation de la pression d'hydrogène est plus bénéfique pour la voie HYD. Pour expliquer l'influence de ces différents paramètres, plusieurs types de sites

actifs, ainsi que différents modes d'adsorption des composés phénoliques ont été proposés permettant d'expliquer la formation de l'ensemble des produits observés expérimentalement. Comme pour les autres phases catalytiques, il a clairement été mis en évidence une très bonne stabilité de ce catalyseur à base de phosphure de nickel, attribuée là encore à l'utilisation d'une pression élevée en hydrogène.

Enfin, il apparait qu'il est possible de promouvoir l'activité de la phase Ni_2P en la déposant sur de la zircone. Cette promotion a été attribuée à un effet de synergie entre ZrO_2 et Ni_2P (Figure i). La zircone permet d'activer le composé oxygéné via son adsorption sur une lacune anionique impliquant une espèce Zr(IV), la phase Ni_2P promouvant (i) soit la rupture de la liaison C-O du composé phénolique donnant directement du toluène, (ii) soit l'hydrogénation du cycle aromatique conduisant, après plusieurs étapes successives, au méthylcyclohexane. Le fait d'utiliser un support acide permet également de réduire fortement la quantité de composés oxygénés. De plus, il a été mis en évidence qu'une phase phosphure de nickel possède des propriétés désoxygénantes beaucoup plus intéressantes qu'un catalyseur uniquement à base de nickel métallique (Figure ii).

Ce travail de thèse a donc permis de discriminer un certain nombre de phases catalytiques susceptibles d'être utilisées dans un procédé d'HDO, qui pourrait être un procédé clé d'une bioraffinerie. Par rapport aux résultats obtenus, il semble clair que les propriétés catalytiques de ces matériaux peuvent encore être optimisées, notamment en modifiant les supports catalytiques utilisés.

Avant de valider un matériau catalytique pour une application donnée, il est évidemment important de le tester dans des conditions plus réalistes. Ainsi, l'utilisation de charges modèles plus complexes, incluant la présence de différentes fonctions oxygénées, notamment des acides carboxyliques provenant de la transformation de micro algues (considérés comme les biocarburants de troisième génération) pourrait constituer l'étape ultérieure.

Résumé : Dans une bioraffinerie, la biomasse peut être transformée par différents procédés (thermiques, chimiques et biochimiques) en carburants et en produits chimiques à haute valeur ajoutée. Plus spécifiquement, le procédé catalytique d'hydrodésoxygénation (HDO) devrait permettre de valoriser à la fois les bio-huiles obtenues par pyrolyse en biocarburants, ainsi que les composés aromatiques oxygénés issus de la dépolymérisation de la lignine en aromatiques simples.

Afin de modéliser la désoxygénation de ces fractions, les isomères du crésol (ortho-, méta- et para-crésol) ont été choisis comme molécules oxygénés modèles. Les réactions ont été effectuées sous haute pression (2-4 MPa) et à des températures comprises entre 250 et 340 °C. Plusieurs phases actives à base de molybdène (sulfures et oxyde) et de nickel (métallique et phosphure) ont été étudiées. L'influence du support des phases oxydes de molybdène (SiO_2, SBA-15, Al_2O_3) et des phases à base de nickel (SiO_2 et ZrO_2) a également été examinée.

Dans ces conditions expérimentales, les composés phénoliques sont désoxygénés selon deux voies de transformations parallèles. La voie de désoxygénation directe (DDO) conduit uniquement au toluène par hydrogénolyse de la liaison C-O. La voie hydrogénante (HYD), quant à elle, conduit à un mélange de produits obtenus après hydrogénation du cycle aromatique, impliquant des réactions d'hydrogénolyse, d'hydrogénation, de déshydratation et d'isomérisation. L'activité des catalyseurs ainsi que la contribution de chaque voie de désoxygénation sont dépendantes de la phase active étudiée, du support choisi ainsi que des conditions opératoires utilisées.

Abstract: In a biorefinery, biomass can be converted by different process (thermal, chemical and biochemical) into fuels and valued-added chemicals. More specifically, the catalytic hydrodeoxygenation (HDO) process could upgrade both bio-oils obtained from pyrolysis into biofuels and oxygenated aromatic compounds from the depolymerization of lignin into aromatics.

In order to model the deoxygenation of these fractions, the cresol isomers (ortho, meta and para-cresol) were chosen as model oxygenated molecules. The reactions were carried out under high pressure (2-4 MPa) and temperatures between 250 and 340 °C. Several active phases based on molybdenum (sulphides and oxide) and nickel (metal and phosphide) have been studied. The influence of the support of the molybdenum oxide phases (SiO_2, SBA-15, Al_2O_3) and of the nickel-based phases (SiO_2 and ZrO_2) was also examined.

Under these experimental conditions, phenolic compounds are deoxygenated by two parallel pathways. The direct deoxygenation (DDO) route only leads to toluene by hydrogenolysis of the C-O bond. The hydrogenating route (HYD), on the other hand, leads to a mixture of products obtained through the hydrogenation of cresol aromatic ring, involving hydrogenolysis, hydrogenation, dehydration and isomerization reactions. The activity of the catalysts as well as the contribution of each deoxygenation pathway are dependent on the active phase studied, on the support chosen as well as on the operating conditions used.